Dipl. Ing. Markus Goldgruber

Nonlinear Seismic Modelling of Concrete Dams

DOCTORAL THESIS

to achieve the university degree of

Doktor der technischen Wissenschaften

submitted to

Graz University of Technology

Tutor

Univ.-Prof. Dipl.-Ing. Dr.techn. Gerald Zenz
Institute of Hydraulic Engineering and Water Resources Management

2. Reviewer

Prof. Vahid Lotfi, PhD
Amirkabir University of Technology - Department of Civil & Enviromental Engineering

Graz, August 2015

AFFIDAVIT

I declare that I have authored this thesis independently, that I have not used other than the declared sources/resources, and that I have explicitly indicated all material which has been quoted either literally or by content from the sources used. The text document uploaded to TUGRAZonline is identical to the present doctoral thesis.

Date

Signature

ABSTRACT

Large dam structures are built as water storage facilities in mountainous regions to use the potential difference for energy production. Geotechnical faults in these zones are not uncommon, which is why earthquakes are a potential hazard to dams. Due to an expected lifetime of more than 100 years the seismic assessment is mandatory to retain the integrity of such structures. The most important part is to ensure the stability of the dam body itself. The dynamic assessment is mostly done by means of finite elements for linear assumptions, which allows for the use of response spectrum methods or modal superposition. Nonlinear simulations are not common and primary used in research, because of the elaborateness and the requirement of a solid theoretical knowledge. They also require time histories with specific time steps of the seismic loading to account for nonlinearities implied to the model, and hence increase the computation time. In case of seismic excitations of dams the reservoir must be taken into account properly. Therefore, this thesis discusses two typical added mass approaches and a newly developed one for inclined surfaces, as well as the more sophisticated acoustic fluid continuum approach.

In this thesis two concrete dam models, a gravity dam and a high arch dam, with different levels in detail are evaluated regarding their nonlinear response at seismic loading. Nonlinearities by means of contact discretization of the base of the gravity dam model are investigated for different friction angles, reservoir models, scaling effects and pre- and post-seismic cases. Furthermore, a comparison of cumulative displacements with a simplified limit equilibrium method is also done. For the arch dam model the focus is on to discretization of the blocks and the base contact. Influences of different modelling methods of the dead weight loading and its impact on subsequent steps in nonlinear simulations are discussed. In addition, linear and nonlinear seismic simulations are compared as well as three reservoir filling levels. Nonlinearities arising from the material due to cracks from seismic excitations are simulated by means of the Extended Finite Element Method (XFEM).

In conclusion, the applicability of nonlinear simulations and its restrictions and differences of the simplified or linear methods are pointed out. Evaluation of displacements and stresses show that the linear approach doesn’t necessarily lead to conservative results and specific parameters might influence the response significantly. Hence, nonlinear simulations should be treated with caution and need comprehensive evaluation of experienced staff with a theoretical and practical knowledge.

KURZFASSUNG

Große Talsperren werden im Gebirge zum Aufstau eines Reservoirs gebaut, um aus dem erzeugten Potential Energie zu gewinnen. Geologische Störzonen sind meist Teil dieser Regionen und somit von Erdbeben betroffen. Aufgrund der Lebensdauer von Talsperren von mehr als 100 Jahren ist es unbedingt nötig, dass die Standfestigkeit solcher Strukturen gewährleistet wird. Dabei steht die Stabilität der Sperre selbst im Vordergrund. Zur dynamischen Vorbemessung wird dabei oft die Finite Elemente Methode mit der Annahme eines linearen Verhaltens herangezogen, was die Anwendung der Antwortspektrenmethode oder Modale Superposition erlaubt. Nichtlineare Simulationen sind meist nicht üblich und aufgrund ihrer Komplexität und der Voraussetzung eines soliden theoretischen Hintergrundes hauptsächlich in der Forschung präsent. Zusätzlich werden für Berechnungen Zeitverläufe mit bestimmten Zeitschritten benötigt um die nichtlineare Antwort der Struktur richtig abzubilden, was zusätzlich die Rechenzeit erhöht. Im Falle von Erdbebenbelastungen von Talsperren muss auch die dynamische Anregung des Reservoirs berücksichtigt werden. Dafür werden in dieser Arbeit neben zwei der meist verwendete Methoden der addierten Massen zusätzlich eine neu entwickelte, zur die Berücksichtigung von geneigten Flächen, präsentiert. Weiters wird auch die Anwendung von direkt modellierten Volumina als Acoustic Fluid Kontinuum diskutiert.

In dieser Arbeit werden zwei Talsperren aus Beton mit unterschiedlichen Detailierungsgraden auf ihr nichtlineares Verhalten bei seismischer Beanspruchung untersucht. Der Einfluss von Nichtlinearitäten bezüglich Kontaktdiskretisierung in der Aufstandsfläche einer Gewichtsmauer wird für unterschiedliche Reibungswinkel, Reservoirmodelle, Skalierungseffekte und pre- und postseismische Fälle überprüft. Des Weiteren wird ein Vergleich der Endverschiebung mit vereinfachten Grenzgleichgewichtsmethoden durchgeführt. Am Bogenstaumauermodell liegt der Fokus auf der Diskretisierung der Blöcke und der Basisfuge. Neben der Auswirkung von unterschiedlichen Simulationstechniken des Eigengewichtszustandes wird auch deren Einfluss auf nachfolgende nichtlineare Berechnungsschritte diskutiert. Zusätzlich werden die Ergebnisse mit denen eines linearen Berechnungsansatzes und drei unterschiedlichen Wasserständen im Speicher verglichen. Nichtlineares Materialverhalten aufgrund von Rissen durch die seismische Belastung wird mit der Extended Finite Element Method (XFEM) simuliert und ausgewertet.

Schlussendlich wird die Anwendbarkeit von nichtlinearen Simulationen, ihre Grenzen und Unterschiede zu vereinfachten oder linearen Methoden aufgezeigt. Die Auswertung von Verformungen und Spannungen zeigen, dass ein linearer Ansatz nicht notwendigerweise zu konservativen Ergebnissen führt und spezielle Parameter das Ergebnis signifikant beeinflussen können. Somit sollten Ergebnisse von nichtlinearen Berechnungen mit Vorsicht behandelt werden und bedürfen einer ausführlichen Evaluierung von erfahrenen Experten mit theoretischem und praktischem Wissen.

ACKNOWLEDGEMENTS

This thesis has been carried out between October 2011 and August 2015 at the Institute of Hydraulic Engineering and Water Resources Management - Graz University of Technology. Without the guidance and encouragement of several people this thesis wouldn't exist.

First of all I want say thank you to Univ.-Prof. Dipl.-Ing. Dr.techn. *Gerald Zenz* for his review, guidance, critical thoughts and advises. Without our fruitful discussions this thesis wouldn't have been possible the way it is. I also want to express my sincere gratitude to Prof. *Vahid Lotfi* for his reviewing and helpful comments to improve this thesis.

A huge thank you to my colleague *Richard Malm* from KTH Royal Institute of Technology for making the collaboration and research stay in Stockholm possible. His expertise and help on the simulations carried out are an essential part of this thesis.

I also want to express my gratitude to all my colleagues from the Institute of Hydraulic Engineering and Water Resources Management for the good atmosphere. Thereby, I especially want to say thank you to *Clemens Dorfmann* for our always rewarding (non-exclusively technical) after work discussions and *Shervin Shahriari* for his contributions to specific parts of this thesis and his help on the evaluation of many results and paper publication.

Special thanks to all *professors, assistants*, *colleagues* and *friends* who helped me on my way.

My last and biggest thank you goes to *my parents* for their support through my whole education and hence making all of this possible and to *Marlene*. Thank you so much.

To Marlene,

my beloved.

ABOUT THE AUTHOR

Personal Data

Name: Markus Goldgruber

Birth date: 20.01.1985

Nationality: Austria

Education

2011 – 2015	Doctoral Programme in Engineering Sciences
2014 (August)	Outgoing – Staff Training, KTH Royal Institute of Technology Department of Civil and Architectural Engineering / Division of Concrete Structures, Stockholm, Sweden; Topic: *3D Arch Dam modelling, nonlinear Finite Element simulations and evaluation of joint openings due to the dynamic process of Fluid-Structure-Foundation-Interaction.*
2012	Advancement Award of ATCOLD (Austrian Committee on Large Dams)
2009 – 2011	Master Programme - Civil Engineering Sciences, Geotechnics and Hydraulics, University of Technology Graz
2010	Winner of the Amann-Foundation for excellent accomplishments in the field of Structural Analysis
2006 – 2009	Bachelor Programme - Civil Engineering Sciences with Environment and Construction Management, University of Technology Graz
1999 – 2004	Technical High School for Mechanical Engineering and Automatization, Kapfenberg

Projects/Surveys and Investigations carried out

Hydraulic Structures – Research Project funded by PÖYRY ENERGY GmbH

- Static and dynamic simulations of concrete dams
- Development of an User Subroutine for Abaqus

ICOLD - 12th International Benchmark Workshop on Numerical Analysis of Dams

- Formulator and reviser of Theme A - Fluid Structure Interaction Arch Dam - Reservoir at Seismic Loading

River Mur Hydropower Plant Graz (Murkraftwerk Graz), Physical model test 1:40

- Evaluation of the model test results for the construction phase and final design regarding normal water depth, weir capacity, turbine inflow velocity, sediment transport, etc.

Hierzmann Arch Dam, Physical model test 1:15

- Evaluation of static and dynamic pressures at the crest and in the stilling basin due to jet impact, weir capacity, influence of different weir designs
- Writing of a script for the evaluation process in Python
- Numerical modelling and simulation of dynamic vibrations due to weir overflow

Weir Gstins, Physical model test 1:30

- Evaluation of the model test results regarding normal water depth, weir capacity, stilling basin capacity, impacts of different designs of the weir and the stilling basin, etc.

Köprü HPP, Turkey, Investigation Report - Köprü – Diversion – Gate; Dynamic Excitation due to underflow

- Numerical Investigations of stop log excitations and abutment forces due to underflow by means of fluid-structure interaction

Publications (Journal Papers, Conference Contributions, Reports, etc.)

Goldgruber, M., Shahriari, S., & Zenz, G. (2015). *Dynamic Sliding Analysis of a Gravity Dam with Fluid-Structure-Foundation Interaction using Finite Elements and Newmark's Sliding Block Analysis.* Rock Mechanics and Rock Engineering, in Press.

Goldgruber, M., Shahriari, S., & Zenz, G. (2014). *Dynamische Wasser-Struktur-Interaktion einer Bogenstaumauer mit unterschiedlichen numerischen Ansätzen (Dynamical Fluid-Structure Interaction of an Arch Dam with different numerical approaches)*. Wasser- und Flussbau im Alpenraum, 29 - 39

Zenz, G., Schneider, J., Goldgruber, M., & Lazar, F. (2014). *Physical model test report – Hierzmann Arch Dam.* Institute for Hydraulic Engineering and Water Resources Management

Zenz, G., Hammer, A., & Goldgruber, M. (2014). *Physical model test report – River Mur Hydropower Plant Graz (Murkraftwerk Graz)*. Institute for Hydraulic Engineering and Water Resources Management

Zenz, G., Hammer, A.; Goldgruber, M.; & Knoll, M. (2014). *Physical model test report – Weir Gstins*. Institute for Hydraulic Engineering and Water Resources Management

Zenz, G., & Goldgruber, M. (2014). *12th ICOLD Benchmark Workshop Conference Proceedings.*

Goldgruber, M. & Zenz, G. (2013). *Benchmark for success.* International water power & dam construction 8, 30 – 32

Goldgruber, M., Zenz, G., & Shahriari, S. (2013). *Dynamic Stability Analysis of a Gravity Dam with Newmark-Method.* Geomechanik Kolloquium Salzburg - Failure Prediction in Geotechnics. 27 – 32

Goldgruber, M., & Feldbacher, R. (2013). *Empirischer Ansatz zur Ermittlung der mitschwingenden Wassermasse bei dynamischer Wasser-Bauwerks-Interaktion (Empirical Approach for Defining the Excited Water Mass for Fluid-Structure Interactions.* 15th JUWI Treffen 2013 - Fachbeiträge zur Tagung, 1 – 6

Goldgruber, M., Zenz, G., & Shahriari, S. (2013). *Influence of damping and different interaction modelling on a high arch dam*. Vienna Congress on Recent Advances in Earthquake Engineering and Structural Dynamics.

Goldgruber, M., Zenz, G., & Shahriari, S. (2013). *2D Dynamic Sliding Analysis of a Gravity Dam with Fluid-Foundation-Structure Interaction.* Geomechanik Kolloquium Salzburg - Failure Prediction in Geotechnics, 23 – 26

Goldgruber, M., Feldbacher, R., & Zenz, G. (2012). *Mitwirkung des Wassers bei Erdbebenberechnungen von Talsperren.* Wasserbausymposium Proceedings, 251 - 258

Zenz, G., Goldgruber, M., & Feldbacher, R. (2012). *Seismic Stability of a Rock Wedge in the Abutment of an Arch Dam.* Geomechanics and Tunnelling 5, 186 – 194

Goldgruber, M. (2012*). Felskeilstabilität im Widerlager einer Bogenstaumauer bei Erdbeben: Numerische Untersuchung (Dam Abutment Stability of an Arch Dam – Numerical Investigation)*. Akademikerverlag

Zenz, G., Feldbacher, R., & Goldgruber, M. (2012). *Hydraulic Structures – Research Report.* Institute for Hydraulic Engineering and Water Resources Management

Goldgruber, M., Feldbacher, R., & Zenz, G. (2011). *Seismic Stability of a Rock Wedge in the Abutment of an Arch Dam.* Geomechanik Kolloquium Salzburg - Calculation Methods in Geotechnics, S. 80 – 87

Presentations/Speeches

Modellwahl für die Erdbebenberechnung von Talsperren (Modelling of Earthquake Simulations of Concrete Dams). ATCOLD Kolloquium. (2015)

Nonlinear Seismic Analysis of an Arch Dam using XFEM. SIMULIA Austria - Regional User Meeting. (2014)

Research Field and Topic. Royal Institute of Technology KTH, Stockholm. (2014)

Research Field and Topic. SWECO AB, Stockholm. (2014)

Sliding Safety and Displacement of a Gravity Dam at Seismic Loading according to Guidelines, Newmark Method and Finite Elements. 7th Vienna Rock Mechanics Colloquium. (2014)

2D Dynamic Sliding Analysis of a Gravity Dam with Fluid-Foundation-Structure Interaction. Geomechanik Kolloquium Salzburg. (2013)

Result comparison for Theme A - Fluid Structure Interaction. 12th International Benchmark Workshop on Numerical Analysis on Dams. (2013)

Influence of damping and different interaction modelling on a high arch dam. Vienna Congress on Recent Advances in Earthquake Engineering and Structural Dynamics. (2013)

Empirischer Ansatz zur Ermittlung der mitschwingenden Wassermasse bei dynamischer Wasser-Bauwerks-Interaktion. 15th JUWI-Treffen. (2013)

Mitwirkung des Wassers bei Erdbebenberechnungen von Talsperren. Wasserbausymposium. (2012)

Dam abutment stability under earthquake loading. 6th Rock Mechanics Colloquium Vienna. (2012)

Dynamic Dam-Reservoir Interaction with different modelling techniques. Dissertation Seminar, TU Graz. (2012)

Seismic stability of a rock wedge in the abutment of an arch dam. Geomechanik Kolloquium Salzburg. (2011)

Lectures (Tutor)

Hydraulic Engineering Basics (Bachelor)

- Structural safety calculation and evaluation of concrete and fill dams

Hydraulic Engineering Advanced (Master)

- Structural safety calculation and evaluation of concrete and fill dams
- Hydraulic assessment and design of operation facilities (Bottom outlet, diversion, spillways, etc.)
- Supervision of preliminary design projects of gravity dams, arch dams and fill dams

Numerics in Hydraulics (Master)

- Introduction to programming with Python

Supervised Master Theses

Radial Gate Excitation on a Gravity Dam due to Seismic Loading. Stefan Pagger (2015)

Arch Dam Design and Optimization. Manuel Pagitsch (2012)

Talsperrenüberwachung einer Gewölbemauer am Beispiel der Hierzmannsperre (Dam Monitoring of the Hierzmann Arch Dam). Herbert Geiger (2012)

CONTENTS

LIST OF FIGURES .... **vii**

LIST OF TABLES .... **xiii**

LIST OF SYMBOLS .... **xv**

1 INTRODUCTION **1**

2 DYNAMIC MODELLING IN THE FINITE ELEMENT METHOD **5**

- 2.1 Direct Time Integration Methods 6
  - 2.1.1 Implicit Time Integration 6
    - 2.1.1.1 Time Integration according to Newmark 6
    - 2.1.1.2 Time Integration according to Hilber, Hughes and Taylor 10
  - 2.1.2 Explicit Time Integration 11
  - 2.1.3 Stability and Accuracy of Time Integration Methods 13
- 2.2 Modal Superposition 15
- 2.3 Structural Damping 17
  - 2.3.1 Rayleigh Damping 18
  - 2.3.2 Modified Rayleigh Damping 20
  - 2.3.3 Problems regarding the Use of Rayleigh Damping in Nonlinear Systems 23

3 FLUID MODELLING METHODS OF DAM-RESERVOIR INTERACTIONS **25**

- 3.1 Added Mass according to Westergaard 26
- 3.2 Added Mass according to Zangar 28
- 3.3 Empirical Added Mass Approach for Inclined Surfaces 30
- 3.4 Added Mass Transformation for Non-Vertical Surfaces 35
- 3.5 Acoustic Fluid 38
  - 3.5.1 Impact of Consideration of the Water Compressibility 39
  - 3.5.2 Coupling of the Acoustic Fluid and Structural Domain 39
  - 3.5.3 Acoustic Fluid Boundary Conditions 41
    - 3.5.3.1 Free Surface Boundary 42
    - 3.5.3.2 Back-End Boundary 42
    - 3.5.3.3 Bottom and Side Boundaries 44

4 SEISMIC DISPLACEMENT OF A GRAVITY DAM **47**

- 4.1 Introduction 47
- 4.2 The Gravity Dam Model 48
- 4.3 Earthquake Acceleration-Time-History Records 49

4.4 Methods for the Displacement Evaluation ... 50
4.4.1 Newmark's Sliding Block Analysis ... 50
4.4.1.1 Yield Accelerations ... 51
4.4.2 Empirical Estimation of the Newmark Displacement ... 54
4.4.2.1 Ambraseys and Menu ... 54
4.4.2.2 Jibson93 ... 55
4.4.2.3 Jibson98 ... 55
4.4.3 The Numerical Method ... 55
4.4.3.1 2D Structural Finite Element Model ... 55
4.4.3.2 Contact Modelling ... 56
4.4.3.3 Reservoir Modelling with the Added Mass Method ... 59
4.4.3.4 Reservoir Modelling with Acoustic Elements ... 59
4.4.3.5 Grout Curtain and Pore Water Pressure ... 59
4.4.3.6 Structural Damping ... 59
4.4.3.7 Dynamic Modelling ... 61
4.5 Results and Discussion ... 62
4.5.1 Results of Newmark's Sliding Block Analysis ... 62
4.5.2 Results of the Numerical Method ... 63
4.5.2.1 Displacement Results for the Model with Grout Curtain ... 63
4.5.2.2 Displacement Results for the Model without Grout Curtain ... 65
4.5.3 Results Comparison between Newmark's Sliding Block Analysis and Finite Element Method ... 67
4.6 Conclusion ... 67
5 LINEAR SEISMIC ARCH DAM SIMULATIONS ... 71
5.1 The Benchmark Workshop ... 71
5.1.1 Focus of the Benchmark Example of Theme A ... 72
5.1.2 General Basic Assumptions ... 72
5.1.3 Model and Geometry ... 73
5.1.3.1 Arch Dam Model ... 73
5.1.3.2 Foundation Model ... 74
5.1.3.3 Reservoir Model ... 74
5.1.3.4 Mesh Properties ... 75
5.1.3.5 Earthquake Acceleration-Time-History-Records ... 76
5.1.3.6 Material Parameters ... 76
5.1.3.7 Loading ... 77
5.1.4 List of Participants, Programs and Approaches ... 77
5.1.5 Discussion and Results ... 79

5.1.5.1 Natural Frequencies 79
5.1.5.2 Displacements 80
5.1.5.3 Stresses 81

5.1.6 Conclusion 83

5.2 Investigation of the Influence of Damping Factors 83

5.2.1 Program Implementation of the Added Mass Approach 84
5.2.2 Damping Factors 84
5.2.3 Results and Discussion 85

5.2.3.1 Natural Frequencies 85
5.2.3.2 Hoop and Vertical Stresses 86

5.2.4 Conclusion 88

6 NONLINEAR SEISMIC ARCH DAM SIMULATIONS 89

6.1 Constructional Details of Arch Dams and Loadings 90

6.1.1 Dead Weight 90
6.1.2 Hydrostatic Water Load 91
6.1.3 Seismic Loading 91
6.1.4 Tensile Stresses at Dam-Rock Interface 92
6.1.5 Construction Stages and Block Joint Grouting 92

6.2 Nonlinear Arch Dam Model 94

6.3 Contact Modelling in the Block Joints 96

6.4 Contact Modelling of the Interface between Dam and Foundation 98

6.5 Material Modelling of the Concrete 99

6.5.1 Compressive Material Behaviour 99
6.5.2 Tensile Material Behaviour 100

6.6 Dead Weight Modelling 101

6.6.1 Without Consideration of Separated Blocks 101
6.6.2 Orthogonal Material Behaviour 102
6.6.3 Separation of Blocks 103
6.6.4 Discrete Blocks with Contact 104
6.6.5 Comparison and Discussion of the Dead Weight Loading 105
6.6.6 Discussion regarding Displacements from the Dead Weight Loading 106
6.6.7 Conclusion of the Dead Weight Loading 107

6.7 Hydrostatic Modelling 107

6.7.1 Influence of Displacements from preceding Dead Weight Simulations 108
6.7.2 Influence of the Tangential Contact Stiffness (elastic slip) 110
6.7.3 Contact Behaviour between the Blocks 112
6.7.4 Principal Stresses of the Linear and Nonlinear Model for Hydrostatic Water Loading 113

6.7.4.1 Minimum Principal Stress Comparison 113
6.7.4.2 Maximum Principal Stress Comparison.. 113
6.8 Seismic Modelling 114
6.8.1 Contact Modelling and Boundary Conditions of the Reservoir 115
6.8.2 Modified Rayleigh Damping Factors 115
6.9 Results of the Nonlinear Seismic Simulations 118
6.9.1 Comparison with Linear Simulations from the Benchmark Workshop 118
6.9.1.1 Comparison of the Displacement 119
6.9.1.2 Comparison of the Hoop Stresses 119
6.9.1.3 Comparison of the Vertical Stresses 120
6.9.2 Influences of Different Reservoir Filling Levels....................................... 120
6.9.2.1 Comparison of the Displacement 121
6.9.2.2 Comparison of the Hoop Stresses 122
6.9.2.3 Comparison of the Vertical Stresses 122
6.9.2.4 Comparison of the Contact Opening in the Base 123
6.9.2.5 Comparison of the Contact Behaviour between Blocks................ 124
6.9.3 Contact Behaviour between the Blocks for increased Seismic Accelerations and different Friction Coefficients 125
6.9.3.1 Contact Behaviour for a Friction Coefficient of 0.5 126
6.9.3.2 Contact Behaviour for a Friction Coefficient of 2.0 127
6.9.4 Nonlinear Material and Crack Propagation with XFEM............................ 129
6.9.4.1 Crack Propagation for a Maximum Acceleration of 2.0 m/s² 129
6.9.4.2 Crack Propagation in only One Block for Higher Accelerations.. 130
6.10 Conclusion of the Nonlinear Seismic Simulations 132
7 CONCLUSION... 135
7.1 Further Research 138
BIBLIOGRAPHY 141
APPENDIX 149
A BASICS OF CONTINUUM MECHANICS 151
A.1 Kinematics of the Continuum 151
A.2 Kinetics of the Continuum.. 157
A.3 Conservation of Mass 161
A.4 Principle of Virtual Work 162
A.5 Application of Strain and Stress Tensors... 163
B INTRODUCTION TO THE EXTENDED FINITE ELEMENT METHOD FOR STRONG DISCONTINUITIES (XFEM) 165

B.1 Modelling Discrete Continuities 165
B.2 Partition of Unity Concept and Enrichment 166
B.3 Level Set Functions and Shifting of the Enrichment 167
B.4 Crack Tip Enrichment 169

C LIST OF ICOLD PUBLICATIONS REGARDING NUMERICAL ANALYSIS OF DAMS 171

C.1 Themes of Benchmark Workshops on Numerical Analysis of Dams from 1991 to 2015 171
C.2 ICOLD Bulletins regarding Dam Analysis and Seismic Modelling 173

LIST OF FIGURES

Figure 2-1: Schematic representation of direct time integration or time-stepping methods 6
Figure 2-2: Constant acceleration distribution between the time step 7
Figure 2-3: Linear acceleration distribution between the time step 7
Figure 2-4: Illustration of the stability of the Newmark algorithm for a simple three storey building for different time steps and approaches... 9
Figure 2-5: Illustration of the central differences approach.. 12
Figure 2-6: Free vibration solution by four numerical methods and the theoretical solution by Chopra (2011)... 14
Figure 2-7: a) Amplitude decay versus $\Delta t/Tn$; b) Definition of AD and PE; c) Period elongation; by Chopra (2011).. 14
Figure 2-8: Illustration of Rayleigh damping.. 19
Figure 2-9: Damping curve before and after modification of the Rayleigh damping................ 21
Figure 2-10: Program flow chart for calculating the modified Rayleigh constants 22
Figure 3-1: Westergaard added mass distribution... 26
Figure 3-2: Comparison between the rigorous and simplified Westergaard equation 27
Figure 3-3: Point of origin of the resultant water mass.. 28
Figure 3-4: Model setup for measuring the dynamic water pressure in a reservoir according to Zangar et al. (1952) 28
Figure 3-5: Streamlines and pressure coefficient in the reservoir by Zangar et al. (1952) 29
Figure 3-6: Maximum pressure coefficient and pressure coefficient at the bottom for different angles of the upstream surface of a dam by Zangar et al. (1952) 30
Figure 3-7: Pressure coefficient for different angles of the upstream surface of a dam by Zangar et al. (1952) 30
Figure 3-8: Finite elements model to investigate the dynamic water pressure distribution over the height of a rigid body with acoustic elements at constant acceleration............ 31
Figure 3-9: Relationship between the depth of the water and the resultant maximum pressure coefficient at the bottom for zero inclination 31
Figure 3-10: Relationship between the maximum pressure in the reservoir and the inclination of the upstream surface... 32
Figure 3-11: Normalized pressure and height relationship and comparison of the height were the maximum pressures occur between the numerical result and equation (3-12). 33
Figure 3-12: Schematic figure for the empirical equation according Goldgruber and Feldbacher (2013).. 33
Figure 3-13: Comparison between the numerical results with acoustic fluid elements and the new empirical formula normalized to the highest pressure 34
Figure 3-14: a) Total added mass for different total reservoir depths and upstream surface inclinations; b) Centroid height hs where the total added mass acts for different total reservoir depths and upstream surface inclinations....................................... 35
Figure 3-15: Mass vector transformation on a two dimensional surface 36
Figure 3-16: Different reservoir boundaries for an acoustic fluid... 42

Figure 3-17: Value of wave reflection coefficient at which finite reservoir effects are not apparent by Baumber (1992) 43
Figure 4-1: Sketch of the Gravity Dam and its dimensions 48
Figure 4-2: Uplift pressure distribution with a fully intact grout curtain (left) and a ruptured (post seismic case) grout curtain (right).......... 49
Figure 4-3: Acceleration-time-history records in 2 directions 50
Figure 4-4: Illustration of Newmark’s Sliding Block Analysis.......... 51
Figure 4-5: Static and dynamic forces on the dam model 52
Figure 4-6: Yield acceleration of the gravity dam for different friction coefficients and water levels 53
Figure 4-7: Yield acceleration by including vertical acceleration for, e.g. $\mu s = 0.84$.......... 54
Figure 4-8: 2D finite element gravity dam model 56
Figure 4-9: Elastic slip and slip tolerance definition based on Dassault Systèmes (2013) 57
Figure 4-10: Normal contact formulation for “Hard Contact” based on Dassault Systèmes (2013).......... 58
Figure 4-11: Gravity dam displacements for different friction coefficients (Newmark’s Sliding Block Analysis) 62
Figure 4-12: Comparison of empirical equations and Newmark’s Sliding Block Analysis.......... 62
Figure 4-13: Gravity dam displacement for different friction coefficients between acoustic elements and Westergaard added mass for a height of 62.5 meters 63
Figure 4-14: Gravity dam displacement for different friction coefficients between acoustic elements and Westergaard added mass for a height of 125.0 meters 64
Figure 4-15: Cumulative displacement comparison for different friction coefficients between the models with acoustic elements, Westergaard added mass and the two different heights of the structure 64
Figure 4-16: Gravity dam displacement for different friction coefficients between acoustic elements and Westergaard added mass for a height of 62.5 meters. Linear pore water pressure distribution in the contact plane (no grout curtain).......... 65
Figure 4-17: Gravity dam displacement for different friction coefficients between acoustic elements and Westergaard added mass for a height of 125.0 meters. Linear pore water pressure distribution in the contact plane (no grout curtain).......... 66
Figure 4-18: Cumulative displacement comparison for different friction coefficients between the models with and without grout curtain and the two different heights of the structure (Only for the model with acoustic elements) 66
Figure 4-19: Comparison of estimated cumulative displacements for different friction coefficient between Newmark’s Sliding Block Analysis and FE Method (62.5 meters high model with grout curtain) 67
Figure 4-20: Failure mechanism; Falling block of an arch dam.......... 69
Figure 5-1: Benchmark workshop arch dam geometry figures from the program Arch Dam Design 73
Figure 5-2: Foundation model.......... 74
Figure 5-3: Reservoir model.......... 74
Figure 5-4: Mesh densities of the coarse and fine arch dam model 75

Figure 5-5: Acceleration-time-history records in 3 directions 76
Figure 5-6: Sections for displacement and stress evaluation 79
Figure 5-7: Main section of the arch dam and up- and downstream definition 79
Figure 5-8: Minimum, maximum and static displacement for all participants in the main section of the arch dam 81
Figure 5-9: Minimum, maximum and static hoop stresses for all participants in the main section on the upstream surface of the arch dam 82
Figure 5-10: Natural frequency comparison of the three modelling methods 85
Figure 5-11: Evaluation heights of the stresses and deformations in the main section on the upstream surface 86
Figure 5-12: Minimum, maximum and static displacement at 220m (crest) and 110m on the upstream surface in the main section 87
Figure 5-13: Minimum, maximum and static hoop stresses at 220m (crest) and 110m on the upstream surface in the main section 87
Figure 5-14: Minimum, maximum and static vertical stresses at 0m (bottom) and 110m on the upstream surface in the main section 87
Figure 5-15: Hoop stresses over the height of the dam for 5% of the critical damping on the upstream surface in the main section 88
Figure 6-1: Building stages of an arch dam with alternating blocks 93
Figure 6-2: Layout of the shear keys and the water stop between two blocks of an arch dam ... 93
Figure 6-3: Illustration of the primary injection and radial force by Widmann (2005) 94
Figure 6-4: Block joint orientation of the original and the new model 95
Figure 6-5: New mesh of the arch dam model for nonlinear simulations 96
Figure 6-6: Highlighted planes between the blocks for the use of the “seam” command 96
Figure 6-7: Normal contact formulation for “Soft Contact” based on Dassault Systèmes (2013) 97
Figure 6-8: Extension of the slave surface (foundation), highlighted in grey 99
Figure 6-9: Plastic stress – strain curve for the compressive behaviour of the concrete 100
Figure 6-10: Vertical stresses [MPa] due to dead weight on the upstream surface without consideration of separated blocks 102
Figure 6-11: Vertical stresses [MPa] due to dead weight on the upstream surface with orthogonal material properties 103
Figure 6-12: Vertical stresses [MPa] due to dead weight on the upstream surface with completely separated blocks 104
Figure 6-13: Vertical stresses [MPa] due to dead weight on the upstream surface with discrete block modelling 105
Figure 6-14: Vertical stress comparison for different dead weight modelling techniques on the upstream (left) and downstream surface (right) in the main section 105
Figure 6-15: Minimum principal stress [MPa] comparison for different dead weight modelling techniques on the upstream surface; a) Isotropic model without separation of blocks, b) Orthotropic model, c) Completely separated blocks, d) Discrete blocks with contact 106

Figure 6-16: Displacement [m] in x-direction for hydrostatic water loading between the general static step (left) and the geostatic step (right) 108
Figure 6-17: Displacement in the main section for hydrostatic water loading (full reservoir case) between the general static step and the geostatic step 109
Figure 6-18: Hoop stresses in the main section for hydrostatic water loading (full reservoir case) between the general static step and the geostatic step 109
Figure 6-19: Contact opening at base due to hydrostatic water loading along the path in the main section 110
Figure 6-20: Displacement in the main section for hydrostatic water loading (full reservoir case) for different slip tolerance Ff values 110
Figure 6-21: Hoop stresses in the main section for hydrostatic water loading (full reservoir case) on the up- and downstream surface for different slip tolerance Ff values.. 111
Figure 6-22: Vertical stresses in the main section for hydrostatic water loading (full reservoir case) on the up- and downstream surface for different slip tolerance Ff values.. 111
Figure 6-23: Arch dam displacement [m] scaled 500 times (left) and contact pressure [MPa] in the main section (right).. 112
Figure 6-24: Minimum principal stresses [MPa] on the upstream surface between the linear (left) and nonlinear model (right) for hydrostatic water loading 113
Figure 6-25: Minimum principal stresses [MPa] on the downstream surface between the linear (left) and nonlinear model (right) for hydrostatic water loading 113
Figure 6-26: Maximum principal stresses [MPa] on the upstream surface between the linear (left) and nonlinear model (right) for hydrostatic water loading 114
Figure 6-27: Maximum principal stresses [MPa] on the downstream surface between the linear (left) and nonlinear model (right) for hydrostatic water loading 114
Figure 6-28: Response spectra for the acceleration-time history in x-direction for modal and modified Rayleigh damping.. 116
Figure 6-29: First 10 natural frequencies of the three reservoir filling levels 117
Figure 6-30: Rayleigh damping curves for the seismic simulations of the linear and nonlinear arch dam model for full reservoir conditions.. 117
Figure 6-31: Comparison of the displacement in the main section between the linear and nonlinear model 119
Figure 6-32: Comparison of the hoop stresses on the upstream (left) and downstream (right) side of the arch dam in the main section between the linear and nonlinear model120
Figure 6-33: Comparison of the vertical stresses on the upstream (left) and downstream (right) side of the arch dam in the main section between the linear and nonlinear model 120
Figure 6-34: Comparison of the displacement in the main section between different reservoir filling levels 121
Figure 6-35: Comparison of the displacement [m] in downstream direction between different reservoir filling levels at the end of the seismic event T_{20} = 20.0 sec (scaled 500 times) 121

Figure 6-36: Comparison of the hoop stresses on the upstream (left) and downstream (right) side of the arch dam in the main section between different reservoir filling levels 122
Figure 6-37: Comparison of the vertical stresses on the upstream (left) and downstream (right) side of the arch dam in the main section between different reservoir filling levels 123
Figure 6-38: Comparison of the contact opening between different reservoir filling levels along the path in the main section 124
Figure 6-39: Maximum contact opening [m] over all frames for a maximum acceleration of 1.0 m/s² in the main section for an empty (left), half (middle) and full reservoir (right) 124
Figure 6-40: Maximum contact slip [m] in downstream direction over all frames for a maximum acceleration of 1.0 m/s² in the main section for an empty (left), half (middle) and full reservoir (right) 125
Figure 6-41: Location of the node for the evaluation of contact behaviour 126
Figure 6-42: Comparison of the contact behaviour between two blocks at the crest for a friction coefficient of 0.5 (5.0 sec < T < 10.0 sec) 127
Figure 6-43: Comparison of the contact behaviour between two blocks at the crest for a friction coefficient of 2.0 (5.0 sec < T < 10.0 sec) 128
Figure 6-44: Maximum principal stresses [MPa] over all frames for a maximum acceleration of 1.0 m/s² on the downstream and upstream surface 129
Figure 6-45: Status of XFEM cracks at specific time instants for a maximum acceleration of 2.0 m/s² 130
Figure 6-46: Translucent arch dam with XFEM cracks after the earthquake (T=20 seconds) for a maximum acceleration of 2.0 m/s² 130
Figure 6-47: Arch dam block (black) which is allowed to crack during simulations with increased accelerations 131
Figure 6-48: Crack propagation in the observed block for maximum accelerations of a) 3.0 m/s², b) 4.0 m/s² and c) 5.0 m/s² 131
Figure 7-1: Failure mechanism; Falling block of an arch dam 139

LIST OF TABLES

Table 2-1: Stability criteria for different time integration methods 13
Table 4-1: Material properties... 56
Table 4-2: Friction coefficients and friction angles 59
Table 4-3: Natural frequencies and Rayleigh damping factors for the model with acoustic elements and Westergaard added mass and a height of 62.5 m.............................. 60
Table 4-4: Natural frequencies and Rayleigh damping factors for the model with acoustic elements and Westergaard added mass and a height of 125 m............................... 61
Table 5-1: Number of elements and nodes of the coarse and fine mesh..................................... 75
Table 5-2: Material properties of the benchmark problem.. 76
Table 5-3: Participants, Programs and Approaches 78
Table 5-4: Natural frequencies 1 – 10... 80
Table 5-5: Mass- and stiffness-proportional Rayleigh damping factors 84
Table 5-6: Modes shapes and corresponding natural frequencies for all three modelling methods.. 85
Table 6-1: Number of elements and nodes of the original coarse mesh and the new mesh........ 95
Table 6-2: Interaction properties between the block joints 97
Table 6-3: Interaction properties of the dam-foundation interface 98
Table 6-4: Material properties for the crack propagation with XFEM in Abaqus/Cae............. 101
Table 6-5: Orthotropic material properties.. 103
Table 6-6: Mass- and stiffness proportional damping factors 116

LIST OF SYMBOLS

$\boldsymbol{M}$	Mass matrix
$\boldsymbol{K}$	Stiffness matrix
$\boldsymbol{R}_t$	Force vector over time
$\ddot{\boldsymbol{u}}_t, \dot{\boldsymbol{u}}_t, \boldsymbol{u}_t$	Acceleration, velocity and displacement vector at time t
$\ddot{\boldsymbol{u}}_{t+\Delta t}, \dot{\boldsymbol{u}}_{t+\Delta t}, \boldsymbol{u}_{t+\Delta t}$	Acceleration, velocity and displacement vector at time $t + \Delta t$
Δt	Time step
τ	Time variable
γ	Newmark time integration parameters
β	Newmark time integration parameters; Stiffness-proportional damping constant for Rayleigh damping
T_n	Natural time period
$\Delta\ddot{\boldsymbol{u}}_t, \Delta\dot{\boldsymbol{u}}_t, \Delta\boldsymbol{u}_t$	Incremental acceleration, velocity and displacement vector at time t
$\Delta\boldsymbol{R}_t$	Incremental force vector over time
$\overline{\boldsymbol{K}}$	Dynamic stiffness or effective stiffness
$\overline{\Delta\boldsymbol{R}_t}$	Effective incremental force vector over time
α	Time integration parameter of the Hilber-Hughes-Taylor method or α-method; Mass-proportional damping constant for Rayleigh damping; Wave reflection factor
$\boldsymbol{u}_{t-\Delta t}$	Displacement vector at time $t - \Delta t$
$\ddot{\boldsymbol{x}}_t, \dot{\boldsymbol{x}}_t, \boldsymbol{x}_t$	Generalized acceleration, velocity and displacement vector at time t
$\boldsymbol{\varphi}$	Eigenvector
$\boldsymbol{\omega}$	Natural frequency vector
$\boldsymbol{\Phi}$	Matrix containing all eigenvectors
$\boldsymbol{\Omega}^2$	Diagonal matrix containing all squared natural frequencies
$\boldsymbol{\zeta}$	Fraction of critical damping or modal damping vector
a_k	Damping constants according to the Caughey Series
$\zeta_{m,i}$	Mass-proportional modal damping factor for mode/frequency i
$\zeta_{st,i}$	Stiffness-proportional modal damping factor for mode/frequency i
$a_{r,i}$	Response accelerations of the Rayleigh damped systems for mode/frequency i
$a_{m,i}$	Response accelerations of the modal damped systems for mode/frequency i
$m_{eff,i}$	Effective mass for mode/frequency i
ΔS	Difference between the Rayleigh and modal damped system
$\omega_{mod,i}$	First frequency for calculating the modified mass- and stiffness-proportional damping constants for Rayleigh damping

$\omega_{mod,j}$	Second frequency for calculating the modified mass- and stiffness-proportional damping constants for Rayleigh damping
$m_w(z)$	Rigorous Westergaard added mass per squaremeter
ρ_w	Density of water
h	Reservoir depth
n	Mode number
c_n	Westergaard constant
z	Reservoir depth variable
g	Gravity
K_w	Bulk modulus/compressibility of water
T	Natural period
f	Natural frequency
c_w	Wave propagation speed
$m_w^*(z)$	Simplified Westergaard added mass per squaremeter
M_w^*	Resultant simplified Westergaard added mass
$h_{w,s}$	Point of origin of the resultant mass M_w^*
p_z	Pressure in depth z
C	Pressure coefficient
a_e	Horizontal earthquake intensity
C_m	Maximum pressure coefficient
L	Length of the acoustic medium
$p_{max,0}$	Maximum pressure at zero inclination of the upstream surface
φ	Inclination of the upstream surface
$p_{max(\varphi)}$	Maximum pressure at inclination φ of the upstream surface
$h_{max,\varphi}$	Height where the maximum pressure occurs
$p_{(\varphi,z)}$	Pressure for inclination φ in depth z for the empirical added mass approach
$m_{(\varphi,z)}$	Mass for inclination φ in depth z for the empirical added mass approach
$m_{(z)}$	Mass for zero inclination in depth z for the empirical added mass approach
h_s	Centroid depth where the total added mass is acting on the upstream surface
n_x	x-component of the normal vector
n_y	y-component of the normal vector
$\boldsymbol{m}$	Mass vector
m_x	x-component of the mass
m_y	y-component of the mass
$m_{x,T}$	Tangential component of the mass m_x
$m_{x,N}$	Normal component of the mass m_x
$m_{y,T}$	Tangential component of the mass m_y
$m_{y,N}$	Normal component of the mass m_y
$\boldsymbol{M}_w^N$	Consistent mass matrix which neglects tangential components

$\boldsymbol{N}_c$	Transformation matrix for the consistent mass matrix
$\boldsymbol{M}^{\boldsymbol{e}}_{\boldsymbol{added}}$	Added mass on the element level
α_z	Pressure constant in a specific depth z in mass per squaremeter
$\boldsymbol{p}$ or $p\boldsymbol{I}$	Pressure tensor
$\boldsymbol{v}$, $\dot{\boldsymbol{v}}$	Particle velocity and acceleration vector
p_{free}	Acoustic fluid pressure on the free surface
f_n	Lysmer-Kuhlemeyer damping force in normal direction
u_n	Displacement in normal direction of the reservoir boundary
u_s	Displacement in shear direction of the reservoir boundary
$p_{reflected}$	Reflected pressure
$p_{incident}$	Incident pressure
L_{min}	Minimum reservoir length
R	Material property ratio
ρ_r	Density of bottom material of the reservoir
c_r	Wave propagation speed of the bottom material of the reservoir
E_r	Young’s modulus of the bottom material of the reservoir
c	Real value of the complex impedance
k	Imaginary value of the complex impedance
$\dot{u}_{out}$	Outgoing velocity of the fluid boundary
$\dot{p}$	Rate of change of the pressure at the fluid boundary
f_r	Fundamental natural frequency of a simplified reservoir with infinite length and constant depth
f_d	Fundamental natural frequency of the dam structure alone
Ω_r	Ratio between the fundamental natural frequency of the reservoir and the fundamental natural frequency of the dam alone
$u_S\|_n$	Normal displacement at the structure boundary
$u_F\|_n$	Normal displacement at the acoustic fluid boundary
$\sigma_S\|_n$	Normal stress at the structure boundary
$-p_F\|_n$	Pressure at the acoustic fluid boundary
$\boldsymbol{N}_S$, $\boldsymbol{N}_F$	Finite element shape function for the structural and fluid domain
$\boldsymbol{M}_S$, $\boldsymbol{M}_F$	Finite element mass matrices for the structural and fluid domain
$\boldsymbol{K}_S$, $\boldsymbol{K}_F$	Finite element stiffness matrices for the structural and fluid domain
$\boldsymbol{D}_S$	Constitutive finite element matrix of structure
$\boldsymbol{u}_S$, $\boldsymbol{p}_F$	Finite element approximation of the displacements and the pressure
$\boldsymbol{f}_S$, $\boldsymbol{f}_F$	Surface loads from the structure and acoustic fluid acting at the boundaries
$\boldsymbol{t}_S$	Surface traction
S	Fluid-structure coupling area
$\boldsymbol{H}_{SF}$	Coupling matrix at the fluid-structure boundary in finite element formulation
$\ddot{u}_{rel}(t)$	Relative acceleration of the rigid block at time t

$a(t)$	Horizontal acceleration of the acceleration-time history at time t
$a_{\mathrm{v}(t)}$	Vertical acceleration of the acceleration-time history at time t
a_y	Yield acceleration
$\dot{u}_{rel}$	Relative sliding velocity
$H_{d(t)}$	Quasi-static hydrodynamic force
H_s	Hydrostatic force
$Ma_{(t)}$	Horizontal inertia force of the rigid block
$Ma_{\mathrm{v}(t)}$	Vertical inertia force of the rigid block
W	Weight of the rigid block
M	Mass of the rigid block
F	Friction force of the rigid block
U	Uplift force
γ_w	Specific weight of the water
$P_{hd}(z)$	Quasi-static hydrodynamic pressure on the upstream surface of the dam
μ_s	Friction coefficient between the rigid block and the foundation
D_N	Newmark displacement in centimetres
a_{max}	Maximum acceleration of the acceleration-time history
I_A	Arias intensity
T_d	Duration of the ground motion
$\gamma_{elastic}$	Elastic slip
F_f	Elastic slip tolerance
$\overline{l_\iota}$	Characteristic length of the contact surface
τ_{crit}	Critical shear stress in the contact plane
μ	Friction coefficient
p	Contact pressure
c_c	Contact clearance

1 INTRODUCTION

Concrete dam structures are mostly built in mountainous regions where active geological fault zones with high seismicity are not uncommon. Compared to buildings construction where large towers, for instance, are designed and built to bear mainly vertical loads, dams are designed to primarily withstand substantial horizontal loads (hydrostatic water load). This fact makes concrete dams more resistant to seismic loads than other buildings. Nevertheless, for dam structures, which have an economical lifetime of more than 100 years, the assessment by means of seismic safety is mandatory, regardless of existing or newly built structures. Guidelines of the ICOLD (2013) – Committee on Computational Aspects of Analysis and Design of Dams are published with recommendations on the role and use of numerical models for static and dynamic dam design. Dam structures undergoing an Operating or Design Basis Earthquake (OBE or DBE) a linear-elastic analysis with higher safety margins is sufficient. Dams which are effected by a Maximum Credible Earthquake (MCE) with a return period of 3000-10000 years might suffer severe damage, but without collapsing. In case of such a scenario nonlinear simulations can be done to evaluate and ensure the structures integrity.

Apart from the assessment to retain the integrity of the structure itself Wieland (2012) pointed out that earthquakes are multi-hazards which can affect large dam projects in many ways. Some of those are:

- Damage of appurtenant structures and equipment
- Rockfall on structures or in the reservoir causing damage or waves
- Fault or mass movements
- Etc.

Furthermore, he mentioned the possibility of large reservoirs triggering seismicity during impounding in the first years of operation. These secondary effects cannot be entirely forecast and can only be accounted for with simplified and conservative approaches.

Nevertheless, in the first place in the seismic assessment of concrete dams stands the stability of the structure itself. By means of finite element analyses many possibilities exist for taking into account the dynamic load from a seismic event. Most standards for earthquake assessment are based on design response spectra for peak ground acceleration at specific areas. Another method would be modal superposition, where preceding frequency/mode analyses are performed and afterwards superposed to get dynamic response of the system. These methods work well for linear problems, but are not applicable to nonlinear systems. In case of large concrete dam structures nonlinear effects like base- and block joint openings or cracks in the structure might not be negligible.

For nonlinear assessments of structures time-histories of the ground motion are needed, because the stiffness might change over time and is generally reduced. This change also influences its natural frequencies and therefore the dynamic behaviour. Due to the fact that seismic events cannot be forecast, site records or artificially generated time histories are used. Such ground motions are then applied to the model to evaluate the dynamic behaviour and hence design a dam that withstands these loads. For dynamic simulations different time integration methods in implicit and explicit formulation are available with their specific advantages and disadvantages. In the implicit family the two most commonly used, and described as part of this thesis, in dynamic analysis nowadays are the one by Newmark (1959) and the one by Hilber, Hughes and Taylor (1977). One explicit method is also discussed. Damping in time domain analyses of discretized systems is mostly introduced by means of Rayleigh damping coefficients, because damping matrices for even simple problems are normally not known. Lord Rayleigh (1877) invented this mass- and stiffness proportional method based on modal analysis already in 1877. For calculating the damping coefficients two specific natural frequencies one has to choose. Since the choice of these modes is an approach mostly based on the effective mass Spears and Jensen (2012) published a method to define these coefficients by fulfilling the dynamic equilibrium between the modal and Rayleigh damped response. Problems accompanying nonlinear simulations by using Rayleigh damping are discussed by Hall (2006).

Dynamically excited structures in general develop inertia forces, but in case of dams additionally the reservoir water must be taken into account. A still well established approach is to use added masses to model the dynamically excited water. The most popular one was developed by Westergaard (1933) during the earthquake assessment of the Hoover dam to evaluate the water pressures. Later, Zangar et al. (1952) performed physical model tests to investigate effects on inclined surfaces. Among many others these two are still the most commonly used by consulting companies due to their convenient implementation and conservative results. Nevertheless, also with Zangar’s equation, rough assumptions are implied by applying them on inclined surfaces, especially near the bottom of the dam. A new empirical equation is developed to overcome the overestimation of the added mass distribution based on numerical results for surfaces with a tip from 0° to 30° degrees.

Apart from added mass approaches a much better way to simulate the constitutive behaviour of the water is to model the water directly as an acoustic fluid. The knowledge of the basics of continuum mechanics is obligatory for the practice of fluid-structure interactions by means of dynamic dam-reservoir problems, where the principles of a Lagrangian and Eulerian description are the basis. The underlying acoustic wave equation has the advantage that it has only one degree of freedom which is the pressure. Commonly used in sound wave analyses this approach offers also a good assumption for modelling dynamically excited reservoirs, where the most interesting factor for the assessment is the additional pressure acting on the structure. Muto et al. (2012) evaluated the applicability of elements based on the acoustic fluid equation. This approach has been used more and more for many dam-reservoir interactions nowadays. Effects of compressibility can also be accounted for directly, which, according to Chopra (2008), can be an important parameter in dam-reservoir interactions and shouldn’t be neglected. Furthermore, the use of boundary conditions regarding reflections can be defined easily. The impact of different reflection coefficients at the back-end boundary (reservoir length effects) have been studied by Baumber (1992). Different reflection coefficients on the sides of the reservoir in the near field of the dam and their affects were investigated by Hall and Chopra (1980) and Fenves and Chopra (1984).

Differences between the added mass approach by Westergaard (simplified and rigorous) and acoustic fluid elements are figured out by applying these methods to a concrete gravity dam structure, which's geometry is based on the Birecik dam in Turkey. Additionally, a foundation-structure interaction by means of contact modelling with finite elements is investigated and compared with Newmark's Sliding Block Analysis, which was developed by Newmark (1965) and later modified by Chopra and Hall (1982) for the application of gravity dam structures. Results of empirical formulas by Jibson (1993), Jibson, Harp and Michael (1998) and Ambrasey and Menu (1988) are also depicted. For the finite element model two scenarios are simulated, a pre and post-seismic case. In the first case the grout curtain is still intact (reduced uplift pressure) and in the second case it's ruptured (linear uplift pressure distribution). Furthermore, all results are figured out for a two times scaled model also to evaluate possible scaling effects.

The effects of different reservoir modelling techniques on the performance of a high Arch Dam (220m) was studied within the "12th International Benchmark Workshop on Numerical Analysis of Dams" in Graz, Austria in October 2013. The "Committee on Computational Aspects of Analysis and Design of Dams" in the International Commission on Large Dams (ICOLD) organizes these workshops every second year. One of the three topics in this benchmark workshop was titled "Fluid Structure Interaction, Arch Dam - Reservoir at Seismic Loading", formulated by the Institute of Hydraulic Engineering and Water Resources Management from Graz University of Technology. The proceedings with a comprehensive representation of all results can be found in Zenz and Goldgruber (2014). Overall 13 participants presented results for the predefined problem. For comparison reasons the whole problem was kept linear. Goldgruber et al. (2013) performed a benchmark test on the same model for differing damping ratios varying from 0% to 10% of the critical damping.

However, it should be obvious that arch dams undergo nonlinear behaviour of different kinds. One is that due the massive amount of concrete and therefore the building phases, such structures are divided into almost independent vertical blocks acting like cantilevers until they are fully grouted and the reservoir is impounded. The impact of separated blocks compared to a continuous body is investigated and effects on the stress level are evaluated. A second discontinuity is implied due to the structure-foundation interaction in the base of the arch dam. Possible openings might occur due to the increasing water pressure from impounding and seismic vibrations. Different reservoir levels as well as different methods for modelling the dead weight case and its influence on following simulation steps are investigated.

Additionally to nonlinearities occurring from contact modelling between blocks and in the base nonlinear material behaviour by means of discrete cracks is also accounted for. This is primary caused by exceedance of the tensile strength of the concrete. Especially arch dams are susceptible to cracks triggered by seismic events. Simulations and modelling of discontinuities are often done with so called smeared models where cracks are enforced on the integration point of the finite element without discretization. A method developed by Belytschko and Black (1999) called Extended Finite Element Method (XFEM) allows for modelling discrete cracks which aren't dependent on the mesh topology. Cracks are therefore allowed to develop freely through elements. The method is based on so called enriched methods, which are in this case the partition of unity method (PUM) and the generalized finite element method (GFEM). The terminology “enriched” refers to the added term in the finite element approximation of displacement, which is also called “enrichment”. Although it’s still a research topic, some commercial (e.g. Abaqus) and open source codes have already implemented this technique.

Crack development in the arch dam is modelled with this applied XFEM and evaluated for five different scales of the same accelerations time history used in the “12th International Benchmark Workshop on Numerical Analysis of Dams” and the results are pointing out the possibilities and borders of such complex nonlinear simulations.

2 DYNAMIC MODELLING IN THE FINITE ELEMENT METHOD

This section gives a brief introduction and a rough overview of commonly used methods for solving the equation of motion stepwise. The following sections about time integration are mostly based on the books by Chopra (2011) and Bathe (2007). The discussed time history methods can be split up into two main procedures, the direct time integration and modal superposition. Quasi-Static methods, response spectrum methods for earthquake analysis and methods in the frequency domain are not discussed in this section, because those are restricted to linear problems.

In direct time integration methods, the underlying kinetic equations are solved step by step and equilibrium is fulfilled for each time step separately. According to which instant of time, t or $t + \Delta t$, is used for the equilibrium of the equation of motion, the schemes can be divided into explicit and implicit integration methods. These methods allow for solving nonlinear problems too.

On the contrary to the direct time integration methods, modal superposition can be used for linear problems with much more numerical efficiency. The idea in this method is to transform the coupled system of equations into a set of uncoupled ones which can later be superimposed to get the systems answer.

From an engineering point of view damping is always hard to define, due to the complexity of the structures, foundations, etc. and the use of different structural elements. Usually, damping in mechanical systems is introduced as viscous (velocity proportional) force in the equation of motion. Hence, a damping factor has to be defined for the structure, which is done by means of a critical (modal) damping ratio. In literature typical modal damping ratios can be found for specific structures and materials. These values are based on measurements and influenced by many factors, including temperature, whereby increasing temperature softens the material and therefore leads to higher damping ratios.

A lot of further damping models exist. One is the hysteretic damping, where a hysteretic damping coefficient is introduced. This model describes the behaviour of a damped vibrating system better, but with the drawback of the requirement of complex analysis. Nevertheless, the damping model discussed in this chapter and applied on the structures later in this thesis is introduced by means of viscous damping.

In numerical simulations a damping matrix has to be defined and therefore a damping value for each degree of freedom (position in the matrix). Since this is almost impossible, for even simple structures, simplifications are made. Usually one modal damping ratio is used for the whole structure. Varying factors for different regions in the model are also possible. For finite element simulations the Rayleigh damping approach, which is a stiffness and mass-proportional damping, is well-established. For the use of this approach additionally to the critical damping factor two natural frequencies have to be known. The determination of these 2 natural frequencies is normally based on experience, the effective mass under consideration and compromises in the damped frequency ranges. A method developed by Spears and Jensen (2012) is introduced in this section which allows determining these natural frequencies based on a mechanical equilibrium.

2.1 Direct Time Integration Methods

For problems with an arbitrary varying force, ground accelerations or nonlinearities it’s not possible to get an analytical solution. Hence, direct time integration or time-stepping methods divide the equation of motion in time steps Δt. In this case the equilibrium is fulfilled at discrete time intervals, but not continuously. The equation of motion at time instant t in matrix notation is

$$\boldsymbol{M}\ddot{\boldsymbol{u}}_t + \boldsymbol{C}\dot{\boldsymbol{u}}_t + \boldsymbol{K}\boldsymbol{u}_t = \boldsymbol{R}_t \tag{2-1}$$

with $\boldsymbol{M}$ as the mass matrix, $\boldsymbol{C}$ as the damping matrix, $\boldsymbol{K}$ as the stiffness matrix and $\boldsymbol{R}_t$ as the varying force over time. The displacement $\boldsymbol{u}_t$, velocity $\dot{\boldsymbol{u}}_t$ and acceleration $\ddot{\boldsymbol{u}}_t$ vectors are assumed to be known at the time t, e.g. if $t = 0$ they are called initial conditions. Direct time integration procedures allow, based on the knowledge of these motion quantities at time t, to calculated the systems response at time $t + \Delta t$ with the equation of motion written as

$$\boldsymbol{M}\ddot{\boldsymbol{u}}_{t+\Delta t} + \boldsymbol{C}\dot{\boldsymbol{u}}_{t+\Delta t} + \boldsymbol{K}\boldsymbol{u}_{t+\Delta t} = \boldsymbol{R}_{t+\Delta t} \tag{2-2}$$

Figure 2-1 depicts a schematic representation of direct time integration or time-stepping schemes.

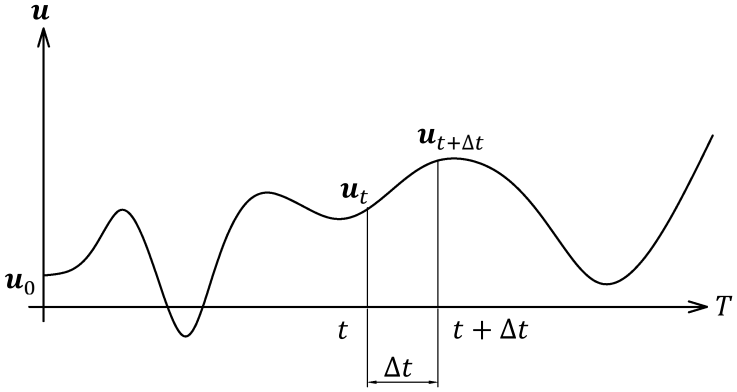

Figure 2-1: Schematic representation of direct time integration or time-stepping methods

Depending on the chosen time integration scheme different assumptions are made for stepping from t to $t + \Delta t$. Three of the most commonly used schemes in finite element simulations are presented in this section, two implicit direct time integration methods and one explicit method.

2.1.1 Implicit Time Integration

2.1.1.1 Time Integration according to Newmark

If the equilibrium equation (equation of motion) at time $t + \Delta t$ is used to solve the dynamic problem the procedure is called implicit time integration or implicit integration method. The most famous time integration scheme of the family of implicit methods is the one developed by Newmark (1959). He derived his equations based on two different assumptions, which are that the acceleration between two instants of time is constant or linear.

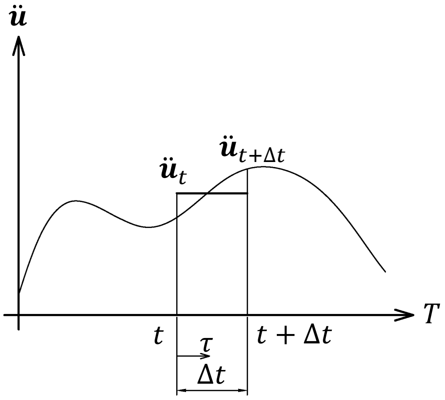

Figure 2-2: Constant acceleration distribution between the time step

By assuming a constant (average) distribution of acceleration, like it's depicted in Figure 2-2, the motion quantities at time $t + \Delta t$ are

$$\ddot{\boldsymbol{u}}(\tau) = \frac{1}{2}(\ddot{\boldsymbol{u}}_t + \ddot{\boldsymbol{u}}_{t+\Delta t}) \tag{2-3}$$

$$\dot{\boldsymbol{u}}_{t+\Delta t} = \int_0^\tau \ddot{\boldsymbol{u}}(\tau)d\tau = \dot{\boldsymbol{u}}_t + \frac{1}{2}\tau(\ddot{\boldsymbol{u}}_t + \ddot{\boldsymbol{u}}_{t+\Delta t}) \tag{2-4}$$

$$\boldsymbol{u}_{t+\Delta t} = \iint_0^{\Delta t} \ddot{\boldsymbol{u}}(\tau)d\tau = \boldsymbol{u}_t + \dot{\boldsymbol{u}}_t\tau + \frac{1}{4}\tau^2(\ddot{\boldsymbol{u}}_t + \ddot{\boldsymbol{u}}_{t+\Delta t}) \tag{2-5}$$

Figure 2-3 shows a linear distribution between the acceleration at time t and the unknown acceleration at time $t + \Delta t$.

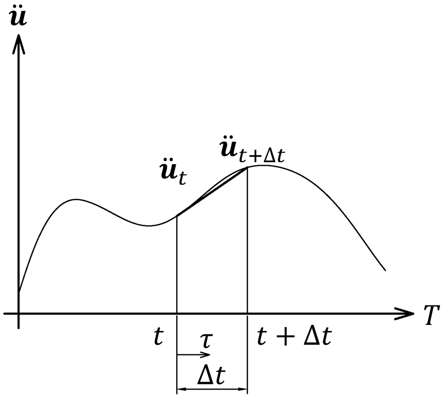

Figure 2-3: Linear acceleration distribution between the time step

A linear distribution of acceleration yields following motion quantities

$$\ddot{\boldsymbol{u}}(\tau) = \ddot{\boldsymbol{u}}_t + \tau\frac{(\ddot{\boldsymbol{u}}_{t+\Delta t} - \ddot{\boldsymbol{u}}_t)}{\Delta t} \tag{2-6}$$

$$\dot{\boldsymbol{u}}_{t+\Delta t} = \int_0^\tau \ddot{\boldsymbol{u}}(\tau) d\tau = \dot{\boldsymbol{u}}_t + \ddot{\boldsymbol{u}}_t \tau + \frac{1}{2\Delta t}\tau^2(\ddot{\boldsymbol{u}}_{t+\Delta t} - \ddot{\boldsymbol{u}}_t) \tag{2-7}$$

$$\boldsymbol{u}_{t+\Delta t} = \iint_0^\tau \ddot{\boldsymbol{u}}(\tau) d\tau = \boldsymbol{u}_t + \dot{\boldsymbol{u}}_t \tau + \ddot{\boldsymbol{u}}_t \frac{1}{2}\tau^2 + \frac{1}{6\Delta t}\tau^3(\ddot{\boldsymbol{u}}_{t+\Delta t} - \ddot{\boldsymbol{u}}_t) \tag{2-8}$$

Combining the equations from the constant and the linear distribution approaches with $\tau = \Delta t$ and adding two constants γ and β gives the basic Newmark equations for the velocity and displacement as follows

$$\dot{\boldsymbol{u}}_{t+\Delta t} = \dot{\boldsymbol{u}}_t + (1-\gamma)\Delta t\, \ddot{\boldsymbol{u}}_t + \gamma \Delta t\, \ddot{\boldsymbol{u}}_{t+\Delta t} \tag{2-9}$$

$$\boldsymbol{u}_{t+\Delta t} = \boldsymbol{u}_t + \dot{\boldsymbol{u}}_t \Delta t + (0.5-\beta)\Delta t^2\, \ddot{\boldsymbol{u}}_t + \beta \Delta t^2\, \ddot{\boldsymbol{u}}_{t+\Delta t} \tag{2-10}$$

The two parameters γ and β are influencing the stability and accuracy of the Newmark time stepping method. With $\gamma = \frac{1}{2}$ and $\beta = \frac{1}{4}$ the constant acceleration is used.

Keeping $\gamma = \frac{1}{2}$ constant and using $\beta = \frac{1}{6}$ will yield the linear acceleration equation. It is worth mentioning that these equations are satisfied for $\gamma = \frac{1}{2}$ and $\frac{1}{6} \leq \beta \leq \frac{1}{4}$, but only unconditionally stable for a $\beta = \frac{1}{4}$ (constant acceleration) with the drawback of less accuracy (see Section 2.1.3). On the contrary, using a linear distribution is only stable if the ratio between the time step and the natural time period of the system is less than 0.551.

$$\frac{\Delta t}{T_n} \leq 0.551 \tag{2-11}$$

Figure 2-4 shows the response of a 3 storey building (3 degrees of freedom) with natural frequencies of $f_1 = 0.434\frac{1}{s}$, $f_2 = 2.28\frac{1}{s}$, $f_3 = 3.83\frac{1}{s}$. Therefore, the stable time step, which has to be used, for covering the highest frequency is

$$\Delta t \leq 0.551 \frac{1}{f_3} = 0.14s \tag{2-12}$$

This figure easily illustrates that the constant approach gives a results even for a time step of 1.0 seconds, but with a significant loss in accuracy compared to the results with $\Delta t = 0.1s$. In contrast to the linear approach where the minimum time step of 0.14 is not adhered and instability is triggered. For an increment of 0.1 seconds both approaches lead to the same results regarding the displacement response. The accuracy and stability of different methods is discussed in Section 2.1.3.

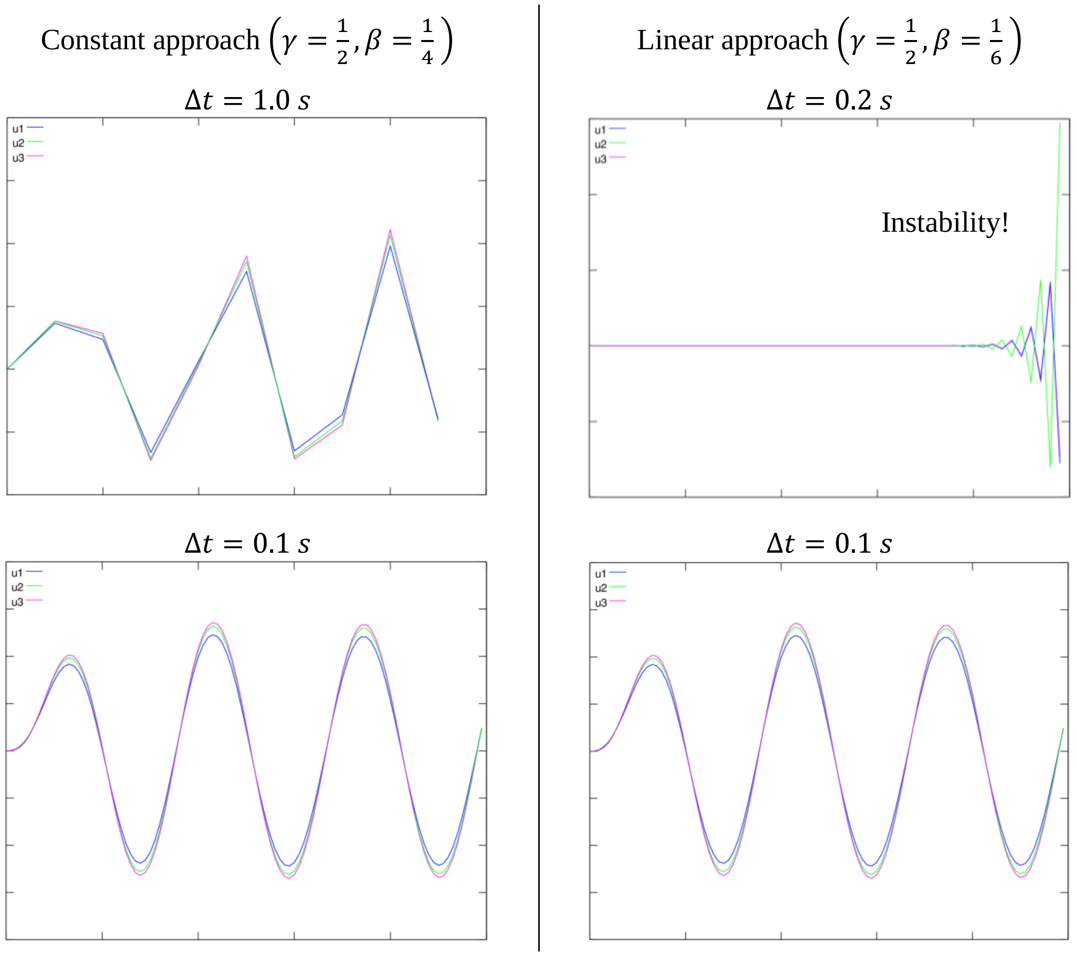
Constant approach $\left(\gamma = \frac{1}{2}, \beta = \frac{1}{4}\right)$

Linear approach $\left(\gamma = \frac{1}{2}, \beta = \frac{1}{6}\right)$

$\Delta t = 1.0\ s$

$\Delta t = 0.2\ s$

$\Delta t = 0.1\ s$

$\Delta t = 0.1\ s$

Figure 2-4: Illustration of the stability of the Newmark algorithm for a simple three storey building for different time steps and approaches

The equation of motion and the Newmark equations can also be written in incremental form by

$$\boldsymbol{M}\Delta\ddot{\boldsymbol{u}}_t + \boldsymbol{C}\Delta\dot{\boldsymbol{u}}_t + \boldsymbol{K}\Delta\boldsymbol{u}_t = \Delta\boldsymbol{R}_t \tag{2-13}$$

With

$$\Delta\ddot{\boldsymbol{u}}_t = \ddot{\boldsymbol{u}}_{t+\Delta t} - \ddot{\boldsymbol{u}}_t \tag{2-14}$$

$$\Delta\dot{\boldsymbol{u}}_t = \dot{\boldsymbol{u}}_{t+\Delta t} - \dot{\boldsymbol{u}}_t \tag{2-15}$$

$$\Delta\boldsymbol{u}_t = \boldsymbol{u}_{t+\Delta t} - \boldsymbol{u}_t \tag{2-16}$$

$$\Delta\boldsymbol{R}_t = \boldsymbol{R}_{t+\Delta t} - \boldsymbol{R}_t \tag{2-17}$$

Combining and substituting these equations with the Newmark equations yields the incremental acceleration and velocity as

$$\Delta\ddot{\boldsymbol{u}}_t = \frac{1}{\beta\Delta t^2}\Delta\boldsymbol{u}_t - \frac{1}{\beta\Delta t}\dot{\boldsymbol{u}}_t - \frac{1}{2\beta}\ddot{\boldsymbol{u}}_t \tag{2-18}$$

$$\Delta\dot{\boldsymbol{u}}_t = \frac{\gamma}{\beta\Delta t}\Delta\boldsymbol{u}_t - \frac{\gamma}{\beta}\dot{\boldsymbol{u}}_t + \Delta t\left(1 - \frac{\gamma}{2\beta}\right)\ddot{\boldsymbol{u}}_t \tag{2-19}$$

Finally, for the Newmark method the equation of motion for linear and nonlinear systems is

$$\begin{aligned}\boldsymbol{M}\left[\frac{1}{\beta\Delta t^2}\boldsymbol{u}_t - \frac{1}{\beta\Delta t}\dot{\boldsymbol{u}}_t - \frac{1}{2\beta}\ddot{\boldsymbol{u}}_t\right] + \boldsymbol{C}\left[\frac{1}{\beta\Delta t}\boldsymbol{u}_t - \frac{\gamma}{\beta}\dot{\boldsymbol{u}}_t + \Delta t\left(1 - \frac{\gamma}{2\beta}\right)\ddot{\boldsymbol{u}}_t\right] \\ + \boldsymbol{K}\Delta\boldsymbol{u}_t = \Delta\boldsymbol{R}_t\end{aligned} \tag{2-20}$$

The motion quantities $\boldsymbol{u}_t$, $\dot{\boldsymbol{u}}_t$ and $\ddot{\boldsymbol{u}}_t$ are known values from the current time t and $\Delta\boldsymbol{u}_t$ with the displacement $\boldsymbol{u}_{t+\Delta t}$ at time $t + \Delta t$ as the only unknown quantity. Solving this equation in terms of $\Delta\boldsymbol{u}_t$ for linear systems is trivial, because the stiffness $\boldsymbol{K}$ is constant. In this case, the whole equation can be rearranged and expressed as

$$\overline{\boldsymbol{K}}\Delta\boldsymbol{u}_t = \overline{\Delta\boldsymbol{R}_t} \tag{2-21}$$

with $\overline{\boldsymbol{K}}$ as the so called “dynamic stiffness” or “effective stiffness” and the “effective force” $\overline{\Delta\boldsymbol{R}_t}$.

$$\overline{\boldsymbol{K}} = \mathbf{K} + \boldsymbol{M}\frac{1}{\beta\Delta t^2} + \boldsymbol{C}\frac{1}{\beta\Delta t} \tag{2-22}$$

$$\overline{\Delta\boldsymbol{R}_t} = \Delta\boldsymbol{R}_t + \left[\boldsymbol{M}\frac{1}{\beta\Delta t} + \boldsymbol{C}\frac{\gamma}{\beta}\right]\dot{\boldsymbol{u}}_t + \left[\boldsymbol{M}\frac{1}{2\beta} + \boldsymbol{C}\Delta t\left(\frac{\gamma}{2\beta} - 1\right)\right]\ddot{\boldsymbol{u}}_t \tag{2-23}$$

In nonlinear material problems the stiffness $\boldsymbol{K}$ changes with $\Delta\boldsymbol{u}_t$ regardless of dynamic or static problems and therefore different at each time instant. Due to the fact that $\boldsymbol{u}_{t+\Delta t}$ isn’t known, it’s not possible to use the secant stiffness $\boldsymbol{K}_{S,t+\Delta t}$ between to time instants t and $t + \Delta t$. So, the tangential stiffness $\boldsymbol{K}_{T,t}$ at the current time t is used instead and

$$\overline{\boldsymbol{K}_{T,t}}\,\Delta\boldsymbol{u}_t = \overline{\Delta\boldsymbol{R}_t} \tag{2-24}$$

is solved iteratively. It’s important to mention that the time step used in nonlinear simulation has big influences on the result, because the introduced error in each iteration step propagates further in each time step. Hence, the influence of the time step should be investigated and the use of a smaller one is mandatory for most of the problems.

2.1.1.2 Time Integration according to Hilber, Hughes and Taylor

Besides the fact that the Newmark method is one of the most used algorithms for solving dynamic problems, it also delivers some drawbacks. Hilber, Hughes and Taylor (1977) introduced a new algorithm, which has some improvements regarding stability and numerical damping compared to Newmark. For dynamic problems sometimes there is no need for the systems high frequency responses. Therefore, numerical damping can be added by increasing the γ value. According to the publication by Hilber, Hughes and Taylor the Newmark method is too dissipative for low frequencies for a fixed time step and $\gamma > 0.5$. Decreasing the time step helps to get rid of the dissipation, but therefore increases the numerical effort. They stated the following requirements in their paper, which are fulfilled by their algorithm:

1. It should be unconditionally stable when applied to linear problems.
2. It should possess numerical dissipation which can be controlled by a parameter other than the time step. In particular, no numerical dissipation should be possible.
3. The numerical dissipation should not affect the lower modes too strongly.

The Hilber-Hughes-Taylor method uses the same basic Newmark equations for the velocity and displacement, equation (2-9) and (2-10), but introduces a parameter α to the equation of motion, which controls the numerical damping. That is why this method or algorithm is also referred to as α-Method.

The equation of motion is now defined as

$$\begin{aligned}\boldsymbol{M}\ddot{\boldsymbol{u}}_{t+\Delta t} + (1+\alpha)\boldsymbol{C}\dot{\boldsymbol{u}}_{t+\Delta t} - \alpha\boldsymbol{C}\dot{\boldsymbol{u}}_t + (1+\alpha)\boldsymbol{K}\boldsymbol{u}_{t+\Delta t} - \alpha\boldsymbol{K}\boldsymbol{u}_t \\ = (1+\alpha)\boldsymbol{R}\boldsymbol{u}_{t+\Delta t} - \alpha\boldsymbol{R}\boldsymbol{u}_t\end{aligned} \tag{2-25}$$

The two parameters γ and β of the Newmark method are consequently also modified by the parameter α.

$$\gamma = \frac{1-2\alpha}{2} \tag{2-26}$$

$$\beta = \frac{(1-\alpha)^2}{4} \tag{2-27}$$

The value α can vary in the range of $-\frac{1}{3} \leq \alpha \leq 0$. A zero value leads to the constant acceleration approach according to Newmark, which is unconditionally stable, second order accurate and results in zero numerical dissipation. On the other hand, $\alpha = -\frac{1}{3}$ accounts for significant numerical damping. The advantage of this method is that introducing numerical damping by adjusting the parameter α doesn’t affect the lower frequencies considerable. This method is preferably used in finite element simulations to neglect high frequency noise which is not contributing to the final solution.

One major drawback of implicit time integration is that the stiffness matrix must be inverted in each time step again to solve equation (2-21) to get the solution for $\boldsymbol{u}_{t+\Delta t}$. This procedure is numerically very costly due to the banded structure of the matrix.

2.1.2 Explicit Time Integration

In contrast to implicit time integration methods (equilibrium at time $t + \Delta t$) in so called explicit time integration or explicit integration methods, the equation of motion (2-1) at time t is used.

$$\boldsymbol{M}\ddot{\boldsymbol{u}}_t + \boldsymbol{C}\dot{\boldsymbol{u}}_t + \boldsymbol{K}\boldsymbol{u}_t = \boldsymbol{R}_t \tag{2-1}$$

Such methods are also called “central difference methods”, because the time derivative of the displacement is based on the finite difference approximation.

For a specific time step Δt, as in Section 2.1.1, the velocity and acceleration with central difference approximations is determined as

$$\ddot{\boldsymbol{u}}_t = \frac{1}{\Delta t^2}(\boldsymbol{u}_{t-\Delta t} - 2\boldsymbol{u}_t + \boldsymbol{u}_{t+\Delta t}) \tag{2-28}$$

$$\dot{\boldsymbol{u}}_t = \frac{1}{2\Delta t}(\boldsymbol{u}_{t+\Delta t} - \boldsymbol{u}_{t-\Delta t}) \tag{2-29}$$

These two equations indicate that the velocity and acceleration is derived just based on the displacements. Figure 2-5 illustrates the idea behind these assumptions.

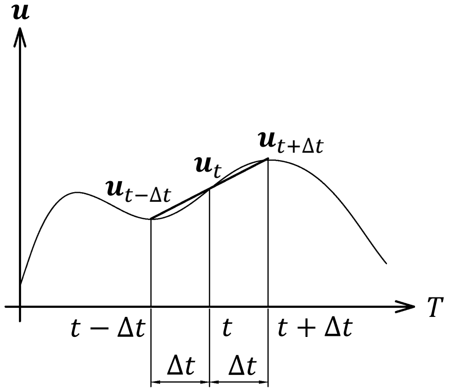

Figure 2-5: Illustration of the central differences approach

Combining the equation of motion at time t and the two motion quantities of the central difference approach gives

$$\begin{aligned}&\left(\frac{1}{\Delta t^2}\boldsymbol{M} + \frac{1}{2\Delta t}\mathbf{C}\right)\boldsymbol{u}_{t+\Delta t} \\ &\qquad = \boldsymbol{R}_t - \left(\boldsymbol{K} - \frac{2}{\Delta t^2}\boldsymbol{M}\right)\boldsymbol{u}_t - \left(\frac{1}{\Delta t^2}\boldsymbol{M} - \frac{1}{2\Delta t}\mathbf{C}\right)\boldsymbol{u}_{t-\Delta t}\end{aligned} \tag{2-30}$$

In a shorter form, similar to equation (2-21),

$$\overline{\boldsymbol{K}}\boldsymbol{u}_{t+\Delta t} = \overline{\boldsymbol{R}_t} \tag{2-31}$$

With the “dynamic stiffness” or “effective stiffness” $\overline{\mathbf{K}}$ and the “effective force” $\overline{\boldsymbol{R}_t}$ as

$$\overline{\boldsymbol{K}} = \left(\frac{1}{\Delta t^2}\boldsymbol{M} + \frac{1}{2\Delta t}\mathbf{C}\right) \tag{2-32}$$

$$\overline{\boldsymbol{R}_t} = \boldsymbol{R}_t - \left(\boldsymbol{K} - \frac{2}{\Delta t^2}\boldsymbol{M}\right)\boldsymbol{u}_t - \left(\frac{1}{\Delta t^2}\boldsymbol{M} - \frac{1}{2\Delta t}\mathbf{C}\right)\boldsymbol{u}_{t-\Delta t} \tag{2-33}$$

At the very beginning of a simulation $\boldsymbol{u}_{0-\Delta t}$ is not known, but can be calculated by using equations (2-28) and (2-29) together with the motion quantities $\boldsymbol{u}_0$, $\dot{\boldsymbol{u}}_0$ and $\ddot{\boldsymbol{u}}_0$ at time t_0.

$$\boldsymbol{u}_{0-\Delta t} = \boldsymbol{u}_0 - \Delta t\dot{\boldsymbol{u}}_0 + \frac{\Delta t^2}{2}\ddot{\boldsymbol{u}}_0 \tag{2-34}$$

The initial acceleration $\ddot{\boldsymbol{u}}_0$ can be calculated with equation (2-1) at time t_0 by

$$\boldsymbol{M}\ddot{\boldsymbol{u}}_0 = \boldsymbol{R}_0 - \boldsymbol{C}\dot{\boldsymbol{u}}_0 - \boldsymbol{K}\boldsymbol{u}_0 \tag{2-35}$$

A closer look at the “dynamic stiffness” $\overline{\boldsymbol{K}}$ reveals that it’s just dependent on the mass and damping matrix, which can be reduced to be diagonal matrices. This means that calculating the inverse is much faster compared to a banded matrix, like the stiffness in implicit time integration methods. On one hand this is an advantage of the explicit time integration methods, but on the other hand a lower time step, dependent on the highest mode n of interest, has to be used to be conditionally stable. The critical time step needed for simple dynamic problems is

$$\frac{\Delta t}{T_n} \leq \frac{1}{\pi} \tag{2-36}$$

Typically a much lower time step is required, dependent on the highest mode n of interest.

2.1.3 Stability and Accuracy of Time Integration Methods

The stability criteria for the methods mentioned in the sections before are summarized in Table 2-1. To adhere to these criteria doesn’t necessarily lead to the right solution. In the case of an unconditionally stable procedure even a high time step will lead to a result, but with loss in accuracy. For conditionally stable algorithms satisfying the stability criterion also doesn’t ensure the right response of the system, because the accuracy is also affected.

Table 2-1: Stability criteria for different time integration methods

		Stability criteria
Implicit Time Integration Methods	**Newmark constant**	Unconditionally stable
	Newmark linear	$\frac{\Delta t}{T_n} \leq 0.551$
	Hilber-Hughes-Taylor	Dependent on α (e.g. $\alpha = 0$ → Newmark’s constant approach)
Explicit Time Integration Methods	**Central differences**	$\frac{\Delta t}{T_n} \leq \frac{1}{\pi}$

The accuracy or error of such methods is mostly compared and measured by means of amplitude decay (AD) and period elongation (PE). Figure 2-6 by Chopra (2011) illustrates the response of a single degree of freedom mass oscillator without damping for different methods and a time step criteria of $\Delta t/T_n; = 0.1$. In this figure the period elongation is easily visible for all time integration methods compared to the analytical solution.

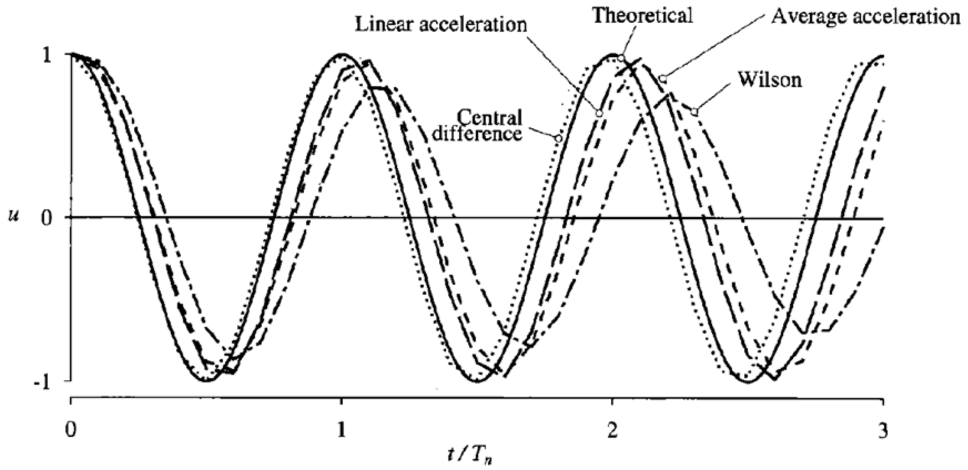

Figure 2-6: Free vibration solution by four numerical methods and the theoretical solution by Chopra (2011)

Figure 2-7 by Chopra (2011) the diagrams of AD and PE as a function of $\Delta t/T_n$. Figure 2-7a shows that all methods lead to zero AD, accept for the one by Wilson, which is attributable to the induced numerical damping of this method.

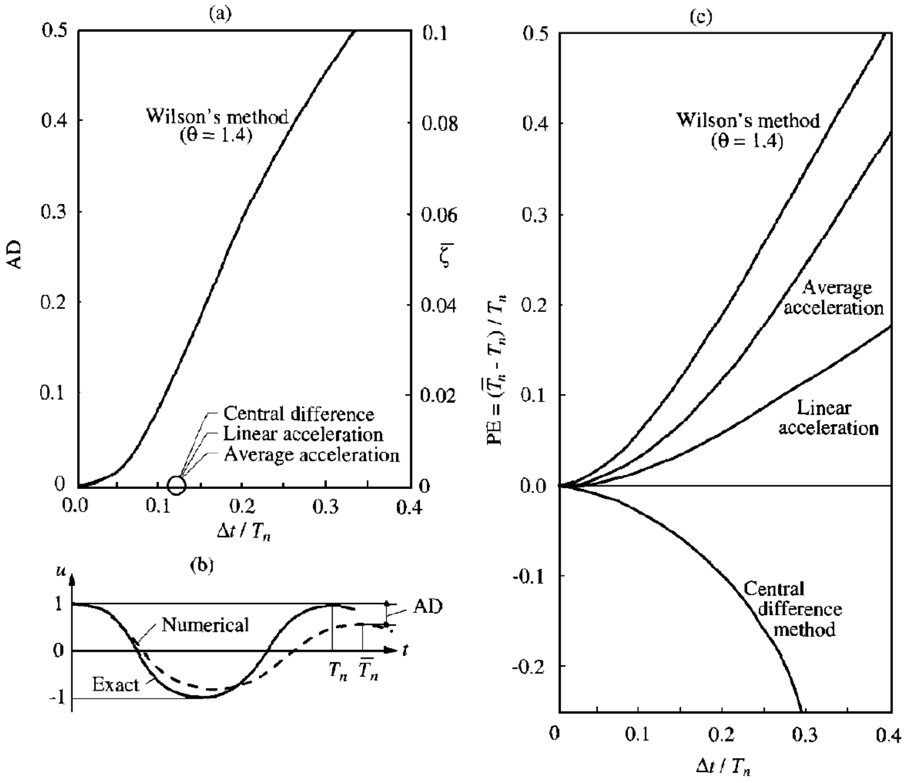

Figure 2-7: a) Amplitude decay versus $\Delta t/T_n$; b) Definition of AD and PE; c) Period elongation; by Chopra (2011)

Figure 2-7b depicts the PE for these four methods. It can be observed that the central differences method yields a period contraction with the highest error even for low $\Delta t/T_n$ ratios compared to the other methods. A steep increase can be seen at approx. $\Delta t/T_n = 0.3$, which is almost the stability criteria of this method of $\Delta t/T_n; = 1/\pi$. On the other hand, Newmark's method with the linear approach gives the most accurate results. The accuracy of the Hilber-Hughes-Taylor method (α-Method) is not explicitly mentioned in this section, because it's rather similar to

Newmark's linear approach, but with some additional advantages mentioned in Section 2.1.1.2. AD and PE diagrams of this method compared to others can be found in Hilber, Hughes and Taylor (1977).

Chopra (2011) also mentioned that the accuracy of the method isn't that much affected by the time step (as long as the stability criterion is fulfilled for specific methods) in multi degree of freedom systems. In finite element analysis the degrees of freedom and hence, the number of natural frequencies might reach very large numbers. Therefore, using the highest frequency for fulfilling the criterion would lead to a very small time step. Nevertheless, dependent on the time integration method the chosen natural frequency can be much smaller, but still giving accurate and stable solutions, as long as the criterion is satisfied.

2.2 Modal Superposition

This section gives a short introduction to the concept of modal superposition and points out the major differences compared to direct time integration methods. Beforehand, modal superposition only allows for analysing linear systems, but with remarkable advantages in computation speed. As already mentioned in the sections before, implicit and explicit time integration have the drawbacks of inverting the stiffness matrix (band structure) or very low time steps, respectively. So, the idea is to reduce the band width of the governing matrices $\boldsymbol{C}$ and $\boldsymbol{K}$ (Note: Massmatrix $\boldsymbol{M}$ can be diagonalized for most problems) or even allow for the use of diagonal matrices. With the assumption that there exists a transformation matrix $\boldsymbol{P}$ and a time dependent vector $\boldsymbol{x}_t$, called generalized displacement, the displacement $\boldsymbol{u}_t$ can be expressed as

$$\boldsymbol{u}_t \ = \boldsymbol{P}\boldsymbol{x}_t \tag{2-37}$$

Combining this expression with the equation of motion (2-1) and multiplying from the left side by $\boldsymbol{P}^T$ yields

$$\boldsymbol{P}^T\boldsymbol{M}\boldsymbol{P}\,\ddot{\boldsymbol{x}}_t + \boldsymbol{P}^T\boldsymbol{C}\boldsymbol{P}\,\dot{\boldsymbol{x}}_t + \boldsymbol{P}^T\boldsymbol{K}\boldsymbol{P}\,\boldsymbol{x}_t = \boldsymbol{P}^T\boldsymbol{R}_t \tag{2-38}$$

Note that $\boldsymbol{P}$ can be any arbitrary nonsingular transformation matrix, but performing an eigenvalue analysis of the undamped equation of motion leads to a convenient definition.

The undamped equation of motion for eigenoscillations is

$$\boldsymbol{M}\ddot{\boldsymbol{u}}_t + \boldsymbol{K}\boldsymbol{u}_t = \boldsymbol{0} \tag{2-39}$$

It is assumed that the solution of the system will be a function of

$$\boldsymbol{u_t} = \boldsymbol{\varphi} sin(\boldsymbol{\omega} t) \tag{2-40}$$

with $\boldsymbol{\varphi}$ as the eigenvector of the system, $\boldsymbol{\omega}$ as the natural frequency and t as time.

Combing equations (2-39) and (2-40) yields the following eigenvalue problem

$$(\boldsymbol{K} - \boldsymbol{\omega}^2\boldsymbol{M})\boldsymbol{\varphi} = \boldsymbol{0} \tag{2-41}$$

Solving this eigenproblem will yield the circular natural frequencies $\boldsymbol{\omega}$ and the eigenvectors $\boldsymbol{\varphi}$ of the system for each natural mode. This procedure is also called modal analysis. These eigenvectors have the property of orthogonality, which implies

$$\begin{gathered}\boldsymbol{\varphi}_i^T \boldsymbol{M} \boldsymbol{\varphi}_j = 0; \quad \boldsymbol{\varphi}_i^T \boldsymbol{K} \boldsymbol{\varphi}_j = 0 \quad \text{for } i \neq j \\ \boldsymbol{\varphi}_i^T \boldsymbol{\varphi}_j = 1 \quad \text{for } i = j\end{gathered} \tag{2-42}$$

The eigenvectors can be written as a set of vectors in matrix form as

$$\boldsymbol{\Phi} = [\boldsymbol{\varphi}_1, \dots, \boldsymbol{\varphi}_n] \tag{2-43}$$

and the squared circular natural frequencies $\boldsymbol{\omega^2}$ in matrix form as

$$\boldsymbol{\Omega^2} = \begin{bmatrix} \omega_1^2 & \cdots & 0 \\ \vdots & \ddots & \vdots \\ 0 & \cdots & \omega_n^2 \end{bmatrix} \tag{2-44}$$

With these two matrices equation (2-41) yields

$$\boldsymbol{K\Phi} - \boldsymbol{M\Phi\Omega^2} = \boldsymbol{0} \tag{2-45}$$

Often it’s convenient to normalize the eigenvectors for each mode so that

$$\boldsymbol{\Phi}^T \boldsymbol{M\Phi} = \boldsymbol{1} \tag{2-46}$$

In this case, equation (2-45) gives

$$\boldsymbol{\Phi}^T \boldsymbol{K\Phi} = \boldsymbol{\Omega^2} \tag{2-47}$$

Hence, we can rewrite the modal equation of motion (2-38) by using the normalized eigenvector matrix (2-43) as

$$\ddot{\boldsymbol{x}}_t + \boldsymbol{\Phi}^T \boldsymbol{C\Phi}\, \dot{\boldsymbol{x}}_t + \boldsymbol{\Omega^2} \boldsymbol{x}_t = \boldsymbol{\Phi}^T \boldsymbol{R}_t \tag{2-48}$$

For undamped problems this equation is completely uncoupled, which means that the matrices are diagonal. In practice damping is present in every structure. Due to the effect that damping describes the energy dissipation of the whole structure and is hard to define it for a whole system, these effects are not uncoupled. Nevertheless, computationally it’s more comfortable to have a diagonal damping matrix. The easiest way is to define a damping factor for each mode separately so that

$$\boldsymbol{\Phi}^T \boldsymbol{C\Phi} \ = 2\boldsymbol{\Omega\zeta} \tag{2-49}$$

This expression is based on the derivation of damped single mass oscillators, where the vector $\boldsymbol{\zeta}$ contains the fraction of the critical damping factors for each mode.

Finally, the fully uncoupled and damped modal equation of motion (2-38) is

$$\ddot{\boldsymbol{x}}_t + 2\boldsymbol{\Omega}\boldsymbol{\zeta}\,\dot{\boldsymbol{x}}_t + \boldsymbol{\Omega}^2\boldsymbol{x}_t = \boldsymbol{\Phi}^T\boldsymbol{R}_t \tag{2-50}$$

Note that $\boldsymbol{\Omega}$ and $\boldsymbol{\Phi}^T$ are matrices with the natural frequencies and natural modes of the order of the degree of freedom of the system. Thus, equation (2-50) is just the summation of all these modes and their answers to a varying force over time $\boldsymbol{R}_t$. This is why it's called modal superposition. Solving this system of equations yields the generalized displacement vector $\boldsymbol{x}_t$ which must be transformed back to the actual displacement vector by

$$\boldsymbol{u}_t = \boldsymbol{\Phi}\boldsymbol{x}_t \tag{2-51}$$

As already mentioned this method is restricted to linear systems. Nevertheless, solving a system of linear equations analogous to single mass oscillators of a finite number and summing up their answers to a specific acceleration time history, for instance, is much faster (even up to a factor of 100) than direct time integration methods.

Considering a structure discretized by means of finite elements can easily reach degrees of freedom of 100000 and even much more. It should be clear that computing all natural frequencies and modes of such structures and using them for modal superposition is not necessary, due to the fact that for most problems the first frequencies (e.g. 10 to 20 modes for earthquake simulations) are the most important ones. In general, the number of modes which should be used for modal superposition is defined by the frequency range of the applied dynamic force and the mass distribution of the structure. In summary, it can be stated that the number of modes used for the simulation are influencing the accuracy of the result, but for most cases the consideration of just a few modes are quite sufficient and yield almost identical results as direct time integration methods with the advantage of being computationally much faster. This fact also allows for simulating stress and pressure pulse propagations in structures where very small time steps have to be used to show such effects.

2.3 Structural Damping

Damping in mechanical systems, especially in the equation of motion, is defined as a velocity dependent quantity (viscous damping), which describes the dissipation of energy during a dynamic oscillation. Damping factors are hard to define for even simple structures. In case of civil engineering structures, where each structure is more or less a prototype, the damping is not known in the design phase. Due to the complexity of some structures and their interaction with the soil or water and the use of different materials it's almost impossible to account for all damping effects separately. Consequently one may use values measured at similar structures, which can be found in relevant literature. These values are mostly stated in terms of the fraction of the critical damping or modal damping factor ζ_i for specific materials, buildings or soils. In modal superposition (Section 2.2) the fraction of critical damping ζ_i can be applied directly on each natural mode separately if needed. On the contrary, in direct time integration methods, the damping matrix $\boldsymbol{C}$ has to be calculated, because the equation of motion isn't uncoupled anymore. Defining damping values for each degree of freedom (position in the matrix $\boldsymbol{C}$) is practically not possible, therefore so called Rayleigh damping is a well-established approach in finite element analyses. Additionally to the classical Rayleigh damping approach a new method for determination of the Rayleigh constants by Spears and Jensen (2012) is introduced.

2.3.1 Rayleigh Damping

Rayleigh damping was originally introduced in accordance with modal analysis by Lord Rayleigh (1877) and later revisited by Adhikari and Srikantha Phani (2007). The idea was to use the damped equation of motion for modal analysis instead of the undamped one, see equation (2-39), but with the advantage of diagonal matrices from $\boldsymbol{\Phi}^T\boldsymbol{M}\boldsymbol{\Phi}$ and $\boldsymbol{\Phi}^T\boldsymbol{K}\boldsymbol{\Phi}$. Therefore, the damping matrix is assumed to be a linear combination of the mass and stiffness matrix

$$\boldsymbol{C} = \alpha\boldsymbol{M} + \beta\boldsymbol{K} \tag{2-52}$$

with α and β as Rayleigh constants or mass- and stiffness-proportional damping factors, respectively, which are dependent on the modal damping ζ_i and two specific natural frequencies ω_i and ω_j. This assumption is a special case of the Caughey series or Caughey damping developed by Caughey and O'Kelly (1965) which describes proportional damping in a general form.

The Caughey Series is defined as

$$\boldsymbol{C} = \boldsymbol{M}\sum_{k=0}^{n-1} a_k\,[\boldsymbol{M}^{-1}\boldsymbol{K}]^{\boldsymbol{k}} \tag{2-53}$$

with n as the order of modes taken into account and a_k for $k = 0,1, \dots n-1$ as damping constants (e.g α and β for Rayleigh damping). For $n = 2$ this equation reduces to Rayleigh Damping. If $n > 2$ the damping matrix is a full matrix. For systems with a high number of degrees of freedom full matrices increase the computational effort significantly in contrast to matrices with a band structure. Hence, Rayleigh Damping is mainly used in numerical analyses and sufficient for a wide range of problems.

Combining equation (2-52) with (2-46), (2-47) and (2-49) yields

$$\alpha + \beta\boldsymbol{\Omega}^{\boldsymbol{2}} \; = 2\boldsymbol{\Omega}\boldsymbol{\zeta} \tag{2-54}$$

or in scalar formulation

$$\alpha + \beta\omega_i^2 \; = 2\omega_i\zeta_i \tag{2-55}$$

Out of this equation the mass-proportional factor for two specific natural frequencies is calculated by

$$\alpha = \zeta_i\frac{2\omega_i\omega_j}{\omega_i + \omega_j} \tag{2-56}$$

and the stiffness-proportional factor by

$$\beta = \zeta_i \frac{2}{\omega_i + \omega_j} \tag{2-57}$$

Figure 2-8 shows the Rayleigh damping and the mass- and stiffness-proportional damping. In this figure one can also see that the specified damping value ζ_i is only complied at the two frequencies of ω_i and ω_j for which the Rayleigh damping factors have been calculated. The frequency range between these two values $\omega_i < \omega < \omega_j$ has less damping and frequencies lower than ω_i or higher than ω_j account for higher damping, than specified. This fact describes one of the drawbacks of Rayleigh damping, which is the choice of the two natural frequencies for calculating the Rayleigh constants α and β.

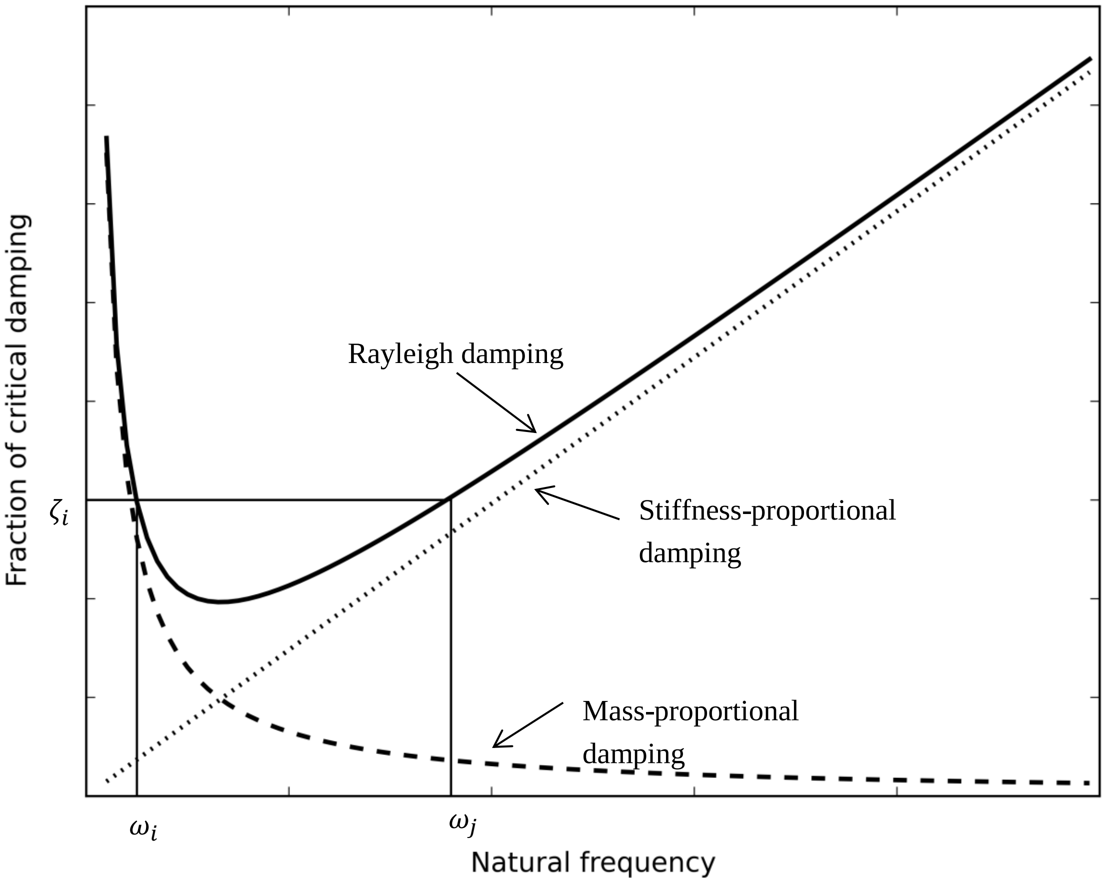

Figure 2-8: Illustration of Rayleigh damping

The two modes which should be used are dependent on the frequency range of the applied dynamic force and the sum of the effective mass in the specified frequency range. If the chosen natural frequencies are too close to each other too much damping could be applied to the entire system. On the other hand, if they are too far apart too less damping for a wide range of frequencies may be accounted for, leading to too conservative results. A new method for determining these constants and natural frequencies under consideration by Spears and Jensen (2012) is introduced in the next section.

2.3.2 Modified Rayleigh Damping

For nonlinear simulations direct time integration methods have to be used, because the stiffness of the system changes over time and superimposing results is not possible. As already mentioned in Section 2.3.1, for Rayleigh damping the Rayleigh constants α and β have to be calculated, based on two natural frequencies and the modal damping factor ζ_i. Figure 2-8 shows that the damping value varies with the frequency. So, determining those frequencies which should be applied to the final model is mostly based on assumptions and compromises in the damped frequency range. The optimum case would be to use one damping value for the whole range, like in modal superposition. Since this isn’t possible with Rayleigh damping, Spears and Jensen (2012) proposed a method which allows for selecting those frequencies based on the difference in the response of the modal and Rayleigh damped system. At first, a modal analysis of the model has to be done, to find its natural frequencies and effective masses. With these frequencies together with the constant modal damping factor ζ and an acceleration time history, which is the dynamic load of the model, an acceleration response spectrum is created. Afterwards, two natural frequencies are chosen to calculate the Rayleigh constants and the corresponding modal damping factors $\zeta_1, \zeta_2, \ldots \zeta_n$ for each mode/frequency i by

$$\zeta_i = \frac{1}{2}\left(\frac{\alpha}{\omega_i} + \beta\omega_i\right) \tag{2-58}$$

Again, like for the constant modal damping, an acceleration response spectrum is created, but now under consideration of different damping factors for each frequency. With the accelerations out of the spectra the response difference is calculated by the sum of all acceleration responses differences with the following equation

$$\Delta S = \sum_{i=1}^{n} (a_{r,i} - a_{m,i})\, m_{eff,i} \approx 0 \tag{2-59}$$

where $a_{r,i}$ and $a_{m,i}$ are the response accelerations of the Rayleigh and modal damped systems and $m_{eff,i}$ is the effective mass, at mode/frequency i and n is the maximum number of modes under consideration. Important to mention, the amount of considered modes/frequencies can influence the result significantly, therefore the percentage of the sum of the effective mass to overall mass should not undergo a specific value. Dependent on the finite element model, normally a value of 100% is not reachable without an increased computational effort, but 70% at least is advisable. If $\Delta S \neq 0$ the Rayleigh constants have to be recalculated for two different frequencies as often as necessary until $\Delta S \approx 0$. The two frequencies $\omega_{mod,i}$ and $\omega_{mod,j}$ and corresponding constants from the last iteration are the ones which give the same global response of the system as if modal damping is applied. Figure 2-9 illustrates both damping curves before and after modification of the Rayleigh damping.

Spears and Jensen have used this approach solely for seismic analysis of structures, but stated that it’s reasonable for a wide range of problems.

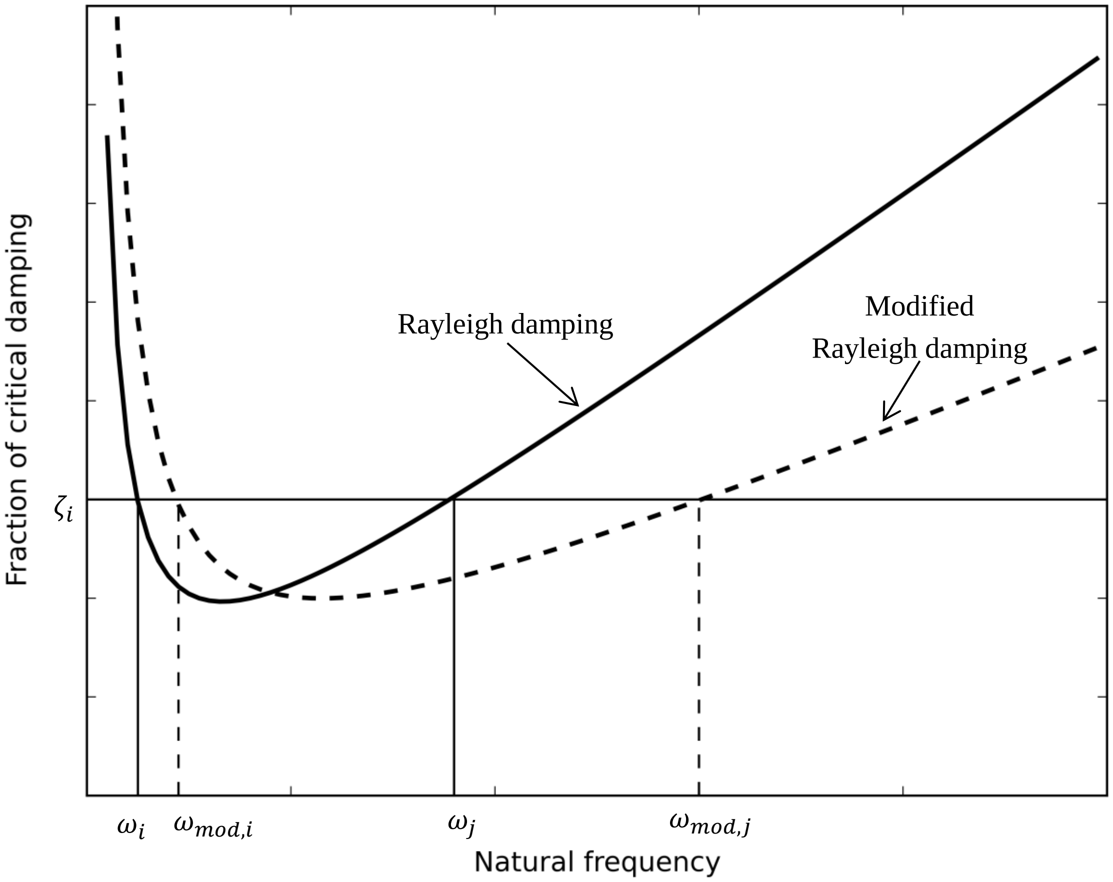

Figure 2-9: Damping curve before and after modification of the Rayleigh damping

Hellgren (2014) used this approach in his master thesis *"Influence of Fluid Structure Interaction on a Concrete Dam during Seismic Excitation"* and showed a program flow chart which described the procedure for calculating the modified Rayleigh constants. Figure 2-10 shows a similar flow chart based on the one by Hellgren (2014).

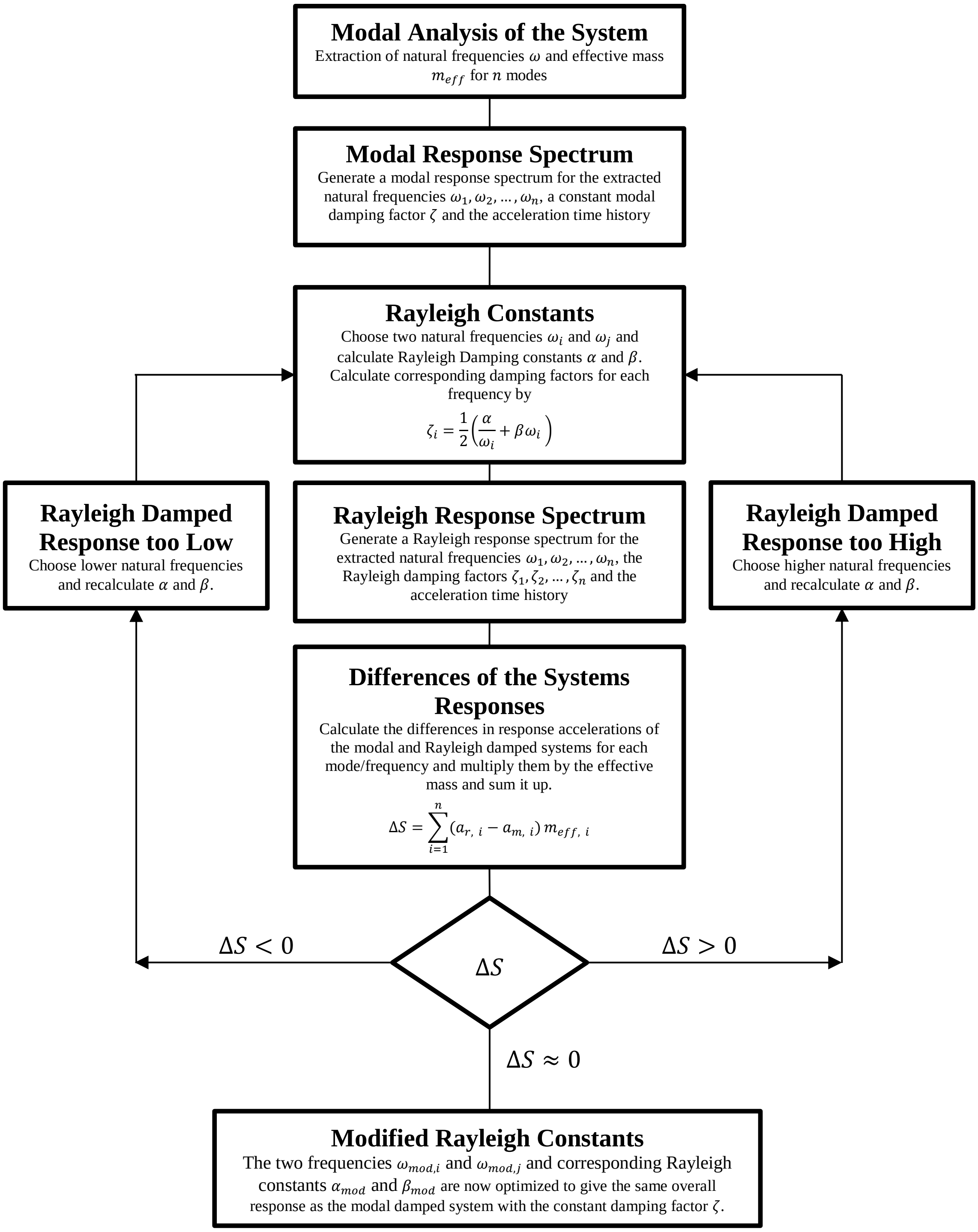

Modal Analysis of the System

Extraction of natural frequencies ω and effective mass m_{eff} for n modes

Modal Response Spectrum

Generate a modal response spectrum for the extracted natural frequencies $\omega_1, \omega_2, \dots, \omega_n$, a constant modal damping factor ζ and the acceleration time history

Rayleigh Constants

Choose two natural frequencies ω_i and ω_j and calculate Rayleigh Damping constants α and β. Calculate corresponding damping factors for each frequency by

$$\zeta_i = \frac{1}{2}\left(\frac{\alpha}{\omega_i} + \beta\omega_i\right)$$

Rayleigh Damped Response too Low

Choose lower natural frequencies and recalculate α and β.

Rayleigh Response Spectrum

Generate a Rayleigh response spectrum for the extracted natural frequencies $\omega_1, \omega_2, \dots, \omega_n$, the Rayleigh damping factors $\zeta_1, \zeta_2, \dots, \zeta_n$ and the acceleration time history

Rayleigh Damped Response too High

Choose higher natural frequencies and recalculate α and β.

Differences of the Systems Responses

Calculate the differences in response accelerations of the modal and Rayleigh damped systems for each mode/frequency and multiply them by the effective mass and sum it up.

$$\Delta S = \sum_{i=1}^{n} (a_{r,\,i} - a_{m,\,i})\, m_{eff,\,i}$$

Modified Rayleigh Constants

The two frequencies $\omega_{mod,i}$ and $\omega_{mod,j}$ and corresponding Rayleigh constants α_{mod} and β_{mod} are now optimized to give the same overall response as the modal damped system with the constant damping factor ζ.

Figure 2-10: Program flow chart for calculating the modified Rayleigh constants

2.3.3 Problems regarding the Use of Rayleigh Damping in Nonlinear Systems

By means of Rayleigh damping the damping matrices are formed by using the initial linear mass- and stiffness matrices of the system. The mass of the system should remain constant over time, even for nonlinear systems if no parts/elements of the structure are excluded during simulation. In contrast to the mass, the stiffness is reduced in nonlinear systems due to softening effects like cracks. Hall (2006) investigated this problem for different civil engineering structures. One of them was a 100 meters high gravity dam for what he evaluated the damping effects due to sliding and cracking at the base for smeared methods (enforcement at integration points without contact discretization). Therefore, he came to the conclusion that the mass-proportional damping forces can imply moderate resistance to sliding. On the other hand, the stiffness-proportional term can obviously inhibit sliding, because of using the initial stiffness matrix for calculation of the damping force. It should be clear that the stiffness of the system is significantly lower if a crack exists. Hence, in such cases a limited value is suggested by Hall (2006). Furthermore, if so called penalty elements (nonlinear axial and shear springs) are used for the contact he stated an additional problem which results out of this discretization method, where springs with very high axial stiffness's are used to prevent surfaces to penetrate. These high values should be omitted in the computation of the stiffness-proportional damping force.

In the end Hall (2006) concluded that Rayleigh damping can, in certain cases, yield too large and unrealistic damping forces and hence be non-conservative. The mass-proportional term has no direct physical meaning and acts as a linear viscous damper on the degrees of freedom of the nodes as external supports, whereas the stiffness-proportional term can be understood as connection between degrees of freedom. For high velocity gradients and a high initial stiffness compared to the nonlinear stiffness these damping forces might be significant and further research is necessary on this topic.

3 FLUID MODELLING METHODS OF DAM-RESERVOIR INTERACTIONS

Dam-reservoir interactions can be categorized as structure excited interactions in hydraulic engineering, which are defined as fluid-structure interaction where the water has to react to a slightly moving structure. This implies that the displacement of the water stays as small as the one of the structure. A typical example for such problems is an earthquake induced vibration of a structure which is fully or partially surrounded by water, e.g. dam structures. The design loads can increase significantly in seismic active areas, leading to a reduced sliding stability, dependent on the dead weight and fracture criteria, which assumes friction and cohesion as resistance. The additionally excited water (reservoir) is an important factor in the assessment and simulation. The easiest way to take the water into account is to use an added mass approach. Upon others the ones mostly used by engineers are the added masses according to Westergaard and Zangar. Among these approaches, a new empirical approach, by Goldgruber and Feldbacher (2013), based on numerical simulations is also introduced in this section. Simplifying the water as mass mostly leads to an overestimation of the results, dependent on the geometry and dimensions of the structure. Additionally to the added mass techniques, the fluid structure interaction of structure excited simulations can also be modelled as acoustic fluid, which is based on the “Conservation of Momentum” and “Conservation of Mass” equations from Appendix A.2.2 and A.3, respectively. Such fluids are commonly used in pressure and sound wave simulations, but give some major advantages for problems where a volume of water is excited moderately. For such problems the pressure distribution and its effect on the structure are from interest. Muto et al. (2012) have compared simulations with structural elements (Lagrangian finite elements), acoustic fluid elements and the closed form solutions according to Housner (1954). Therefore, they simulated a rectangular reservoir interacting with a rigid wall, by applying a sinusoidal ground motion for 6 seconds. The conclusion was that structural elements are not appropriate for such a case, because of their transient, self-oscillating behaviour if no artificial damping is introduced. The system’s response for the acoustic fluid elements simulation was instead very close to Housner’s closed form solution, which justified the use of these elements for structure-reservoir interactions. In Section 5.2, a similar problem is investigated, but applied on a non-rigid 220 meters high arch dam. It reveals the commonly known fact, that an added mass technique yields higher stresses, deformations, etc. compared to acoustic fluid elements and additionally that it’s also independent of the damping factors used. Furthermore, the conclusion is that the additional mass can affect the structures dynamic behaviour significantly, especially for slender structures over 100 meters. The use of acoustic elements, due to their better constitutive description (compressibility) of the water, is also recommended in this work. Nevertheless, the added mass technique is still widely used, especially for preliminary designs, due to its convenient way of applicability and conservative results and hence is discussed in this chapter. Structural or lagrangian finite elements are not described due to their disadvantages for modelling the water of structure excited fluid-structure interaction problems, which have been mentioned above.

3.1 Added Mass according to Westergaard

Westergaard (1933) derived his equation on an analytical basis where the water pressure is described as an added mass, acting on the upstream surface of a dam structure and the rest of the water is assumed to be inactive. He developed an equation for the mass as a function of the depth of the reservoir. Moreover, the idealized two dimensional dam is assumed to be rigid and vertical. The reservoir is infinite in length and has a rectangular shape. The added water mass per squaremeter at the interacting surface in a specific depth z of the dam surface with these assumptions is calculated by

$$m_w(z) = \frac{8\rho_w h}{\pi^2} \sum_{n=1,3,\dots}^{\infty} \frac{1}{n^2 c_n} sin\left(\frac{n\pi z}{2h}\right) \tag{3-1}$$

with

$$c_n = \sqrt{1 - \frac{16\rho_w h^2}{n^2 K_w T^2}} \tag{3-2}$$

the natural frequency of the reservoir

$$f = \frac{1}{T} = \frac{1}{4h}\sqrt{\frac{K_w}{\rho_w}} = \frac{c_w}{4h}, \tag{3-3}$$

the compressibility K_w, the water depth h, the density of the water ρ_w and the wave propagation speed c_w. Figure 3-1 shows the added mass distribution according to the Westergaard equation. It also indicates that the tangent at the bottom of the water reservoir is dependent on the order n of the sum of equation (3-1). A higher order increases the accuracy of the added mass distribution.

Added mass distribution according to Westergaard

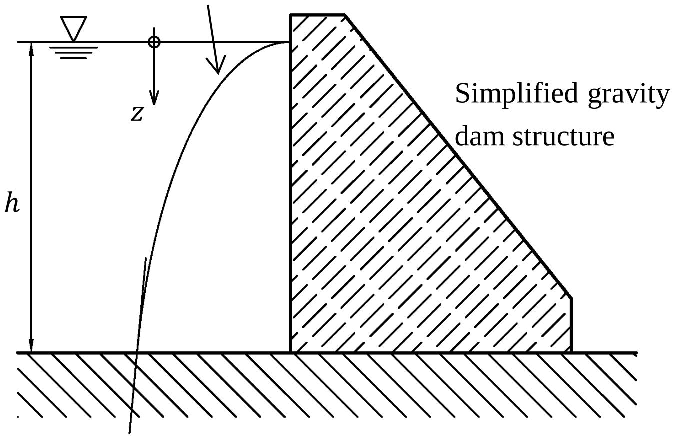

Inclination of the tangent on the bottom is dependent on the order n

Figure 3-1: Westergaard added mass distribution

Worth mentioning is that the more commonly known equation for calculating the added mass per squaremeter according to Westergaard is

$$m_w^*(z) = \frac{7}{8}\rho_w\sqrt{hz} \tag{3-4}$$

This simplified equation neglects the effects of compressibility of the water and the influence of the natural frequency of the reservoir and therefore over estimates the mass at the top and bottom part of the interacting surface between body and water of approximately 10%. This fact is illustrated in Figure 3-2. This figure also shows that taking into account an order of $n = 11$ of equation (3-1) is sufficient. Higher orders influence the mass distribution just slightly.

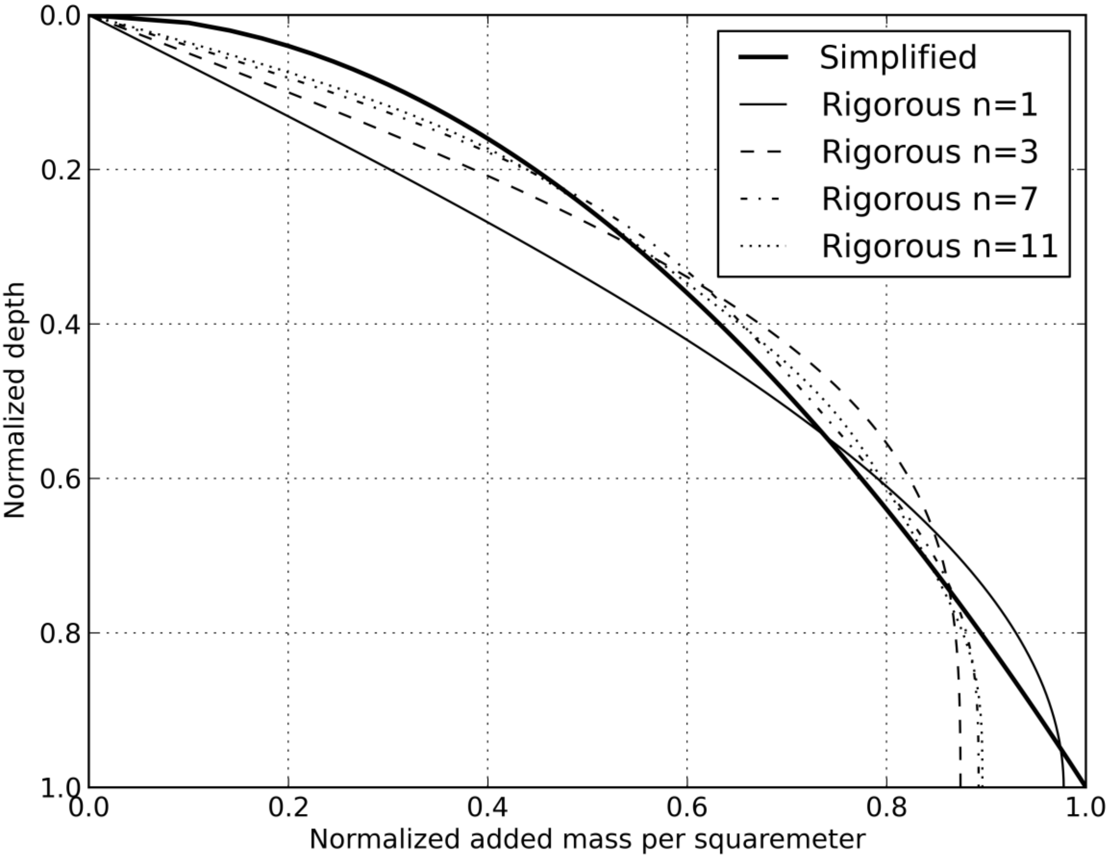

Figure 3-2: Comparison between the rigorous and simplified Westergaard equation

The popularity of the simplified equation is based on the fact that its conservative and it can be easily applied in quasi static analyses, where mass points instead of continua are used to calculate the global equilibrium. The overall mass of the water per meter acting on the upstream surface is computed by integrating equation (3-4) over the height of the water by

$$M_w^* = \int_0^h \frac{7}{8}\rho_w\sqrt{hz}dz = \frac{7}{12}\rho_w h^2 \tag{3-5}$$

This resultant mass is acting in the centre of the integrated area, which is approx.

$$h_{w,s} = \frac{2}{5}h \tag{3-6}$$

Figure 3-3 illustrates the point of origin of the resultant mass M_w^*.

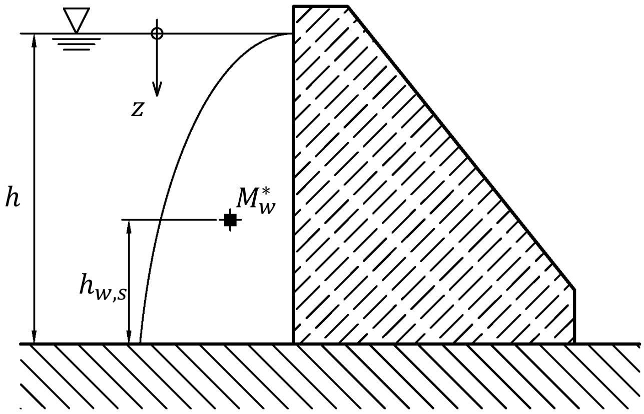

Figure 3-3: Point of origin of the resultant water mass

3.2 Added Mass according to Zangar

In contrast to Westergaard, Zangar et al. (1952) published a paper called *„Electric analog indicates effect of horizontal earthquake shocks on dams"*, where he derived an equation for the pressure distribution over the height of the dam experimentally. His model test consists of a tray representing the reservoir and the dams' rigid upstream surface. The electrolyte he used for the reservoir is tap water. Instead of using a shake table and measuring the pressure directly, a linear varying potential boundary (analog to the potential of water in each depth) on the upstream surface and a constant potential on the bottom is installed. Figure 3-4 illustrates the electrical analog model test setup by Zangar for measuring the dynamic pressure in a reservoir.

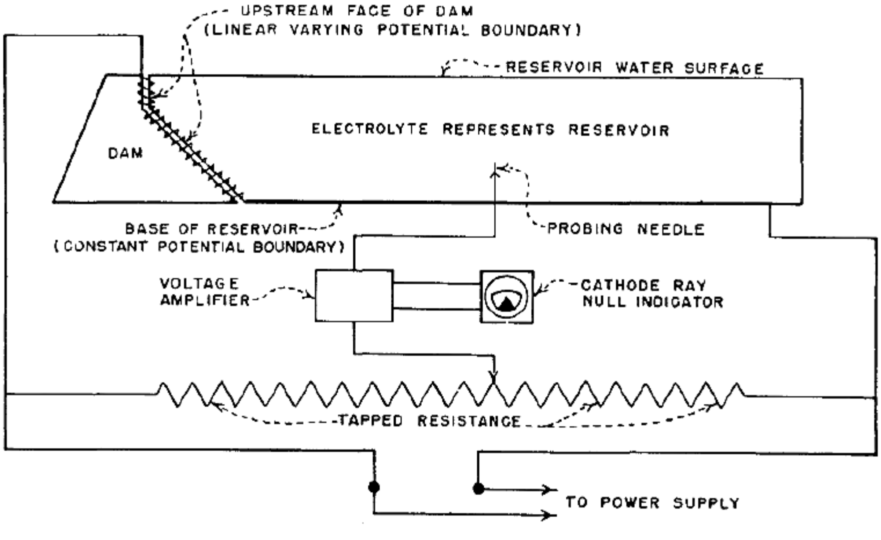
UPSTREAM FACE OF DAM
(LINEAR VARYING POTENTIAL BOUNDARY)
RESERVOIR WATER SURFACE
ELECTROLYTE REPRESENTS RESERVOIR
DAM
BASE OF RESERVOIR
(CONSTANT POTENTIAL BOUNDARY)
PROBING NEEDLE
VOLTAGE AMPLIFIER
CATHODE RAY NULL INDICATOR
TAPPED RESISTANCE
TO POWER SUPPLY

Figure 3-4: Model setup for measuring the dynamic water pressure in a reservoir according to Zangar et al. (1952)

The coherence between the pressure increase due to a seismic event and the magnitude of the acceleration for a rigid structure is described as

$$p_z = C a_e \rho_w \, h \tag{3-7}$$

or in terms of the mass per squaremeter

$$m_z = C \rho_w \, h \tag{3-8}$$

with C as the pressure coefficient, α_e as the horizontal earthquake intensity and h as the reservoir depth.

The measured electric potential in the reservoir is analog to the streamlines of the water and therefore, the pressure or pressure coefficient (perpendicular to the streamlines). Furthermore, this analog and model setup is only valid under the assumption of incompressible water and a rigid structure. Figure 3-5 shows a general plot of the streamlines and corresponding pressure coefficients C.

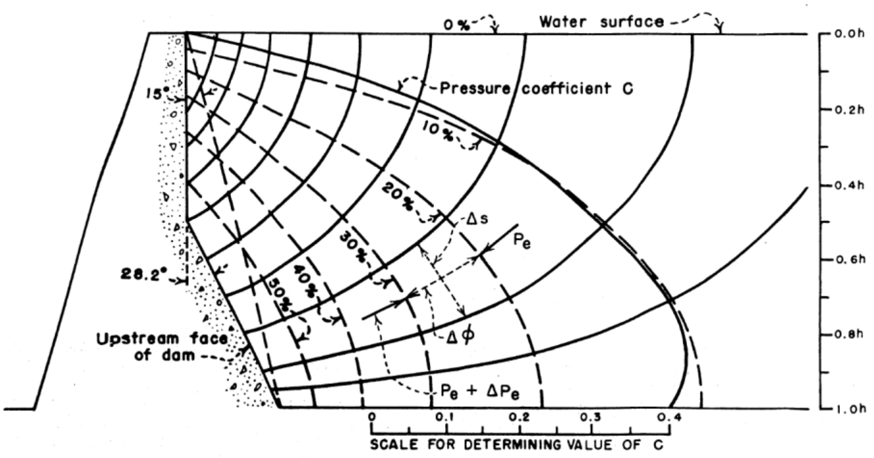

Figure 3-5: Streamlines and pressure coefficient in the reservoir by Zangar et al. (1952)

In the case of a constant inclined upstream surface Zangar derived a parabolic shape of the mass or pressure distribution based on the experimental results for different angles, which is

$$C = \frac{C_m}{2}\left[\frac{z}{h}\left(2 - \frac{z}{h}\right) + \sqrt{\frac{z}{h}\left(2 - \frac{z}{h}\right)}\right] \tag{3-9}$$

The constant factor C_m is defined as the maximum occurring pressure coefficient for one inclination and z is the depth variable. The relationship between the angles and the pressure coefficient on the bottom and the maximum pressure coefficient is depicted in Figure 3-6. This figure also indicates that the maximum pressure coefficient ($C = 0.73$) is only occurring at zero inclination. For higher inclinations the coefficient reduces. The pressure coefficients between the experiment and equation (3-9) are shown in Figure 3-7. In this figure it can also be seen that the maximum is moving upward in the reservoir with the increase in inclination.

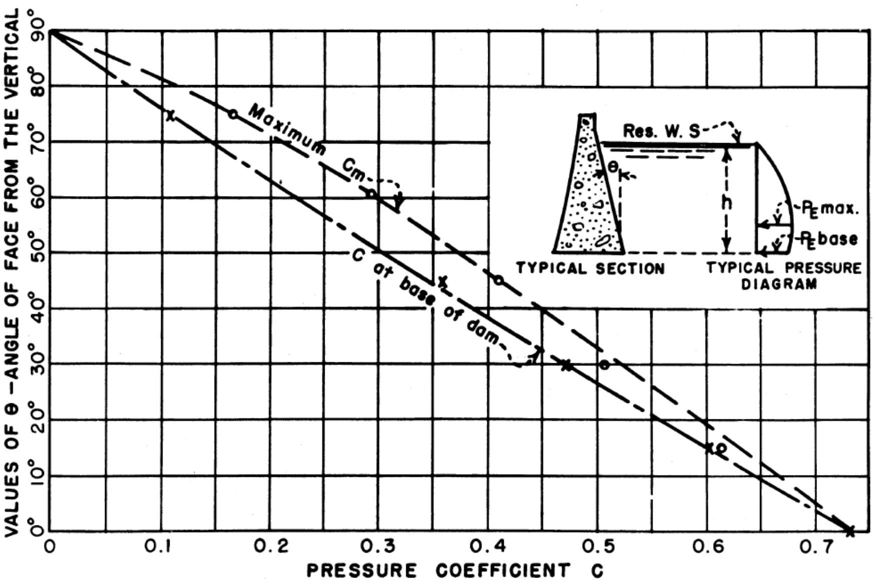

Figure 3-6: Maximum pressure coefficient and pressure coefficient at the bottom for different angles of the upstream surface of a dam by Zangar et al. (1952)

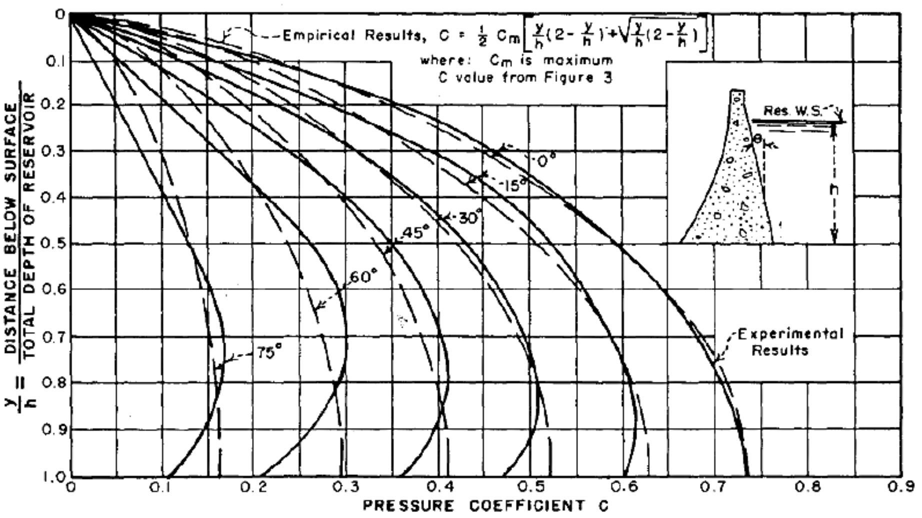

Figure 3-7: Pressure coefficient for different angles of the upstream surface of a dam by Zangar et al. (1952)

3.3 Empirical Added Mass Approach for Inclined Surfaces

The problem in the approaches of Westergaard and Zangar is that their formulas don't consider the inclination regarding the added mass in the right way. The Westergaard equation, simplified or rigorous, don't account for any inclination and therefore, neglects the upward moving maximum pressure for inclinations greater than zero and the change in the added mass distribution. On the other hand, Zangar accounts for the inclination in his formulas, but also simplifies them in a way so that the maximum occurs on the bottom and not in a lower depth. Numerical simulations with an acoustic fluid approach show the same behaviour as the experiments by Zangar and are a decent way to simulate the reservoir's dynamic behaviour. Acoustic fluids are particularly described in Section 3.5.

Goldgruber and Feldbacher (2013) had the idea to simulate the interaction for different heights and inclinations of the dam and use the resultant pressure curves to develop a formula, which describes this relationship and allows for a more exact distribution of the added mass. Hence, a numerical model using structural and acoustic elements for the fluid-structure interaction to investigate the pressure distribution is generated. The finite element model is shown in Figure 3-8. The depth of the water and the height of the structure vary between 10.0 and 250.0 meters to evaluate any scale effects. A constant acceleration variation between 1.0 m/s² and 4.0 m/s² has also been done. Both, the change in depth and acceleration had no qualitative effect on the pressure distribution on the structure. The inclination of the interface between water and dam varies between 0° and 30° in steps of 10°. The maximum of 30° has been chosen because higher values are unusual for such structures.

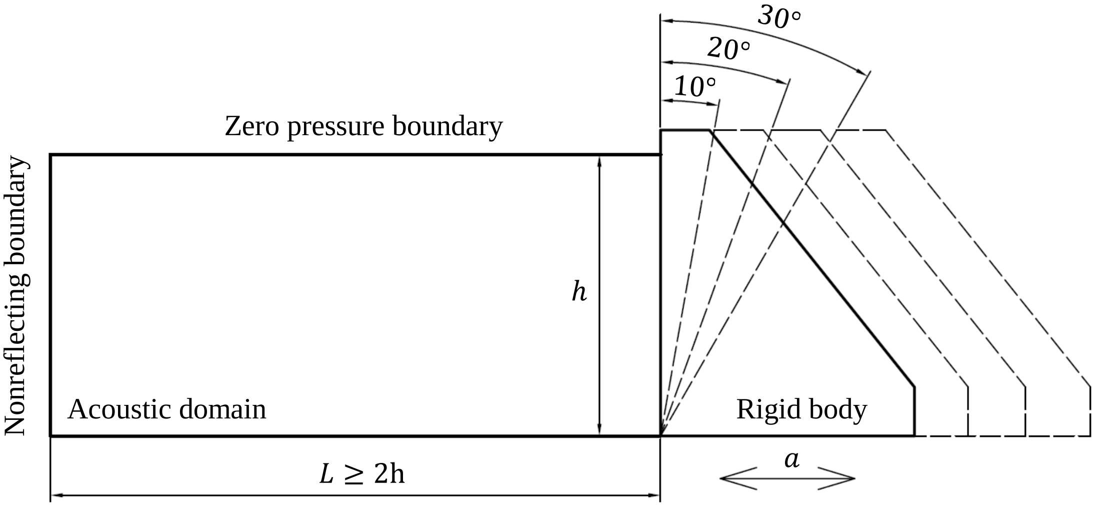

Figure 3-8: Finite elements model to investigate the dynamic water pressure distribution over the height of a rigid body with acoustic elements at constant acceleration

The diagram in Figure 3-9 depicts that the maximum pressure coefficient at the bottom of the reservoir for a completely vertical upstream surface of the dam stays almost constant for the investigated heights of 10.0 to 250.0 meters. The very small differences ($\Delta C = 0.0025$) emerge from numerical errors. The numerically calculated values of C are quiet near to 0.707, which corresponds to the sine or cosine of 45° and therefore $1/\sqrt{2}$. (Note: Zangar obtained a value of approximately 0.73 for zero inclination)

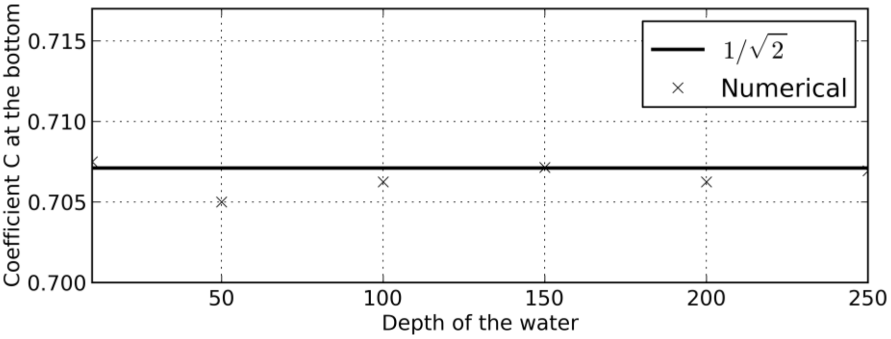

Figure 3-9: Relationship between the depth of the water and the resultant maximum pressure coefficient at the bottom for zero inclination

Therefore, equation (3-7) for the maximum pressure at the bottom and zero inclination can be rewritten as

$$p_{max,0} = 0.707\rho_w\, h\, a_e \tag{3-10}$$

Due to the fact that this equation only describes the pressure for the deepest point of the reservoir and a vertical surface, a relationship between the inclination and the maximum has to be found. The evaluation of the maximum pressure in the acoustic medium yields an almost linear behaviour regardless of the height where the pressure occurs (Figure 3-10). Zangar found the same connection in his experimental results, see Figure 3-6.

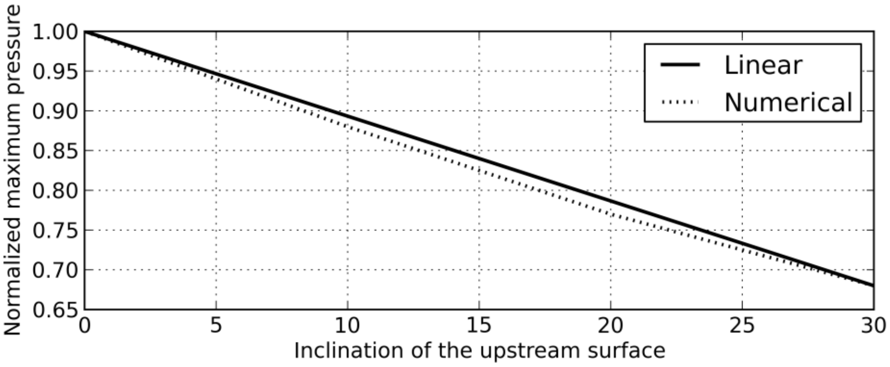

Figure 3-10: Relationship between the maximum pressure in the reservoir and the inclination of the upstream surface

With the conservative assumption that the relation is linear, the maximum pressure in dependency of the inclination φ (in degrees) and based on equation (3-10) is

$$p_{max(\varphi)} = p_{max,0}(1 - 0.011\varphi) \tag{3-11}$$

The inclination doesn't just influence the pressure, but also the depth where the maximum occurs. The maximum moves upward as the angle φ increases. Figure 3-11 shows the results of the simulations with the acoustic fluid and the pressure over the height of the dam.

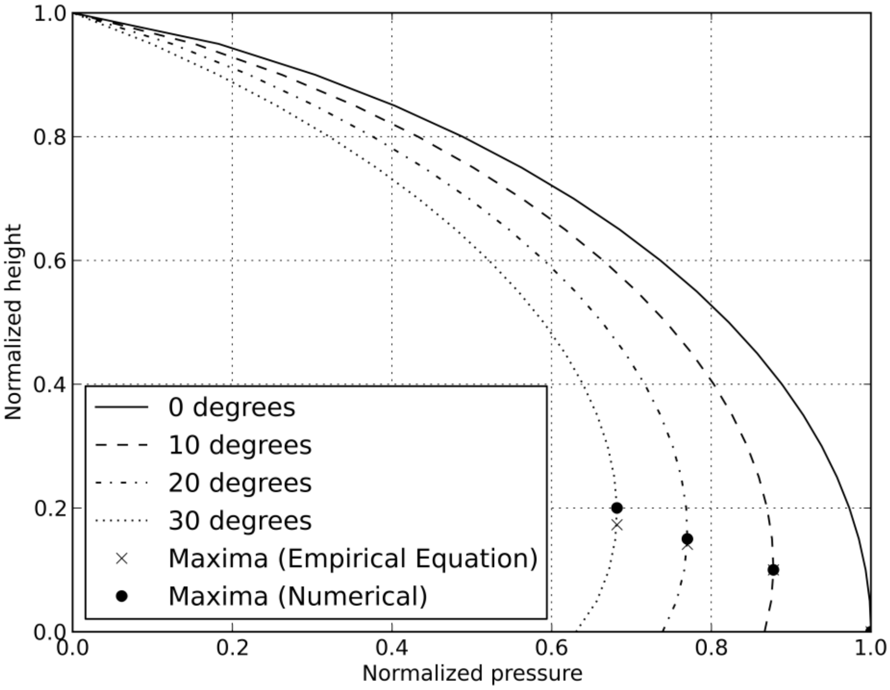

Figure 3-11: Normalized pressure and height relationship and comparison of the height were the maximum pressures occur between the numerical result and equation (3-12)

For the coherence between the angle (in degrees) and the height the following simplified relation has been found

$$h_{\max(\varphi)} = \sqrt{\frac{\varphi}{1000}}\,h \tag{3-12}$$

The negligible height difference calculated with this equation and the numerical result is also depicted in Figure 3-11.

Evaluations of a high number of finite element simulations have been used to find a proper function to describe the pressure distribution curves of Figure 3-11. The formula should also be dependent on the depth and the inclination of the upstream surface. After trying different functions, the cosine to the power of 0.6 plus a correction factor for the inclination of 0.005φ appeared to give the most satisfying results.

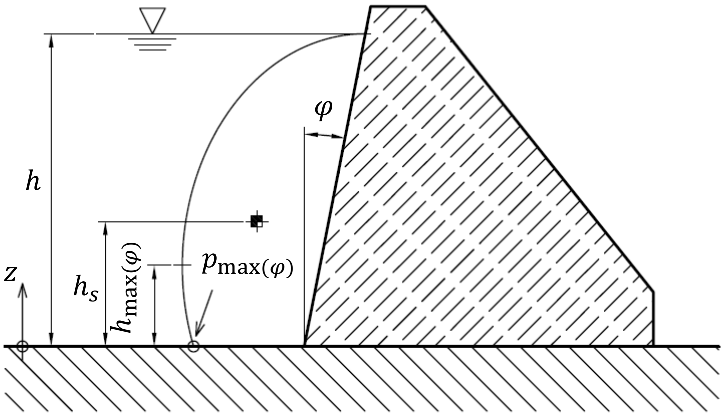

Figure 3-12: Schematic figure for the empirical equation according Goldgruber and Feldbacher (2013)

Together with equations (3-10) to (3-12) the new empirical equation is

$$p_{(\varphi,z)} = p_{max(\varphi)} \cos\left(\frac{z - h_{\max(\varphi)}}{h - h_{\max(\varphi)}} \frac{\pi}{2}\right)^{0.6+0.005\varphi} \tag{3-13}$$

or in terms of the added mass per squaremeter

$$m_{(\varphi,z)} = m_{max(\varphi)} \cos\left(\frac{z - h_{\max(\varphi)}}{h - h_{\max(\varphi)}} \frac{\pi}{2}\right)^{0.6+0.005\cdot\varphi} \tag{3-14}$$

In the special case of zero inclination equation (3-14) simplifies to

$$m_{(z)} = 0.707\rho_w\, h \cos\left(\frac{z}{h}\frac{\pi}{2}\right)^{0.6} \tag{3-15}$$

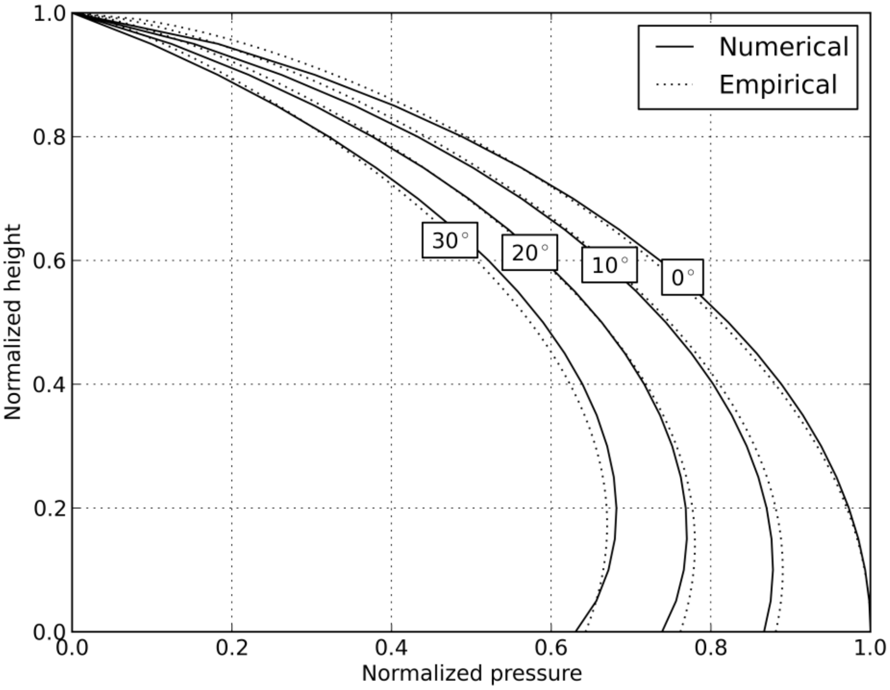

Figure 3-13: Comparison between the numerical results with acoustic fluid elements and the new empirical formula normalized to the highest pressure

Figure 3-13 shows the comparison between the numerical results with the acoustic fluid and the new empirical formula normalized to the highest pressure.

Figure 3-14a depicts the integrated added mass (total added mass on the upstream surface) for different total depths of the reservoir h and inclinations. For example, a reservoir with a depth of 125 meters and 10° inclination results in a total added mass of 7.5 kilotons (kt) per meter (in-plane direction). Figure 3-14b relates the centroid depth z_s where the total added mass acts to the total height of the reservoir. The differences between inclinations is negligible and centroid depth can be approximated by

$$h_s \approx \frac{2}{5} h \tag{3-16}$$

Which is identical to the centre from the Westergaard added mass approach from equation (3-6).

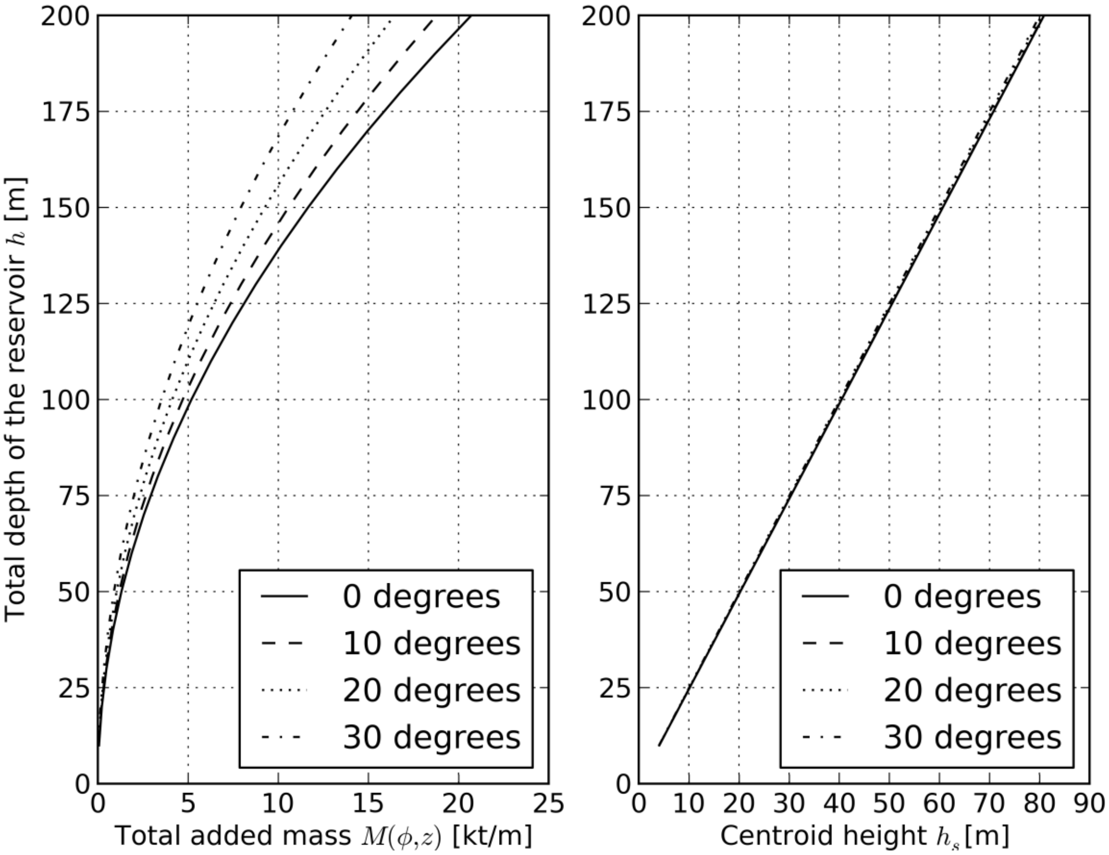

a) b)

Figure 3-14: a) Total added mass for different total reservoir depths and upstream surface inclinations; b) Centroid height h_s where the total added mass acts for different total reservoir depths and upstream surface inclinations

In conclusion, this empirical formula is applicable to fluid-structure interaction problems dealing with inclined surfaces up to 30°. Errors, which are implied with the often used simplified Westergaard equation or Zangar’s equation for nonzero angles are avoided. Apart from the gravity dam investigated in here, the application of this equation on an arch dam compared to other added mass approaches is shown in Section 5.2.

3.4 Added Mass Transformation for Non-Vertical Surfaces

Westergaard derived his equation for the added mass approach assuming a completely vertical surface. For such cases, the water mass only acts horizontal (perpendicular to the interacting surface) on the dam surface during a seismic event. Considering an inclined surface, the added mass and furthermore, the corresponding forces have to be adjusted in a way, that no shear forces out of these masses are mobilized, because water pressure can only develop normal dynamic forces. So, the added mass has to be considered, acting in perpendicular direction and therefore split up into a consistent mass matrix. The derivation of this transformation matrix can be easily described by considering a simple two dimensional case, where the mass distribution in cartesian coordinates on the dam is in arbitrary direction ($m_x \neq m_y$) and the normal vector is known.

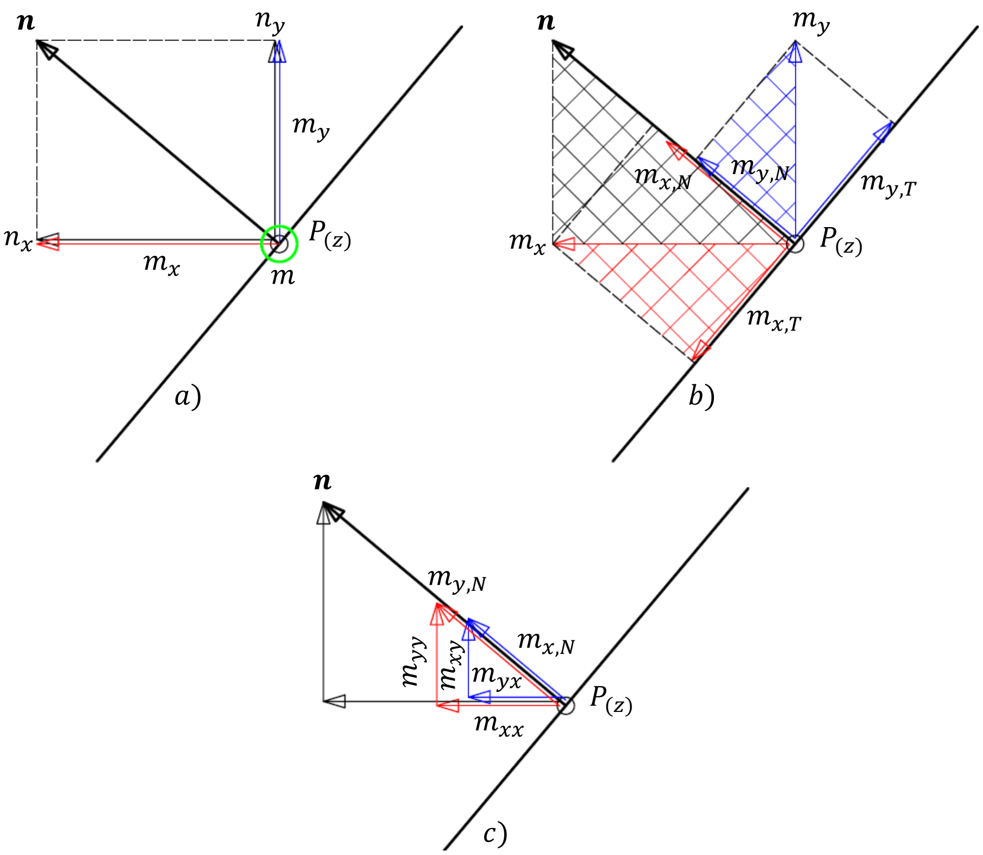

Figure 3-15: Mass vector transformation on a two dimensional surface

Figure 3-15 shows the procedure for achieving the transformation matrix and therefore, the consistent mass matrix. First, in Figure 3-15a an arbitrary acting mass m at a specific point P in depth z is split up in its two directions x and y by multiplication with the normalized normal vector $\boldsymbol{n}$ $(|\boldsymbol{n}| = 1)$ with its corresponding components n_x and n_y

$$m_x = mn_x; \quad m_y = mn_y; \tag{3-17}$$

Figure 3-15b shows the three similar triangles which have the following property

$$\frac{n_y}{n_x} = \frac{m_{x,T}}{m_{x,N}} = \frac{m_{y,N}}{m_{y,T}}; \quad \frac{n_x}{|\boldsymbol{n}|} = \frac{m_{x,N}}{m_x}; \quad \frac{n_y}{|\boldsymbol{n}|} = \frac{m_{y,N}}{m_y} \tag{3-18}$$

Due to the fact that the tangential components of the mass should be neglected, only the masses in normal direction are from interest, which are

$$m_{x,N} = m_x n_x \tag{3-19}$$

$$m_{y,N} = m_y n_y \tag{3-20}$$

Figure 3-15c shows the resultant mass quantities in normal direction $m_{x,N}$ and $m_{y,N}$ which can be split up again in x and y direction, because of the similar triangles and normalization they can be written as

$$\begin{pmatrix} m_{xx} \\ m_{xy} \end{pmatrix} = m_x n_x \begin{pmatrix} n_x \\ n_y \end{pmatrix} \tag{3-21}$$

$$\begin{pmatrix} m_{yx} \\ m_{yy} \end{pmatrix} = m_y n_y \begin{pmatrix} n_x \\ n_y \end{pmatrix} \tag{3-22}$$

In matrix formulation, the consistent mass matrix in normal direction can be found by combining equations (3-21) and (3-22)

$$\begin{bmatrix} m_{xx} & m_{xy} \\ m_{yx} & m_{yy} \end{bmatrix} = \begin{bmatrix} m_x & 0 \\ 0 & m_y \end{bmatrix} \begin{bmatrix} n_x n_x & n_x n_y \\ n_y n_x & n_y n_y \end{bmatrix} \tag{3-23}$$

Considering the mass as a scalar quantity, e.g. the Westergaard added mass $m_w(z)$ in a specific depth z, equation (3-23) reduces to

$$\boldsymbol{M}_w^N = m_w(z)\, \boldsymbol{N}_c \tag{3-24}$$

with the transformation matrix

$$\boldsymbol{N}_c = \begin{bmatrix} n_x n_x & n_x n_y \\ n_y n_x & n_y n_y \end{bmatrix} \tag{3-25}$$

For problems in three dimensions, e.g. arch dams, the interacting surface where the masses should be applied is curved. The matrix in three dimensional cartesian coordinates can easily be achieved just by extending it with the z coordinate, which gives

$$\boldsymbol{N}_c = \begin{bmatrix} n_x n_x & n_x n_y & n_x n_z \\ n_y n_x & n_y n_y & n_y n_z \\ n_z n_x & n_z n_y & n_z n_z \end{bmatrix} \tag{3-26}$$

The consistent mass matrix $\boldsymbol{M}_w^N$ for the added mass matrix has also been derived by Kuo (1982) in a similar way, and is often stated as *Generalized Westergaard Added Mass*.

The transformation matrix can also be shown by means of finite elements. Integration of the pressure on a surface over the area S in finite element formulation (Shape function $\boldsymbol{N_S}$ for the structure) can be described by the following equation

$$\int \boldsymbol{N_S^T}\, \boldsymbol{n}\, \boldsymbol{p}\, dS \tag{3-27}$$

The pressure $\boldsymbol{p}$ can be split up in a constant value α_z, which is the mass per squaremeter in a specific depth z, and the finite element approximation of the acceleration normal to the surface.

$$\boldsymbol{p} = \alpha_z \boldsymbol{n}^T \boldsymbol{N_S}\, \ddot{\boldsymbol{u}}|_{\boldsymbol{n}} \tag{3-28}$$

Combining these two equation (without the acceleration) yields the added mass matrix at the element level

$$\boldsymbol{M}_{\boldsymbol{added}}^e \int \alpha_z \boldsymbol{N_S^T}\, \underbrace{\boldsymbol{n}\, \boldsymbol{n}^T}_{\boldsymbol{N}_c}\, \boldsymbol{N_S} dS \tag{3-29}$$

Herein the term $\boldsymbol{n}\,\boldsymbol{n}^T$ gives the same transformation matrix as in equation (3-26).

3.5 Acoustic Fluid

Acoustic fluids or acoustic elements in finite element analyses are special purpose elements which are describing the sound wave/pressure distribution over time in acoustic media like gases or water. Commonly used in sound simulations, such elements also allow for simulating fluid-structure interaction problems if the following assumptions are valid:

- the fluid is compressible (density changes due to pressure variations),
- the fluid is inviscid (no viscous dissipation),
- the fluid is irrotational,
- there is no mean flow of the fluid (only small translations and small velocity $v \ll$)[1]
- no body forces

The acoustic fluid equation is a combination of the "Conservation of Momentum" (Equation (A-43)) from Section A.2.2 and the "Continuity Equation" (Equation (A-63)) from Section A.3. By taking into account that stresses in an acoustic fluid are just described by the pressure $\boldsymbol{\sigma} = -\boldsymbol{p} = -p\boldsymbol{I}$ (Note: Deviatoric components are zero and $\boldsymbol{p}$ has a negative sign to yield positive pressures), neglecting all external forces and applying the assumption from above, equation (A-43) yields

$$\nabla \cdot \boldsymbol{p} + \rho_w \dot{\boldsymbol{v}} = 0 \tag{3-30}$$

The "Continuity Equation" for an acoustic medium with a constant water density ρ_w is

$$\frac{\partial \rho}{\partial t} + \rho_w \nabla \cdot \boldsymbol{v} = 0 \tag{3-31}$$

For solving this set of equations (2 equations, 3 unknowns) a constitutive equation or constitutive law is needed to describe the differential pressure-density relationship in a compressible fluid, which is defined by

$$\partial p = c_w^2 \partial \rho \tag{3-32}$$

with the wave propagation speed c_w as a material property which is calculated by

$$c_w = \sqrt{\frac{K_w}{\rho_w}} \tag{3-33}$$

The time derivative of equation (3-31) gives

$$\frac{\partial^2 \rho}{\partial t^2} + \rho_w \nabla \cdot \dot{\boldsymbol{v}} = 0 \tag{3-34}$$

---

[1] This assumption yields that $\dot{\boldsymbol{v}} = \frac{Dv}{Dt}$ (Material time derivative) simplifies to $\frac{\partial v}{\partial t}$ and hence equations (3-30) and (3-31) can also be written in terms of the reference coordinates $\nabla_{\boldsymbol{x}} = \nabla_{\boldsymbol{X}} = \nabla$.

The rate of change of velocity (acceleration) in this equation $\dot{\boldsymbol{v}}$ can now be substituted by rearranging equation (3-30). In combination with the constitutive law from equation (3-32) the acoustic wave equation is

$$\frac{\partial^2 \boldsymbol{p}}{\partial t^2} - c_w^2 \nabla^2 \cdot \boldsymbol{p} = 0 \tag{3-35}$$

3.5.1 Impact of Consideration of the Water Compressibility

In contrast to simplified added mass approaches, water compressibility is directly accounted for if the reservoir is modelled by equation (3-35). Chopra (1968) investigated the response of gravity dams for models with an incompressible and a compressible reservoir and therefore found that the key parameter for the significance of the compressibility is the ratio between the natural frequency of the reservoir to the natural frequency of the dam. The first natural frequency of the reservoir can be approximated by

$$f_r = \frac{c_w}{4h} \tag{3-36}$$

In case of a concrete gravity dam the ratio between both frequencies should not be lower than 2.0, otherwise compressibility must be taken into account.

$$\Omega_r = \frac{f_r}{f_d} \begin{cases} < 2.0 & reservoir\ compressible \\ > 2.0 & reservoir\ incompressible \end{cases} \tag{3-37}$$

Chopra (1968) also showed that even for unrealistically low values of the concrete's Young's modulus the effects of compressibility are significant for the response due to vertical ground motion.

Later, in 1987, Fok and Chopra (1987) investigated the response of arch dams for different values of the Young's modulus, three different height-to-width ratios, two thicknesses and compressibility effects. They came to the similar conclusion as Chopra (1968) that the ratio Ω_r influences the response between a compressible and incompressible reservoir the most. The criteria of ratios higher than 2.0, like for gravity dams, cannot be determined, because too many parameters (ground motion direction, Young's modulus, geometry, etc.) affecting the systems response. Additionally, the wave absorptions effects on the boundaries of the reservoir will not be represented properly if compressibility is omitted.

Nevertheless, the consideration of a compressible reservoir for modelling dam-reservoir interaction is recommended for most problems, because first, the response might be significantly underestimated and second, the constitutive behaviour of water is modelled more accurately.

3.5.2 Coupling of the Acoustic Fluid and Structural Domain

On the contrary to added mass methods, where additional masses are just attached to the upstream surface of the structure, for models with acoustic elements a volume of water has to be generated and directly coupled to the structure. This section should roughly describe the way of coupling of these two different domains, which are in this case the structure and the fluid described by the acoustic wave equation. In the interface between these domains the coupling and boundary conditions together with the equilibrium of stresses (pressure) and continuity of displacement must be fulfilled. Based on Davidsson (2004) the governing equations and acoustic-structural coupling can be summarized as follows:

$$Governing\ Structural\ Equation\text{:}\quad \nabla_{\boldsymbol{x}} \cdot \boldsymbol{\sigma} + \boldsymbol{f} - \rho \dot{\boldsymbol{v}} = 0 \tag{A-43}$$

$$Governing\ Fluid\ Equation\text{:}\quad \frac{\partial^2 \boldsymbol{p}}{\partial t^2} - {c_w}^2 \nabla^2 \cdot \boldsymbol{p} = 0 \tag{3-35}$$

$$Continuity\ of\ Displacement\text{:}\quad u_S|_n = u_F|_n \tag{3-38}$$

$$Equilibrium\ of\ Stresses\ (Pressure)\text{:}\quad \sigma_S|_n = -p_F|_n \tag{3-39}$$

The governing structural equation is simply "Cauchy's First Law of Motion" from the Appendix A.2.2 and the governing fluid equation is the acoustic wave equation from Section 3.5. The continuity of displacements between both domains in equation (3-38) is fulfilled in normal outward direction at the coupling boundary. The equilibrium of stresses states that the pressure in the acoustic fluid has to be equal to the stress acting normal on the boundary of the structure. Furthermore, Davidsson (2004) derived these equations for finite elements leading to the following governing systems of equation (without any external forces) for the structural and fluid domain, respectively, in weak formulation

$$\int \boldsymbol{N}_S^T \rho_S \boldsymbol{N}_S dV \ddot{\boldsymbol{u}}_S + \int (\tilde{\nabla} \boldsymbol{N}_S)^T \boldsymbol{D}_S \tilde{\nabla} \boldsymbol{N}_S dV \boldsymbol{u}_S = \int \boldsymbol{N}_S^T \boldsymbol{t}_S dS \tag{3-40}$$

$$\int \boldsymbol{N}_F^T \boldsymbol{N}_F dV \ddot{\boldsymbol{p}}_F + {c_w}^2 \int (\nabla \boldsymbol{N}_F)^T \nabla \boldsymbol{N}_F dV \boldsymbol{p}_F = c_w^2 \int \boldsymbol{N}_F^T \boldsymbol{n}^T \nabla p_F \, dS \tag{3-41}$$

Or in a simplified form in matrix notation

$$\boldsymbol{M}_S \ddot{\boldsymbol{u}}_S + \boldsymbol{K}_S \boldsymbol{u}_S = \boldsymbol{f}_F \tag{3-42}$$

$$\boldsymbol{M}_F \ddot{\boldsymbol{p}}_F + \boldsymbol{K}_F \boldsymbol{p}_F = \boldsymbol{f}_S \tag{3-43}$$

$\boldsymbol{M}_S$, $\boldsymbol{M}_F$ are the mass matrices and $\boldsymbol{K}_S, \boldsymbol{K}_F$ are the stiffness matrices in finite element formulation, containing the constitutive matrix $\boldsymbol{D}_S$, shape functions $\boldsymbol{N}$ and material density ρ for each domain. The vectors $\boldsymbol{u}_S$ and $\boldsymbol{p}_F$ are the finite element approximation of the displacements and the pressure. On the right hand side of these equations the vectors $\boldsymbol{f}_S$ and $\boldsymbol{f}_F$ are the surface loads from the structure and acoustic fluid acting at the boundaries.

By means of Cauchy's stress tensor (Equation (A-35)) the surface traction from the right hand side of equation (3-40) can be expressed as

$$\boldsymbol{t}_S = \boldsymbol{pn} \tag{3-44}$$

Therefore, the coupling force from the acoustic domain in terms of the fluid pressure $\boldsymbol{p}_F$, which acts on the structure, in finite element formulation is

$$\boldsymbol{f}_F = \int \boldsymbol{N}_S^T \boldsymbol{n} \boldsymbol{N}_F dS \, \boldsymbol{p}_F \tag{3-45}$$

The force from the structure $\boldsymbol{f}_S$ on the acoustic fluid boundary can be derived by the relationship

$$\nabla p_F = -\rho_w \frac{\partial^2 \boldsymbol{u}_F}{\partial t^2} \tag{3-46}$$

Furthermore, applying the continuity of displacement from equation (3-38) yields

$$\boldsymbol{n}^T \nabla p_F = -\rho_w \frac{\partial^2 \boldsymbol{N}_F \boldsymbol{u}_F|_n}{\partial t^2} = -\rho_w \frac{\partial^2 \boldsymbol{N}_S \boldsymbol{u}_S|_n}{\partial t^2} = -\rho_w \boldsymbol{n}^T \boldsymbol{N}_S \ddot{\boldsymbol{u}}_S \tag{3-47}$$

Finally, substituting this equation in the right hand side term of equation (3-41) gives the force acting on the acoustic fluid in terms of structural acceleration

$$\boldsymbol{f}_S = -\rho_w c_w^2 \int \boldsymbol{N}_F^T \boldsymbol{n}^T \boldsymbol{N}_S \, dS \ddot{\boldsymbol{u}}_S \tag{3-48}$$

With

$$\boldsymbol{H}_{SF} = \int \boldsymbol{N}_S^T \boldsymbol{n} \boldsymbol{N}_F \, dS \tag{3-49}$$

the coupled system of equations expressed in matrix notation now is

$$\begin{bmatrix} \boldsymbol{M}_S & 0 \\ \rho_w {c_w}^2 \boldsymbol{H}_{SF}^T & \boldsymbol{M}_F \end{bmatrix} \begin{bmatrix} \ddot{\boldsymbol{u}}_S \\ \ddot{\boldsymbol{p}}_F \end{bmatrix} + \begin{bmatrix} \boldsymbol{K}_S & -\boldsymbol{H}_{SF} \\ 0 & \boldsymbol{K}_F \end{bmatrix} \begin{bmatrix} \boldsymbol{u}_S \\ \boldsymbol{p}_F \end{bmatrix} = \begin{bmatrix} 0 \\ 0 \end{bmatrix} \tag{3-50}$$

This derivation of the coupling between a structure and an acoustic fluid constitutes a brief summary and should just point out how it is achieved by means of finite elements. From equation (3-50) it can be observed that the coupling terms are acting on the diagonal parts of the stiffness and mass matrices, which makes it numerically costlier.

A more thorough explanation and further studies of such coupled systems can be found in Davidsson (2004) on which this section is based on.

3.5.3 Acoustic Fluid Boundary Conditions

Apart from the coupling of the structure and the fluid, additional boundary conditions have to be specified in dynamic simulations where the fluid is modelled directly. In case of dam-reservoir interactions three additional boundaries need prescribed conditions. These are the free surface on the top, the back end and the bottom/sides of the reservoir (Figure 3-16).

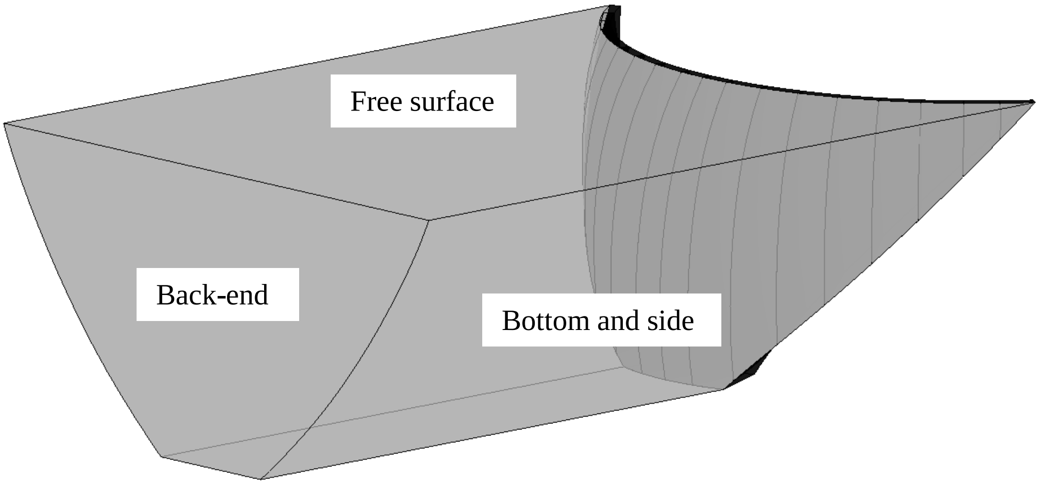

Figure 3-16: Different reservoir boundaries for an acoustic fluid

3.5.3.1 Free Surface Boundary

On the top of the reservoir a free water surface needs to be specified. To achieve this constitutive behaviour a simple pressure boundary condition has to be set to zero.

$$p_{free} = 0 \tag{3-51}$$

In case of a seismic analysis with an acoustic fluid this surface will be horizontal throughout the whole time span of the simulation. This means that pressure waves on the surface are neglected. Nevertheless, in nature, waves would be present, but stay small compared to the dimensions of the reservoir. A possibility to account for such surface motion effects is the use of an impedance boundary condition, which is further discussed in Section 3.5.3.3.

3.5.3.2 Back-End Boundary

Considering a reservoir in nature the boundary at the back-end is defined by the surrounding environment, where surfaces are not following a geometric definition. In numerical simulations modelling these curvatures exactly is mostly not necessary. A simplified geometry with appropriate boundary conditions describing the reservoir length effect is sufficient for most cases. This is due to the fact that reservoirs in nature can be kilometres long and the absorbing behaviour of the environment using a non-reflecting boundary is legit. In case of waves incident mainly normal to the back-end out of the seismic interaction between the structure and the reservoir Lysmer and Kuhlemeyer (1969) developed an absorbing boundary condition by using viscous boundary tractions, like dashpots. The damping force in normal direction is

$$f_n = \rho_w c_w \frac{\partial u_n}{\partial t} \tag{3-52}$$

In this case pressure waves approaching normal to the boundary will be completely absorbed by this condition. For waves with arbitrary angles absorption is still present, but not that effective. Dependent on geometry of the structure the induced waves due to the interaction might not be travelling parallel through the reservoir and approaching normal to the back-end boundary (see boundary in Figure 3-16). Apart from equation (3-52) different additional boundary condition for pressure wave absorptions exist, e.g. for spherical absorptions. Nevertheless, if the reservoir length is sufficiently long the reflected waves will just have a negligible influence on the structure, even if the boundary is fully reflective. Attarnejad and Lohrasbi (2008) investigated different length to height ratios of the reservoir with a total height of 180 meters by applying the El Centro earthquake motion, but with full reflection at the back-end. Therefore, they came to the conclusion that for a length of the reservoir model of at least four times the height of the structure the influence is negligible (<1%). If an absorbing – non-reflecting boundary – at the end of the reservoir is appropriate to use (dependent on the site conditions) the length can be decreased. Baumber (1992) investigated in his PhD thesis "Reservoir Length Effects on Seismic Response of Concrete Gravity Dams" wave reflection coefficients at the reservoir boundaries analytically. He showed significant effects on the crest accelerations if fully or partly reflective surfaces at the back-end for different length to height ratios are used.

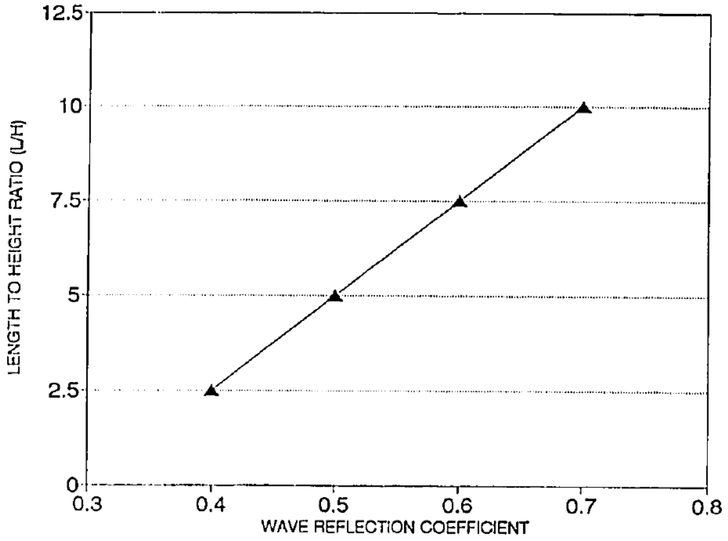

Figure 3-17: Value of wave reflection coefficient at which finite reservoir effects are not apparent by Baumber (1992)

The wave reflection coefficient at a boundary is defined as the ratio of the amplitude of reflected to incident pressure wave.

$$\alpha = \frac{p_{reflected}}{p_{incident}} \tag{3-53}$$

Hence, a reflection coefficient of 1.0 means full reflection, 0.0 total absorption (non-reflecting boundary) and -1.0 equals to a reflection with a phase reversal. Figure 3-17 by Baumber (1992) indicates that using a length to height ratio of 2.5 for the model and additionally a reflection coefficient of 0.4 reflection effects are negligible. Therefore, this diagram allows for the assumption that for non-reflecting boundary conditions even lower length to height ratios are possible. Nevertheless, he also states that these results are referring to a gravity dam, which is more rigid than, e.g. an arch dam and hence the flexibility might influence these results.

Chatterjee (2013) simulated a similar problem with simplified triangle geometry and an acoustic fluid by means of finite elements. He stated that by using a length to height ratio of 1.0 in coherence with a non-reflecting boundary is sufficient for neglecting possible reflection from a non-normal incident.

From these insights, following minimum lengths are recommended for reservoirs modelled as acoustic fluid despite of the structure to avoid reflection issues:

- $L_{min} \geq 4H$ if boundary is fully reflecting at the back end
- $L_{min} \geq 2H$ if boundary is non-reflecting at the back end

Furthermore, Chopra (2008) summarized factors that should be considered in earthquake analyses of arch dams. One of these was the use of absorbing boundaries, if applicable, because otherwise the results might be too conservative. This fact was also found by Hellgren (2014), where he investigated 3 different boundary conditions at the back-end (total reflection, zero pressure and non-reflecting) of the linear arch dam model from Section 5.1.3. He concluded that the resulting differences between stresses and displacements in general are small, whereby the non-reflecting boundary showed the smallest results.

3.5.3.3 Bottom and Side Boundaries

In numerical simulations of dams often a simplified geometry of the water reservoir, like in Figure 3-16, is used. The boundary conditions on the back-end are discussed in Section 3.5.3.2, where mostly an infinite reservoir with a non-reflecting boundary is assumed. For the bottom and side boundaries this assumption is not legit, because reflections of pressure waves in the near-field are existent and hence will affect the dynamic behaviour of the structure. This fact has been excessively studied by Hall and Chopra (1980) and Fenves and Chopra (1984).

The rate of reflection is characterized by the foundation material and usually defined by the wave reflection factor α from equation (3-53). This factor in terms of the material parameters can also be written as

$$\alpha = \frac{1 - R}{1 + R} \tag{3-54}$$

With R as the ratio between the density ρ_w, ρ_r and wave propagation speed c_w, c_r of the water and the foundation material

$$R = \frac{\rho_w c_w}{\rho_r c_r} = \frac{\sqrt{\rho_w K_w}}{\sqrt{\rho_r E_r}} \tag{3-55}$$

Combining these two equations gives

$$\sqrt{\rho_r E_r} = \frac{1 + \alpha}{1 - \alpha} \sqrt{\rho_w K_w} \tag{3-56}$$

Absorption effects of incident pressure waves are often modelled as boundary conditions on the reservoir bottom by using impedance values of the materials. The impedance is defined as

$$c = \sqrt{\rho_r E_r} \tag{3-57}$$

So, equation (3-56) allows for calculation of the impedance c of the boundary of the acoustic fluid if the wave reflection factor α is known. According to Dassault Systèmes (2013) the boundary condition along an acoustic fluid boundary is

$$\dot{u}_{out} = \frac{1}{k}\dot{p} + \frac{1}{c}p \tag{3-58}$$

This equation describes the outgoing velocity, where $\frac{1}{k}$[2] is the proportionality coefficient between the pressure and the displacement normal to the surface, and $\frac{1}{c}$[4] is the proportionality coefficient between the pressure and the velocity normal to the surface. Both of them are also referred to as admittance (inverse of the impedance).

The term $\frac{1}{k}$ can be neglected if displacement of the boundary or a volumetric drag is not existent, otherwise for free surfaces (see Section 3.5.3.1) sloshing effects can be modelled by using an impedance value of

$$k = \rho_w g \tag{3-59}$$

Dependent on the site conditions (bottom material) wave reflection factors can vary significantly. On site measurements by Ghanaat and Redpath (1995) at 7 dams showed that α can vary between -0.55 and 0.77, whereas negative values indicate sediments with trapped gas, normal sediment low values of 0.1 to 0.5 and rock 0.5 and higher. Nevertheless, a full reflection with a factor of $\alpha = 1.0$ will not appear in nature and even a small drop from 1.0 to 0.75 leads to significant decreases in the response on the stress level. This behaviour was observed by Lin et al. (2008) and Hellgren (2014) for two different arch dams. Furthermore, both found also that for wave reflection factors below 0.75 the stresses decrease only slightly. The same behaviour was observed for a gravity dam by Hall et al. (1998).

Therefore, it can be concluded that the assumption of a full reflection leads to conservative results, but might overestimate the response significantly. Rigorous modelling of the geometry and coupling of the fluid and foundation boundary should be considered if reflections in the near field of the dam structure due to a curved or oblique reservoir are expected. Furthermore, accelerations at the fluid-foundation boundary induce additional pressure waves into the reservoir and might also affect the response of the structure.

---

[2] The impedances c and k are also referred to as real and imaginary part of the complex impedance, respectively, which is usually frequency dependent and used for problems where a volumetric drag is present.

4 SEISMIC DISPLACEMENT OF A GRAVITY DAM

4.1 Introduction

Investigations of the sliding stability of gravity dams and rock blocks at seismic loading depicts that many additional factors are influencing the dynamic behaviour of the system. Treating the gravity dam as rigid block may lead to wrong results regarding stresses and displacements, due to the self-oscillations of the structure. Additionally to the dynamic load from the excited structure and water, there are also static loads acting on the structure like the hydrostatic water load and the pore water pressure in the contact plane, which is also influenced by a grout curtain, drainage systems and fault zones. Due to the self-weight one gets shear resistance and cohesion in the contact plane according to the Mohr-Coulomb failure criterion, which are the only two parameters against sliding of the model.

Gravity dam stability against sliding failure mechanism (under seismic conditions/loading) can be assessed by following different approaches:

- Limit equilibrium method considering the inertial forces as static permanent loads
- Newmark’s Sliding Block Analysis or dynamic simplified approach, which computes the permanent displacement of a rigid block under seismic excitation
- True dynamic analyses with the finite element method (FEM)

The simplified and the true dynamic analyses lead to the evaluation of the relative displacement of the gravity dam. The relative displacement is the fundamental requirement to assess the dam safety.

Newmark (1965) derived an analytical method to calculate the possible displacements of embankment dams based on a critical acceleration at which sliding starts. In the past and now, this method is also used for rock sliding evaluation at seismic loading. Later, based on Newmark’s Sliding Block Analysis, Chopra and Hall (1982) derived the critical acceleration for gravity dam structures or more generally speaking, structures which are also loaded by water pressures and uplift and not just by dead weight.

Besides the analytical ways, contact modelling with finite elements, especially for dynamic problems, is a complicated numerical procedure. Many parameters, e.g. time-integration schemes and time integration factors may be influencing the results significantly. Therefore, dynamic investigations of structures with contact modelling must be examined critically.

This work provides a comparison between the Newmark based sliding block method published by Chopra and Hall (1982), different empirical formulas like those from Jibson (1993), Jibson, Harp and Michael (1998) and Ambrasey and Menu (1988), and the finite element method utilizing added masses and acoustic elements. It should also show the applicability of these different methods to sliding problems of gravity dams and rock blocks interacting with the water.

This section is almost entirely based on the paper by Goldgruber & Shahriari, et al. (2015), except for a few changes in the content and additional/formatted diagrams.

4.2 The Gravity Dam Model

The structure of interest is a concrete gravity dam. The focus of this work is the sliding safety of such a structure on a horizontal rock foundation due to seismic loading.

The geometry of the gravity dam is based on the dimensions of the Birecik dam (Figure 4-1) and has therefore a height of 62.5 meters. The base of the dam has a width of 45.0 meters. A grout curtain is situated 7 meters in distance from the upstream surface of the dam and it reaches 30 meters into the foundation. This leads to an uplift pressure decrease to 2/3 of the maximum pressure (Figure 4-2) from the reservoir water level, which is a common assumption for safety assessments of concrete dams for simplified methods.

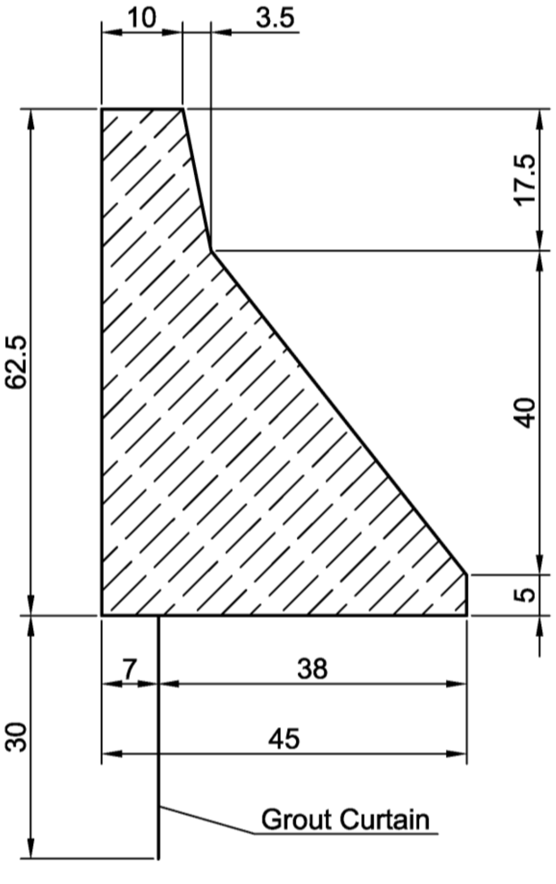

Figure 4-1: Sketch of the Gravity Dam and its dimensions

In the case of a seismic event it cannot be ensured that the grout curtain is still working properly. So, the conservative assumption was made that the pore water pressure distribution will be linear from the upstream to the downstream surface. Such a distribution can be assumed as a post-earthquake case.

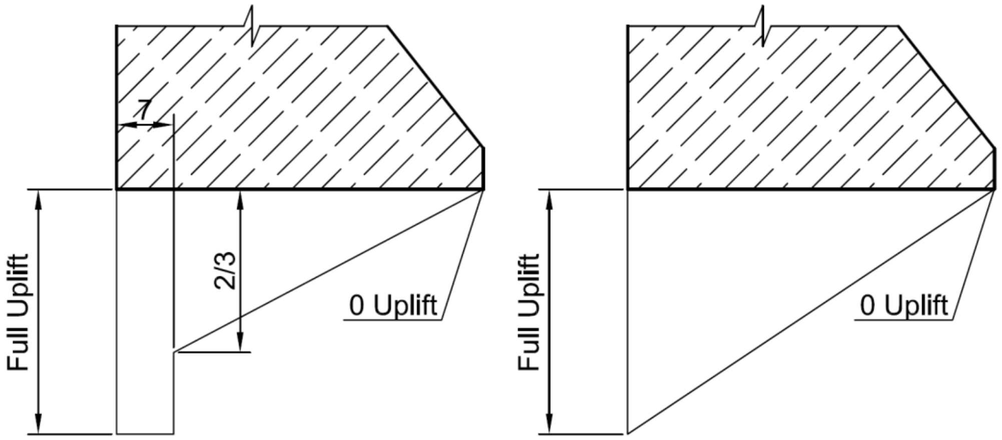

Figure 4-2: Uplift pressure distribution with a fully intact grout curtain (left) and a ruptured (post seismic case) grout curtain (right)

Additional investigations of the whole model have been done with a scale factor of 2.0. This means that the height of the dam is increased to 125 m. This is done to evaluate the influence of scaling effects of the fluid modelling techniques explained in Chapter 3.

4.3 Earthquake Acceleration-Time-History Records

Acceleration-time-histories are based on design spectra according to the peak ground acceleration (PGA) and the normalized spectra for a specific area. To define such a spectrum, mostly empirical methods in coherence with free field records of seismic events are used. Some of them are

- the Newmark Method for spectra,
- the US-NRC-Spectra from the United States,
- the HSK-Spectra from Switzerland and
- a study on spectra by McGuire (1974).

The one used in the Austrian guideline for earthquake assessment of dams (2001) is based on the study by McGuire (1974), which is only applicable to rock foundations and alluvium. These spectra are not applicable to underground conditions where significant amplifications due to sediments are expected. In this case further studies on the influence of the underground have to be done.

For nonlinear assessments of structures time-histories of the ground-acceleration are needed. The two orthogonal independent acceleration-time-histories used in this study are shown in Figure 4-3 and generated according to the spectra from the Austrian guideline mentioned above, by using the program SIMQKE from Massachusetts Institute of Technology (1976).

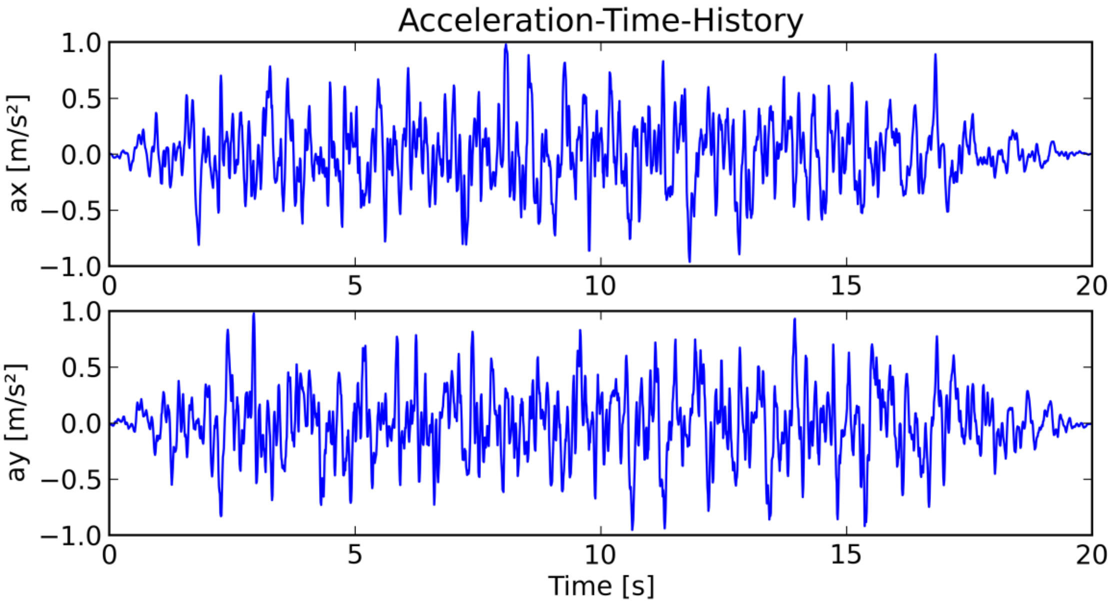

Figure 4-3: Acceleration-time-history records in 2 directions

From a practical point of view using just one artificial acceleration record has the drawback that it only covers one specific frequency range. Therefore, the use of several different records for the practical assessment of seismic excited structures is recommended, because the exact amplitude or frequency of an earthquake is not predictable. A simplification often done by engineers is to scale the records to increase or decrease the amplitude, without changes in the frequency range. However, measurements of real earthquakes have shown that the frequency changes with the intensity. Therefore, the applied motion can lead to conservative or under estimated results. This means that the consideration of the expected amplitude in coherence with the frequency is unconditionally recommended for the assessment.

The accelerations in the model are applied in both directions, horizontal (x) and vertical (y), on the foundation boundaries in normal direction with a maximum acceleration of 1.0 m/s² (0.1g).

4.4 Methods for the Displacement Evaluation

4.4.1 Newmark's Sliding Block Analysis

The pseudo-static method of analysis provides the factor of safety but no information on displacements associated with the failure. Since earthquake-induced accelerations vary with time, the pseudo-static factor of safety will vary throughout a ground-motion. Newmark (1965) proposed a method of analysis that estimates the permanent displacement of a slope subjected to ground-motions by assuming a rigid block resting on an inclined plane. When a block is subjected to a pulse of acceleration that exceeds the yield acceleration, the block will move relative to the ground. The relative acceleration is given by:

$$\ddot{u}_{rel}(t) = a(t) - a_y \qquad (4\text{-}1)$$

Where $\ddot{u}_{rel}$ is the relative acceleration of the block, $a(t)$ is the ground acceleration at time t and a_y is the yield acceleration. By integrating the relative acceleration twice and assuming linear variation of acceleration the relative velocity and displacement at each time step can be obtained (Figure 4-4).

Sliding is initiated in the downstream direction when the upstream ground acceleration $a(t)$ exceeds the yield acceleration a_y. Downstream sliding ends when the sliding velocity $\dot{u}_{rel}$ is zero and the ground acceleration drops below the yield acceleration.

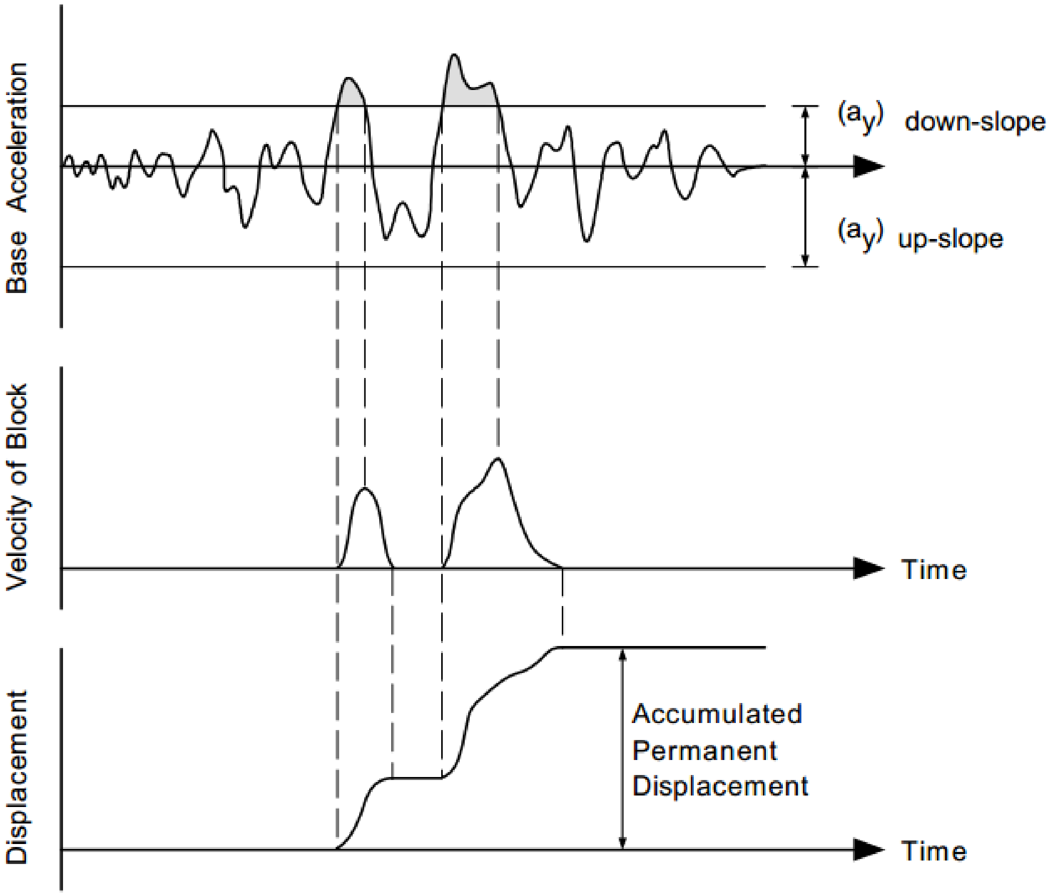

Figure 4-4: Illustration of Newmark's Sliding Block Analysis

4.4.1.1 Yield Accelerations

Conducting a Newmark analysis requires characterization of two key elements. The first element is the dynamic stability of the rigid block and it can be quantified as the yield or critical acceleration a_y. This parameter is the threshold ground acceleration necessary to overcome sliding resistance force and initiate permanent block movement. The second parameter is the ground motion record to which the block will be subjected.

To perform a Newmark analysis the gravity dam assumed to be a rigid body of mass m and weight G supported on horizontal ground that is subjected to acceleration $a(t)$. In reality, the dam is bonded to the foundation, however, in this study the dam is assumed to rest on horizontal ground without any mutual bond and the only force against sliding of the dam is the friction force between the base of the dam and the ground surface. Selecting an appropriate friction coefficient μ_s is complicated because after earthquake forces overcome the bond between dam and foundation rock, the cracked surface will be rough and the friction coefficient for such a surface is significantly higher than for a planar dam-foundation interface.

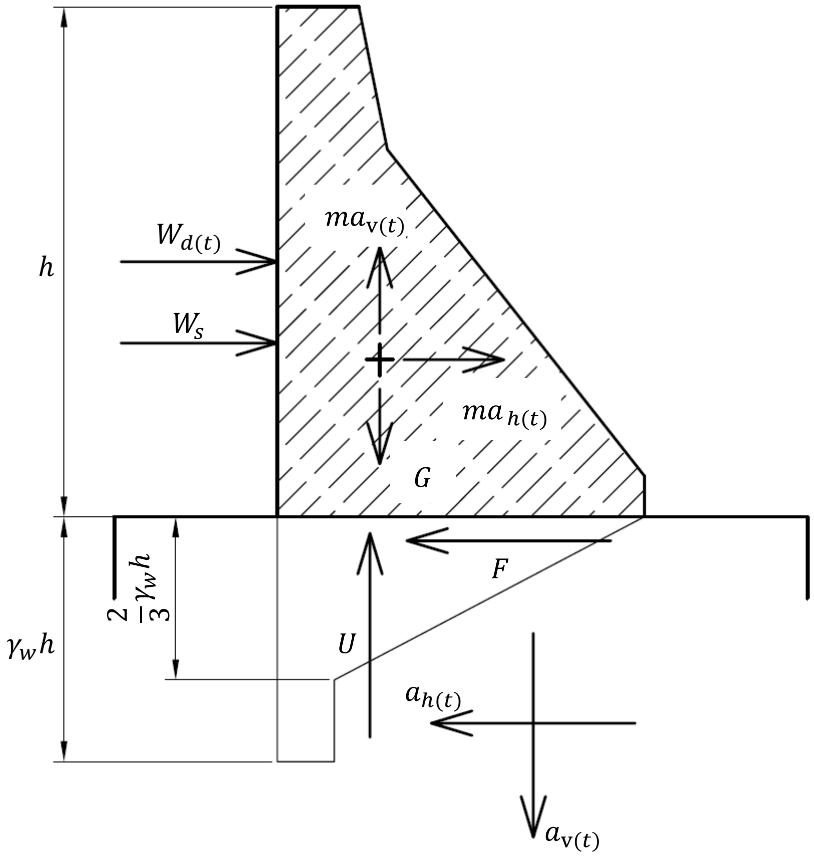

Figure 4-5: Static and dynamic forces on the dam model

The hydrostatic force W_s acting on the face of the dam is always pushing the dam in the downstream direction. The inertia force associated with the mass of the dam is $-(G/g)a(t)$ and it is acting opposite to the acceleration direction. Therefore, the accelerations in Figure 4-5 are acting at the foundation and positive in their respective directions.

The hydrodynamic force can be determined as below:

$$W_d(t) = -a_{h(t)} \int P_{hd}(z)\, dz = -M_w^* a_{h(t)} \tag{4-2}$$

Where $P_{hd}(z)$ is the hydrodynamic pressure on the upstream face of the dam due to unit acceleration in the upstream direction and M_w^* is the added mass which moves with the dam and produces inertia force. The added mass M_w^* (in this case) is determined by Westergaard's simplified equation (3-4) from Section 3.1.

Consider the equilibrium of forces shown in Figure 4-5, where the friction force F before the dam starts to slide is:

$$F = \mu_s (G - U)$$

Where U is the uplift force due to Figure 4-2 at the base of the dam with grout curtain and G is the dead weight. The dam is in a state of incipient sliding in the downstream direction when the upstream acceleration $a(t)$ reaches the yield acceleration a_y. The yield acceleration can be calculated by Chopra and Hall (1991):

$$a_y = \frac{1}{m + M_w^*}\left[\mu_s(G - U) - W_s\right] \tag{4-3}$$

Due to the hydrostatic force always acts in the downstream direction, the yield acceleration necessary to slide the dam downstream is significantly smaller than that for upstream sliding, therefore, the upstream sliding in a full reservoir case is negligible even for very strong earthquakes.

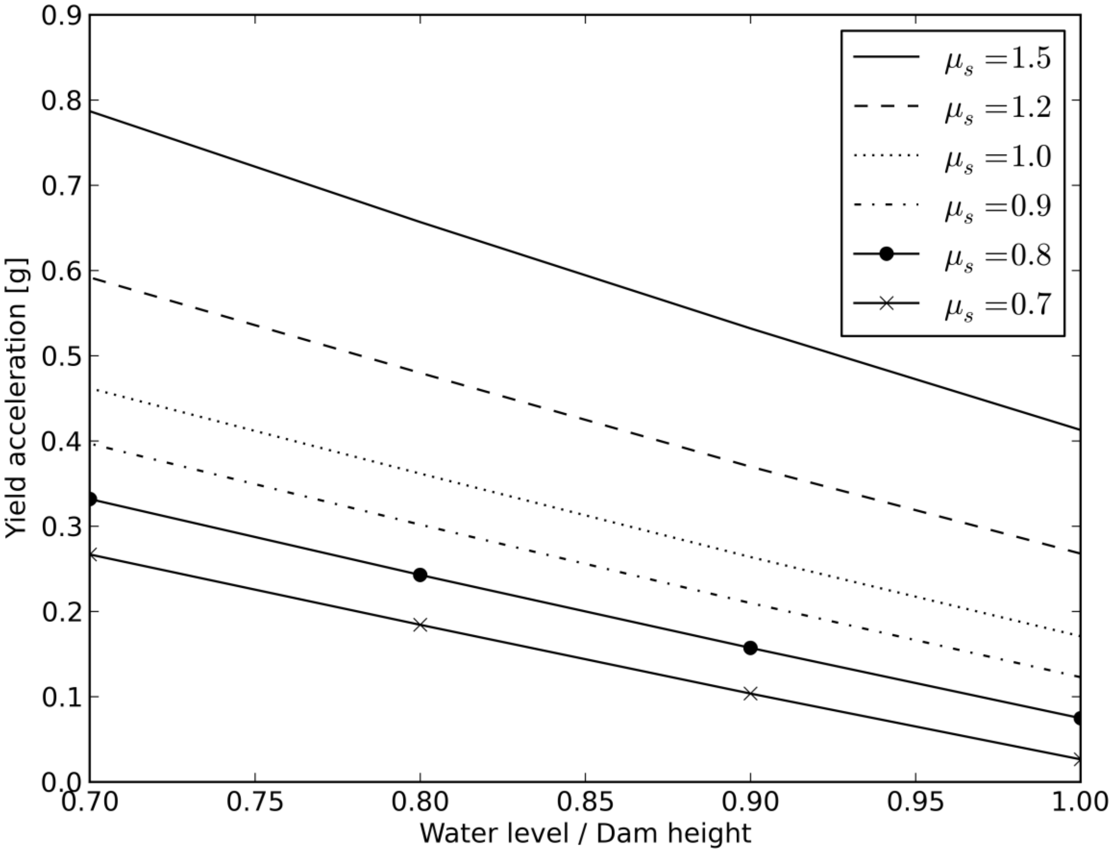

Figure 4-6: Yield acceleration of the gravity dam for different friction coefficients and water levels

Because downstream sliding is the most significant mode of motion of the rigid gravity dam, it is necessary to investigate the downstream yield acceleration that initiates the motion. As it is shown in Figure 4-6 the yield acceleration increases with an increasing friction coefficient and of course it is decreasing with higher water level to dam height ratio because of the higher static and hydrodynamic forces. In reality, a practical range of the friction coefficient is between 1.0 and 1.5 and the dam height to water level ratio is between 0.9 and 1.0, therefore the yield acceleration necessary to initiate the motion is between 0.2g to 0.5g. Because of the mutual bond between the dam and the foundation these values are higher and therefore a very strong ground motion is required to slide the dam in downstream direction.

The ground acceleration in two dimensional dynamic analyses has two components. The horizontal component of the ground motion is considered in the governing equation of motion and determination of the yield acceleration. To consider also the vertical acceleration, the assumption here is that a vertical acceleration a_v influences the weight of the dam G (but not the reservoir added mass) at each time step, therefore the weight of the structure will be:

$$G(t) = m(g - a_v(t)) \tag{4-4}$$

The time-dependent yield acceleration for consideration of a vertical acceleration can be determined by:

$$a_y(t) = \frac{1}{m + M_w^*}\left[\mu_s(G(t) - U) - W_s\right] \tag{4-5}$$

Figure 4-7 shows the yield acceleration for the dam including vertical acceleration for $\mu_s = 0.84$. It can be seen that the yield acceleration is constant when considering horizontal excitation only. On the other hand, when vertical excitation is included in the analysis as described above, this value a_y is changing over the entire duration of the earthquake.

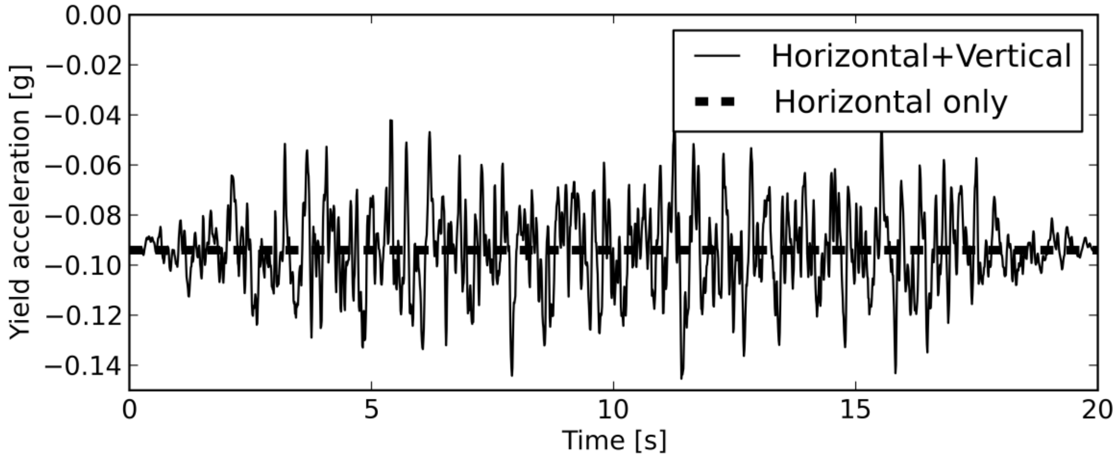

Figure 4-7: Yield acceleration by including vertical acceleration for, e.g. $\mu_s = 0.84$

4.4.2 Empirical Estimation of the Newmark Displacement

4.4.2.1 Ambraseys and Menu

Newmark's Sliding Block Analysis depends on the acceleration records and determining a proper acceleration-time-history for a specific site is complicated and time consuming. The empirical formulas were developed to estimate the Newmark displacement based on past strong-motion records. Ambraseys and Menu (1988) proposed various regression equations to estimate the Newmark displacement as a function of yield and maximum acceleration based on 50 strong-motion records from 11 earthquakes. They concluded that the following equation with a standard deviation of 0.3 is the best to characterize the results of their study:

$$log\, D_N = 0.90 + log\left(\left(1 - \frac{a_y}{a_{max}}\right)^{2.53}\left(\frac{a_y}{a_{max}}\right)^{-1.09}\right) \quad \pm 0.30 \tag{4-6}$$

4.4.2.2 Jibson93

Where a_y is the yield acceleration, a_{max} is the maximum acceleration and D_N is the Newmark displacement in centimeters. Different forms of equations have been proposed in other studies with additional parameters to estimate Newmark's displacement. Jibson (1993) proposed the following regression equation which is known as Jibson93 and it's based on 11 acceleration records which are suitable for a_y values of 0.02, 0.05, 0.10, 0.20, 0.30 and 0.40g with a standard deviation of 0.409:

$$log\, D_N = 1.460 log I_A - 6.641 a_y + 1.546 \qquad \pm 0.409 \tag{4-7}$$

Where a_y is the yield acceleration in g's, I_A is the Arias intensity in meters per second and D_N is the Newmark displacement in centimeters. The Arias intensity (1970) is a measure of the strength of a ground motion and can be determined by the equation

$$I_A = \frac{\pi}{2g} \int_0^{T_d} a_{(t)}^2 dt \tag{4-8}$$

Where g is the gravity, $a_{(t)}$ is the ground motion acceleration and T_d is the duration of the ground motion. The Arias intensity measures the total acceleration content of the records and it provides a better parameter for describing the content of the strong-motion record than does the peak acceleration. It can also be understood as the total energy per unit weight stored by undamped oscillators after the earthquake duration T_d.

4.4.2.3 Jibson98

In the Jibson93 equation, a_y is a linear term and it makes the model overly sensitive to small changes of yield acceleration. Jibson et al. (1998) modified the equation to make all terms logarithmic and then performed a rigorous analysis of 555 strong-motion records from 13 earthquakes for the same a_y values as indicated for Jibson93 to generate the following regression equation:

$$log\, D_N = 1.521 log I_A - 1.993 a_y - 1.546 \qquad \pm 0.375 \tag{4-9}$$

4.4.3 The Numerical Method

4.4.3.1 2D Structural Finite Element Model

The 2D structural model contains three parts, the gravity dam, the foundation and the reservoir, which are assembled together by specific interaction conditions. The finite element dam model is discretized with linear quadrilateral and triangular elements. The linear triangular elements are only used near the contact surface between dam and foundation, because of the mesh refinement, due to the use of linear elements. The finite element foundation model has a total length of 300.0 meters and a height of 100.0 meters. The boundaries are fixed normal to their surface for static loading conditions. This model is fully discretized with linear quadrilateral elements.

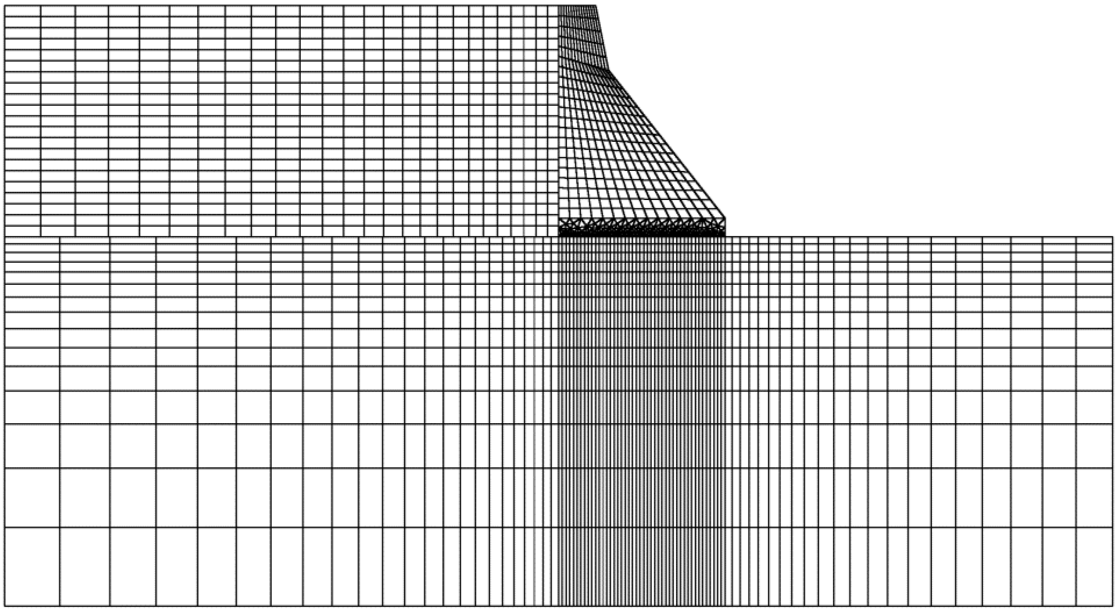

Figure 4-8: 2D finite element gravity dam model

Table 4-1: Material properties

	Density [kg/m^3]	**Permeability [m/s]**	**Poisson ratio [-]**	**Youngs/Bulk modulus [MPa]**
Gravity Dam	2500	0	0.17	25000
Foundation	0	10^{-4}	0.2	30000
Grout Curtain	0	10^{-8}	0.2	27000
Reservoir	1000	-	-	2200

Furthermore, to evaluate the effects of the interaction with the added mass method compared to the model with the acoustic volume, a second model has been made and scaled by the factor of 2.0, resulting in a height of 125.0 meters.

4.4.3.2 Contact Modelling

Besides the structural modelling, the contacts between the different parts have to be defined. For the interaction of the gravity dam and the reservoir, the coupling is set to “tie constraint”, so no relative movement is possible.

Tangential Contacts

The interaction modelling between the dam and the foundation is much more complicated. The contact modelling parameters have been chosen as simple as possible to get proper and converging results, which could not be that easy to achieve in a transient dynamic simulation. The contact in ABAQUS/CAE is defined as finite sliding with a “surface to surface” discretization. For the tangential behaviour, the penalty formulation is used, which means that the friction angle and a maximum elastic slip have to be specified. The friction angle is changed in each simulation separately and for the elastic slip γ_e the default value for the slip tolerance of $F_f = 0.005\ (0.5\%)$ is used with the relationship

$$\gamma_e = F_f \overline{l_\iota} \tag{4-10}$$

with $\overline{l_\iota}$ as the characteristic contact element surface dimension. An exceedance of this value results in permanent displacement. One can increase this value for better computational efficiency, but therefore losing accuracy. Figure 4-9 illustrates the sticking-slipping behaviour for the defined parameters based on the critical shear stress τ_{crit}, which is calculated by

$$\tau_{crit} = \mu p \tag{4-11}$$

where p is the contact pressure. In the sticking state the frictional shear stress is

$$\tau = \kappa \gamma_e \tag{4-12}$$

with κ as the shear traction slope, which is an artificial stiffness allowing the gradually increase of shear stresses up to τ_{crit}, which can also be understood as yield shear criteria.

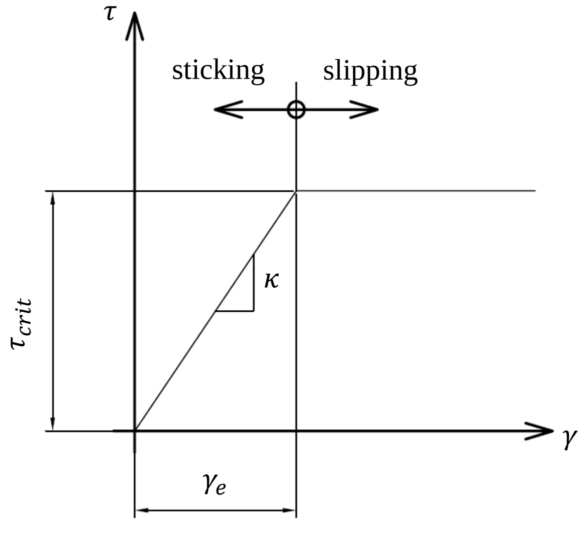

Figure 4-9: Elastic slip and slip tolerance definition based on Dassault Systèmes (2013)

Note, that the elastic slip describes the tangential contact stiffness of two surfaces, which can be understood as linear spring stiffness. High values increase the allowable movement before slipping starts and therefore introduces an artificial spring to the contact. For specific problems with a small amount of elements in the contact plane and therefore a relatively large value of $\overline{l_\iota}$ (characteristic contact element surface dimension) the default value for the slip tolerance F_f of 0.005 leads to high elastic slip γ_e values and might not be acceptable. For the gravity dam model the mesh size in the contact plane is chosen small, so the default slip tolerance of 0.5 % is appropriate. With a contact element length of 0.5 meters and the default tolerance, the allowed elastic slip for this model is approx. 2.5 millimetres. Based on the dimensions of the structure and the full contact length of 45.0 meters this value is acceptable, but not larger.

For other problems, where the mesh in the contact plane might be coarse, a parameter study is recommended. The influence of different values on a coarse contact mesh and recommendations for the elastic slip for an arch dam model is discussed in Section 6.7.2.

Normal Contacts

The normal contact formulation is set to "Hard Contact" (Figure 4-10). Additionally to these parameters any separation of the contact surfaces is neglected, in order to reach convergence more easily. This means that openings between the dam and foundation are not possible and only relative slipping is allowed. The contact modelling and the accompanying convergence problems are also the main reason for using linear elements instead of quadratic ones. The "Hard Contact" formulation which is depicted in Figure 4-10 only allows for two states of the contact, open or closed. When the contact is open (clearance $c_c \neq 0$), no contact pressure p exist and if it is closed (clearance $c_c = 0$), any arbitrary value for p is possible.

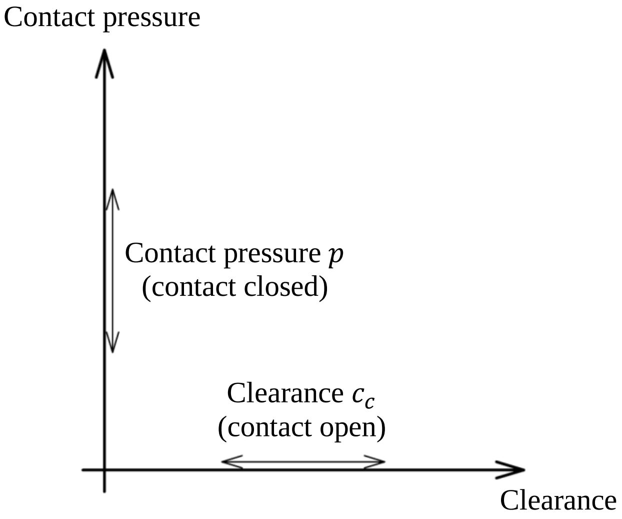
Contact pressure
Contact pressure p (contact closed)
Clearance c_c (contact open)
Clearance

Figure 4-10: Normal contact formulation for "Hard Contact" based on Dassault Systèmes (2013)

Another possibility, if convergence problems are present, would be the use of the "Soft Contact" formulation with e.g. "Exponential Pressure-Clearance Relationship", which is used and described in Section 6.3.

The cohesion is neglected in all simulations, so the friction angles used, can be understood as the residual friction angle.

The simulations of the models with a height of 62.5 meters and 125.0 meters respectively and also for the two reservoir modelling techniques described in Section 3.1 and 3.5 are performed for different friction angles and zero inclination in the contact plane. The friction coefficient starts at 1.0 (45 degrees) and is reduced in 5 steps until the displacement is getting progressive. Table 4-2 shows the friction coefficients and corresponding friction angles used for the simulations.

Table 4-2: Friction coefficients and friction angles

Friction angle	45.0°	40.0°	37.6°	35.0°	33.4°	33.0°
Friction coefficient	1.00	0.84	0.77	0.70	0.66	0.65

4.4.3.3 Reservoir Modelling with the Added Mass Method

Two different ways to calculate the added water mass are used, the simplified and the rigorous formula according to Westergaard from Section 3.1. For the application of these masses in the Abaqus/Cae model of the dam, a User Subroutine called UEL (User Element) was written. This subroutine calculates the mass for every node of an element surface, e.g. 3 nodes for a quadratic formulation and 2 nodes for a linear shell element, and distributes it evenly.

4.4.3.4 Reservoir Modelling with Acoustic Elements

Additionally to the added mass approach acoustic elements are used to simulate the interaction. The generated acoustic volume has a length of 150.0 meters (300.0 meters for the two times scaled model) and the same height as the gravity dam model. Quatrilateral elements are used as for the foundation. The boundary condition on the upstream end of the reservoir is set to non-reflecting, which means that the pressure is completely absorbed, this boundary formulation is described by Lysmer and Kuhlemeyer (1969). Furthermore, on the water surface the acoustic pressure is set to zero to account for the free surface. The boundary at the reservoir bottom is totally reflecting and no accelerations are applied.

4.4.3.5 Grout Curtain and Pore Water Pressure

The grout curtain is situated 7 meters away from the upstream surface of the dam and reaches 30 meters into the rock foundation. The distribution of the pore water pressure in the foundation is simulated in a steady-state step for full reservoir conditions (62.5 m and 125.0 m of water pressure, respectively) on the upstream surface and zero water pressure on the downstream surface. The permeability of the rock and the grout is written down in Table 4-1. In an earthquake scenario one cannot necessarily assume that the grout curtain will still be fulfilling its purpose. For this case the pore water pressure distribution under the structure is assumed linear. This effect on the systems behaviour is also examined.

4.4.3.6 Structural Damping

For all simulations Rayleigh damping is applied to the model. According to the fact that tests on existing dam structures showed that the critical damping factor can vary between 3% and 10% according to ICOLD (2010), the critical damping factor used is 5%. The mass- and the stiffness-proportional damping factors for two specific natural frequencies and the critical damping are calculated with the equations (2-56) and (2-57).

For the two different heights, 62.5 meters and 125.0 meters, and two different modelling techniques of the water, one gets 4 models to calculate the Rayleigh damping factors. The frequencies and corresponding modes of the structure calculated with numerical software must be examined in detail. Some modes, especially when acoustic elements are used, are not contributing to the structures behaviour. This modes and frequencies have been filtered based on the participating factors and mass contribution. This means, modes with a low effective mass contribution have been neglected. In Table 4-3 and Table 4-4 the frequencies and the corresponding Rayleigh damping factors for the 4 models are listed. The mass and stiffness proportional damping factors have been calculated for 1st and 5th natural frequency for each of the 4 models, based on the sum of the effective mass. All models but the one with acoustic elements and a height of 62.5 meters are reaching a percentage of more than 90%. The two used frequencies for the damping factors are left the same to make it more comparable to the one with the Westergaard added mass.

The problems with Rayleigh damping in nonlinear simulations, published by Hall (2006) and mentioned in Section 2.3.3, by using the initial stiffness matrix are not crucial in this problem, because Dassault Systèmes (2013) in the Abaqus 6.13-EF Documentation states that the (elastic) stiffness at the current state (time) is used for calculating the stiffness-proportional damping stresses.

Table 4-3: Natural frequencies and Rayleigh damping factors for the model with acoustic elements and Westergaard added mass and a height of 62.5 m

	Mode	**Frequency [1/s]**	**Sum of the Effective Mass [%]**	**Mass proportional Damping α**	**Stiffness proportional Damping β**
Acoustic Elements	1	3.6	35.4	1.9	0.0007
	2	9.9	54.3		
	3	12.2	68.4		
	4	17.1	78.2		
	5	18.0	79.1		
Westergaard Added Mass	1	3.6	59.5	1.8	0.0008
	2	8.4	89.8		
	3	10.6	91.3		
	4	14.9	97.7		
	5	15.9	99.0		

Table 4-4: Natural frequencies and Rayleigh damping factors for the model with acoustic elements and Westergaard added mass and a height of 125 m

	Mode	**Frequency [1/s]**	**Sum of the Effective Mass [%]**	**Mass proportional Damping α**	**Stiffness proportional Damping β**
Acoustic Elements	1	1.8	52.2	0.9	0.0015
	2	4.9	72.1		
	3	6.1	85.4		
	4	8.5	95.9		
	5	9.0	96.7		
Westergaard Added Mass	1	1.8	59.9	0.9	0.0015
	2	4.3	89.5		
	3	5.3	90.7		
	4	8.1	97.0		
	5	8.8	98.3		

4.4.3.7 Dynamic Modelling

In the final step of the simulation, the seismic loading is applied. The accelerations are acting in horizontal (x) and vertical (y) direction on the foundation boundaries. For solving the equation of motion, implicit direct time integration according to Hilber, Hughes and Taylor (1977) from Section 2.1.1 is used. Because of convergence issues in the contact modelling the time integration parameter α is set to -0.333. This value accounts for maximum numerical damping, which means that the high frequency responses of the structure are neglected and convergence is reached more easily. The accelerations in the time histories are defined for every 0.01 second, which is almost 3 times lower than the criteria for covering the response of the first mode. The influence of higher modes is assumed to be small. Otherwise the time step must be reduced.

$$\Delta t = \frac{1}{10 f_1} \leq \frac{1}{10 \cdot 3.6} = 0.028 \tag{4-13}$$

Therefore, for each simulation one has 2000 time steps for the 20 seconds seismic event. The acceleration-time-histories are depicted in Figure 4-3 in Section 4.3.

4.5 Results and Discussion

4.5.1 Results of Newmark’s Sliding Block Analysis

The first part of the study was to perform a rigorous rigid-block analysis for the gravity dam for various friction coefficients. The assumed uplift distribution corresponds to the left sketch in Figure 4-2 (Intact grout curtain). The integration procedure was programed in MATLAB for friction coefficients of 0.84, 0.77, 0.7, 0.66, and 0.65.

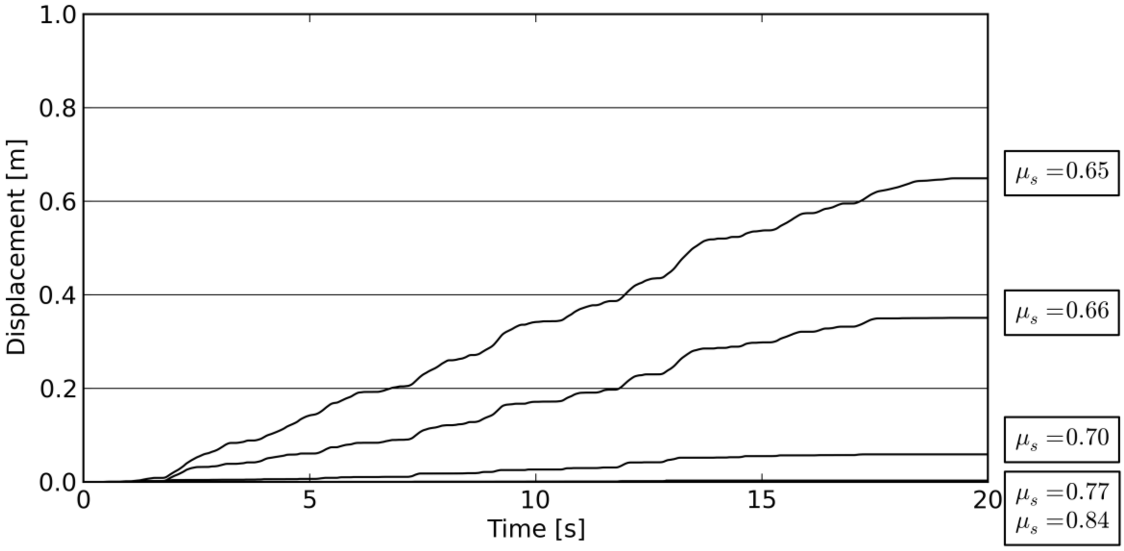

Figure 4-11: Gravity dam displacements for different friction coefficients (Newmark’s Sliding Block Analysis)

Figure 4-11 shows the displacements of the dam for different friction coefficients. The yield acceleration correspondent to friction coefficient 1.0 is well above the peak acceleration 0.1g and no displacement occurred. On the other hand, the total displacements of lower friction coefficients changed dramatically from 0.7 to 0.65.

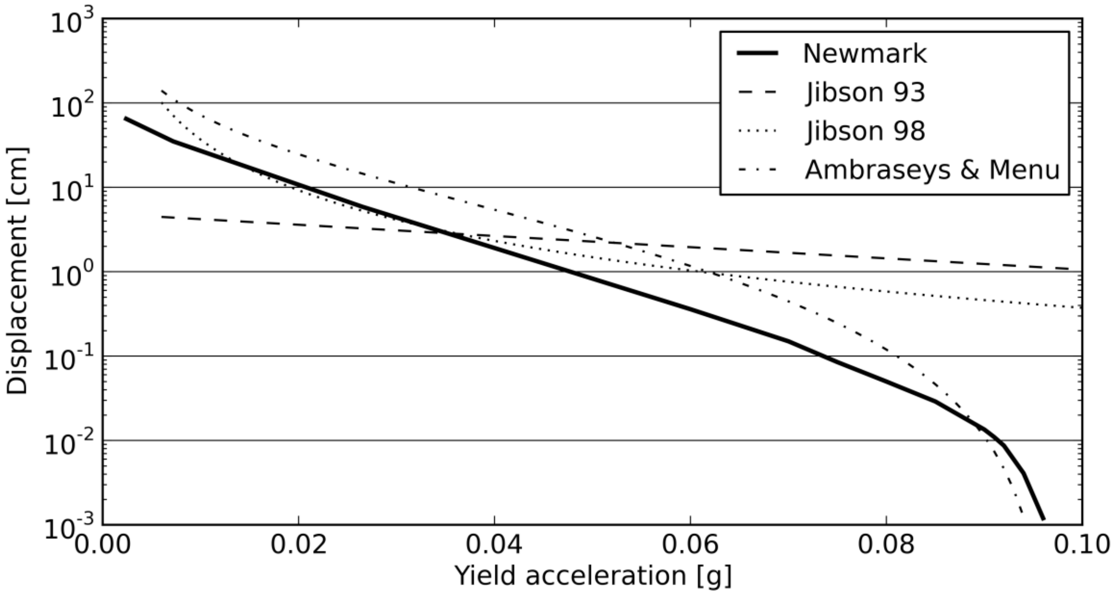

Figure 4-12: Comparison of empirical equations and Newmark’s Sliding Block Analysis

In the second part, empirical relations have been investigated for different yield accelerations and the results are compared with the rigorous Newmark analysis. It can be seen from Figure 4-12, that from yield acceleration 0.04g to 0.01g where we have significant displacements, the Jibson98 regression equation estimated the total displacements fairly close to those from rigorous analysis. Although, one has a negligible displacement for yield acceleration larger than 0.07.

4.5.2 Results of the Numerical Method

4.5.2.1 Displacement Results for the Model with Grout Curtain

Figure 4-13 and Figure 4-14 show the relative displacement in the contact plane between the dam and the rock foundation for the specific friction coefficients over the 2000 time steps (20 seconds) and the different water/reservoir modelling techniques. In these simulations, the grout curtain is assumed to be still intact.

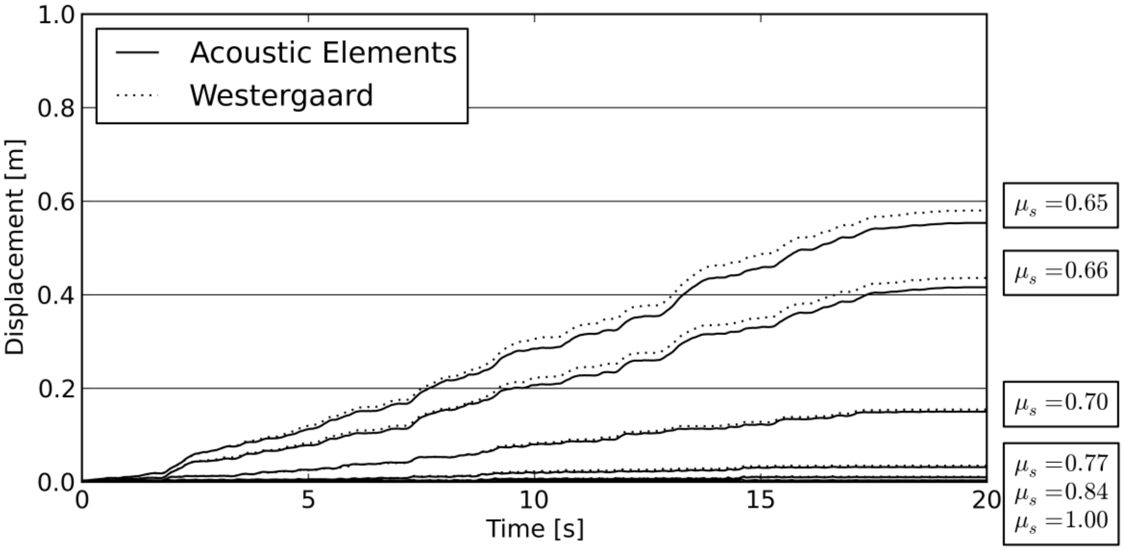

Figure 4-13: Gravity dam displacement for different friction coefficients between acoustic elements and Westergaard added mass for a height of 62.5 meters

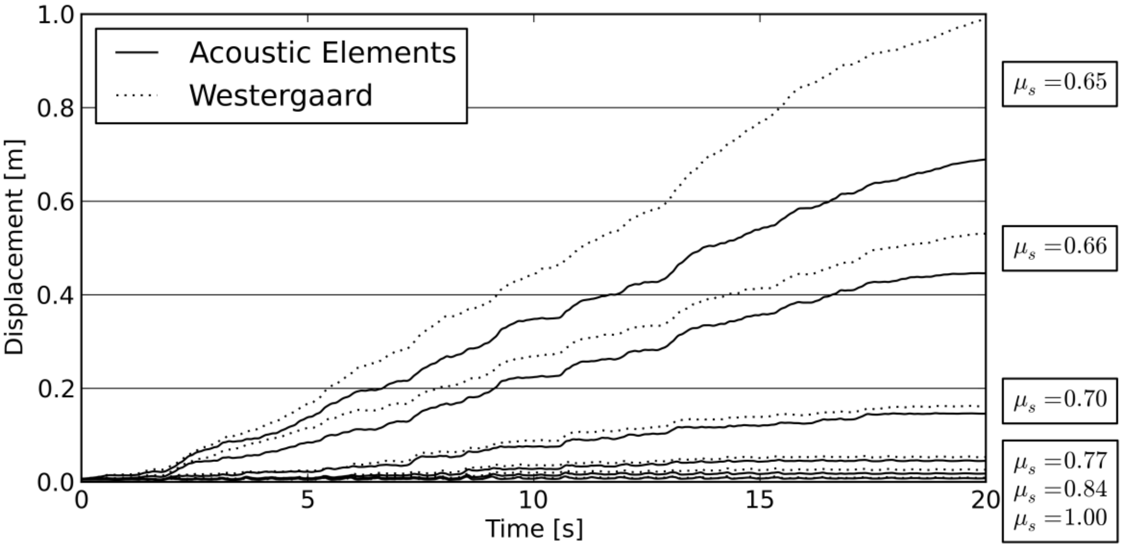

Figure 4-14: Gravity dam displacement for different friction coefficients between acoustic elements and Westergaard added mass for a height of 125.0 meters

Figure 4-15 is showing the cumulative displacements between the acoustic elements and the Westergaard added mass for the two investigated heights of the dam and the differing friction coefficients.

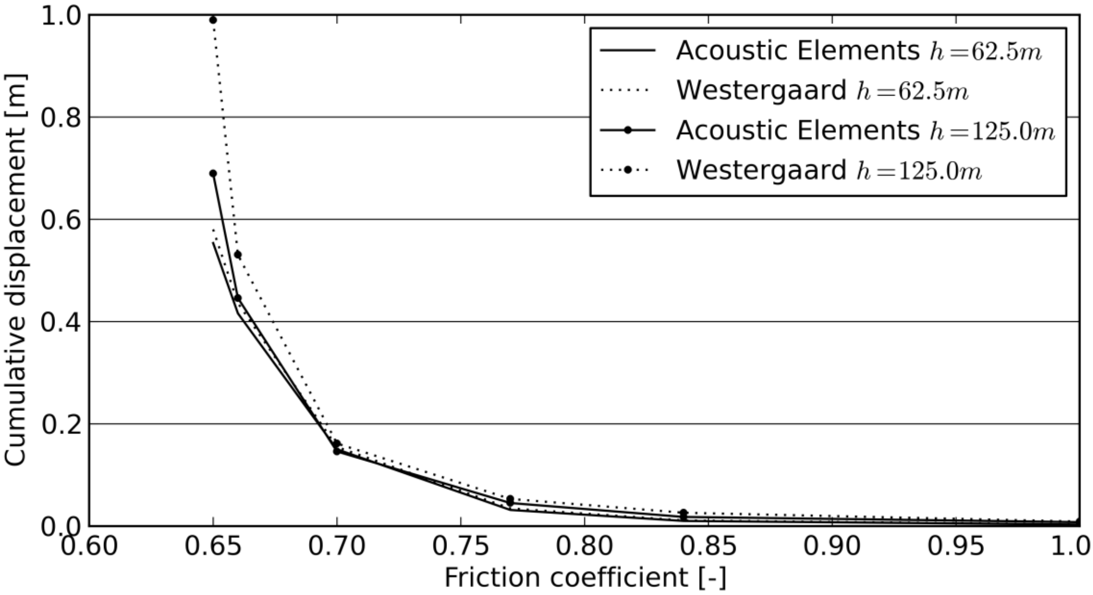

Figure 4-15: Cumulative displacement comparison for different friction coefficients between the models with acoustic elements, Westergaard added mass and the two different heights of the structure

Using two different modelling techniques of the reservoir, the acoustic elements and the Westergaard added mass approach showed that the results of displacement over time are not differing much until a coefficient of 0.7. The higher the friction coefficient gets the more similar both results are. For lower values, the increased mass due to the use of the Westergaard method, compared to the acoustic elements, is also increasing the movement. This behaviour can be observed in Figure 4-13 (height of 62.5 meters) and even better in Figure 4-14 (height of 125.0 meters). No significant difference in the cumulative displacement can be seen between the two modelling techniques of the reservoir, especially for the one with 62.5 meters. The 125.0 meters high dam model shows higher differences for the low friction coefficients of 0.66 ($\Delta u = 10\ cm$) and 0.65 ($\Delta u = 30\ cm$), but for values up from 0.7 they are the same. Therefore it can be concluded that the displacements due to seismic loading and lowering of the friction coefficient behaves more or less the same for both kinds of the reservoir discretization. The end-displacement of the gravity dam, after 20 seconds of transient earthquake, starts to get progressive after reaching a friction coefficient of approx. 0.77 (37.6 degrees) for both model heights (62.5 m and 125.0 m). Reducing the friction coefficient even more, results in a failure of the system at a value of 0.65 (33 degrees).

Worth mentioning is that simulations with the simplified Westergaard formula worked well for the 62.5 meters high structure, but not anymore for the one with 125.0 meters. This led to the use of the rigorous Westergaard formula from equation (3-1). Applying this distribution of added mass worked for the higher model. This happened due to the overestimation of the water mass at the bottom directly at the contact plane of 10% (Figure 3-2) with the simplified equation.

4.5.2.2 Displacement Results for the Model without Grout Curtain

Figure 4-16 and Figure 4-17 show the relative displacement in the contact plane between the dam and the rock foundation for the specific friction coefficients over the 2000 time steps (20 seconds) and the different water/reservoir modelling techniques. In these simulations, the grout curtain is assumed to be not working and therefore not reducing the pore water pressure. This yields higher pressures and a linear distribution from the upstream to the downstream surface of the dam (Figure 4-2).

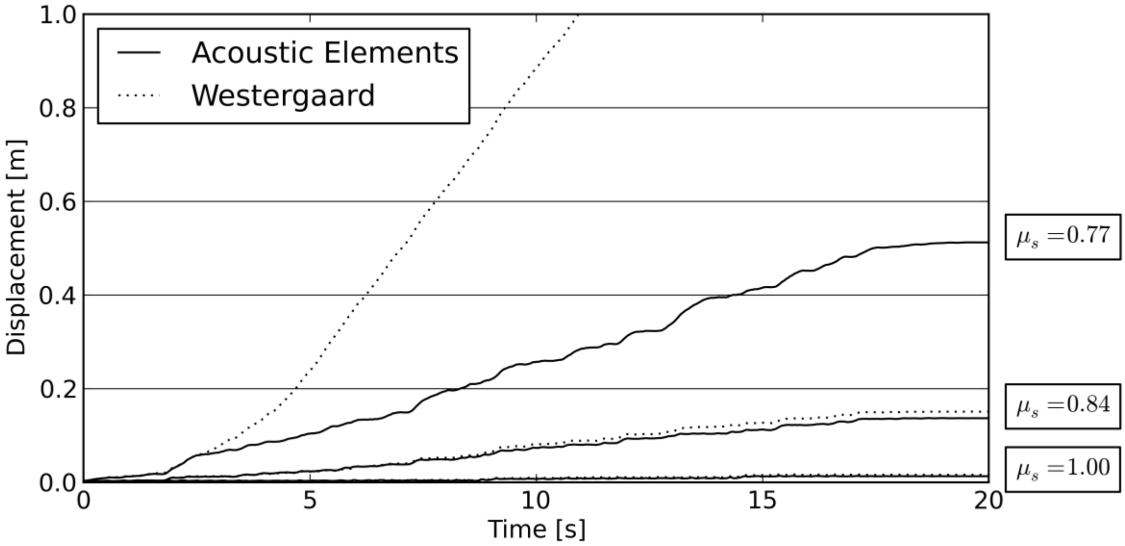

Figure 4-16: Gravity dam displacement for different friction coefficients between acoustic elements and Westergaard added mass for a height of 62.5 meters. Linear pore water pressure distribution in the contact plane (no grout curtain)

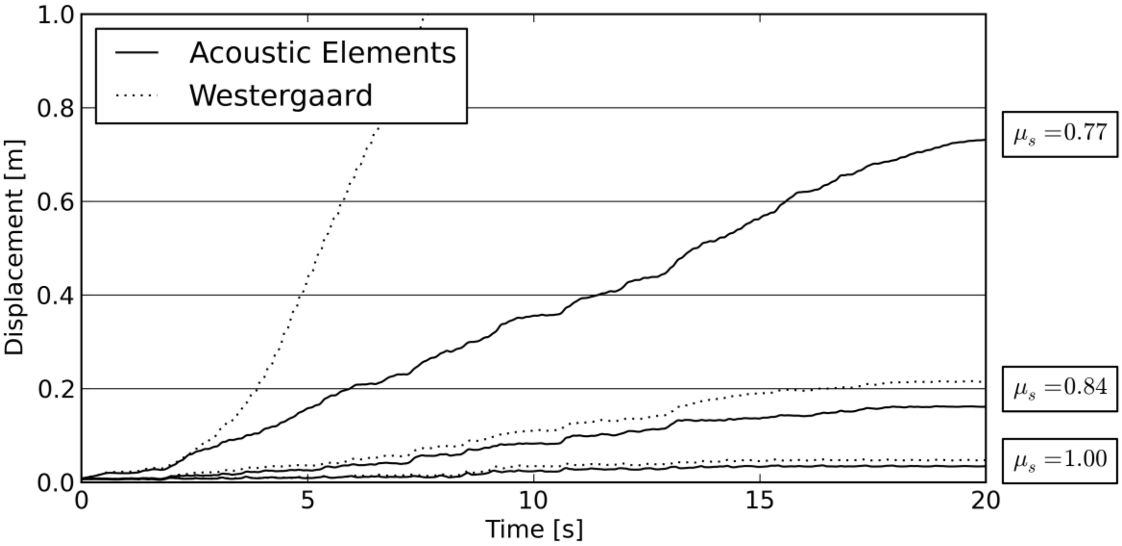

Figure 4-17: Gravity dam displacement for different friction coefficients between acoustic elements and Westergaard added mass for a height of 125.0 meters. Linear pore water pressure distribution in the contact plane (no grout curtain)

Figure 4-18 shows the cumulative displacement comparison between the models with and without grout curtain for the reservoir discretization with the acoustic elements.

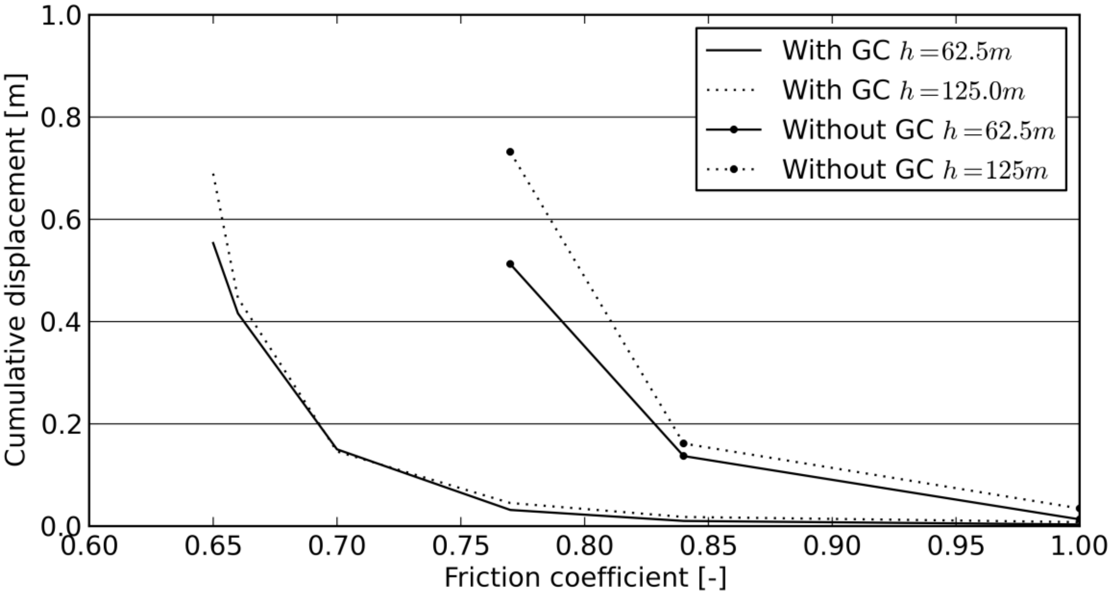

Figure 4-18: Cumulative displacement comparison for different friction coefficients between the models with and without grout curtain and the two different heights of the structure (Only for the model with acoustic elements)

Investigations of the displacement behaviour for conditions where the grout curtain isn't working anymore, which means that the pore water pressure in the contact plane is linear from the upstream to the downstream surface of the dam, the simulation didn't converge anymore already at a friction coefficient of 0.7 (35 degrees) for all models. In Figure 4-16 and Figure 4-17 only the results up from a friction coefficient of 0.77 are shown. The Westergaard added mass method for both heights at this value after a time step 250 (2.5 seconds) is resulting in a continuous sliding of the dam and therefore a failure. This isn't observed for the acoustic elements method. Comparing the end displacements between the models with and without grout curtain for the coefficient of 0.77 shows a rather significant increase. The displacement of the model with a height of 62.5 meters is raised by a factor 10 and for the higher model it even raises up by a factor of 15. In the case that the grout curtain isn't working properly anymore, the displacement starts to get progressive after reaching a friction coefficient of approx. 0.84 (40 degrees). Worth mentioning that the modelling technique of the reservoir isn't influencing the end displacement significantly for values up from 0.84 in the case of a ruptured grout curtain. The Westergaard added mass technique is providing slightly higher values and is therefore conservative.

4.5.3 Results Comparison between Newmark's Sliding Block Analysis and Finite Element Method

The cumulative displacements which were calculated with the rigorous rigid block method are compared with those calculated by the finite element method for different friction coefficients (Figure 4-19). Including vertical acceleration in the rigid block method increased the cumulative displacements by increasing sliding phases. Furthermore, the analysis which takes into account the flexibility of the dam (FEM) shows higher sliding displacements for friction coefficient between 0.66 and 0.77. Comparison of cumulative displacements for higher friction angles ($\mu_s \geq 0.77$) indicates that rigid block method estimated displacements relatively close to the values from FEM analysis. Finally, scaling the body of the dam by a factor of 2 does not change the displacements due to having similar yield accelerations.

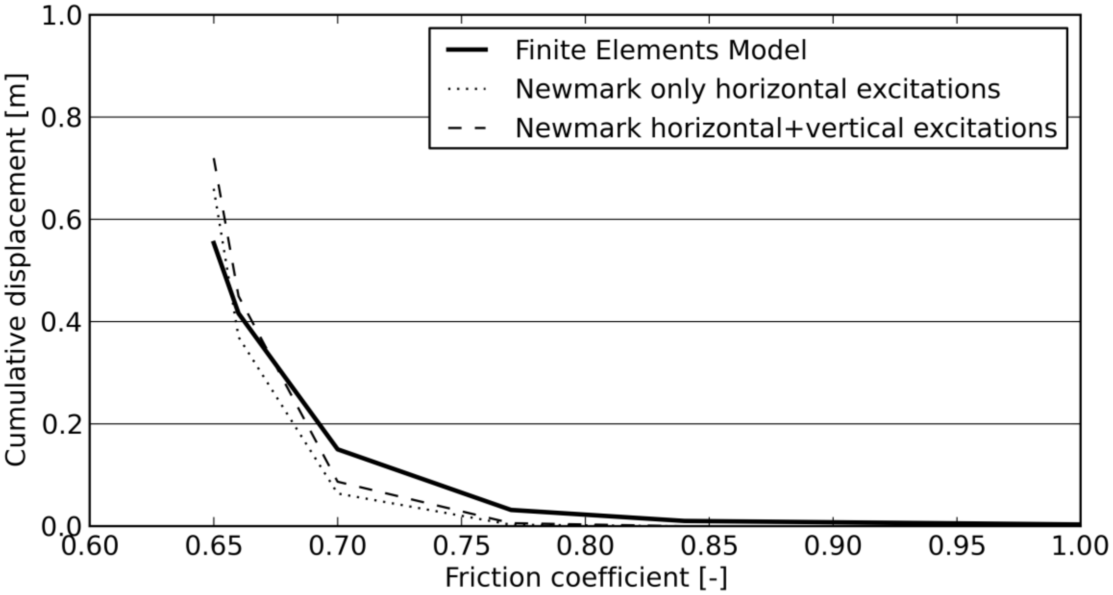

Figure 4-19: Comparison of estimated cumulative displacements for different friction coefficient between Newmark's Sliding Block Analysis and FE Method (62.5 meters high model with grout curtain)

4.6 Conclusion

Although Newmark's Sliding Block Analysis is easy to apply to a gravity dam model, the determination of appropriate friction coefficients is complicated for the dam and foundation interface. Very small changes in friction coefficients can lead to very large differences in displacements. The other key element in this analysis is choosing appropriate ground-motion records. Choosing a ground-motion record with low peak value can lead to underestimation of the displacements. Further investigations are required for choosing appropriate friction coefficient and earthquake records.

Comparison of empirical regression equations and rigorous Newmark analysis has shown that in this study, the Jibson98 equation can estimate the sliding displacements for low friction coefficients ($\mu \leq 0.77$) and yield acceleration between 0.04g to 0.01g fairly close to those from the rigorous sliding-block. The problem with the empirical formulas is that user can not include vertical acceleration in the calculation of the cumulative displacements.

The investigation of the problem with the numerical method showed that different modelling techniques of the reservoir don’t have a considerable impact on the results of the displacement. The same applies also for different heights of the structure if the friction coefficient doesn’t reach a low and critical value. Nevertheless, one should be aware of the fact that this just holds for the relative displacements between two parts, but can influence stresses, velocities, accelerations, displacements, etc., significantly. Having a look at the resultant displacements of the structure for different friction coefficients it is shown, that by reaching a specific value, in this case 0.77 with and 0.84 without grout curtain, the displacement gets progressive. Using the simplified formula of the Westergaard added mass for such problems may lead to overestimated results, wrong system behaviour and a divergent behaviour of the numerical procedure. On the contrary the use of the rigorous formula did work out for simulations where the simplified one predicted a failure. Assuming a linear pore water pressure states that the functionality of a grout curtain is a prerequisite, because otherwise the structure may fail even much faster. Nevertheless, in practice the grout curtain may crack and leak during a seismic event and therefore the uplift will be increased. The assumed linear distribution is a conservative approach in this case, due to the fact that the pore water pressure will not propagate like that in just a few seconds of the earthquake.

The negligence of the cohesion in the simulations leads to conservative results and a remaining safety margin, however it can be concluded that the failure of such a structure will happen suddenly after reaching a specific value of resistance.

Though this work is focused on the investigation of a concrete dam, the proposed methods can also be applied on problems regarding rock wedges in abutments of structures interacting with surrounded water. Further possibilities of application of this method are the investigation of discrete cracks in dam blocks and their behaviour regarding seismic excitations. Figure 4-20 shows the failure mechanism of a cracked arch dam block. Note that, normally, falling to the front side of an arch isn’t a potential mechanism, due to the radial block joint orientation (see Section 6.1 and 6.3).

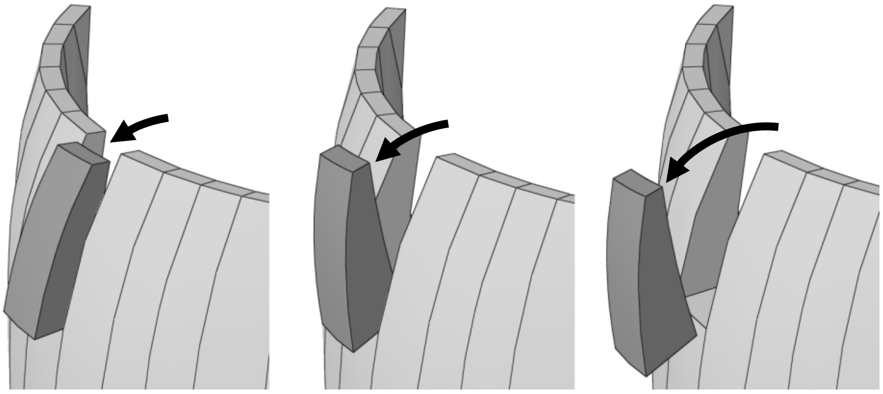

T_1 T_2 T_3

Figure 4-20: Failure mechanism; Falling block of an arch dam

5 LINEAR SEISMIC ARCH DAM SIMULATIONS

5.1 The Benchmark Workshop

For the International Commission on Large Dams (ICOLD) the “Committee on Computational Aspects of Analysis and Design of Dams” is the general Organizer of Benchmark Workshops. This 12th Benchmark Workshop was held in the city of Graz from 2nd – 4th of October 2013.

Advanced numerical tools with user friendly interfaces are available and widely used for structural analyses. Such numerical analyses require a solid theoretical background of the applicability of methods to be used. On the other hand, the results gained need a careful interpretation with respect to the underlying assumptions and their practical relevance. ICOLD benchmark examples of generalized engineering problems are devoted to bridge the gap between numerical analyses, the interpretation of results and their theoretical as well as practical relevance. Since 1991, eleven benchmark workshops have been organized for different numerical problems in the field of concrete and fill dams under static and dynamic loading conditions. The results of these benchmark workshops are made available to the dam engineering community on the internet and in proceedings (http://www.icold-cigb.org). A list of bulletins and former benchmark workshops can be found in Appendix C.

The 12th Benchmark Workshop provided an excellent opportunity for engineers, scientists and operators to present and exchange their experiences and the latest developments related to the design, performance and monitoring of dams. Three example topics and an open theme were formulated and discussed:

- **Theme A:**
  Fluid Structure Interaction, Arch Dam - Reservoir at Seismic Loading
  Formulators: Gerald Zenz, Markus Goldgruber

- **Theme B**
  Long Term Behaviour of Rockfill Dams
  Formulators: Camilo Marulanda, Joan Manuel Larrahondo

- **Theme C**
  Computational Challenges in Consequence Estimation for Risk Assessment
  Formulators: Yazmin Seda-Sanabria, Enrique E. Matheu, Timothy N. McPherson

Theme A was formulated, evaluated and discussed by the author of this thesis in conjunction with Prof. Gerald Zenz from the Institute of Hydraulic Engineering and Water Resources Management, Graz University of Technology. The following sections are just dealing with the Theme A topic *“Fluid Structure Interaction, Arch Dam - Reservoir at Seismic Loading”*. A short summary of the problem definition is also introduced as well as a summary of the results. Detailed information of all themes and results can be found in Zenz and Goldgruber (2014).

5.1.1 Focus of the Benchmark Example of Theme A

Challenges of the analyses of concrete dams are always the definition of material parameters, the spatial discretization and the appropriate simulation of loading sequences. Additionally, specific attention is paid on the structural integrity and entire safety under seismic loading conditions. To account for this problem, the interaction of the dam and the reservoir was the topic of Theme A.

By means of the finite element method linear and nonlinear analyses under dynamic excitation are carried out. However, for the required and appropriate simulation of the dam reservoir interaction different approaches are used. With respect to future nonlinear dynamic analyses, these simulations herein are in the time domain only.

The simulations of earthquake excitation of arch dams have shown that the analyzed stresses in the structure could vary significantly based on the interaction modelling. This benchmark now intends to compare different modelling techniques and will show the amount of deviations. All investigations are carried out for an artificially generated symmetric arch dam with simplified loading and boundary conditions. Every participant was allowed to choose his own order of details in the modelling.

The main goal of the example was the application of different approaches like:

- Added mass technique (Section 3.1, 3.2)
- Acoustic fluid (Section 3.5)
- Fluid dynamics

Further on, the usage of different boundary conditions is possible for:

- Reservoir - Foundation
- Reflecting (on the bottom and the sides)
- Non-reflecting (at the end of the reservoir)

The modelling of the block joint or base opening – due to tensile stresses and nonlinear material effects - was not focus of this benchmark example. However, these effects were carried out after the workshop for a slightly modified model by the author of this thesis in conjunction with Richard Malm from KTH Royal Institute of Technology in Stockholm during a research stay in summer 2014. A detailed description of these simulation and their results compared to the linear ones from the benchmark workshop are discussed in Chapter 6.

5.1.2 General Basic Assumptions

The following general basic assumptions and boundary conditions for the investigations had to be used:

- Same spatial discretization (Model/Mesh) of the structure, foundation and reservoir
- Same material parameters
- Acceleration-time-history in x-,y-,z-direction
- Reservoir is infinite in length (non-reflecting)
- Rayleigh damping

- Results to be compared – visualization

5.1.3 Model and Geometry

Arch dam, foundation and reservoir models for the benchmark have been generated and were provided to each participant.

5.1.3.1 Arch Dam Model

- Symmetric Geometry
- Total Height: 220 meters
- Valley width (crest): ~ 430 meters
- Valley width (bottom): ~ 80 meters

The arch dam geometry (Figure 5-1) has been generated with the program Arch Dam Design, which was developed as part of the master thesis by Pagitsch (2012).

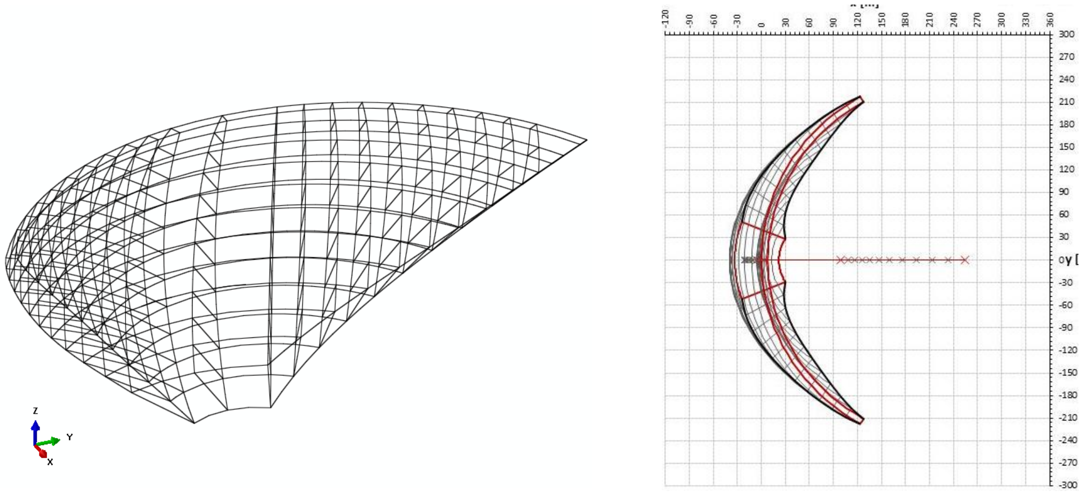
Z
Y
X
-120
-90
-60
-30
0
30
60
90
120
150
180
210
240
270
300
330
360
300
270
240
210
180
150
120
90
60
30
0 y [
-30
-60
-90
-120
-150
-180
-210
-240
-270
-300

Arch Dam Model

Plan View

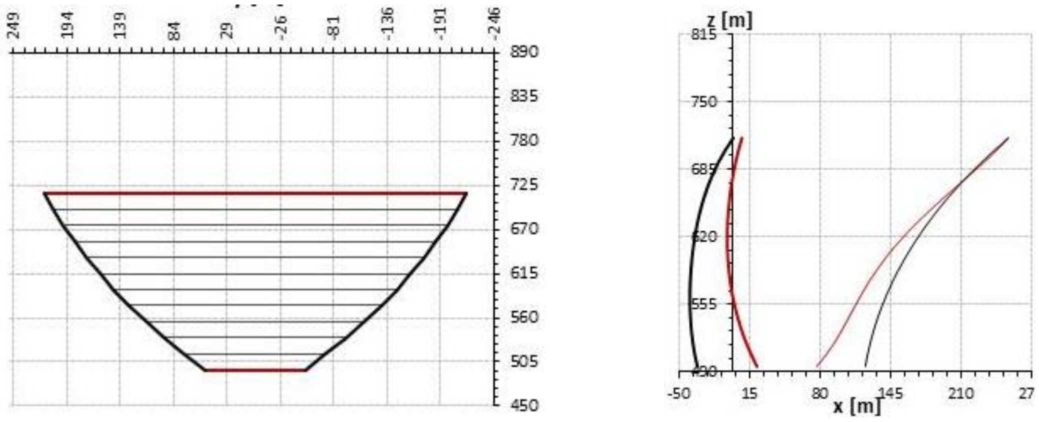
249
194
139
84
29
-26
-81
-136
-191
-246
890
835
780
725
670
615
560
505
450
z [m]
815
750
685
620
555
490
-50
15
80
145
210
27
x [m]

View from the upstream

Main section

Figure 5-1: Benchmark workshop arch dam geometry figures from the program Arch Dam Design

5.1.3.2 Foundation Model

Symmetry is used for the foundation model too and the dimensions are as follows:

- Height: 500 meters
- Length: 1000 meters
- Width: 1000 meters

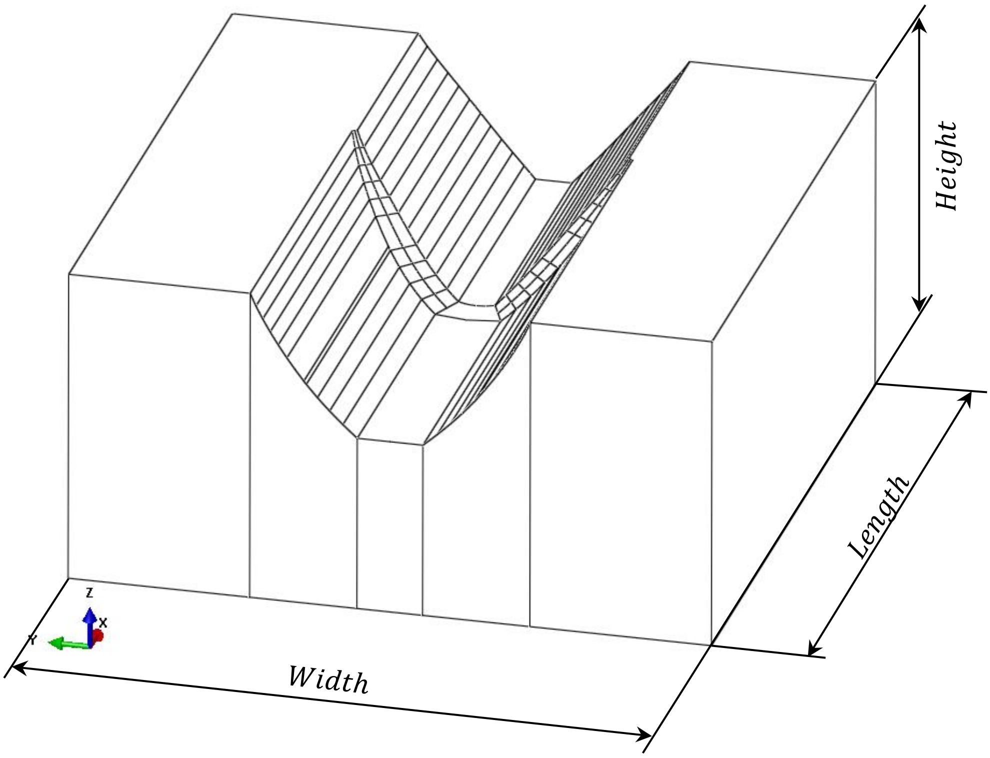

Figure 5-2: Foundation model

5.1.3.3 Reservoir Model

The reservoir length has an assumed minimum of 460 meters (> 2x height of the dam) and the volume should be discretized by an acoustic fluid or fluid dynamics approach.

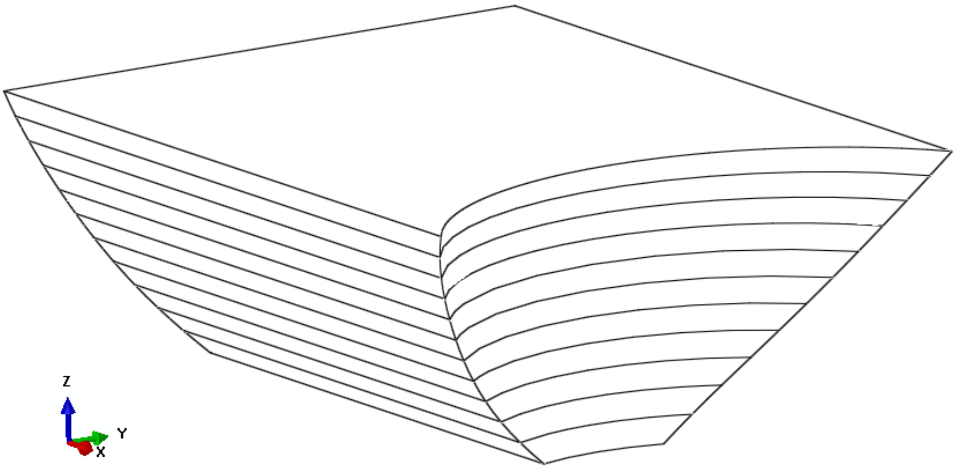

Figure 5-3: Reservoir model

5.1.3.4 Mesh Properties

Two different Meshes of the entire system were provided for investigations, as these are a coarse and a fine mesh. The main difference in mesh density occurs in the arch dam model. The meshes of the coarse and fine arch dam model are depicted in Table 5-1.

Table 5-1: Number of elements and nodes of the coarse and fine mesh

	Coarse Mesh	**Fine Mesh**
Arch Dam	2083 Nodes 356 Elements	13733 Nodes 2736 Elements
Foundation	11608 Nodes 2340 Elements	13298 Nodes 2700 Elements
Reservoir	12493 Nodes 2640 Elements	12493 Nodes 2640 Elements
Sum	**26184 Nodes** **5336 Elements** **53000 DOFs**	**39524 Nodes** **8076 Elements** **80000 DOFs**

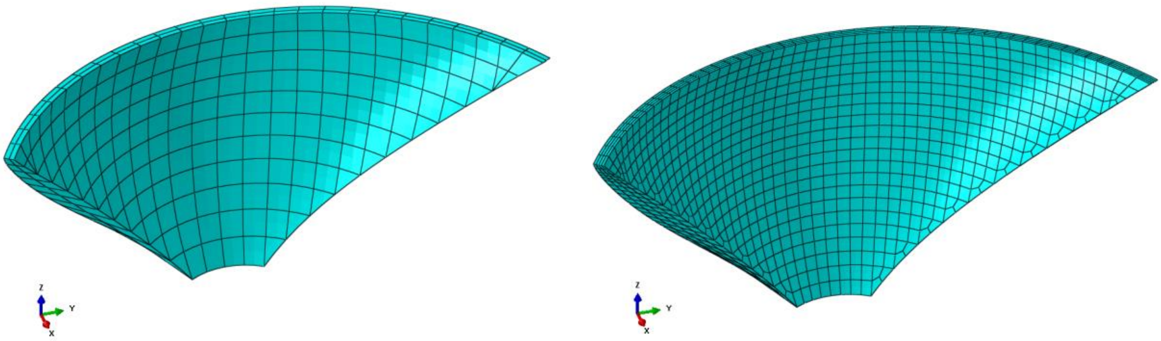

Figure 5-4: Mesh densities of the coarse and fine arch dam model

5.1.3.5 Earthquake Acceleration-Time-History-Records

The same acceleration-time-histories as in Section 4.3 are used for these simulations except for an additional acceleration in z-direction. The acceleration-time-histories are shown in Figure 5-5.

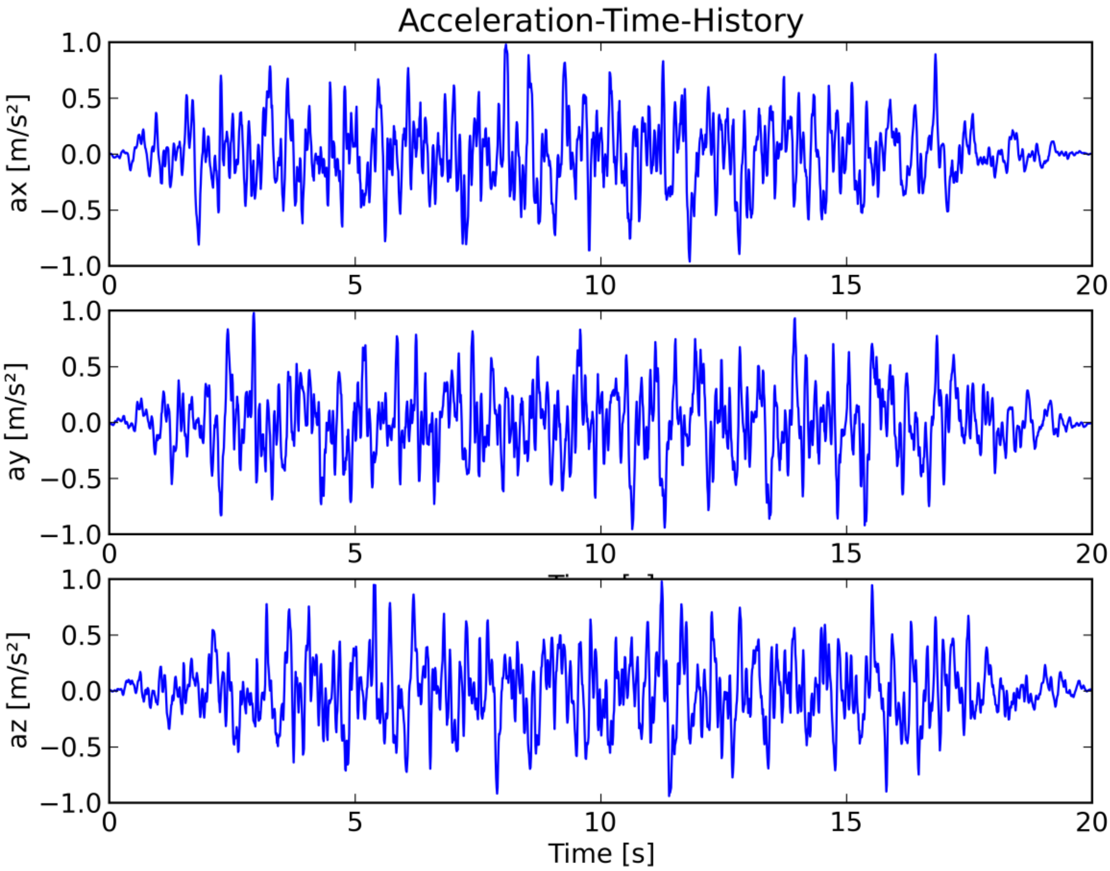

Figure 5-5: Acceleration-time-history records in 3 directions

5.1.3.6 Material Parameters

The Material properties are defined for isotropic and homogenous conditions.

Table 5-2: Material properties of the benchmark problem

	Density [kg/m³]	Poisson ratio [-]	Young's/Bulk modulus [MPa]
Arch Dam	2400	0.167	27000
Foundation	0	0.2	25000
Reservoir	1000	-	2200

5.1.3.7 Loading

The following loading sequence was intended to be used.

- Gravity
- Hydrostatic water pressure (full supply water level = crest height)
- Seismic loading (modal superposition or direct time integration)

5.1.4 List of Participants, Programs and Approaches

Overall 11 participants from 9 different countries (Switzerland, Netherlands, France, Germany, Sweden, Italy, Iran, Romania and Austria) were contributing to the workshop and decided to solve the problem. Each participant had the opportunity to choose his preferred numerical program and modelling technique to account for the fluid structure interaction.

The "Reference Solution" (REF) in the diagrams and tables doesn't claim to be the optimum solution. It shows the results of the simulations done at the Institute for Hydraulic Engineering and Water Resources Management by the author of this thesis.

Table 5-3 lists the participants and their used programs and approaches. The information in the last column should point out some specific differences between the participants which may influence the results and are worth mentioning. Some of the participants have provided results of more than just one simulation, but for the comparison just one of these has been used. All the other results of the approaches and models can be found in Zenz and Goldgruber (2014).

All participants had to evaluate natural frequencies, mode shapes, displacements and stresses. In the case of dynamic simulations one will get minimum and maximum values. Therefore, in the diagrams in the results section every participant has three lines, the minimum (left line) and the maximum line (right line) which indicate the minimum and maximum values out of the time history records and the line for static loading (middle line). This middle line indicates the static value out of the sum of the two load cases, gravity and hydrostatic water load. To retain the overview in the diagrams, the minimum, maximum and static values are not explicitly mentioned in the legend.

Table 5-3: Participants, Programs and Approaches

		FE Program	**Method**	**Mesh**	**Additional Informations**
A	Maltidis et al. (2014)	Abaqus	Acoustic Elements	Coarse	7.5% critical damping
B	Kikstra et al. (2014)	Diana	Acoustic Elements	Coarse	Compressible Fluid, Hybrid Frequency-Time Domain (HFTD) method
C	Faggiani et al. (2014)	Cant-SD	Acoustic Elements	Coarse	
D	Tzenkov et al. (2014)	Diana	Acoustic Elements	Coarse	Same as participant B, Construction steps for loadcase dead weight
E	Chambart et al. (2014)	Diana	Added mass (Westergaard)	Fine	$E_{dyn} = E_{sta} * 1.25$
F	Popovici et al. (2014)	Abaqus	Acoustic Elements	Coarse	
G	Malm et al. (2014)	Abaqus	Acoustic Elements	Fine	Infinite Elements at the boundaries, Acceleration-Time-History applied on the bottom of the model
H	Brusin et al. (2014)	Fenas Eccon IPP	Added mass (Westergaard)	Fine	Construction steps for loadcase dead weight
I	Shahriari (2014)	Ansys	Added mass (Westergaard)	Coarse	Use of the full Westergaard formula (Period/Frequency dependent)
J	Frigerio et al. (2014)	Comsol	Acoustic Elements	Coarse	
K	Diallo et al. (2014)	Code_Aster	Incompressible Finite Element added mass	Coarse	Method to calculate the added mass matrices representing the fluid-structure interaction with a potential approach
REF		Abaqus	Acoustic Elements	Coarse	Simulations done by the author of this thesis

5.1.5 Discussion and Results

Following results should be evaluated and plotted by all participants

- First 10 natural frequencies and mode shapes including the interaction with the reservoir
- Hoop stresses, vertical stresses and min./max. principal stresses for the static and dynamic load (min./max.) for 3 different sections (Main section and ~45 degrees on the left and right hand side) on the upstream and downstream surface of the dam.
- Radial displacement for the static and dynamic load (min./max.) only for main (middle) section

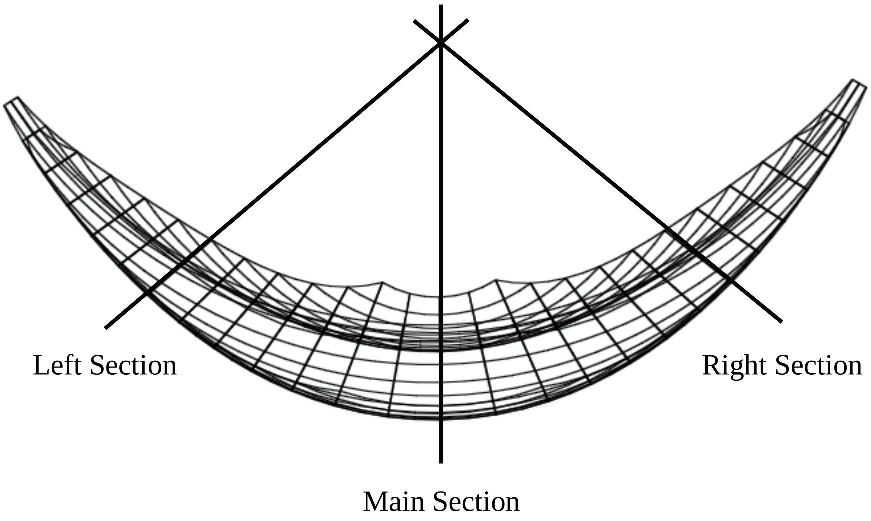

Figure 5-6: Sections for displacement and stress evaluation

The following tables and figures are showing just a few results in the main section of the arch dam (Figure 5-6 and Figure 5-7) of the evaluations of the simulations by the participants. Additional depictions can be found in Zenz and Goldgruber (2014).

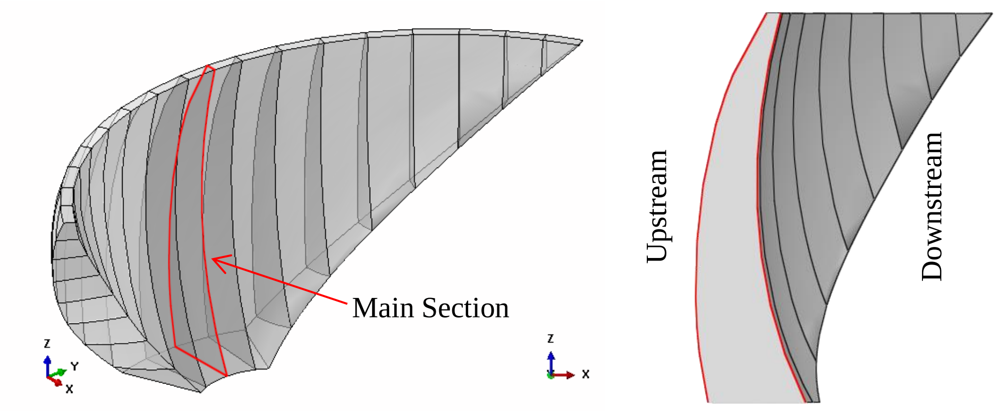

Figure 5-7: Main section of the arch dam and up- and downstream definition

5.1.5.1 *Natural Frequencies*

The corresponding natural frequencies to each node are listed in Table 5-4.

The criteria to compare the results are only the natural frequencies – no shape deformation, nor mass contribution to the different modes and directions are considered. For commenting in detail, this information would have been valuable, but wasn't requested.

The lower frequencies compared to the others of the first two modes of participants H and I are due to the use of the added mass approach. Although participant E is also using Westergaard's approach, the frequency is higher than for H and I, this fact is attributable to the increased Young's-modulus they used. The overestimation of the additionally excited mass leads to slightly lower natural frequencies, while the remaining are around 1.5 Hz. Noticeable is that the participants who used the program Diana (B, D and E) are getting higher frequencies starting from the third. This counts also for the participant K, who used the Open Source software Code_Aster. All other participants are getting more or less the same natural frequencies for the first 10 modes.

Table 5-4: Natural frequencies 1 – 10

Participant	**Mode**									
	1	**2**	**3**	**4**	**5**	**6**	**7**	**8**	**9**	**10**
A	1.47	1.54	1.55	2.11	2.33	2.46	2.61	2.97	3.25	3.37
B	1.57	1.60	2.36	2.94	3.04	3.72	3.88	4.56	4.78	4.80
C	1.54	1.55	2.05	2.22	2.41	2.83	2.98	3.37	3.40	3.79
D	1.57	1.62	2.36	2.94	3.04	3.72	3.87	4.56	4.76	4.80
E	1.43	1.47	2.21	2.61	2.81	3.27	3.56	4.09	4.37	4.37
F	1.54	1.56	1.93	2.30	2.48	3.04	3.12	3.29	3.61	3.71
G	1.51	1.54	1.90	2.22	2.42	2.96	3.01	3.28	3.59	3.76
H	1.26	1.32	2.01	2.36	2.50	3.00	3.17	3.65	3.70	3.88
I	1.28	1.33	1.91	2.37	2.38	2.91	2.98	3.61	3.62	3.85
J	1.54	1.55	2.09	2.22	2.33	2.51	2.83	2.96	3.19	3.37
K	1.57	1.62	2.35	2.95	3.03	3.72	3.85	4.56	4.88	5.13
REF	1.54	1.54	2.05	2.29	2.54	2.96	3.21	3.36	3.76	3.91

5.1.5.2 Displacements

The comparison of the displacements is done for the main (middle) section only (Figure 5-7). The static loading accounts for dead weight and water loading together. No temperature loading is accounted for.

The static displacement reveals that many results show almost the same behaviour, except those from participants D, E, H and K. The higher static displacement of participants D, H and K are due to modelling of the construction stages.

The dynamic displacements are, as expected, varying in a wider range. Especially worth mentioning is also the result by participant G, he, as the only one, used infinite elements on the vertical boundary and applied the acceleration-time-history record on the bottom of the foundation model, which is the reason for in general higher values. The lower values of radial displacement of participant E are a result of the higher Young's modulus used.

Figure 5-8 shows the combined (Gravity and Hydrostatic) displacement of the arch dam for all participants. Separated plots of the static and dynamic displacement can be found in Zenz and Goldgruber (2014).

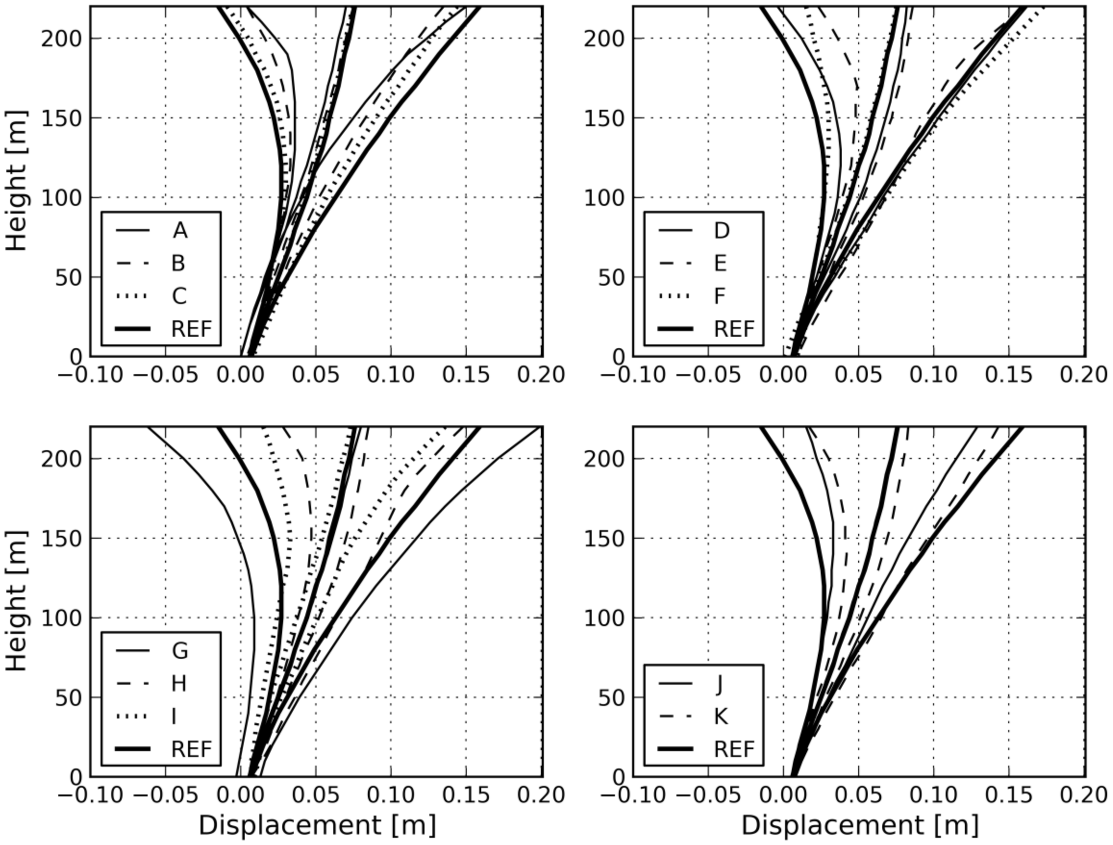

Figure 5-8: Minimum, maximum and static displacement for all participants in the main section of the arch dam

5.1.5.3 Stresses

The comparison of the stresses of each of the participants and each of the diagrams are focused on essential aspects. Therefore, the discussion is kept general and just the quality of some graphs and values is discussed, but not the quantity in detail. Every participant has used his own preferred program, modelling technique and approach, so different results have been expected.

As it was up to the participant to use immediate or stepped construction sequences, the stress distribution differs. A 0.5 MPa difference for the static loading, at a stress level of 6.0 MPa, one might accept, but not larger (Figure 5-9).

Worth mentioning are the dynamic results by participant G. He used, as already mentioned in the discussion of the displacements, infinite elements and applied the acceleration time history just on the bottom of the model. So the same as for the displacements counts here, the stresses in contrast to the others are far the highest in almost each diagram and beyond awaited results.

Participants B and D used the program Diana with the Hybrid Frequency-Time Domain Method (HFTD-Method), which takes frequency dependent properties, such as compressibility of fluid, reservoir-bottom absorption and far-field reflection, into account. Both of them got similar results compared to the others, which prove the usability of this sophisticated analysis method on the one hand – but shows the applicability of less elaborated models, under these assumptions, too.

Figure 5-9 shows the combined (Gravity and Hydrostatic) hoop stresses for the upstream surface of the arch dam for all participants. Separated plots of the static and dynamic hoop stresses and plots of the right and left sections can be found in Zenz and Goldgruber (2014) as well as vertical stresses and principal stresses.

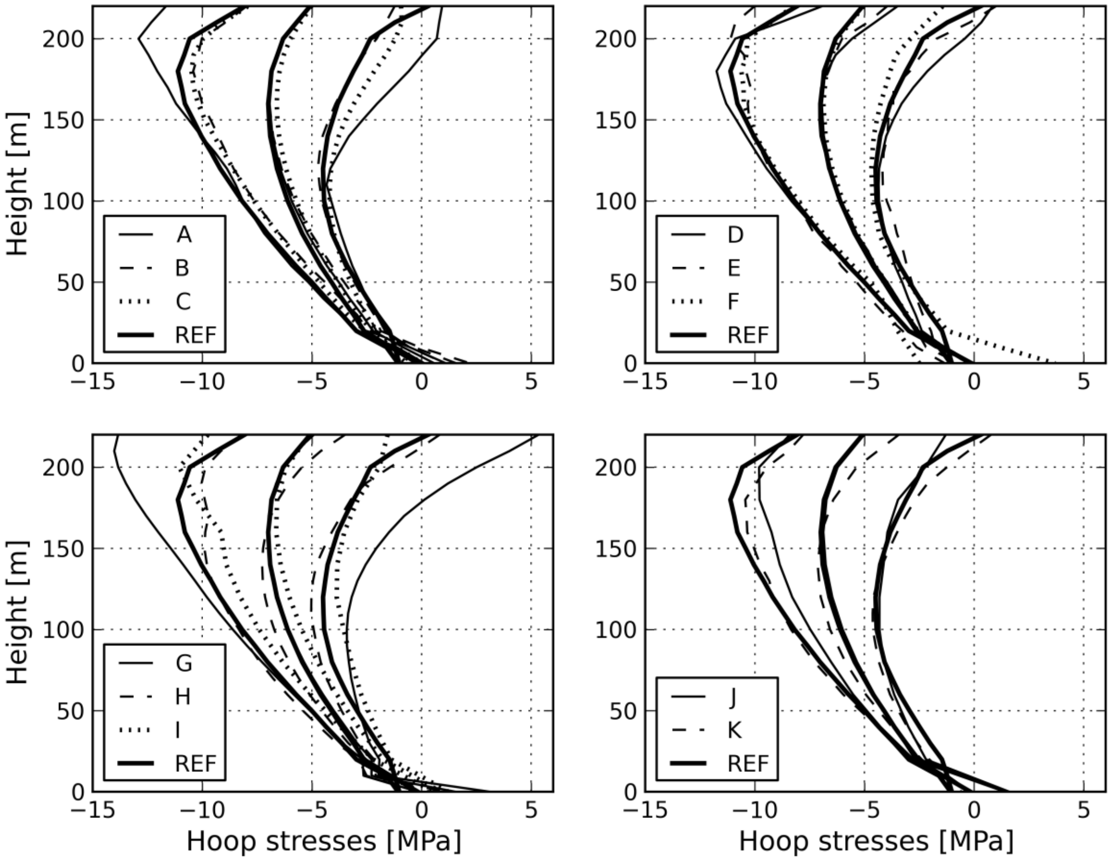

Figure 5-9: Minimum, maximum and static hoop stresses for all participants in the main section on the upstream surface of the arch dam

Participant K was the only one who used the Open Source software Code_Aster. Such software, which is mostly used at research facilities and universities, is license free, but often more difficult to apply than commercial ones. Nevertheless, the provided results are matching with the results from the other participants, except participant G. His displacement and stress results where much larger than that from the others, because the acceleration-time-histories were only applied on the base of the foundation model and not on the side boundaries.

It is worth mentioning, that the added mass approach (according to Westergaard) is able to provide comparable results under the circumstances of this benchmark. All of the three contributors (E, H and I) using this approach are in the range of expected results.

5.1.6 Conclusion

The comparison of all participants shows that despite of the same boundary conditions (geometry, finite element mesh, load cases, material properties, linear analysis, etc.) still assumptions are required and taken to find a solution based on the investigated problem. These additional assumptions are starting with the application of the construction sequence, increase of material properties for dynamic loading, abutment boundary properties, application of dynamic loading and some specific assumptions based on the program used.

Best practice examples and recommendations are published in ICOLD Bulletins and are available for engineers. However, for any specific problem to be solved, the assumptions for an analysis applied need to be reconfirmed in the light of the entire problem. In general it is astonishing, to see the large differences between the results of individual.

Everybody had the opportunity to choose his preferred modelling technique to account for the fluid structure interaction, but most of the contributors used either an added mass technique or acoustic elements. In practice it is still common to use an added mass approach according to Westergaard. Normally this assumption yields conservative results in contrary to modelling with acoustic elements. The solution of participant e.g. I, who has used Westergaard’s formula with its fully, frequency dependent extension, shows very similar results to those analyzed using “higher” constitutive models. This behaviour is also illustrated in Section 3.1.

According to the results of participants using either the coarse or fine mesh the influence on the frequencies, displacements and stresses within the structure is just marginal.

The purpose of choosing this arch dam example (220m in height, totally symmetric) wasn’t just for evaluating the influence of different modelling techniques, but also for engineers, scientists and operators to have a kind of reference solution. The diagrams and tables of the results of all participants should help to quantify and compare frequencies, displacements and stresses of such a structure.

Concluding, everybody should be aware of the fact, that results of such simulations should be treated critically, because mistakes in modelling and application cannot be entirely excluded. Usually, reference solutions from former comparable projects for validation should be used to prove the results for plausibility.

5.2 Investigation of the Influence of Damping Factors

Damping factors or damping-matrices are not a material parameter, which can be easily tested in a laboratory. However, with different in situ methods on existing structures it is possible to account for the hysteretic damping, but in the design phase of structures damping factors are unknown quantities. Therefore it is common to use viscous damping. In numerical simulations these factors can be applied by using so called Rayleigh damping (Section 2.3.1). For concrete structures or especially dams the damping factor is accounted for with approximately 5 % of the critical damping. Investigations of existing dam structures in the past showed that this factor could vary between 1 to 7 percent (or be even much higher), which leads to an increase or decrease of the stress level due to the excitation.

Within this investigation based on the benchmark model the influence on stresses in the dam structure is investigated by applying different damping factors. The interaction with the water is accounted for by using the simplified Westergaard equation (Section 3.1), Zangar (Section 3.2), the ne empirical approach (Section 3.3) and additionally a volume discretization with acoustic elements (Section 3.5). The impact of varying damping factors and different interaction modelling on the stress level in the dam is investigated at different heights in the main section of the dam (Figure 5-6).

5.2.1 Program Implementation of the Added Mass Approach

Three different ways to calculate the added water mass are used for the simulations which are carried out with the finite element program Abaqus/Cae. For the application of these masses in the arch dam model the same user subroutine as in Section 4.4.3 has been used but for three dimensional surfaces. Similar to the subroutine for two dimensional surfaces the mass for every node of an element surface is distributed evenly to each node, i.e. eight nodes for a quadratic formulation of a brick element and 6 nodes for a quadratic wedge element.

5.2.2 Damping Factors

For all simulations Rayleigh damping from Section 2.3.1 is applied to the model. The stiffness- and mass-proportional damping factors are calculated for the first and forth natural frequency of the dam-reservoir system. According to the fact that tests on existing dam structures showed that the critical damping factor can vary between 3% and 10%, ICOLD (2010), the factors which are used are varied from 1% to 10%, in steps of 1 percent. The corresponding Rayleigh damping factors calculated with equation (2-56) and (2-57) are listed in Table 5-5.

Table 5-5: Mass- and stiffness-proportional Rayleigh damping factors

Critical Damping	**0.01**	**0.02**	**0.03**	**0.04**	**0.05**	**0.06**	**0.07**	**0.08**	**0.09**	**0.1**
Mass-proportional $\boldsymbol{\alpha}$	0.084	0.169	0.253	0.337	0.422	0.506	0.590	0.675	0.759	0.843
Stiffness-proportional $\boldsymbol{\beta}$	0.001	0.002	0.003	0.004	0.005	0.006	0.007	0.008	0.009	0.011

For the damping of the rock mass, the simplification has been made, that the same Rayleigh damping factors are used as for the dam structure.

5.2.3 Results and Discussion

5.2.3.1 Natural Frequencies

Looking at the natural frequencies of the four different modelling techniques the acoustic elements show the highest frequency for the first three modes. The added mass methods are overestimating the interacting mass and therefore result in lower frequencies. Zangar’s approach and the empirical equation from Section 3.3 are almost identical and give slightly higher frequencies than the one by Westergaard, which is attributable to better description of the water mass distribution (Figure 3-7, Section 3.2 and Figure 3-13, Section 3.3).

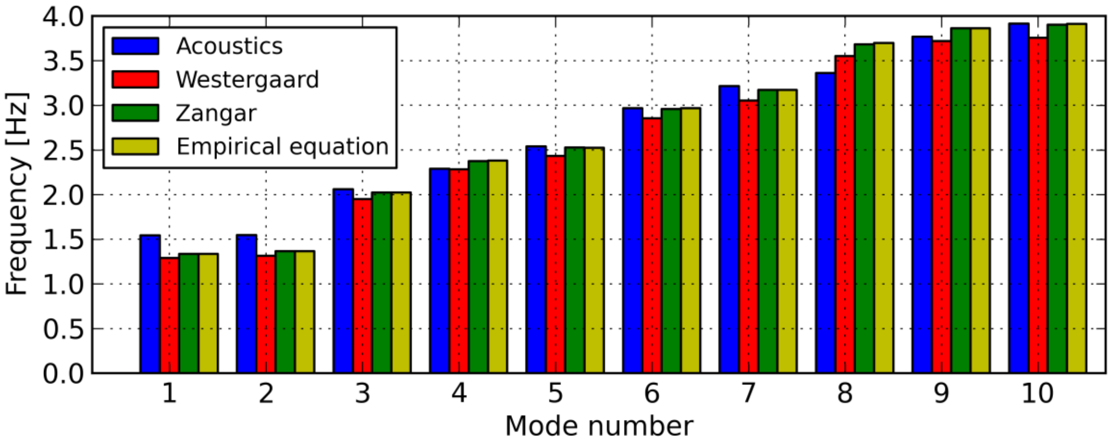

Figure 5-10: Natural frequency comparison of the three modelling methods

The mode shapes of the dam structure for all methods are depicted in Table 5-6. Zangar’s and the empirical equation are giving the same shapes, which is correspondent with their natural frequencies.

Table 5-6: Modes shapes and corresponding natural frequencies for all three modelling methods

Mode	**Acoustic Elements**	**Westergaard**	**Zangar/Empirical**
1	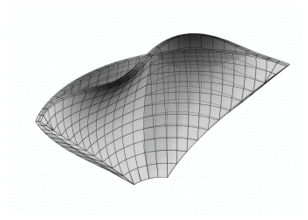 $f_1 = 1.54\,Hz$	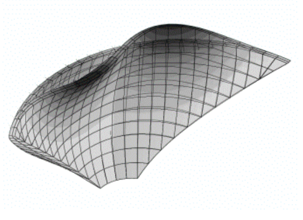 $f_1 = 1.29\,Hz$	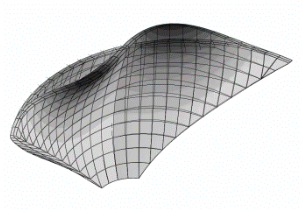 $f_1 = 1.33\,Hz$
2	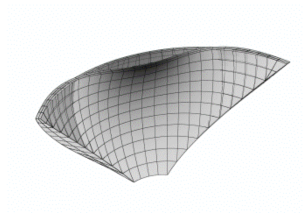 $f_2 = 1.54\,Hz$	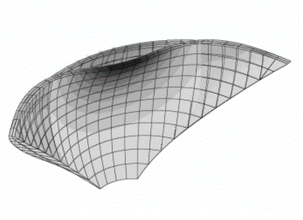 $f_2 = 1.31\,Hz$	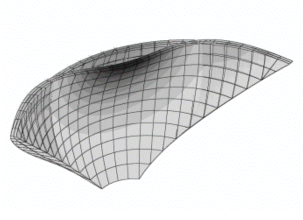 $f_2 = 1.36\,Hz$

3	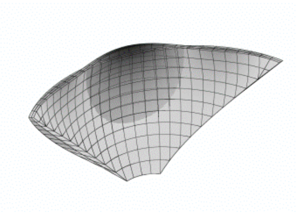 $f_3 = 2.05\ Hz$	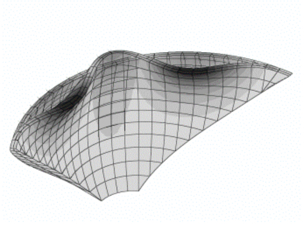 $f_3 = 1.95\ Hz$	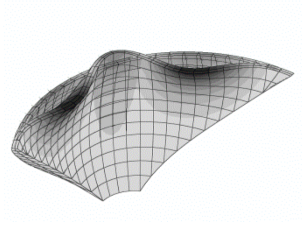 $f_3 = 2.02\ Hz$
4	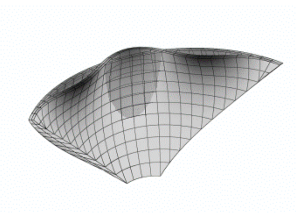 $f_4 = 2.29\ Hz$	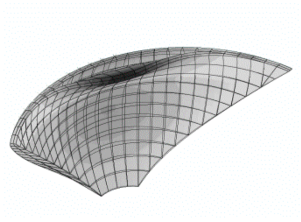 $f_4 = 2.28\ Hz$	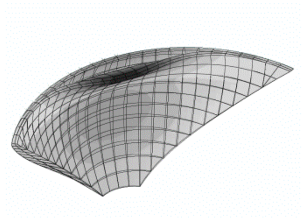 $f_4 = 2.37\ Hz$

5.2.3.2 Hoop and Vertical Stresses

The following figures show the minimum/maximum stresses and displacements for two specific nodes for damping factors between 1% and 10% of the critical damping.

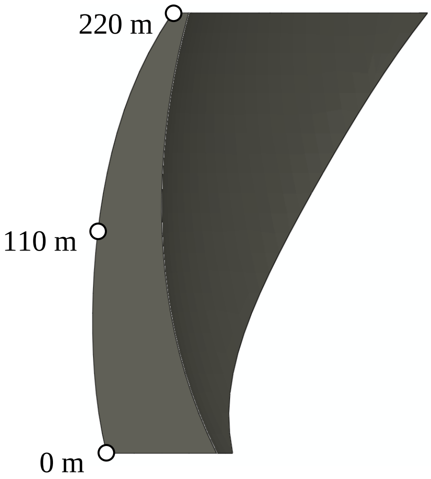

Figure 5-11: Evaluation heights of the stresses and deformations in the main section on the upstream surface

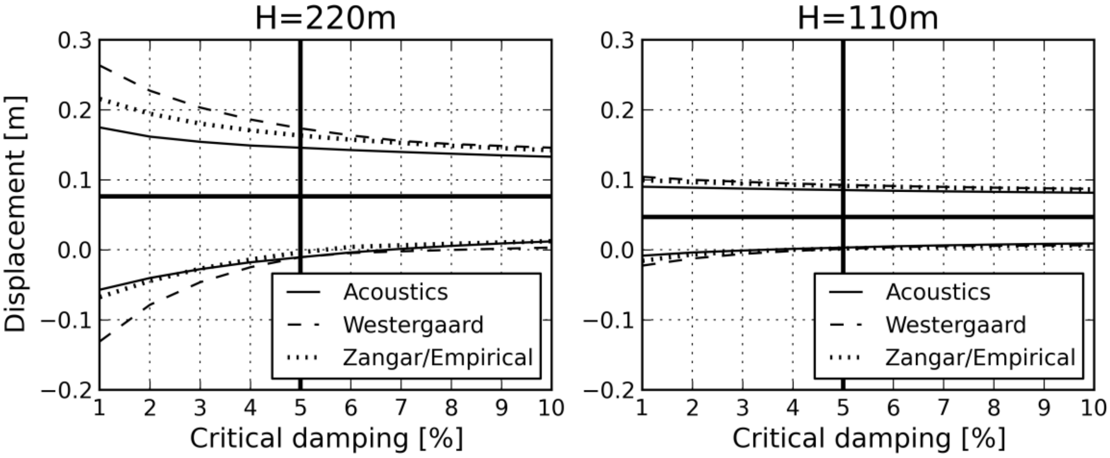

Figure 5-12: Minimum, maximum and static displacement at 220m (crest) and 110m on the upstream surface in the main section

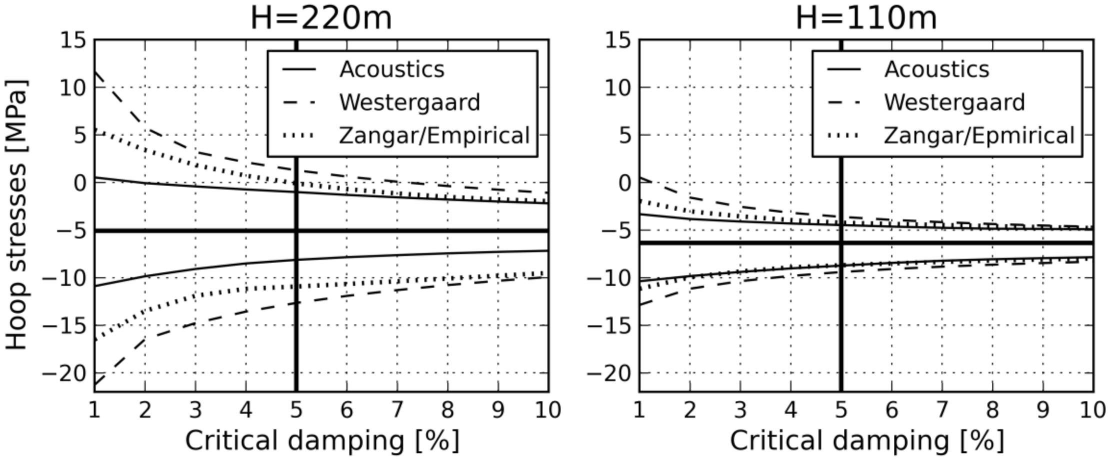

Figure 5-13: Minimum, maximum and static hoop stresses at 220m (crest) and 110m on the upstream surface in the main section

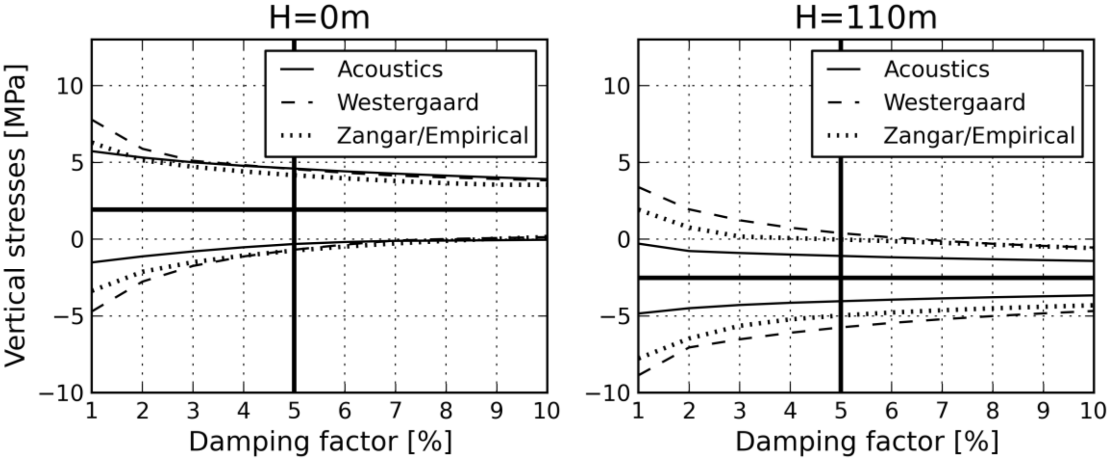

Figure 5-14: Minimum, maximum and static vertical stresses at 0m (bottom) and 110m on the upstream surface in the main section

The stress development due to the variation of the critical damping factor decreases fast for factors between 1% and 3% for the Westergaard approach. These curves are showing a more or less logarithmic behaviour and seem to converge to a specific stress level when the damping is increased. The same holds for the displacements.

Figure 5-15 shows the evaluation for the hoop stresses for the model with 5% damping. A significant increase in stresses is observed at heights of about 170 meters for the added mass techniques. On the other hand the results at heights up to 100 meters are fairly close, especially the ones from Zangar and the empirical approach compared to the acoustic elements. Furthermore, Zangar and the empirical approach lead to almost identical stress levels.

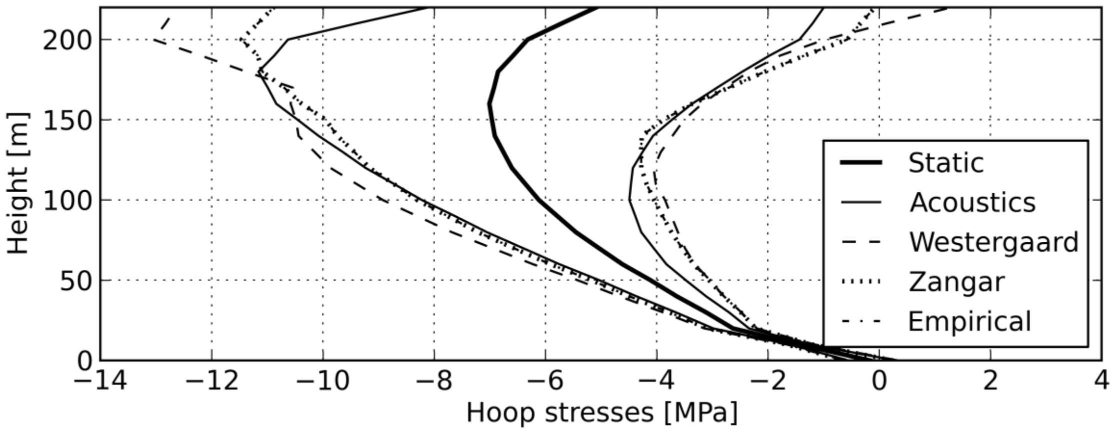

Figure 5-15: Hoop stresses over the height of the dam for 5% of the critical damping on the upstream surface in the main section

5.2.4 Conclusion

Finally, it can be concluded, that the added mass technique, for modelling such problems, should just be used for estimation purposes. The stress level could be overestimated by more than 100%, compared to the acoustic elements, especially in areas near the crest. This large stress increase can also be observed in the benchmark workshop, where Chambart et al. (2014) also used the Westergaard equation and got similar results. Furthermore, the assumption of 5% damping for most of the problems is legitimate. A slight change of ±2% doesn't influence the stresses/displacements significantly. This study also proves the applicability of the empirical added mass equation from Section 3.3.

6 NONLINEAR SEISMIC ARCH DAM SIMULATIONS

Arch dams are designed as relatively thin structures compared to gravity concrete dams. Their generally double-curved geometry allows for transferring the occurring horizontal loads into the side abutment and not only into the base, whereby the forces and stresses are mostly compressive. These structures are to a higher extent susceptible to earthquake excitation, due to their reduced stiffness and therefore, lower natural frequencies, which might resemble typical earthquake frequency ranges. In such a case, where the frequency content of the structure and the excitation are similar, the loads are increased significantly and nonlinear effects, e.g. cracks are triggered and lead to redistribution of forces in the structure. They have substantial extra capacities to be overload until a more severe damage occurs, which leads to a collapse and uncontrolled water loss. Especially in seismic active areas high dams need to be investigated carefully. The stresses in the structure could be increased up to 100 percent due to a seismic event compared with normal static loading conditions. Investigations of the dynamic behaviour with numerical simulations are very helpful, though it is not easy to account for the inherent nonlinearities. A part of the nonlinear behaviour in dynamic simulations is modelled with damping to account for the energy dissipation. On the other hand, increasing computer capabilities and sophisticated programs allow for direct simulations of nonlinearities, e.g. contact and material. In the case of arch dams the impact of the block joint or base opening, due to tensile stresses and nonlinear material effects, is of great interest, because of their possible separation and therefore increased pore water propagation. For example, cracks in the base can highly influence the stability of dam structures, on the contrary to openings between the blocks where sealing strips made of elastic material are situated over the whole height to prevent the water penetration. Furthermore, nonlinear effects lead to rearrangements of the stress path and therefore different stress levels at specific regions. Considering dynamic loading from seismic events, such as cracks – dependent on the intensity – will occur. To evaluate these seismic effects in addition to static nonlinearities on an arch dam structure the model from the benchmark workshop with the same dimensions is used (see section 5.1.3). Besides different reservoir levels also increasing earthquake intensities are discussed. A large part of this work was done during a research stay/collaboration at KTH Royal Institute of Technology in Stockholm in conjunction with Richard Malm from the Division of Concrete Structures.

A vast amount of research on the nonlinear behaviour of concrete dams has been done by Zhang et al. (2013) at the Tsinghua University. A collection of papers which address this topic has been published in their book *"Seismic Safety Evaluation of Concrete Dams: A Nonlinear Behavioral Approach".* Apart from the safety of such structures, the nonlinear response and cracking behaviour of concrete is also discussed. Not only numerical simulations of dams are done, but also physical model tests on shake tables for specific dam structures.

6.1 Constructional Details of Arch Dams and Loadings

Widmann (2005) stated the following requirements which have to be met to opt for the construction of an arch dam:

- Due to the higher concentrated and therefore higher loads acting on the abutment area than in the case of embankment dams, the dam must rest on very stable rock.
- To ensure the economically efficient production of concrete of adequate and uniform quality. Suitable aggregates must be available in sufficient quantity in the immediate vicinity of the dam site.
- For cement meeting the requirement, the transport distance to the construction site must be within economically acceptable limits.
- The crest length should not exceed seven times, better yet five times the dam height. This geometrical limit is required for static reasons, since the bearing capacity of the arches decreases with increasing length relative to the dam height and required vertical cross sections approximate those of gravity dams. In such a case, however, the higher construction expenses are no longer offset by the concrete cubature saved.

If these requirements are fulfilled the design of an arch dam with first estimations of the main dimensions can start. Further optimizations of the geometry are done depending on the site and loading conditions usually with the help of numerical software.

Loadings acting on an arch dam can be categorized in permanent loads, like dead weight, hydrostatic water pressure, temperature etc. and temporary load cases like seismic excitations, iced pressure, etc., respectively. Herein only the ones which are applied to the arch dam model in the simulations later in this section are briefly described. Further and more detailed explanations of load cases can be found in Widmann (2005) and ICOLD (2013) - Guidelines for Use of Numerical Models in Dam Engineering.

6.1.1 Dead Weight

Generally, concrete dam structures are built in vertical independent blocks in the first place. After or already during construction the blocks are grouted and therefore coupled, which allows for transferring loads horizontally. Nevertheless, dead weight stresses in such structures should be simulated for independent cantilevers as long as they are standing freely and are not grouted, otherwise completely different vertical stress levels may develop, dependent on the width to height ratio of the structure. These stresses are further primary influencing the design and optimization of the shape. Due to the stepwise construction, reservoir filling and grouting different stress states arise at different elevations. Therefore, grouted blocks at the base act monolithic and upper new casted blocks are still independent. By taking these effects into account horizontal arch stresses in the dead weight loading case are also existent.

Further descriptions of the grouting process and dead weight simulations can be found in Sections 6.1.5 and 6.6, respectively.

6.1.2 Hydrostatic Water Load

The hydrostatic water load can be separated into different kinds of loads, the hydrostatic water pressure on the upstream surface and uplift water pressure in the base or joints of the foundation rock. The hydrostatic water pressure may vary dependent on the hydrological data. In the assessment an arch dam for the Probable Maximum Flood (PMF) with return periods between 5000 and 10000 years higher water levels and hence, higher pressures may arise. In this scenario severe damage of the structure is possible and a nonlinear analysis should be contemplated to ensure the stability. For lower hazards linear-elastic simulations with suitable safety margins is sufficient.

For very high arch dams ICOLD (2013) stated the following example:

"For very high (more than 300 m) arch dams, the water pressure close to the toe is even higher than the concrete tensile strength; in such cases, the damaging mechanism of concrete is highly influenced by possible hydraulic fracture, and it is quite different from small structures where this phenomenon is negligible. This means that all calculation methods well calibrated for arch dams with standard size (H=50-150 m) are disqualified for such exceptional structures. Only realistic models working with effective stresses are able to overcome the dimension difficulty."

This means also that the uplift water pressures in the base and possible horizontal cracks at the upstream surface should not be neglected. These pressures lead to a reduced sliding safety at the base or increased vertical compressive stresses within the dam.

It is worth mentioning that the hydrostatic water load must also be applied to the surrounding foundation and not only to the dam's upstream surface, because of the (tensile stress-) effects mentioned in Section 6.1.4.

A typical uplift pressure distribution for gravity or arch dams with a grout curtain can be found in Figure 4-2.

6.1.3 Seismic Loading

For seismic loads a similar differentiation according to the intensity and duration is done as for the flood case of the hydrostatic water load. In case of the assessment of the structure for a Maximum Credible Earthquake (MCE) with a return period between 3000 and 10000 years, severe damage is allowed, as long as the integrity is assured. Nonlinear analysis can be utilized to assess the stability afterwards. As for the hydrostatic case, here also for lower hazards, like Operating (or Design) Basis Earthquake (OBE or DBE) linear-elastic simulations with suitable safety margins are sufficient.

In numerical simulations the evaluation of the seismic response of arch dams is recommended to be done with ground accelerations, although specific field data is usually not available. A possibility to overcome this problem is to use similar records or generating artificial acceleration-time histories based response spectra of site data and applying them to the model boundary.

An important role in seismic simulations of dams plays the reservoir and its hydrodynamic forces. Numerical programs allow for different approaches for the constitutive behaviour of the water. Although, added mass techniques are still used, the approach of an acoustic fluid continuum is generally accepted, because of its accurate descriptions for reservoirs. A discussion of different reservoir models can be found in Chapter 3.

6.1.4 Tensile Stresses at Dam-Rock Interface

Often details must be considered in modelling and simulation of arch dams. One important problem is the dam-rock interface or dam base, where usually high tensile stresses are expected and hence cracks are caused. Based on Widmann (2005) such cracks are triggered by:

- Tensile stresses normal to the base

  These stresses can lead to openings normal to the dam base and therefore water penetration. They are influenced by the shape of the arch dam and must be evaluated and examined in detail. The two main influences which affect the tensile stresses in this area are the ratio between the deformation moduli of the concrete and the rock and loads from the reservoir acting on the boundaries of the valley.

  In linear simulations this interface is mostly planar and glued together and the stresses are evaluated in the area near the base. On the other hand, nonlinear simulations by means of contact discretization, these effects can directly be modelled by allowing the interface to open.
- Horizontal tensile stresses in the longitudinal direction of the valley

  These tensile stresses occur parallel to the dam-rock interface and are evoked by the horizontal component of the resultant force at the base. In contrast to the tensile stresses normal to the base, these stresses are not as influenced by the shape of the dam, but by the dam height. They can also lead to increased openings in rock joints and therefore the possibility of water flow under the dam and the risk of instability of the abutment. The typical counter measure for this problem is the installment of a grout curtain near the upstream surface of the dam. Nevertheless, vertical cracks may occur in the foundation near the base and larger radial displacements will arise.

  In linear simulations with a tied contact between the dam and foundation these effects are not taken into account. In case of nonlinear contact simulations a discretization of the interface with specific frictional parameters is possible. Therefore, additional displacements of the dam body can be considered by this assumption.
- Horizontal tensile stresses transverse to the valley

  Transverse tensile stresses might occur due to deformations of the valley flanks and are caused by the hydrostatic water pressure or corresponding deformations of the abutment. Openings parallel to the valley can be triggered. As for the horizontal tensile stresses in the longitudinal direction of the valley they are also almost not influenced by the dam design.

  These effects are rarely taken into account in either linear or nonlinear simulations.

6.1.5 Construction Stages and Block Joint Grouting

Concrete has the property that when it’s cast into place and starts hardening it generates heat and cools down again afterwards. During cooling and shrinkage due to hardening the concrete volume decreases and it develops tensile stresses, which may lead to cracks. To overcome this problem dams are subdivided into vertical blocks in radial direction. Generally, these blocks have a width of about 20 meters, dependent on the properties of the concrete used and built alternating.

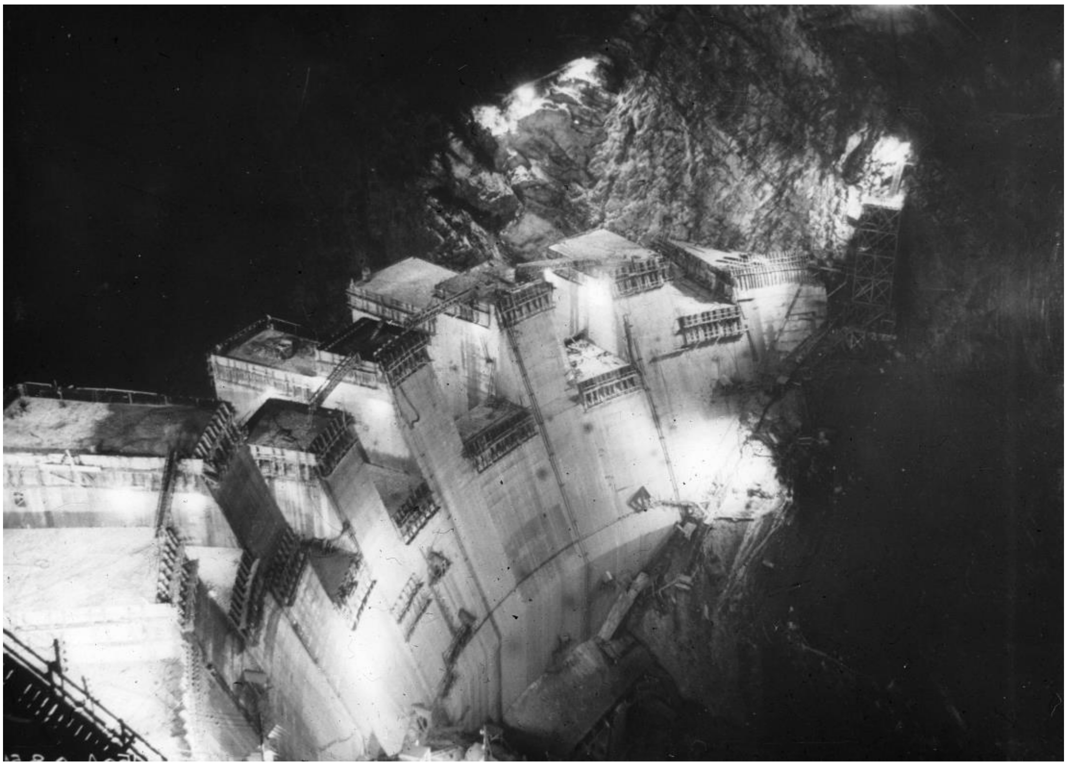

Figure 6-1: Building stages of an arch dam with alternating blocks

Between those joints so called shear keys in vertical direction are designed to inhibit radial but not vertical displacement of the blocks. Depending on the shear key type locking in vertical direction is also possible. Nevertheless, Figure 6-2 shows the vertical shear keys and the water stop configuration between two blocks of an arch dam. The water stop is made of elastic material to prevent the water penetration into the block joints during and after impounding of the reservoir.

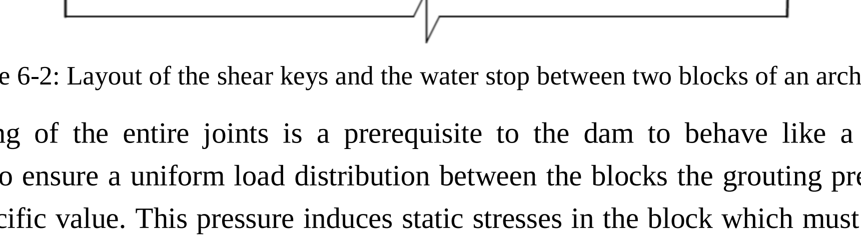

Figure 6-2: Layout of the shear keys and the water stop between two blocks of an arch dam

The grouting of the entire joints is a prerequisite to the dam to behave like a monolithic structure. To ensure a uniform load distribution between the blocks the grouting pressure must reach a specific value. This pressure induces static stresses in the block which must be limited.

Depending on the grouting order following forces are acting on the block according to Widmann (2005):

- Tangential forces, if the adjacent joints are open or subjected to a lower grouting pressure than the joint to be grouted.
- Radial forces, if two adjacent joints are filled with water or with grout that has not hardened. (Figure 6-3)

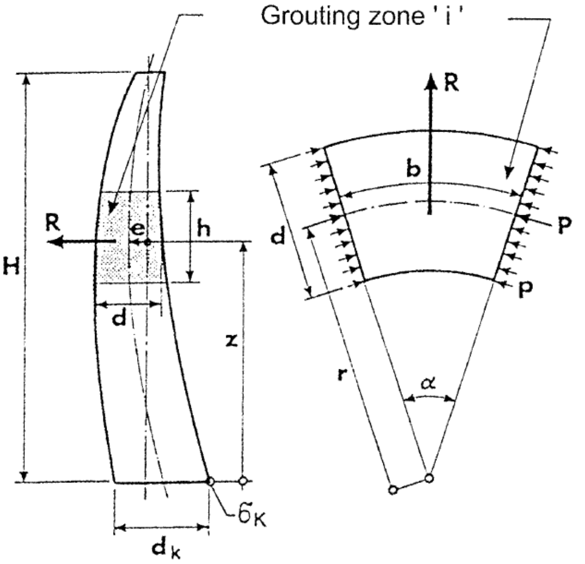

Figure 6-3: Illustration of the primary injection and radial force by Widmann (2005)

Not only does the height of the block joint grouting area influence the stresses in the blocks, but also the sequence. Generally, grouting starts at the base and continuous to the top of the dam, hence stresses due to subsequent construction stages and dead weight are acting on a monolithic horizon. However, two different possibilities of the grouting order on each horizon are possible, which are from the centre to the flanks or vice versa. Independent of the order, tangential stresses in the blocks will develop. One possibility to reduce these stresses is to fill adjacent blocks with water to attain counter pressure; on the other hand this procedure will induce radial stresses, due to the pressure from both joints (Figure 6-3).

6.2 Nonlinear Arch Dam Model

Figure 5-6 shows the original geometry with the block joint definition from Section 5.1.3.1. These joint orientations in real projects are more or less radial and dependent on the elevation, which means that they are usually curved surfaces. Consequently, for proper simulations of the block joint openings and relative displacements between those, the model from the benchmark workshop is modified. Figure 6-4 shows the original and new block joint orientation. For the new one the assumptions is made that it’s now radially oriented to the crest of the arch dam and furthermore completely vertical (same radial orientation from the crest to the base). This orientation is closer to typical construction (with curved surfaces), but is still different, because normally it should be radial on each elevation. The block joint width of approximately 30 meters is defined, because of the concrete casting properties (hydration and shrinkage).

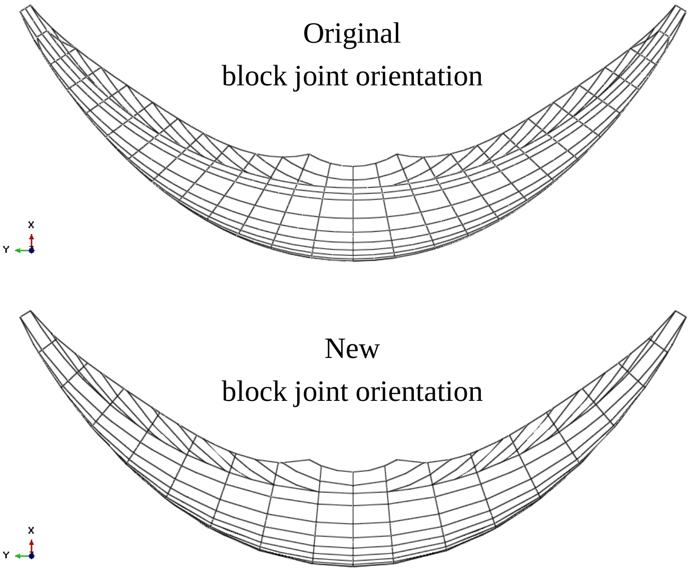

Figure 6-4: Block joint orientation of the original and the new model

A new mesh for the whole model is also generated. The mesh density is increased, because of the contact simulations which are done with linear elements (reduces convergence problems in the contact plane) instead of quadratic one as in Section 5.1.3.4, where the dam, foundation and blocks are tied.

Table 6-1 lists the number of elements and nodes (linear formulation) of the new model compared to the original coarse mesh from the benchmark problem with the quadratic formulation. The new mesh of the arch dam model for the nonlinear simulations is depicted in Figure 6-5. For all parts of the model linear elements with reduced integration are chosen. The name of these elements in Abaqus is C3D8R.

Table 6-1: Number of elements and nodes of the original coarse mesh and the new mesh

	Original Coarse Mesh	**New Mesh**
Arch Dam	2083 Nodes 356 Elements	7975 Nodes 4804 Elements
Foundation	11608 Nodes 2340 Elements	7344 Nodes 5890 Elements
Reservoir	12493 Nodes 2640 Elements	7248 Nodes 6105 Elements
Sum	**26184 Nodes** **5336 Elements** **53000 DOFs**	**22567 Nodes** **16799 Elements** **47000 DOFs**

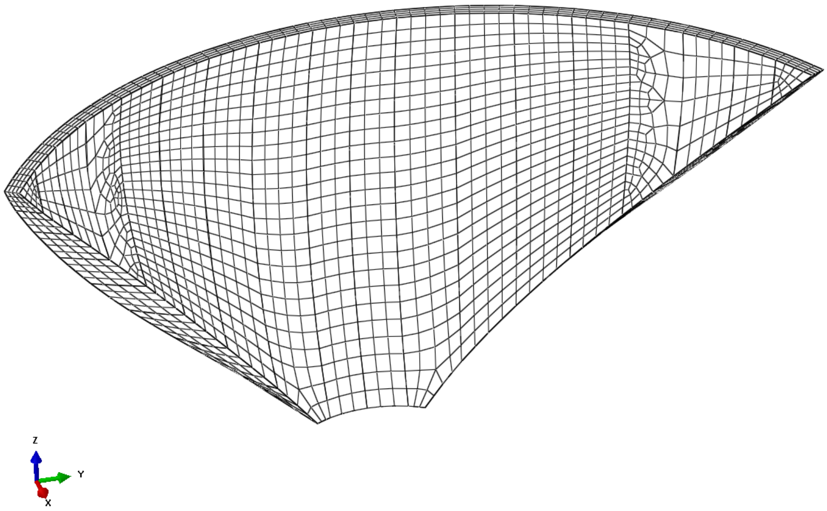

Figure 6-5: New mesh of the arch dam model for nonlinear simulations

6.3 Contact Modelling in the Block Joints

For the contact modelling in the block joints the program Abaqus/Cae allows for different discretization methods. One possibility would be the separation of each block into a part and defining an interaction between them. This procedure is time consuming and can lead to additional problems regarding convergence and contact initialization. Another more easy way that Abaqus/Cae is providing (especially for crack simulations) is to use the "seam" command which separates all blocks without creating block parts.

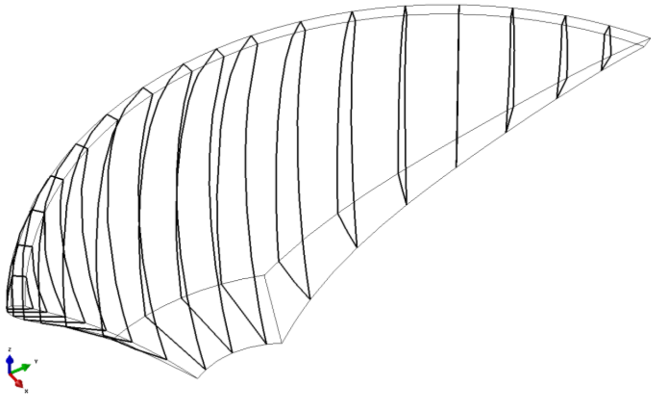

Figure 6-6: Highlighted planes between the blocks for the use of the "seam" command

After the definition of these seams the interaction is modelled with "general contact" with the contact domain to be "All* with self". This type recognizes the separated blocks after seaming automatically and initializes the contact between them. The interaction properties of the block joints for the contact behaviour in tangential and normal direction are defined in Table 6-2.

Tassios and Vintzēleou (1987) published a paper "Concrete-to-Concrete Friction" where they investigated the load transfer along unreinforced concrete interfaces for smooth, rough and sand-blasted surfaces. For smooth surfaces they found out that the influence of the compression stress (varying from 0.5 to 2.0 MPa) has just a minor influence on the friction leading to values of 0.4 to 0.5. In the case of rough interfaces the friction coefficients are varying more dependent on the compression stress. Therefor they also performed cyclic tests and variations of the slip displacements. These tests lead to values between 0.5 and 0.7 for relatively small displacements after the sixth cycle for a compressive stress of 0.5 to 2.0 MPa. With the assumption that the condition of the block interface is somewhere between smooth/rough and hoop stresses (compressive stress between the blocks) in the range of 4.0 to 7.0 MPa (Figure 5-9) in the upper part ($H = 100\text{m} \div 220\text{m}$), the conservative friction coefficient of $\mu = 0.5$ is chosen for the simulations.

Table 6-2: Interaction properties between the block joints

Tangential behaviour	Penalty	$\mu = 0.5$
		$F_f = 0.0001$ (slip tolerance)
Normal behaviour	Soft contact (exponential)	$p_0 = 1.0\ MPa$
		$c_{c,0} = 0.001$ m
		Constraint enforcement method = default

For the tangential direction the penalty contact formulation with the slip tolerance parameter is used. Figure 4-9 in Section 4.4.3.2 illustrates the relationship between this parameter and the critical shear force. The slip tolerance parameter, which describes the contact stiffness in tangential direction, is changed from the default value of 0.005 to 0.0001 to reduce the artificial tangential stiffness.

The normal contact formulation is set to "Soft Contact" with an "Exponential Pressure-Clearance Relationship", which is depicted in Figure 6-7. It allows for contact penetration/over-closure after a specific contact pressure p_0, where the clearance is zero, is mobilized and therefore generates a numerical damping effect. In addition, an initial clearance $c_{c,0}$, which is present at the start of an analysis, has also to be defined. This formulation is recommended if convergence problems dominate the analysis. Nevertheless, the results must be examined thoroughly, because the resultant opening/closure is affected by these parameters.

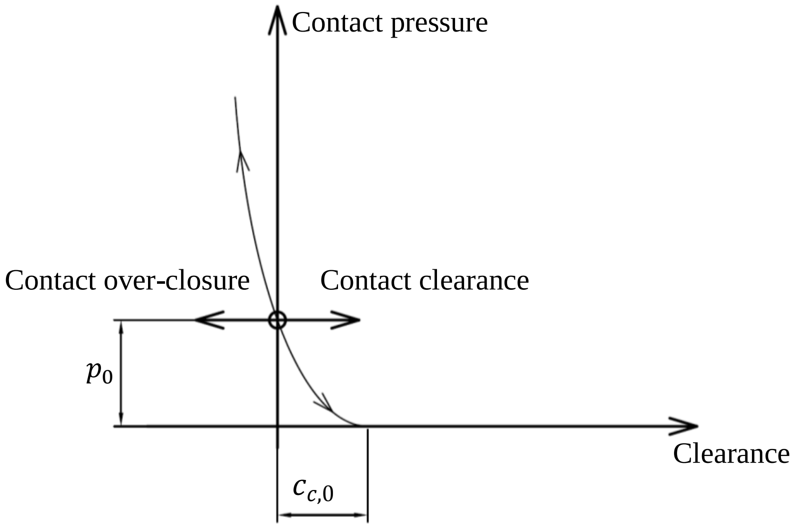

Figure 6-7: Normal contact formulation for "Soft Contact" based on Dassault Systèmes (2013)

6.4 Contact Modelling of the Interface between Dam and Foundation

In contrast to the block joints, for the contact in the base no additional split or seaming is necessary, because the arch dam and the foundation are already separated parts. The possibility of using the “general contact” is restricted to one interaction and one property, hence the type “surface-to-surface contact” with the parameters in Table 6-3 is used. Abaqus/Cae allows for some additional adjustments for the contact formulation. For the case of these simulations the “finite sliding” formulation with “surface-to-surface” discretization is chosen. The “slave adjustment tolerance for adjustment zone” is set to a value of 1.0 meter to improve the convergence behaviour during initialization. Additionally, as with the block contact, the slip tolerance, has also been adjusted and changed from the default value of 0.005 to 0.0001. During evaluation of the results a huge influence on displacements and stresses of this value between dam and foundation is observed for the arch dam model. A discussion and comparison for this issue is done in Section 6.7.2. A more detailed description of the tangential contact can be found in Section 4.4.3.2 and especially in the Abaqus/Cae documentation by Dassault Systèmes (2013).

Table 6-3: Interaction properties of the dam-foundation interface

Tangential behaviour	Penalty	$\mu = 1.0$
		$F_f = 0.0001$ (slip tolerance)
Normal behaviour	Hard contact	separation allowed
		Constraint enforcement method = default

In contrast to the block joint contact, the hard contact formulation for the behaviour in normal direction is used here. A description can be found in Section 4.4.3.2.

The “surface-to-surface contact” formulation requires the definition of the interacting surfaces to be either the slave or master surface. The general recommendation is to choose the surface with the coarser mesh to be the master surface. The Abaqus/Cae documentation states that for a “node-to-surface” discretization the slave/master surface determination has a much higher influence than for the “surface-to-surface” discretization which is used in these simulations. Nevertheless, for all simulations the foundation is chosen to be the master and the arch dam the slave surface. This configuration appeared to give the best results with less convergence problems. Furthermore, the master surface (foundation) is extended beyond in-contact borders where the slave surface (bottom of the arch dam) ends. This extend of the surface is depicted in Figure 6-8 and highlighted in grey. It is not obligatory to do that, but for the algorithm it’s much easier to find the “normals” on the corner to initialize the contact and therefore improves convergence.

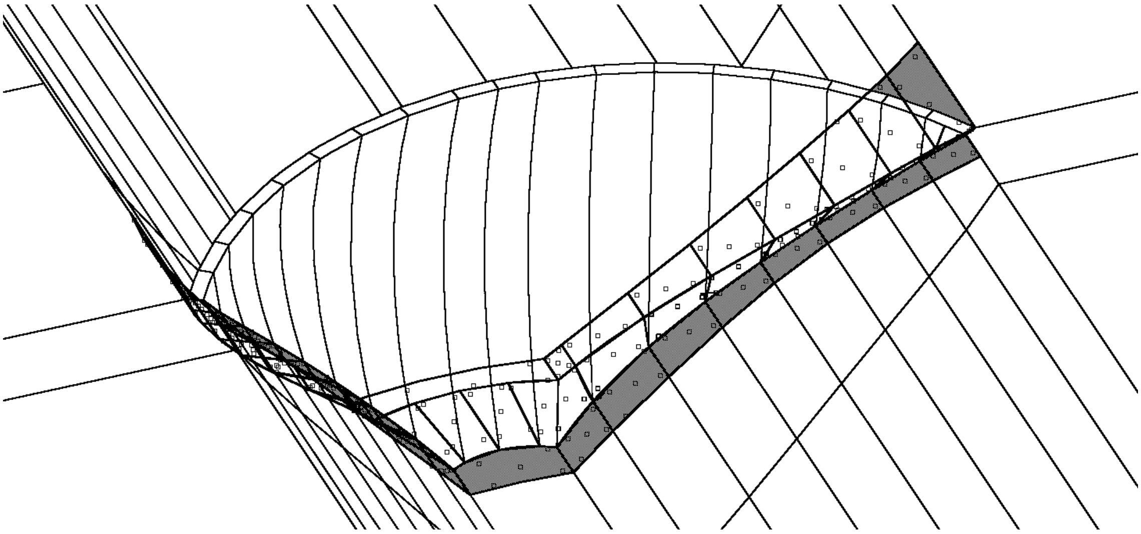

Figure 6-8: Extension of the slave surface (foundation), highlighted in grey

6.5 Material Modelling of the Concrete

Additionally to the contact nonlinearities, nonlinear material properties are applied for the concrete of the arch dam, but not for the rock foundation. As long as the material stays in the elastic domain, the properties from the benchmark workshop are used (Table 5-2).

6.5.1 Compressive Material Behaviour

A typical elastic-plastic curve with isotropic hardening (default) for the compressive material behaviour of the concrete with an ultimate compressive strength of 28.0 MPa is chosen. Isotropic hardening means that the yield surface is expanding uniformly in all stress directions and hence increases or decreases the yield stress as plastic strains occur. This approach is commonly used for metals and therefore also referred to as “metal plasticity”. The reason behind using it for the concrete is that compression damage is not expected (see maximum compressive stresses in Figure 5-9). So, this material model is only valid for the compressive stresses. In case of tensile stresses and possible cracking, the material behaviour from Section 6.5.2 is used. The plastic stress – strain curve and the corresponding values are depicted in Figure 6-9. This curve is based on the definition in Eurocode 2 (EN 1992-1-1:2004).

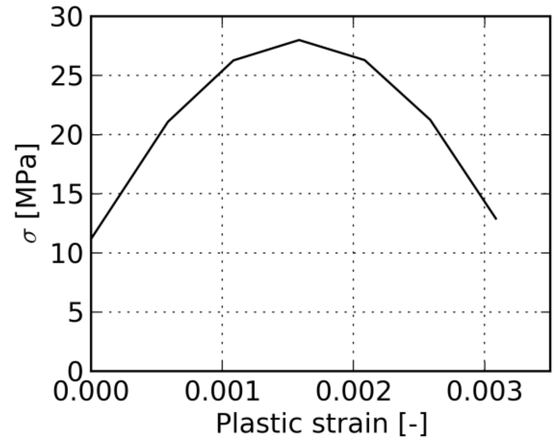

σ [MPa]	Plastic strain [-]
11.2	0.000
21.1	0.000585
26.3	0.001085
28.0	0.001585
26.3	0.002085
21.3	0.002585
12.9	0.003085

Figure 6-9: Plastic stress – strain curve for the compressive behaviour of the concrete

6.5.2 Tensile Material Behaviour

The nonlinear behaviour of the concrete for tension compared to compression is more complex due to the low tensile strength of the material (cracking). Generally, the tensile strength is about 10% of the compressive strength. Hence, cracks may occur even under the static loading case (Gravity and hydrostatic) at the upstream heel. For the dynamic/seismic loading case high tensile stresses and hence fractures can normally not be avoided. To account for this material behaviour XFEM (Extended Finite Element Method) is used, which is briefly described in Appendix B. Therefore, damage criteria have to be defined. The stress based crack initiation quantity is set to be the maximum principal stress with a tolerance of 5%. The damage evolution (softening due to cracking) is defined by the fracture energy with an exponential degradation and a mode mix of normal and shear modes with the Benzeggagh-Kenane (BK) form. The BK form is recommended for cases where shear cracks behave the same in both directions, which is legit for concrete. The fracture energy for concrete according to Bangash (2001) typically varies between 50 and 200 Nm/m². Hence, the fracture energy for mode I, tensile cracks, (e.g. normal direction) is assumed to be 135 Nm/m². Furthermore, the fracture energy in the first and second shear direction (mode II and III) are set higher than the one in normal direction, to allow the crack evolution primarily perpendicular to the crack surface. All properties are summarized in Table 6-4.

Table 6-4: Material properties for the crack propagation with XFEM in Abaqus/Cae

Damage initiation	
Criterion:	Maximum principal stress
Tensile strength	2.2 MPa
Damage evolution	
Type:	Energy
Softening:	Exponential
Mixed mode behaviour	Benzeggagh-Kenane (BK), Power = 1.0
Fracture Energy in normal direction	135 Nm/m²
Fracture Energy in the first shear direction	1000 Nm/m²
Fracture Energy in the second shear direction	1000 Nm/m²

One major drawback of simulations with XFEM in Abaqus/Cae 6.13 that was observed during this thesis is that the program only allows for one crack per region to propagate. In other words, for the example of seismic simulations of the arch dam, if the crack initialization starts on one side of the block, no further crack will appear on it, regardless of the stress level. Nevertheless, qualitative evaluations of the cracks and the location of appearance on the structure are possible and can be adducted for assessments.

6.6 Dead Weight Modelling

Arch dams are alternately built in separated blocks (Figure 6-1). This means that the blocks are not fully in contact until they are grouted and an isotropic approach of the global behaviour at gravity loading leads to wrong results. To consider the way of construction of an arch dam several possibilities exist. Some of them are introduced and compared in the following sections.

6.6.1 Without Consideration of Separated Blocks

The simplest way for simulating the gravity on an arch dam is to model it as fully isotropic continuum without consideration of any discontinuity of the blocks. This rough approach leads to a wrong behaviour of the whole structure, because shear stresses are fully transferred and the blocks are “hanging” on each other. Therefore, an isotropic system may over- or underestimate the stresses in the structure. Figure 6-10 shows the vertical stress distribution on the upstream surface of the dam without consideration of separated blocks. This approach results in maximum vertical stresses at the base of approx. -5.0 MPa.

Note, this “hanging” effect is dependent on the geometry, especially on the width at the crest to height ratio in v-shaped valleys. For this structure the ratio is approx. 2 (width = 430 m, height = 220 m). In case of higher ratio this effect might not be as influential.

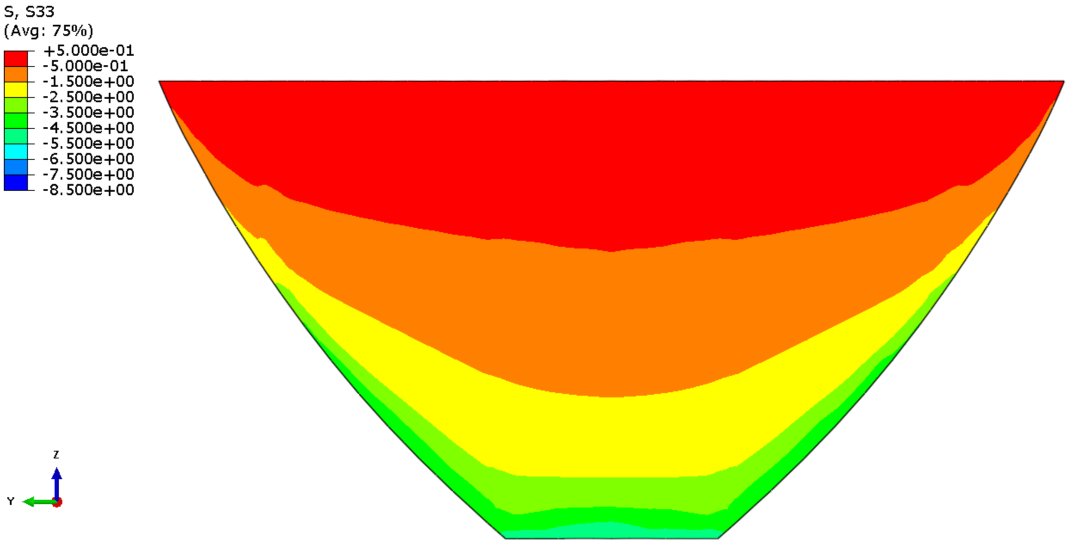

Figure 6-10: Vertical stresses [MPa] due to dead weight on the upstream surface without consideration of separated blocks

6.6.2 Orthogonal Material Behaviour

The effect of “hanging” due to the shear stresses from the isotropic approach can be avoided by using an orthotropic material behaviour. This approach allows for different stiffness in different orthogonal directions. In case of an arch dam structure at gravity loading, only the vertical stiffness wants to be accounted for. Hence, horizontal normal forces and vertical shear forces should be omitted. Horizontal forces between the blocks are transferred normal to each separating plane. Therefore, a cylindrical coordinate system for the different material properties in each direction is used. The centre of this coordinate system should be different on each elevation, because of differing horizontal radii. However, the assumption of using one mean radius (the top of the dam in this case) is sufficient for this approach. To change the material definition, in this case orthotropic for the gravity step and further on isotropic conditions for subsequent steps (e.g. hydrostatic water load) a user material as a subroutine in Abaqus/Cae is used. Such a subroutine, called UMAT, has been developed as part of a research project about hydraulic structures for PÖYRY ENERGY Ltd. (GmbH) at the Institute for Hydraulic Engineering and Water Resources Management by Zenz, Feldbacher and Goldgruber (2012). It allows for different material properties and sums up the results after each step. This is only allowed for linear system behaviour, because of superimposing the results of each step. The properties from Table 5-2 corresponding to directions in which the stiffness should be neglected are divided by a factor of 100. The orthotropic material properties for the cylindrical coordinate system for the arch dam are listed in Table 6-5 with following notation:

- “1” corresponds to the radial direction
- “2” corresponds to the tangential direction
- “3” corresponds to the vertical direction

Table 6-5: Orthotropic material properties

Young’s modulus	Shear modulus	Poisson ratio
E_1 = 27000 MPa	G_{12} = 89.2 MPa	γ_{12} = 0.00167
E_2 = 270 MPa	G_{13} = 8920 MPa	γ_{13} = 0.167
E_3 = 27000 MPa	G_{23} = 89.2 MPa	γ_{23} = 0.00167

Figure 6-11 shows the vertical stress distribution on the upstream surface of the dam with orthogonal material behaviour. This approach results in maximum vertical stresses at the base of approx. -8.5 MPa.

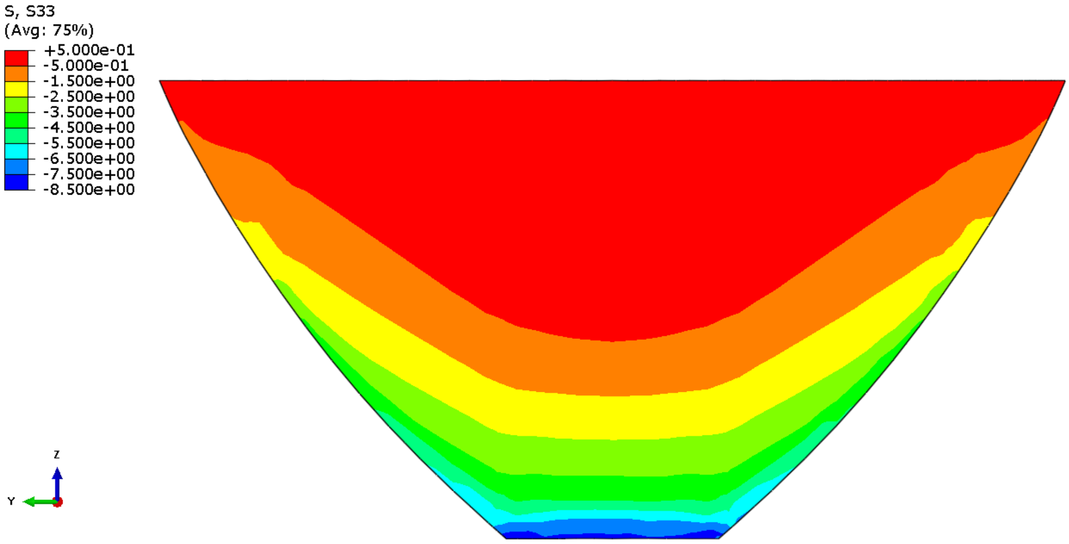

Figure 6-11: Vertical stresses [MPa] due to dead weight on the upstream surface with orthogonal material properties

6.6.3 Separation of Blocks

A common, but also simple approach is to separate the simulation of the gravity load in three steps. In these steps the gravity load on different block sets are calculated. In the first step, e.g. every block with an even number and in the second step every block with an odd number is simulated. In the third step the results from the blocks are superimposed, giving the stress level in the structure from gravity load for subsequent steps. This way of modelling the gravity load has been used by Tzenkov et al. (2014) and Chambart et al. (2014) at the benchmark workshop from Section 5.1. Here again, as already mentioned in Section 6.6.2, this procedure is also only applicable to a linear system behaviour, because of the superposition of the results and it accounts for absolutely no interaction between the blocks. Figure 6-12 shows the vertical stress distribution on the upstream surface of the dam with completely separated blocks. This approach results in maximum vertical stresses at the base of approx. -6.0 MPa.

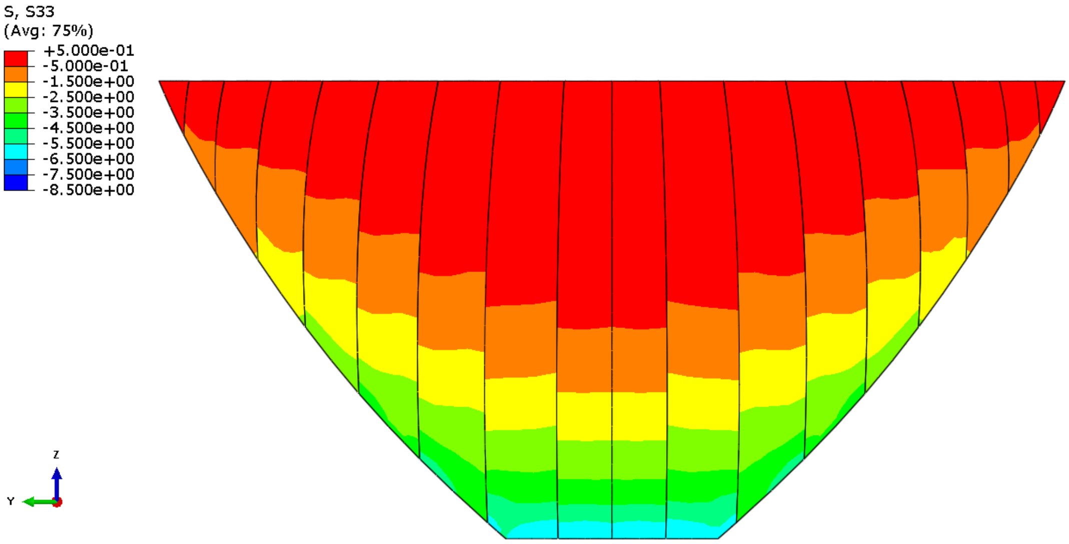

Figure 6-12: Vertical stresses [MPa] due to dead weight on the upstream surface with completely separated blocks

6.6.4 Discrete Blocks with Contact

In this discretization technique the blocks are not completely separated as in Section 6.6.3. This way of modelling is more realistic, due to the fact that the blocks are grouted during construction and shear keys are designed between them. Therefore, they are coupled with a contact formulation and hence can transfer shear and normal forces dependent on the defined tangential and normal behaviour according to Section 6.3. It is worth mentioning that in nature a full contact in the early stage of construction, due to temperature effects and shrinkage of the concrete, is not present until grouting. Hence, the assumption of a frictional contact with a coefficient of 0.5 between the blocks might be too high for the gravity simulation step and refers to a state after grouting. Nevertheless, the influence is small, compared to the model with completely separated blocks from Section 6.6.3. The base contact is tied to the underlying foundation (no relative displacement) and requires no additional contact formulation for the simulations of the gravity loading, because during and after construction an opening or displacement of the base is not expected (see way of construction in Section 6.1) and stays fully in contact (Note: In contrast to hydrostatic loading which may lead to openings, see Section 6.7). This way of modelling the gravity loading gives the most accurate results regarding the vertical stresses and global behaviour. Figure 6-13 shows the vertical stress distribution on the upstream surface of the dam for discrete blocks with contact. This approach results in maximum vertical stresses at the base of approx. -6.0 MPa.

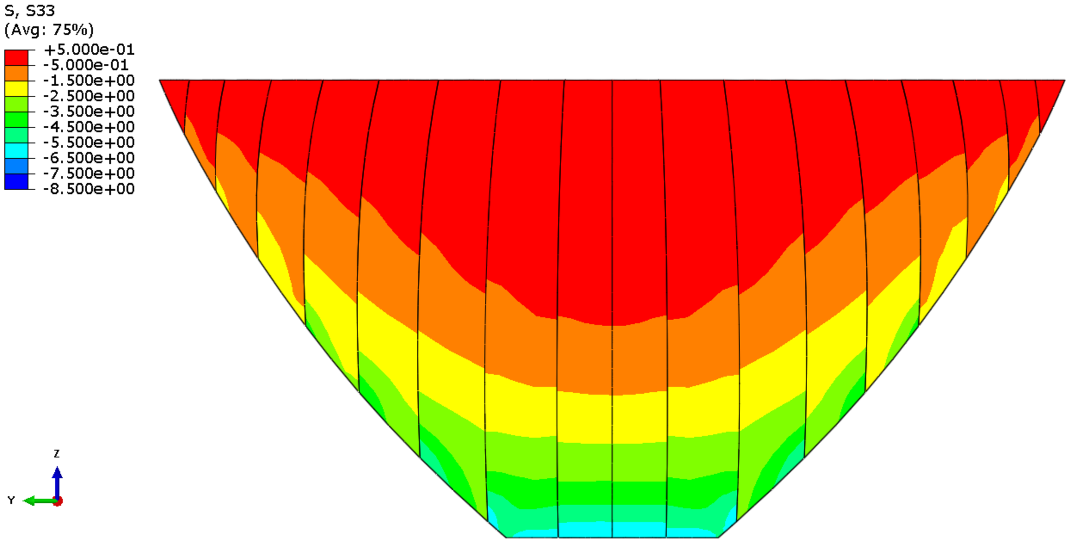

Figure 6-13: Vertical stresses [MPa] due to dead weight on the upstream surface with discrete block modelling

6.6.5 Comparison and Discussion of the Dead Weight Loading

Figure 6-14 shows that the simulation of the dead weight with a completely isotropic material behaviour is not acceptable for investigations of the structure regarding gravity loading. The isotropic simulation leads to underestimated results, especially at the base on the upstream surface (-5.0 MPa), compared to the results from the orthotropic and separated blocks models (-6.0 MPa). On the downstream surface of the dam, the minimum stresses are also lowered by a value of -1.5 MPa from -3.5 MPa down to -2.0 MPa.

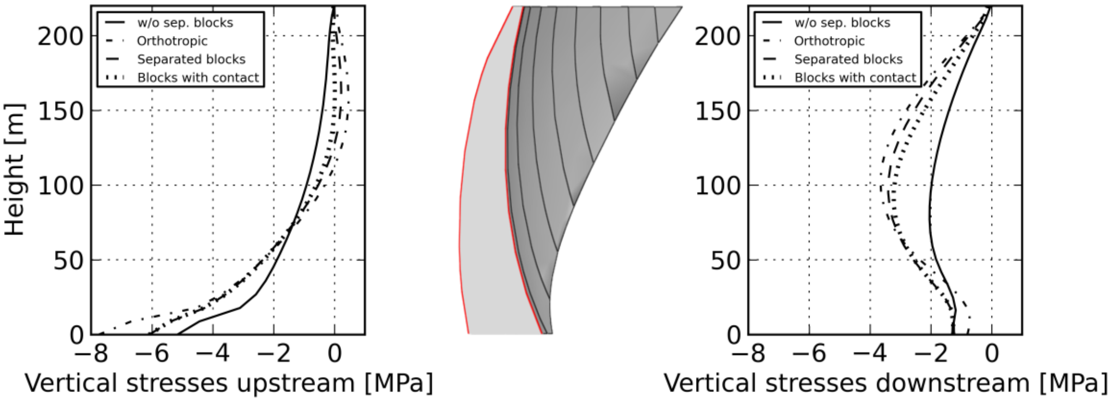

Figure 6-14: Vertical stress comparison for different dead weight modelling techniques on the upstream (left) and downstream surface (right) in the main section

On the other hand, the orthotropic material description leads to conservative results compared to the models with separated blocks. The vertical stresses on the upstream base are increased by -2.0 MPa to approx. -8.0 MPa which is attributable to the drastically decreased shear modulus for the material in vertical direction. The models with the block separation – with or without contact – yield almost the same results over the whole height of the structure with a minimum vertical stress of -6.0 MPa at the upstream base and -3.5 MPa on the downstream surface at a height of 100 meters.

For comparison reasons the minimum principal stresses are depicted in Figure 6-15.

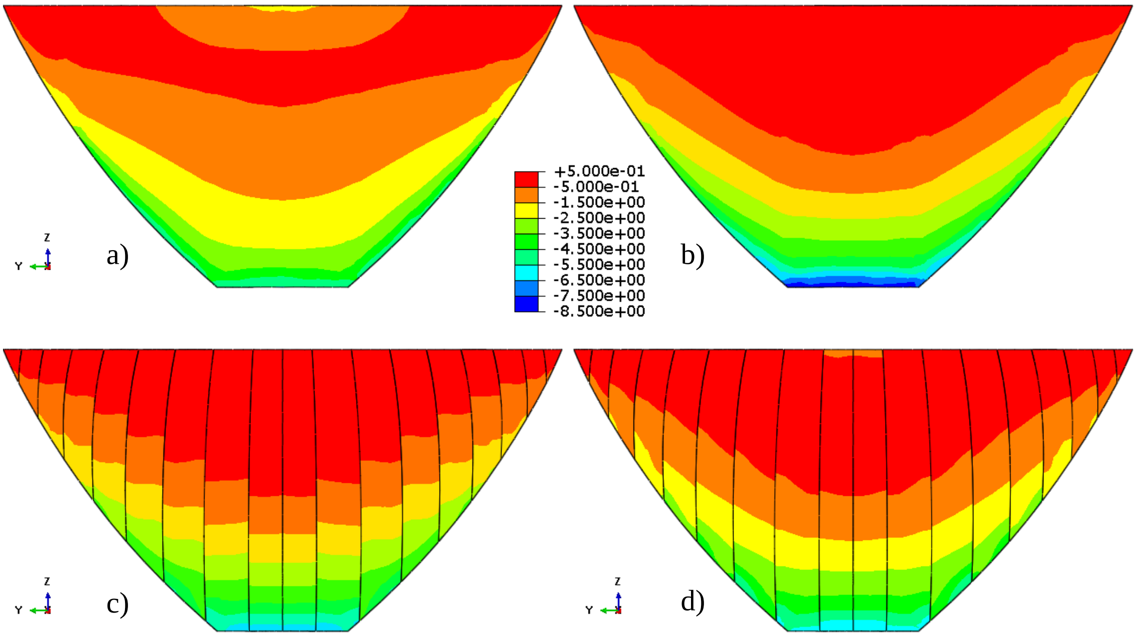

Figure 6-15: Minimum principal stress [MPa] comparison for different dead weight modelling techniques on the upstream surface; a) Isotropic model without separation of blocks, b) Orthotropic model, c) Completely separated blocks, d) Discrete blocks with contact

6.6.6 Discussion regarding Displacements from the Dead Weight Loading

In finite element analyses of mechanical systems solving the system of equations yields the displacement and hence strains and stresses. This implies that only a deformed system results in stresses. In case of civil engineering structures, where the gravity is mostly the essential loading, these displacements during construction are compensated and the structures are built according to the design drawings. This fact leads to the problem in the simulations that the gravity loading is acting on the structure and therefore a displacement is computed. As long as these displacements are small and the systems behaviour is linear they can be ignored and subtracted from subsequent steps and only the stresses are considered and added to further results. If the simulations are nonlinear, e.g. contacts or plasticity, this procedure is not valid. Stresses, displacements, etc. then are dependent on their history. In other words, these results effect further simulation steps and lead to wrong result. Some numerical programs offer the possibility to overcome this problem with a special procedure for solving the system for a state of zero displacement put with the stresses from the applied loading. In Abaqus/Cae this step is called “Geostatic”. It allows for predefined stress conditions, like stresses in soil layers of geotechnical problems, as well as arbitrary loadings. The program iterates to find a solution which is in equilibrium with the loading and zero displacement. In case of arbitrary loadings, a tolerance for the maximum error in displacement must be defined. The default value Abaqus/Cae uses is 10^{-5}, which is described as the ratio between the maximum absolute displacement and the characteristic element length. This procedure is applicable to linear and nonlinear systems, respectively. The influence of using displacements from gravity loading or not for subsequent nonlinear simulation steps regarding the base opening, displacements and stresses are discussed in Section 6.7.

6.6.7 Conclusion of the Dead Weight Loading

Negligence of the discontinuity due to the block joints is not legitimate for dead weight simulations of an arch dam. Major underestimations of vertical stresses are possible (Figure 6-14). The most accurate way of modelling gravity load for such a structure is to use separated blocks with a contact formulation for investigations of the nonlinearities. In cases where only linear results are from interest, separated blocks without any interaction is legit and allow for transferring the resultant stresses to subsequent steps. Therefore, the use of separated blocks without joints in contact is recommended if simulations are carried out just linear. If the contact behaviour between the blocks and their influence to subsequent steps is of interest a nonlinear simulation is required.

Regarding the problems with displacements and stresses described in Section 6.6.6 the effects are discussed in Section 6.7, because the computed displacement have just a minor influence on the dead weight results, but will be effecting subsequent steps.

6.7 Hydrostatic Modelling

After the construction is finished the block joints are grouted and the hydrostatic water load due to the filling of the reservoir is acting on the dam and the structure behaves more or less isotropic. At full reservoir conditions the maximum hydrostatic water load pushes the dam forward and the upstream heel tends to open. These openings are usually expected and countermeasures (e.g. grouting), are installed during construction. Nevertheless, such openings cannot be completely prevented or neglected, hence it’s important to know where and in which size they appear whereby the shape of the valley also affects the response. Otherwise the water propagates uncontrolled through the base and foundation and leads to unintended uplift and pore-water pressures and hence may cause a failure of the structure.

After the gravity step the hydrostatic water load acting on the dam and the underlying foundation is usually applied. For these simulations the preceding dead weight is simulated with blocks in contact (discretization method from Section 6.6.4) with the exception that the tied contact has to be changed to the properties from Section 6.4 in this step, because the program doesn’t allow for major contact modifications between two steps.

As already discussed in Section 6.6.6 the effects on the base opening and radial deformation due to computed displacements from the gravity loading are investigated. The results from the standard static (with displacements out of gravity) and the so called “Geostatic” (displacements due to gravity are zero) simulations are compared.

To evaluate the influence of different reservoir water levels following cases are investigated and compared in Section 6.9:

- Full reservoir conditions (water level = 220 meters)
- Half full reservoir (water level = 110 meters)

- Empty reservoir (water level = 0 meters)

6.7.1 Influence of Displacements from preceding Dead Weight Simulations

Displacements are results of loads on a structure and so are stresses. In case of structures, which are built according to their design drawings, these displacements are compensated during construction, but stresses remain. Dependent on the dimensions and the discretization (linear – nonlinear) of the investigated structure, these displacements are mostly negligible. For the arch dam model the influence on the base contact openings and the radial displacements are evaluated, therefore the hydrostatic water load (full reservoir case) is applied on the following two models for comparison:

- General static computation of the gravity loading and corresponding displacements are retained
- Geostatic computation of the gravity loading: Iteration to find equilibrium between zero displacement and stresses resulting from the gravity loading, with a maximum error in displacement of 10^{-3})

Figure 6-16 shows the differences in displacement for gravity and hydrostatic loading of the whole structure and Figure 6-17 in the main section. A closer look at Figure 6-16 the contour plot reveals that with the geostatic step procedure, the whole structure behaves much more isotropic due to the hydrostatic loading. The steps between the blocks for the radial displacement almost disappeared.

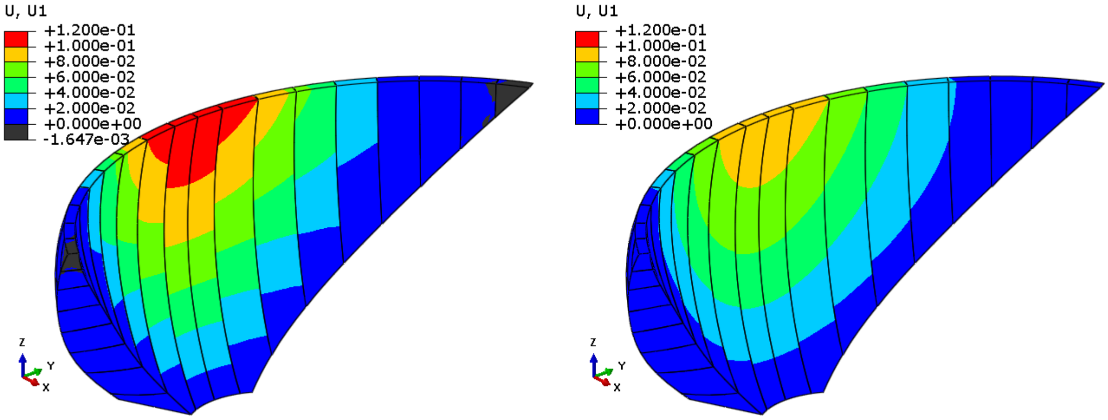

Figure 6-16: Displacement [m] in x-direction for hydrostatic water loading between the general static step (left) and the geostatic step (right)

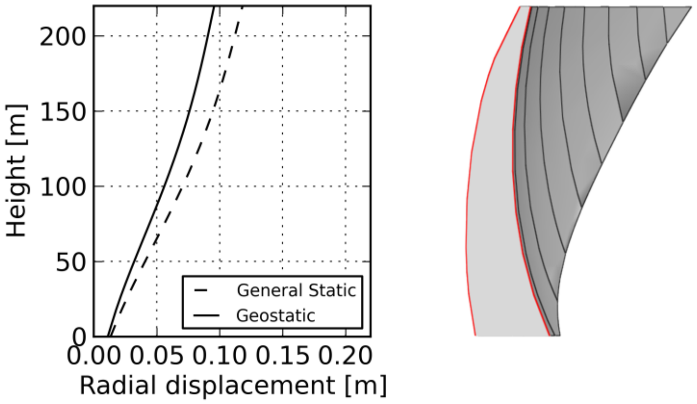

Figure 6-17: Displacement in the main section for hydrostatic water loading (full reservoir case) between the general static step and the geostatic step

As for the contact opening, also here differences in the displacement are observable over the height of the structure (Figure 6-17). For the hydrostatic step the displacements are increased by approx. 0.02 meters from 0.10 to 0.12 meters (Figure 6-17).

Figure 6-18 shows that the hoop stresses in the main section on the up- and downstream surface of the structure are also affected by the procedures. The structure shows a completely different behaviour, where for the geostatic step the hoop stresses are more concentrated on the upstream surface and approx. 1.5 MPa higher. On the downstream the general static procedure almost yields 2.0 MPa higher hoop stresses.

These differences are only triggered by the initial displacements of the gravity loading. The standard way of dead weight simulation, where displacements are computed and retained, allows also for blocks to open before the hydrostatic load is applied. On the other hand, by using the geostatic procedure, all displacements and openings for dead weight loading are zero, which represents the structure in nature better.

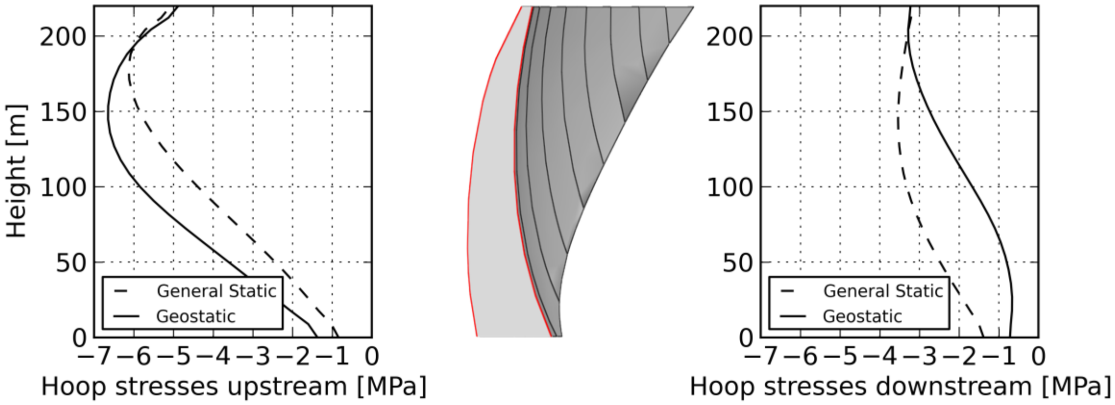

Figure 6-18: Hoop stresses in the main section for hydrostatic water loading (full reservoir case) between the general static step and the geostatic step

Figure 6-19 depicts the effects on the contact opening computation with and without retained displacements from the gravity loading. It can be immediately seen that pre-displacements have a significant influence on the openings. The model with the geostatic step reduces the contact opening at the upstream heel from 8.0 to 3.0 millimetres. Both openings reach almost 27 meters into the base (Figure 6-19).

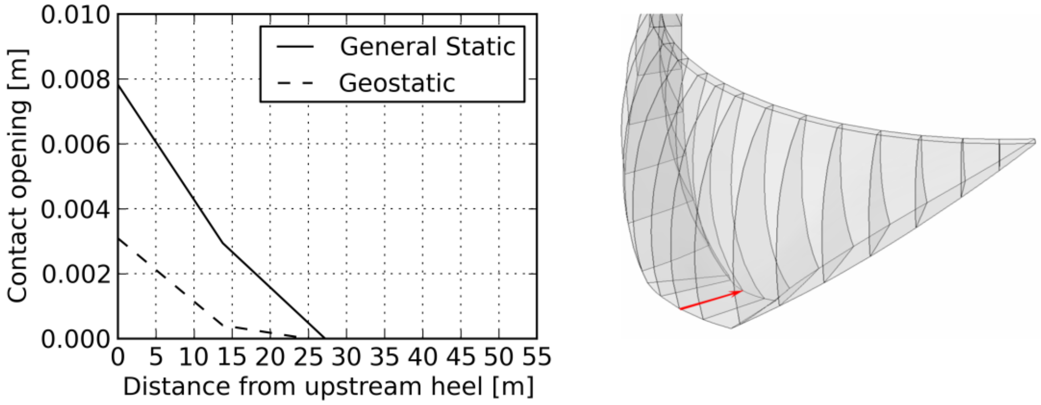

Figure 6-19: Contact opening at base due to hydrostatic water loading along the path in the main section

6.7.2 Influence of the Tangential Contact Stiffness (elastic slip)

The elastic slip parameter γ_e allows for adjustment of the tangential contact stiffness before slipping of the surfaces ends in permanent displacement (Figure 4-9 in Section 4.4.3.2). Recovering equation (4-10) $\gamma_e = F_f \overline{l_i}$ one can see that this value is dependent on the slip tolerance F_f and the characteristic contact element surface dimension $\overline{l_i}$. Hence, for a small element number in the contact plane the element length and the allowed elastic slip increases. This fact leads to unrealistic contact formulations which not only changes the contact displacement but might also affect the global behaviour and stresses. A parameter study on the arch dam model shows the influence of different values changing from the default slip tolerance F_f of 0.005 down to the final value used for the simulation of 0.0001. Additionally a completely tied contact between dam and foundation is also evaluated and depicted in the diagrams.

Figure 6-20 shows the influence of the slip tolerance F_f in the main section for hydrostatic water loading (full reservoir case). A significant reduction from 0.17 meters ($F_f = 0.005;\ default$) to 0.09 ($F_f = 0.0001$) can be observed. This fact indicates that the default value of slip tolerance is not applicable to this contact discretization with a rather coarse mesh (4 elements á ~14 meters in radial direction) and yields a much higher displacement of the whole structure than expected. Figure 6-20 also reveals that a slip tolerance of 0.0001 and the tied contact at the base almost yield the same results, except near the base.

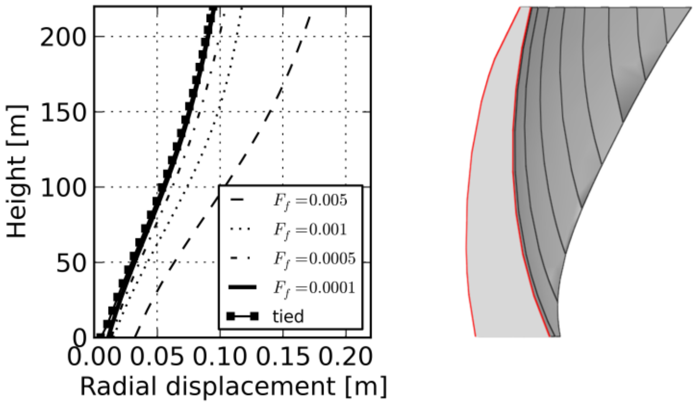

Figure 6-20: Displacement in the main section for hydrostatic water loading (full reservoir case) for different slip tolerance F_f values

The influence of the slip tolerance on the hoop stresses is also significant. Figure 6-21 shows the hoop stresses in the main section for hydrostatic water loading (full reservoir case) on the up- and downstream. A maximum difference of 2.0 MPa therefore occurs on the upstream surface of the dam, whereby the differences on the downstream surface at the base are even higher by the amount of 4.0 MPa. As for the displacements Figure 6-21 also reveals that a tied contact yields almost identical results, except near the base again.

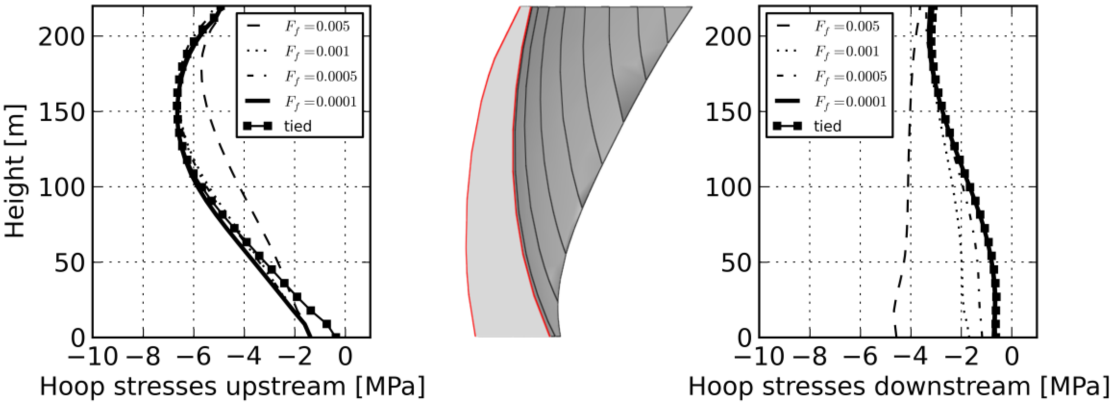

Figure 6-21: Hoop stresses in the main section for hydrostatic water loading (full reservoir case) on the up- and downstream surface for different slip tolerance F_f values

These diagrams lead to the fact that also the global behaviour of the structure is influenced by the slip tolerance. The stiffness in the contact plane is reduced by using relatively large values, which resembles a soft and artificial spring between those surfaces. This behaviour can be observed in Figure 6-20, where the radial displacement is increased and furthermore in Figure 6-21, which depicts completely different stress distribution due to this factor.

A similar change is observed for the vertical stresses in Figure 6-22. The stresses on the upstream surface are not as affected as on the downstream surface. Here again the tied contact and the discrete contact show the same results.

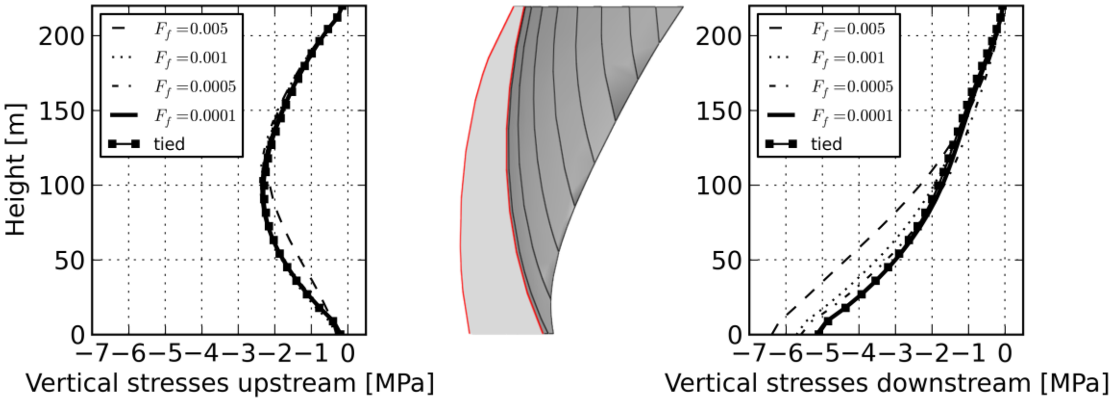

Figure 6-22: Vertical stresses in the main section for hydrostatic water loading (full reservoir case) on the up- and downstream surface for different slip tolerance F_f values

It can be concluded that a wrong (high) slip tolerance value introduces artificial tangential stiffness which is not present in reality and therefore can totally change the behaviour of the structure. In the case of the arch dam model the displacements and stresses are influenced considerably. Smaller tolerances correspond to more realistic interactions of contact surfaces, but with a higher numerical effort. The slip tolerance should be chosen with caution under consideration of the mesh size in the contact plane. Based on these results and the maximum element length in the contact plane an allowed elastic slip not larger than 3.0 millimetres is recommended. For example, the maximum elastic slip for this structure and maximum contact mesh size (4 elements á ~14 meters in radial direction) therefore is

$$\gamma_e = 0.0001 \cdot 14.0\, m = 0.0014\, m \ \equiv 1.4\, mm$$

On the other hand, simulations with a completely tied contact at the base of the dam lead to almost identical results. Hence, if the contact behaviour at the dam abutment (e.g. contact opening) is not the main interest, this interaction can be omitted.

6.7.3 Contact Behaviour between the Blocks

Figure 6-23 shows the arch dam model cut in the symmetric plane for the deformed and undeformed state and the contact pressure in the main section after hydrostatic loading. The 500 times scaled figure on the left side indicates that no relative displacement between the blocks is observed. Furthermore, for the hydrostatic loading case they stay fully in contact, so no contact opening between the blocks were found. The right side of the figure shows that the contact pressure on the downstream side reduces to 0.5 MPa and on the upstream side up to maximum of 6.5 MPa. The same stress levels can be seen in the diagram with hoop stresses in Figure 6-21.

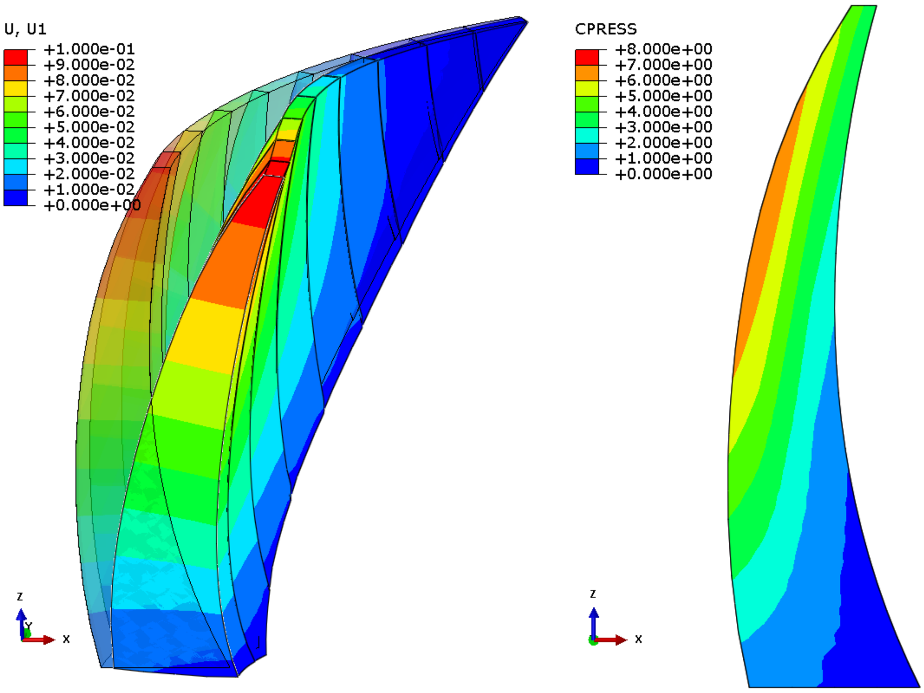

Figure 6-23: Arch dam displacement [m] scaled 500 times (left) and contact pressure [MPa] in the main section (right)

6.7.4 Principal Stresses of the Linear and Nonlinear Model for Hydrostatic Water Loading

In this section the principal stress propagation between the linear and nonlinear model for hydrostatic loading conditions are compared. The linear model corresponds to the modelling from the benchmark workshop in Section 5.1.3.

6.7.4.1 Minimum Principal Stress Comparison

Figure 6-24 shows the minimum principal stresses (compressive stress) on the upstream surface between the linear and nonlinear model for hydrostatic water loading. It can be immediately seen that the stress distribution changes significantly. The maximum compressive stress reduces from -7.0 MPa (linear model) to -5 MPa (nonlinear model).

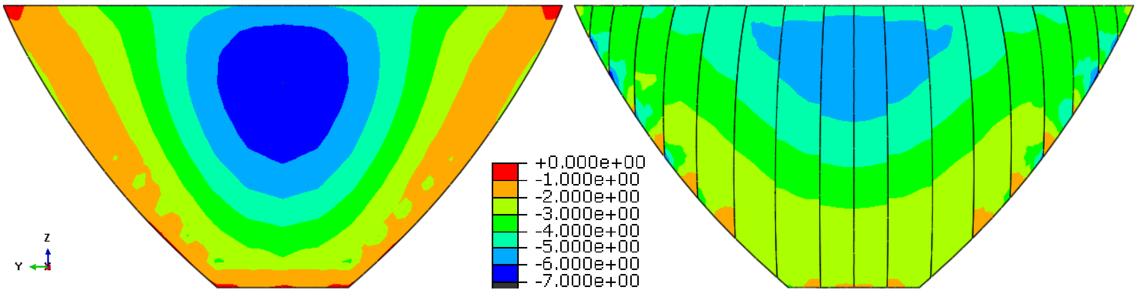

Figure 6-24: Minimum principal stresses [MPa] on the upstream surface between the linear (left) and nonlinear model (right) for hydrostatic water loading

Figure 6-25 shows the minimum principal stresses on the downstream surface. Here again, the stress pattern changes significantly. Stress peaks are, as expected, developing in the corners of the discrete blocks in the nonlinear model. This is not the case in the linear model due to the completely isotropic and homogenous dam body, but stresses along the edge on the downstream side are of nearly the same magnitude (-12MPa).

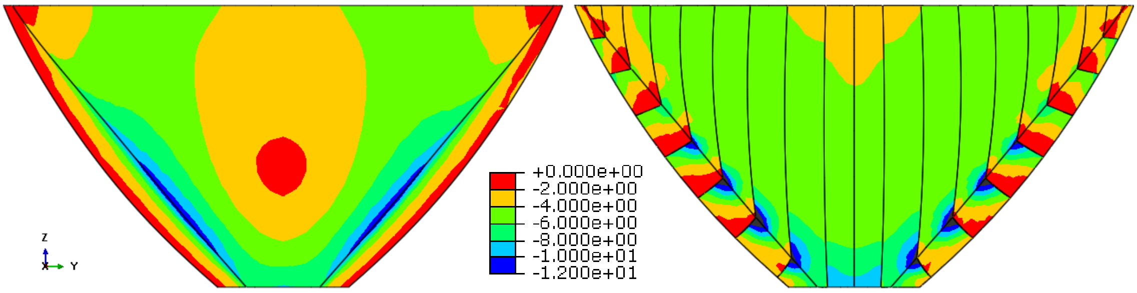

Figure 6-25: Minimum principal stresses [MPa] on the downstream surface between the linear (left) and nonlinear model (right) for hydrostatic water loading

6.7.4.2 Maximum Principal Stress Comparison

Figure 6-26 shows the maximum principal stresses (tensile stress) on the upstream surface between the linear and nonlinear model for hydrostatic water loading. Due to the allowed opening at the bottom the tensile stresses in the nonlinear model disappear at the base of the upstream side. Only small tensile stresses of around 0.5 MPa can be found in the blocks slightly above the base. However, in the linear model quite high tensile stresses of 4.0 MPa can be observed, which is attributable to the tied contact between the dam and the foundation.

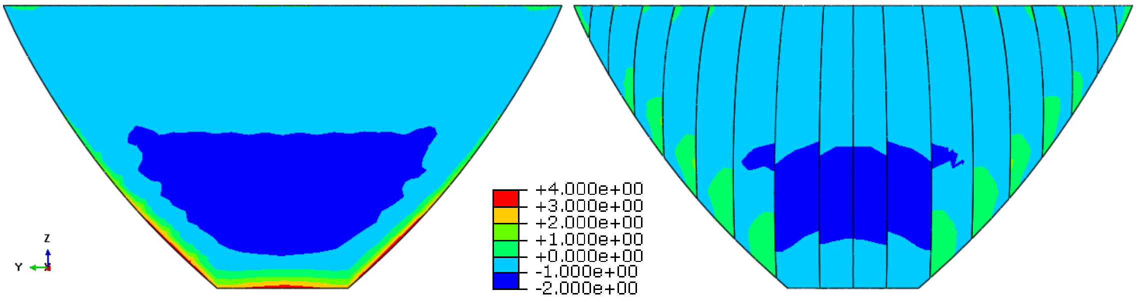

Figure 6-26: Maximum principal stresses [MPa] on the upstream surface between the linear (left) and nonlinear model (right) for hydrostatic water loading

Figure 6-27 shows the maximum principal stresses on the downstream surface. Only slight changes in the stress propagation between the two models are visible. The maximum tensile stress over the whole surface for both models is varying from 0.0 MPa to 0.5 MPa. Slightly larger values are only observed near the top of the nonlinear model at the interfaces between the blocks and reaching a maximum of about 1.0 MPa.

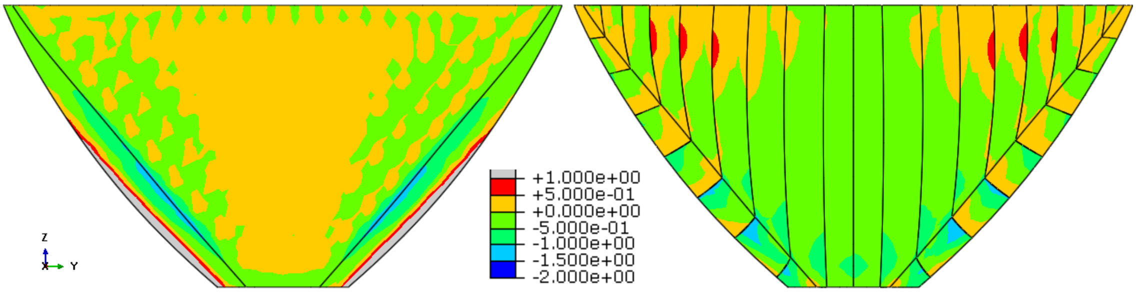

Figure 6-27: Maximum principal stresses [MPa] on the downstream surface between the linear (left) and nonlinear model (right) for hydrostatic water loading

6.8 Seismic Modelling

The same acceleration-time-histories as for the linear seismic arch dam simulations from Chapter 5 are used and applied normal to the boundaries of the foundation model. Furthermore, to investigate the nonlinear material effects modelled with the XFEM method the acceleration-time-histories are scaled two times to account for a stronger motion. For the XFEM simulations it is not able to use a preceding geostatic step in Abaqus/Cae, which means that all nonlinear material comparisons are based on the general static dead weight simulations with retained displacements from this step.

The interaction between the dam and the reservoir is accounted for in all simulations as acoustic fluid (Section 3.5). Damping of the system is defined by means of Rayleigh damping factors calculated by the approach of Spears and Jensen (2012) from Section 2.3.2.

6.8.1 Contact Modelling and Boundary Conditions of the Reservoir

For the contact between the arch dam and the reservoir – modelled as acoustic fluid – a tie constraint is defined. This type of constraint allows neither separation nor a relative slip, which also counts for the acoustic fluid elements (have to stay continuous) themselves. This implies that all relative displacement of the blocks in following steps won’t result in a relative displacement in acoustic domain. To bridge this problem and to make the coupling with a discontinuous structural domain possible, the program projects all computed loads at the interface from subsequent steps back to the initial nodal position of the reservoirs interface.

At the back-end boundary of the reservoir a non-reflecting (viscous) boundary condition (Section 3.5.3 and 4.4.3.4) is defined, hence all waves are absorbed. No boundary conditions (absorptions, reflections) are specified on the sides. This accounts for total reflection, which is a conservative approach compared to problems in nature where waves are absorbed by the vegetation, sediments and rock mass (Section 3.5.3.3). Effects of excitations (interaction between reservoir and foundation) at the reservoir boundaries have been neglected.

6.8.2 Modified Rayleigh Damping Factors

For all nonlinear seismic simulations modified Rayleigh damping factors according to Spears and Jensen (2012) from Section 2.3.2 are used. Therefore, a constant critical damping of 5% for the whole structure is assumed. A frequency analysis of the structure is performed for a total of 200 modes (corresponds to 98% of effective mass) to extract the natural frequencies and effective masses. For the calculation of the damping factors only the effective masses in x-direction (up- to downstream) are used, which is sufficient. Otherwise three different – directional dependent – damping factors (x-, y- and z-direction) would be calculated, but are not able to define as a material parameter and not necessary to use.

The procedure from Section 2.3.2 to calculate the modified Rayleigh damping factors was implemented into a python script. One needs two natural frequencies for calculating the mass- and stiffness proportional factors. For the first one the first natural frequency (assumption) is used and the second one is iteratively determined by the procedure according to Spears and Jensen (2012). The result for the second one is the 29th mode with a corresponding natural frequency of 6.25 Hz for the full reservoir case. Figure 6-30 depicts the Rayleigh damping curves for the damping used in Section 5.2 (Investigation of the Influence of Damping Factors) compared to the newly modified damping curve. The results of the mass- and stiffness proportional damping factor calculation for full, half-full and empty reservoir case are listed in Table 6-6.

Table 6-6: Mass- and stiffness proportional damping factors

	1st frequency [Hz]	**2nd frequency [Hz]**	**Mass-proportional $\boldsymbol{\alpha}$**	**Stiffness-proportional $\boldsymbol{\beta}$**
Rayleigh damping from Section 5.2 for the linear model				
Full reservoir	1st Mode $f_1 = 1.54$	4th Mode $f_4 = 2.29$	0.422	0.005
Modified Rayleigh damping factors for the nonlinear model				
Full reservoir	1st Mode $f_1 = 1.54$	29th Mode $f_{29} = 6.25$	0.777	0.002
Half full reservoir	1st Mode $f_1 = 1.91$	17th Mode $f_{17} = 6.21$	0.916	0.002
Empty reservoir	1st Mode $f_1 = 1.91$	12th Mode $f_{12} = 6.14$	0. 916	0.002

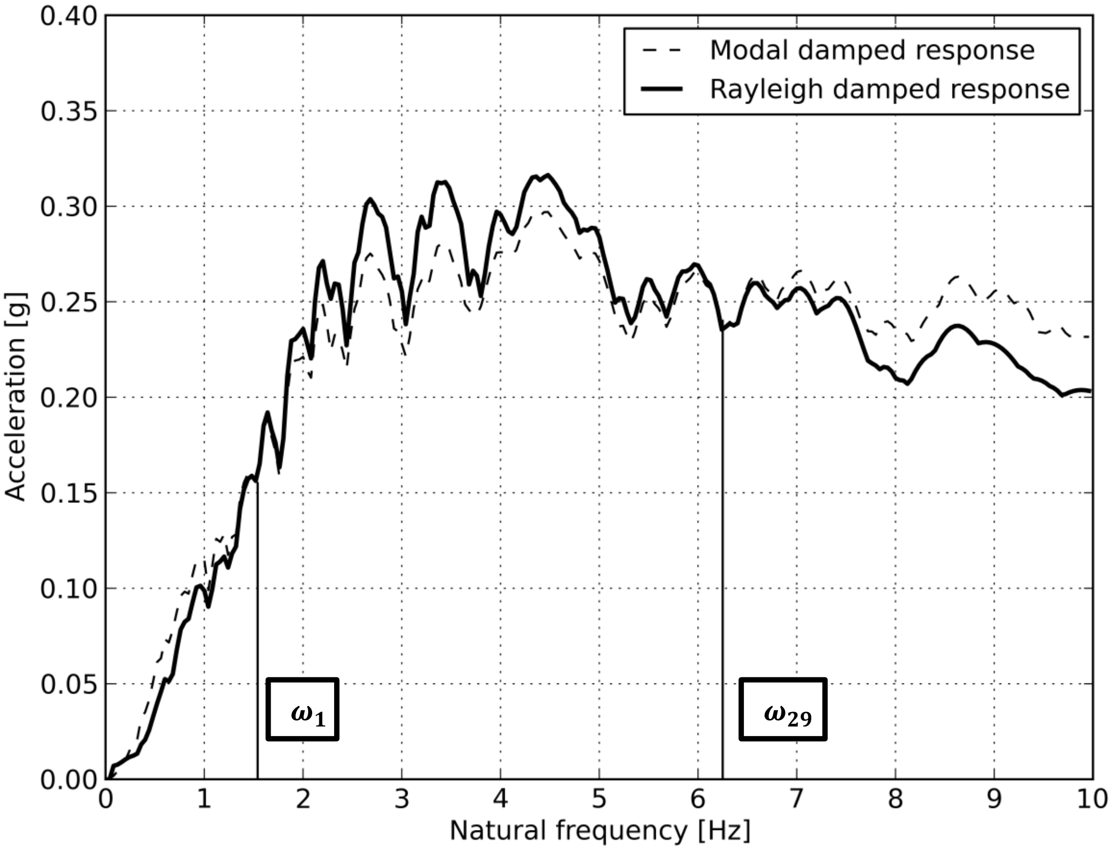

Figure 6-28: Response spectra for the acceleration-time history in x-direction for modal and modified Rayleigh damping

Figure 6-28 shows the response spectra for the modal and modified Rayleigh damped system. It also indicates what Figure 6-30 depicts, which is lower damping between the natural frequencies ω_1 and ω_{29} and therefore a higher acceleration response than for modal damping. For frequencies above ω_{29} the system experiences higher damping, hence lower acceleration response.

Figure 6-29 shows the impact of the reservoir filling level on the natural frequencies for the first 10 modes. A lower reservoir level therefore yields higher frequencies, which is based on the fact that the mass of the overall system is reduced. Corresponding mode shapes for mode one to four can be found in Section 5.2.3.1.

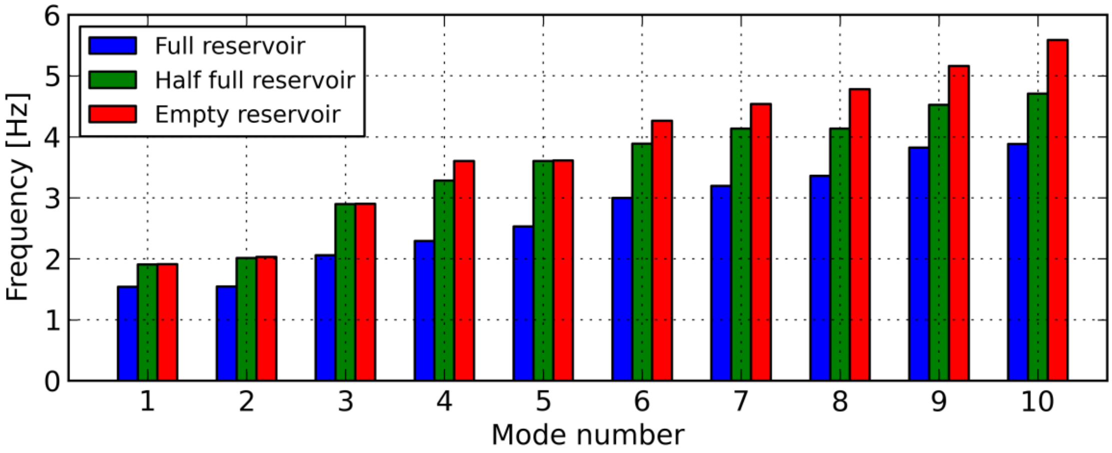

Figure 6-29: First 10 natural frequencies of the three reservoir filling levels

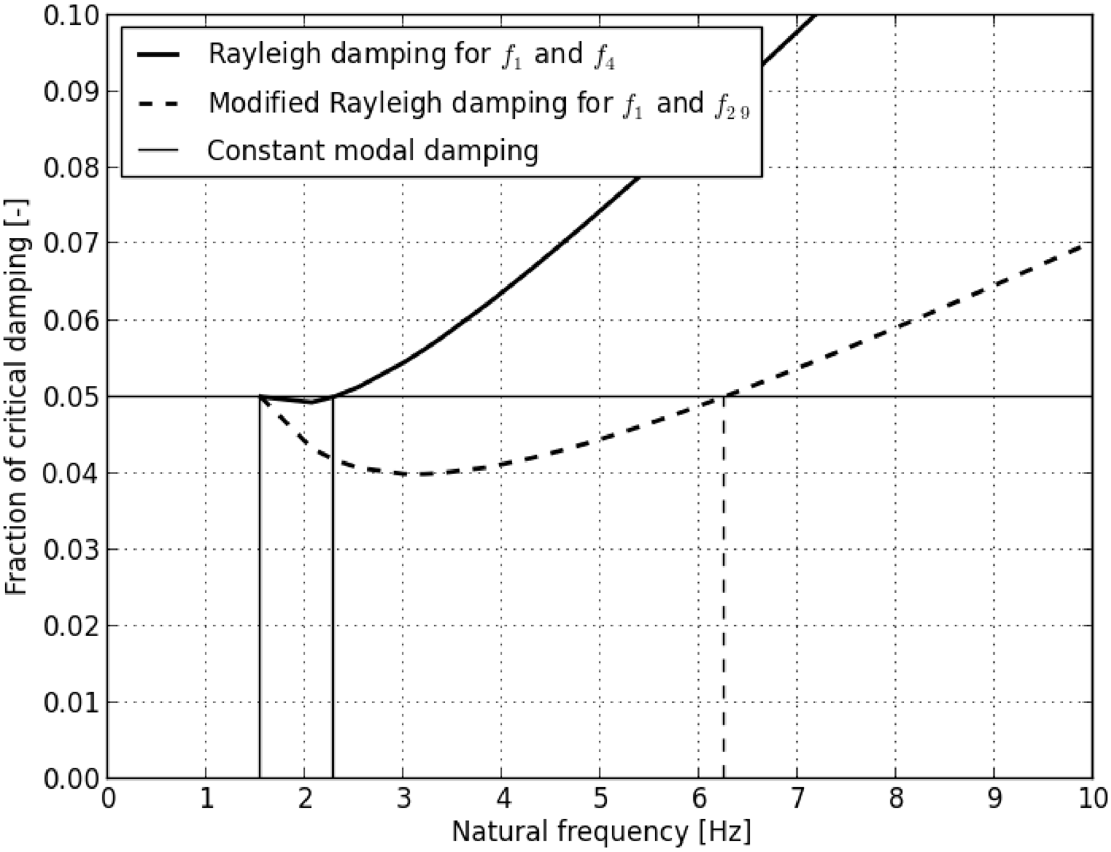

Figure 6-30: Rayleigh damping curves for the seismic simulations of the linear and nonlinear arch dam model for full reservoir conditions

Figure 6-30 states that if the 1st and 4th mode are used the frequency range in between them is damped with approx. 5% of the critical damping. All higher modes have significantly higher damping ratios and are dominated by the stiffness-proportional factor. On the other hand, the modified Rayleigh damping factors are calculated based on the equilibrium of the effective mass times the difference in response acceleration between the modal and Rayleigh damped systems. This approach leads to lower critical damping factors between the 1st and 29th mode, down to 4% and increased damping for higher modes.

The differences in damping factors and corresponding frequencies between the half full and empty reservoir case are marginal and figures of the damping curves for the half full and empty reservoir case are not explicitly plotted.

The problems with Rayleigh damping in nonlinear simulations, published by Hall (2006) and mentioned in Section 2.3.3, by using the initial stiffness matrix are not crucial in this problem, because Dassault Systèmes (2013) in the Abaqus 6.13-EF Documentation states that the (elastic) stiffness at the current state (time) is used for calculating the stiffness-proportional damping stresses.

6.9 Results of the Nonlinear Seismic Simulations

In this section different simulations with different models are compared. Besides the comparison between the linear and nonlinear models, the effects of different reservoir filling levels are investigated. Furthermore, the crack propagation with the XFEM method is examined for increased accelerations. Specific result evaluations of minimum-maximum stresses and displacements are only done for the main section of the arch dam. Furthermore, contact openings are investigated in the abutment of the dam.

Following nonlinearities are taken into account in the seismic simulations:

- Contact between the dam and the foundation
- Contact between the blocks
- Nonlinear material in the compressive state according to Section 6.5.1
- Nonlinear material in the tensile state with XFEM according to Section 6.5.2

For all simulations, except for the nonlinear material simulations with XFEM, the model from Section 6.7 with the geostatic procedure is used. XFEM simulations in combination with a geostatic step definition is not yet supported by Abaqus, which is why the dead weight simulation is performed by a general static step where displacements from the gravity are retained.

6.9.1 Comparison with Linear Simulations from the Benchmark Workshop

In this section the results from the completely linear-isotropic model without any contact modelling from the benchmark workshop (reference solution) is compared with the nonlinear model.

Following diagrams show three lines for each model, the minimum (left line) and the maximum line (right line), which indicate the minimum and maximum values out of the time history records and the line for static loading (middle line). This middle line indicates the static value out of the sum of the two load cases, gravity and hydrostatic water load. To retain the overview in the diagrams, the minimum, maximum and static values are not explicitly mentioned in the legend.

6.9.1.1 *Comparison of the Displacement*

The displacements show a slight increase compared to the linear model. The displacements for static loading are increased by approx. 1.0 centimetre to the results from the benchmark workshop from Section 5.1.5.2. This fact is attributable to the discrete block modelling. The base displacement for both models is approx. 1.0 centimetre.

The increase in displacement (minimum-maximum) due to the seismic loading between the two models is nearly the same.

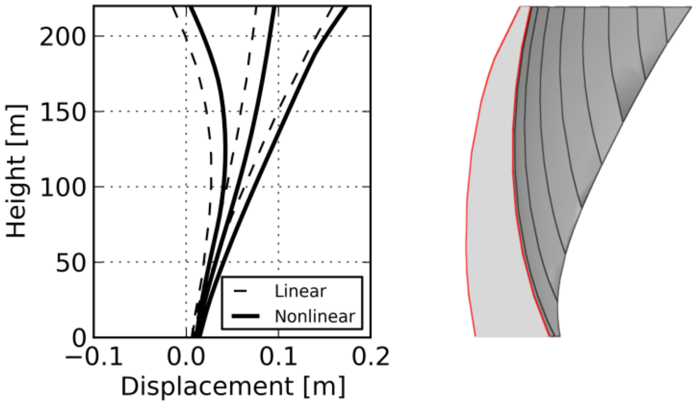

Figure 6-31: Comparison of the displacement in the main section between the linear and nonlinear model

6.9.1.2 *Comparison of the Hoop Stresses*

In contrast to the displacements the hoop stresses in the main section are decreased for the upstream surface. The static stresses are almost the same. The minimum hoop stresses are decreased from -11.5 MPa to -10.0 MPa at H = 175.0 m. The maximum values on the upstream surface occur at the base, with smaller differences between both models. (Figure 6-32)

On the downstream surface in the main section the structure shows higher stresses due to the nonlinearities. The stresses at the bottom are decreased from 0.0 MPa to -1.0 MPa, whereas the stresses on top are differing more. The minimum hoop stress on the top is changed from -5.5 MPa to -7.0 MPa. (Figure 6-32)

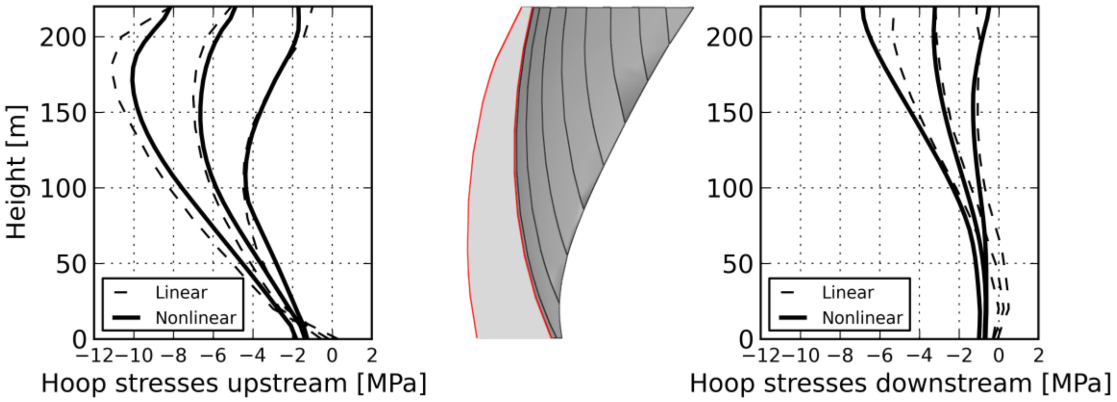

Figure 6-32: Comparison of the hoop stresses on the upstream (left) and downstream (right) side of the arch dam in the main section between the linear and nonlinear model

6.9.1.3 Comparison of the Vertical Stresses

The vertical stresses on the upstream surface are similar for both models, except near the base. The linear model allows for tensile stresses, whereas the nonlinear model, due to the contact discretization, does not. Therefore, the maximum vertical stresses between the models are reduced from 4.0 MPa to 0.0 MPa on the upstream surface (Figure 6-33). Zero stress in this case implies that a crack at the upstream heel is fully developed. This fact can be abstracted from the results of the linear model, where the maximum tensile stress of approx. 2.0 MPa of concrete is exceeded by 100% (4.0 MPa).

On the downstream surface almost a constant increase of compressive stress is noticeable with maximum values at the base of -6.0 MPa (linear and nonlinear). The maximum tensile stress occurs at a height of 170 meters for both models of about 1.0 to 1.5 MPa.

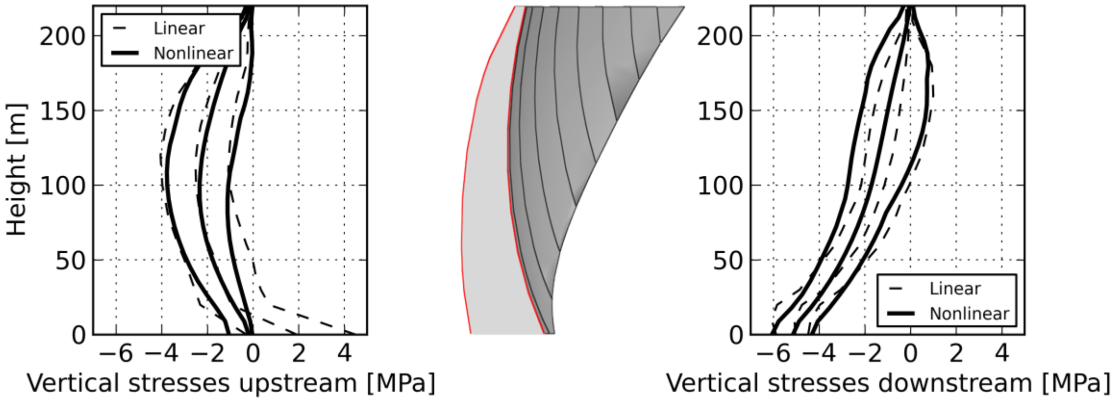

Figure 6-33: Comparison of the vertical stresses on the upstream (left) and downstream (right) side of the arch dam in the main section between the linear and nonlinear model

6.9.2 Influences of Different Reservoir Filling Levels

In this section the effects on the stresses, displacements and contact opening of three different reservoir filling levels are compared.

Following diagrams show three lines for each model, the minimum (left line) and the maximum line (right line), which indicate the minimum and maximum values out of the time history records and the line for static loading (middle line). This middle line indicates the static value out of the sum of the two load cases, gravity and hydrostatic water load. To retain the overview in the diagrams, the minimum, maximum and static values are not explicitly mentioned in the legend.

6.9.2.1 Comparison of the Displacement

Figure 6-34 shows the displacements for the three reservoir levels. For the empty case the minimum displacements of -0.10 meters indicate that the dam tends to bend backwards due to the seismic loading. For the half full case the minimum and maximum displacements are -0.08 meters and 0.03 meters respectively. Generally speaking, the full reservoir case yields much higher and only positive (in downstream direction) displacements compared to the empty and half-filled ones. This behaviour can also be observed in Figure 6-35.

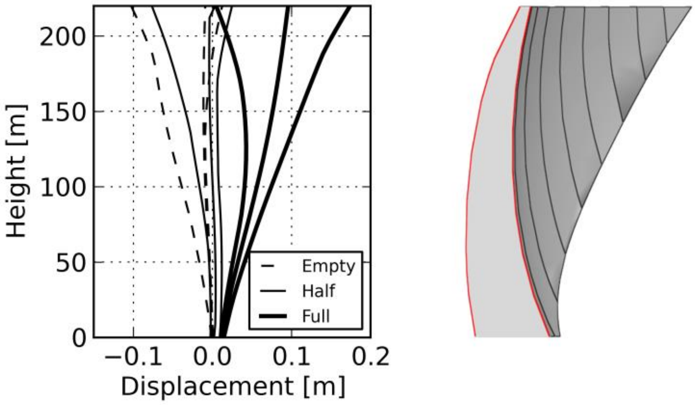

Figure 6-34: Comparison of the displacement in the main section between different reservoir filling levels

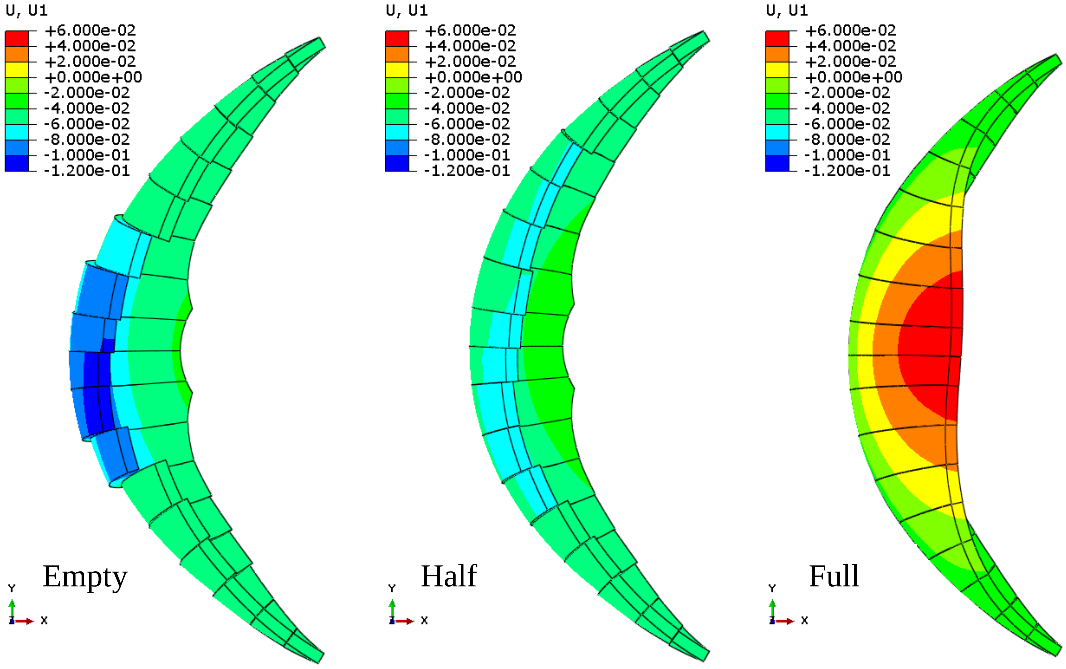

Figure 6-35: Comparison of the displacement [m] in downstream direction between different reservoir filling levels at the end of the seismic event T_{20} = 20.0 sec (scaled 500 times)

6.9.2.2 *Comparison of the Hoop Stresses*

Figure 6-36 immediately depicts that an increase of the reservoir depth from a half-filled to a fully-filled one totally changes the systems behaviour regarding the stresses despite of the up- or downstream surface. On the other hand, the differences between the empty and half case are small. These huge differences for filling levels between a full and half-full reservoir have also been observed by Chopra and Gupta (1982) by performing analysis in the frequency domain of a gravity dam. Later, in 2007, Sarkar, Paul and Stempniewski (2007) found the same behaviour in time domain analyses and concluded that a filling level below 70% has no significant impact on the dynamic response.

For the empty reservoir case the maximum hoop stresses on the upstream surface reduce to zero for heights between 50 meters and 220 meters (blocks are opening – no tensile stresses or cohesion is accounted for). The minimum hoop stresses at the crest are increased to -3.0 MPa. A similar behaviour can be observed for the half full reservoir, which reduces to zero up from a height of approx. 100 meters. The minimum value at the crest is -3.5 MPa.

On the downstream surface the biggest differences between the empty and half-filled reservoir are located at the crest. The minimum and maximum stresses at the base up to a height of 70 meters stay the same, which is approx. -1.0 MPa.

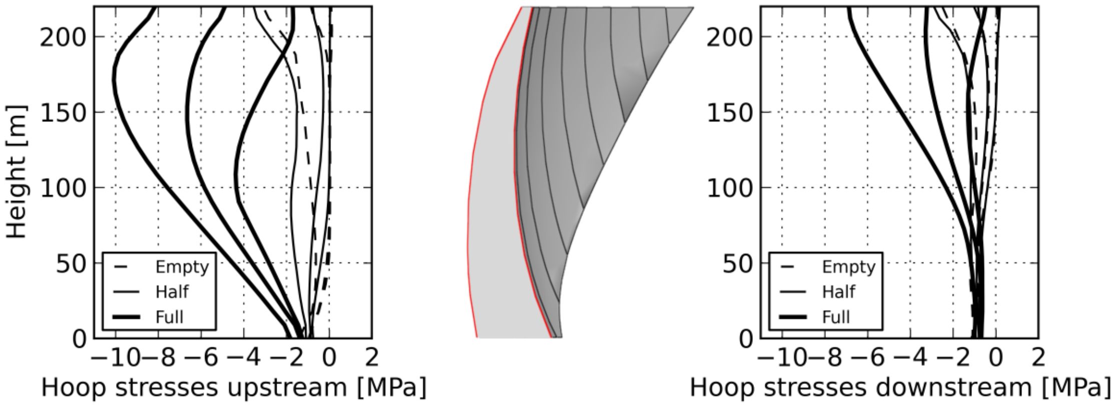

Figure 6-36: Comparison of the hoop stresses on the upstream (left) and downstream (right) side of the arch dam in the main section between different reservoir filling levels

6.9.2.3 *Comparison of the Vertical Stresses*

The same behaviour as for the hoop stresses between a half and fully-filled reservoir can be observed for the vertical stresses in Figure 6-37. The stress distribution changes completely, whereas the empty and half cases are almost identical once again. Qualitatively the full reservoir stresses on the upstream surface behave similar to the stresses on the downstream surface for the empty and half case and vice versa. This indicates a bending to the downstream direction for a full reservoir and in the upstream direction for a half-filled and empty reservoir.

On the upstream surface the minimum vertical compressive stress at the base is reduced from -9.0 MPa to -6.0 MPa, for the empty and half-filled case, respectively. The maximum stresses occur at a height of 150 meters with positive (tensile) values around 1.0 to 1.5 MPa.

On the downstream surface the minimum vertical stresses are lower than for the full reservoir case, because of the bending behaviour to the upstream direction. They are reduced to -3.5 MPa for both cases (half full and empty) at a height of approx. 120 meters. The maximum values result in tensile stresses of 0.5 to 1.0 MPa at heights of 25 meters and 150 meters. The minimum vertical stress at the base decrease from -6.0 (full) to -3.0 MPa and -1.5 MPa, for the empty and half-filled case, respectively

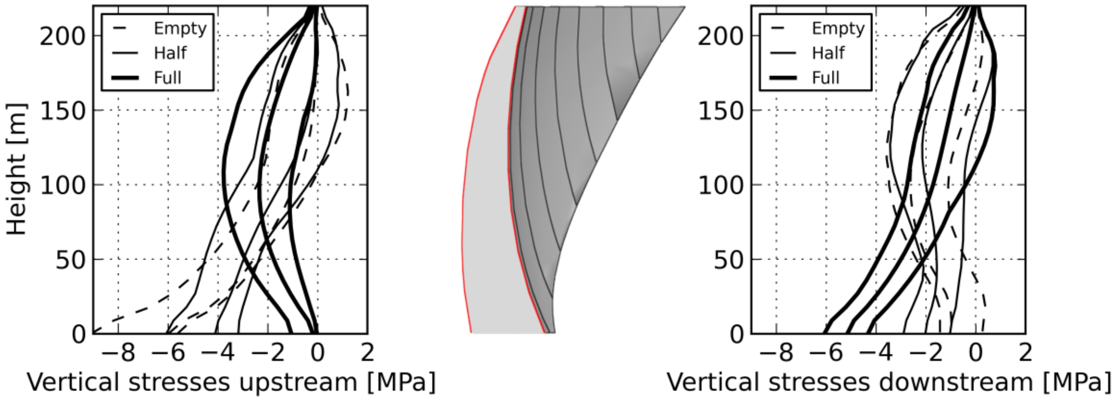

Figure 6-37: Comparison of the vertical stresses on the upstream (left) and downstream (right) side of the arch dam in the main section between different reservoir filling levels

6.9.2.4 *Comparison of the Contact Opening in the Base*

The results of the base opening in Figure 6-38 confirm the behaviour observed in the vertical stress evaluation. In the empty and half reservoir case the arch dam tends to bend or lean back (upstream). Possible effects of penetrating water into the upstream opening are not accounted for.

The maximum contact opening out of the seismic simulation along the path in the main section for the full reservoir case is 0.007 meters at the upstream heel and reduces to zero till a base depth of approx. 27.0 meters. In contrast, the opening of the empty case appears on the downstream heel with a maximum of 0.0015 meters, whereby no opening for the half-full reservoir is observed (line not visible in Figure 6-38). Comparing these results with the openings from the hydrostatic loading from Figure 6-19 shows that for the full reservoir case the opening due to the seismic excitation increases by more than 100% from 0.003 meters to 0.0075 meters. The length of the opening is not increased.

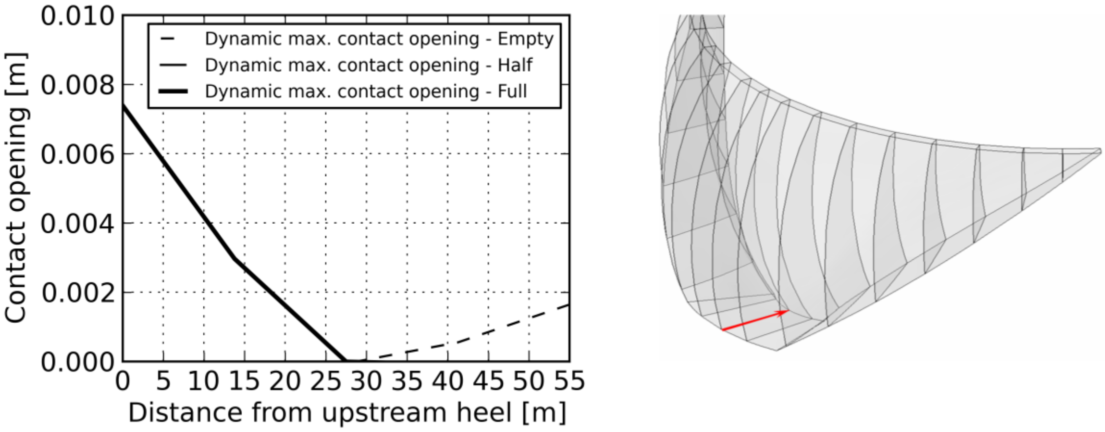

Figure 6-38: Comparison of the contact opening between different reservoir filling levels along the path in the main section

6.9.2.5 Comparison of the Contact Behaviour between Blocks

Figure 6-39 compares the maximum contact openings over all dynamic frames in the main section for different reservoir filling levels. The left one shows the opening if the reservoir is empty and therefore the dam tends to bend to the upstream side. This case also indicates the largest opening with 0.004 meters. It is worth mentioning that between the blocks no tensile resistance is accounted for. Hence, this evaluation reflects a post-cracked state. However, the half-full case shows openings of approx. 0.002 meters in the upper part. The full reservoir yields no contact opening during the whole seismic event. The black pattern in the main section indicates negative values, which are resulting out of the soft contact formulation.

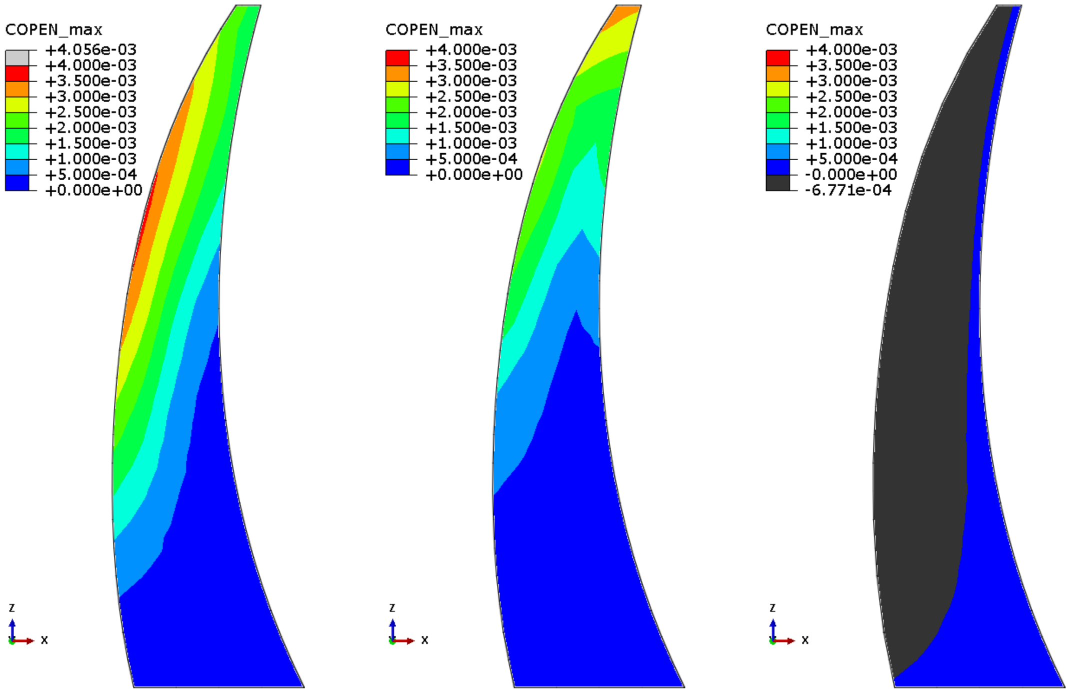
COPEN_max
+4.056e-03
+4.000e-03
+3.500e-03
+3.000e-03
+2.500e-03
+2.000e-03
+1.500e-03
+1.000e-03
+5.000e-04
+0.000e+00
z
x
COPEN_max
+4.000e-03
+3.500e-03
+3.000e-03
+2.500e-03
+2.000e-03
+1.500e-03
+1.000e-03
+5.000e-04
+0.000e+00
z
x
COPEN_max
+4.000e-03
+3.500e-03
+3.000e-03
+2.500e-03
+2.000e-03
+1.500e-03
+1.000e-03
+5.000e-04
-0.000e+00
-6.771e-04
z
x

Figure 6-39: Maximum contact opening [m] over all frames for a maximum acceleration of 1.0 m/s² in the main section for an empty (left), half (middle) and full reservoir (right)

Figure 6-40 compares the maximum contact slip (relative displacement) in downstream direction over all dynamic frames in the main section for different reservoir filling levels. The left one shows the slip if the reservoir is empty and therefore results in a relative displacement between the blocks of 0.015 meters. The half-full case yields the highest value of 0.03 meters. However, no relative displacement of the blocks for the full reservoir can be observed. The slip between the blocks is also visible in Figure 6-35. It is important to say that these evaluations are only done for the main section, therefore larger slips might occur in other section.

Out of Figure 6-39 and Figure 6-40 it can be concluded, that for simulations of a full reservoir case the discrete block modelling can be neglected, because openings and relative displacements won't develop due to the high contact pressure for an even low friction coefficient of 0.5. Nevertheless, this behaviour is also influenced by the peak ground acceleration, which is only 1.0 m/s² in this case. Section 6.9.3 shows the effects of an increased acceleration of 3.0 m/s² and two different friction coefficients.

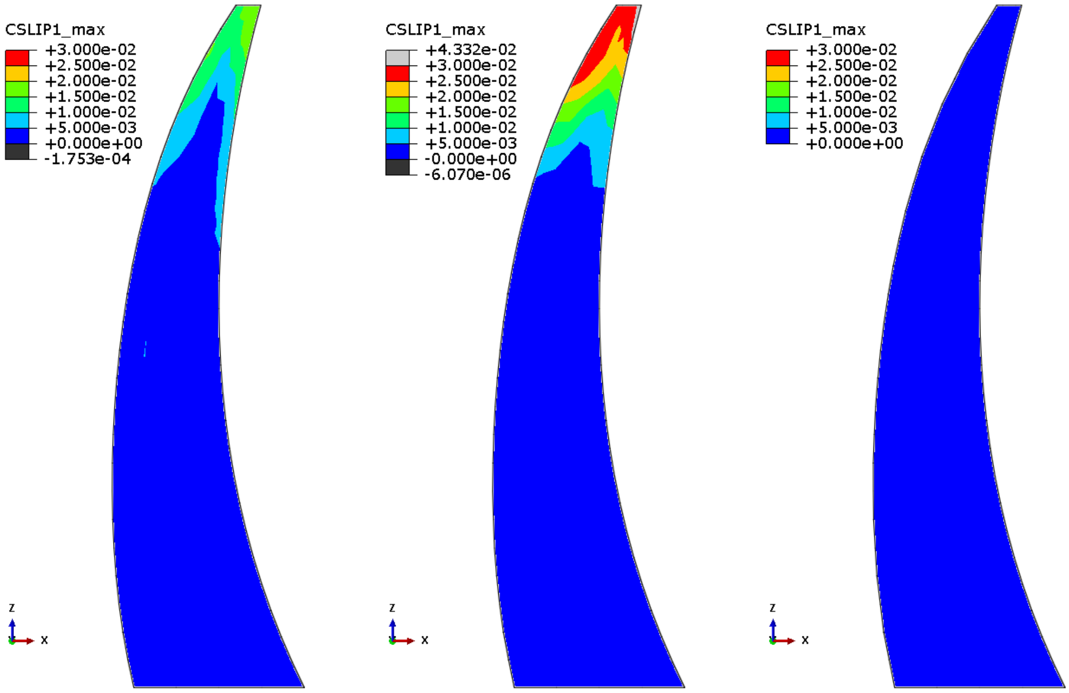

Figure 6-40: Maximum contact slip [m] in downstream direction over all frames for a maximum acceleration of 1.0 m/s² in the main section for an empty (left), half (middle) and full reservoir (right)

6.9.3 Contact Behaviour between the Blocks for increased Seismic Accelerations and different Friction Coefficients

As depicted in Figure 6-39 and Figure 6-40 the full reservoir case doesn't lead to openings or slips in the main section for a maximum acceleration of 1.0 m/s². For that reason the acceleration is increased to a maximum of 3.0 m/s² to evaluate the contact behaviour between the blocks more elaborate for a completely impounded reservoir. The major interest in this investigation is the interaction between the opening, relative displacement and corresponding contact pressure. Therefore, for these simulations the contact at the base is tied. For the contact between the blocks, two different configurations in tangential direction are examined:

- Friction coefficient of 0.5 from Section 6.3
- Increased friction coefficient of 2.0

In the case of a friction coefficient of 0.5 (26.6°) the concrete to concrete contacts are relatively smooth and conservative regarding their relative movement. However, the increased friction coefficient of 2.0 (63.4°) should account for the shear keys in the block joints (Section 6.1.5), which are installed to lock the relative displacement of the blocks. The expected behaviour is such that no slip should occur as long as the surfaces are in contact (off-shearing of the shear keys is not reckoned with). Hence, relative movement is only allowed if the contact pressure drops to zero and the joint opens.

For both friction coefficients the behaviour is evaluated for one node at the crest in the main section. The location of the node is depicted in Figure 6-41.

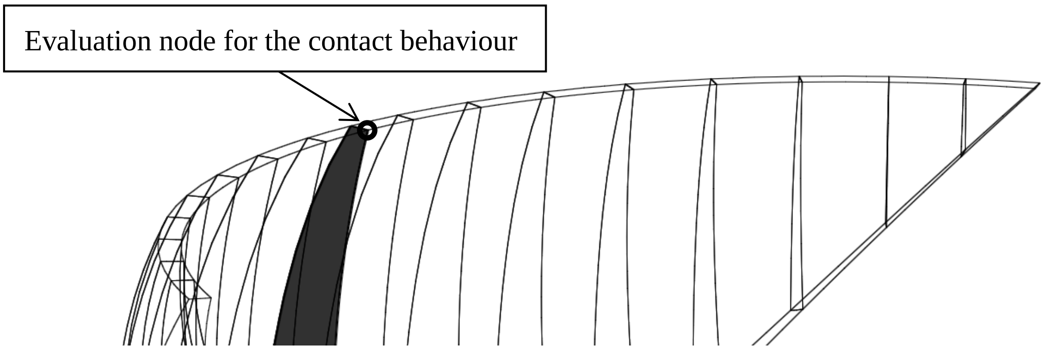

Figure 6-41: Location of the node for the evaluation of contact behaviour

6.9.3.1 Contact Behaviour for a Friction Coefficient of 0.5

Figure 6-42 shows the contact opening, contact pressure and relative displacement at the evaluated node from Figure 6-41 between the 5th and the 10th second of the seismic excitation for a friction coefficient of 0.5. As expected, if the contact opens the pressure drops to zero. In this case mostly a relative displacement in the joint occurs. This can be observed at T = 5.0 s, where the contact opens (pressure zero) and a negative relative slip from 0.005 meters to -0.03 meters appears. Such a large displacement isn't necessarily happening any time the pressure reduces to zero, as can be seen between 8.5 and 9.2 seconds. Nevertheless, the friction coefficient of 0.5 used in these simulations also results in relative displacements if the contact pressure is present, but only in small amounts.

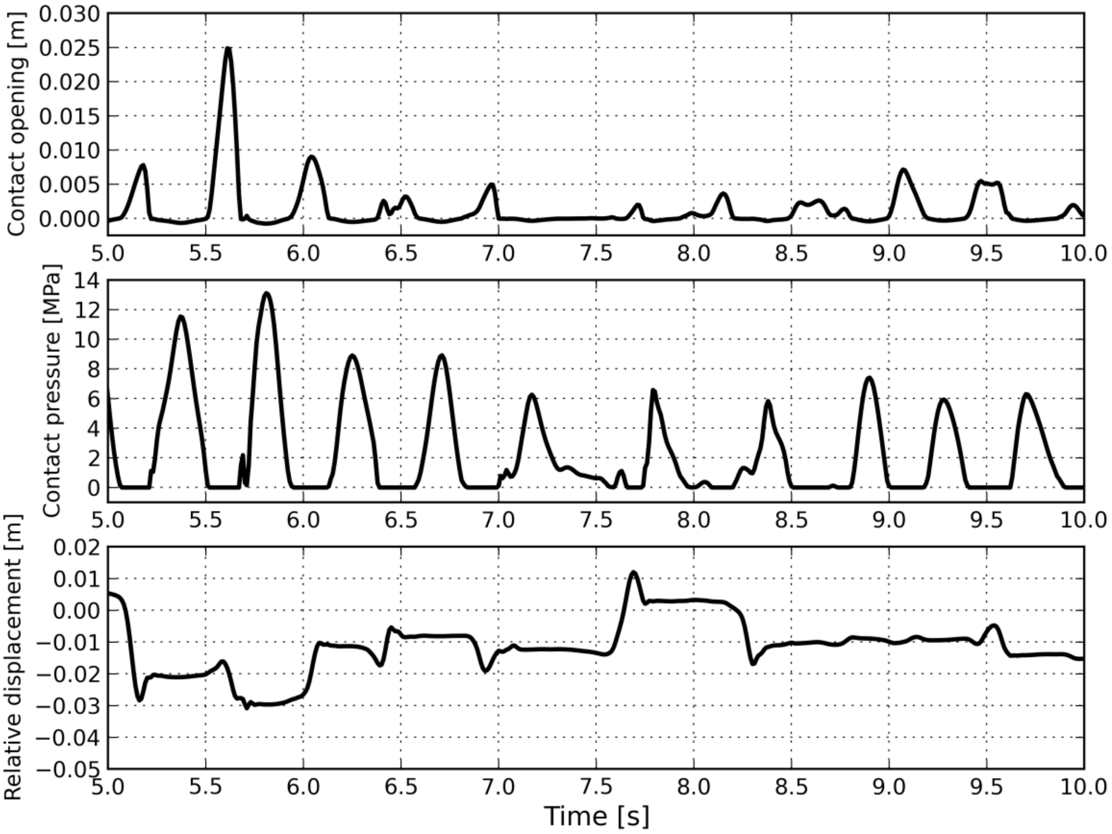

Figure 6-42: Comparison of the contact behaviour between two blocks at the crest for a friction coefficient of 0.5 (5.0 sec < T < 10.0 sec)

6.9.3.2 Contact Behaviour for a Friction Coefficient of 2.0

Figure 6-43 shows the contact opening, contact pressure and relative displacement at the evaluated node from Figure 6-41 between the 5th and the 10th second of the seismic excitation for a friction coefficient of 2.0. As in the diagram in the section before, if the pressure drops to zero, the contact opens. Overall almost the same behaviour as in Figure 6-42 where a friction coefficient of 0.5 is used can be observed. The time histories of the contact opening and pressure are almost identical for both coefficients. However, the relative displacement changed. Qualitatively it’s almost the same, but the amount of displacement increased. This can be attributed to the larger energy stored and released at the moment when the contact opens for a friction coefficient of 2.0, compared to 0.5, where the frictional contact is “softer”. Furthermore, as intended with the increased coefficient, if the blocks are in contact zero relative displacement is observed.

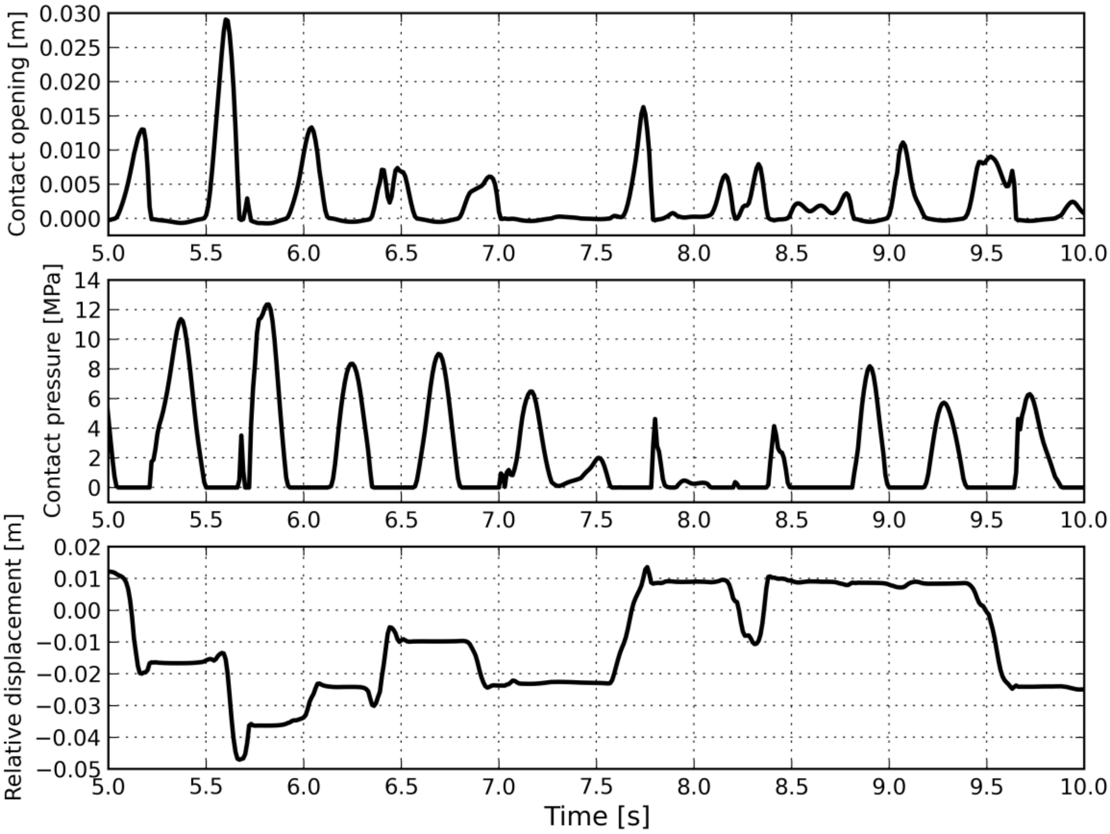

Figure 6-43: Comparison of the contact behaviour between two blocks at the crest for a friction coefficient of 2.0 (5.0 sec < T < 10.0 sec)

Lotfi and Espandar (2002) and Arabshahi and Lotfi (2009) did similar investigations on a thin double-curved arch dam with a height of 130 meters and maximum accelerations up to 0.6g in horizontal direction and 0.4g in vertical direction. They applied the following three different sliding models to the contraction joints:

- Opening without sliding
- Simplified sliding model, which reduces the stiffness to zero if the tensile and shear strength is reached
- Opening with sliding based on Mohr-Coulomb, which takes also cohesion into account

Among these models they also varied the friction coefficient, cohesion, tensile strength and Young’s modulus ratios between the foundation and the dam for contraction, perimeter and horizontal lift joints. Overall 11 different models were evaluated. They found that simplified models are not suitable due to the fact that they only allow sliding if the joints fully open and hence cannot capture the critical response of the dam. In comparison to the results from Figure 6-42 and Figure 6-43 they concluded that the friction coefficient is the most influential factor for the sliding. However, the differences of relative displacement for a coefficient of 0.5 and 2.0 weren’t as large as one would expect in the simulations in this section. This might be attributable to the geometry and the higher acceleration used by Arabshahi and Lotfi (2009). Further investigation on this topic regarding shear keys and their seismic behaviour is recommended.

6.9.4 Nonlinear Material and Crack Propagation with XFEM

Figure 6-44 depicts the maximum principal stresses (maximum tensile stress) for the accelerations from Figure 5-5 with $a_{max} = 1.0\ m/s^2 (\approx 0.1g)$ over all frames. It indicates that the allowed tensile stress of 2.2 MPa isn't exceeded through the earthquake duration. Hence, no cracks start to develop up- or downstream for this acceleration. The maximum occurring tensile stress is 1.5 MPa.

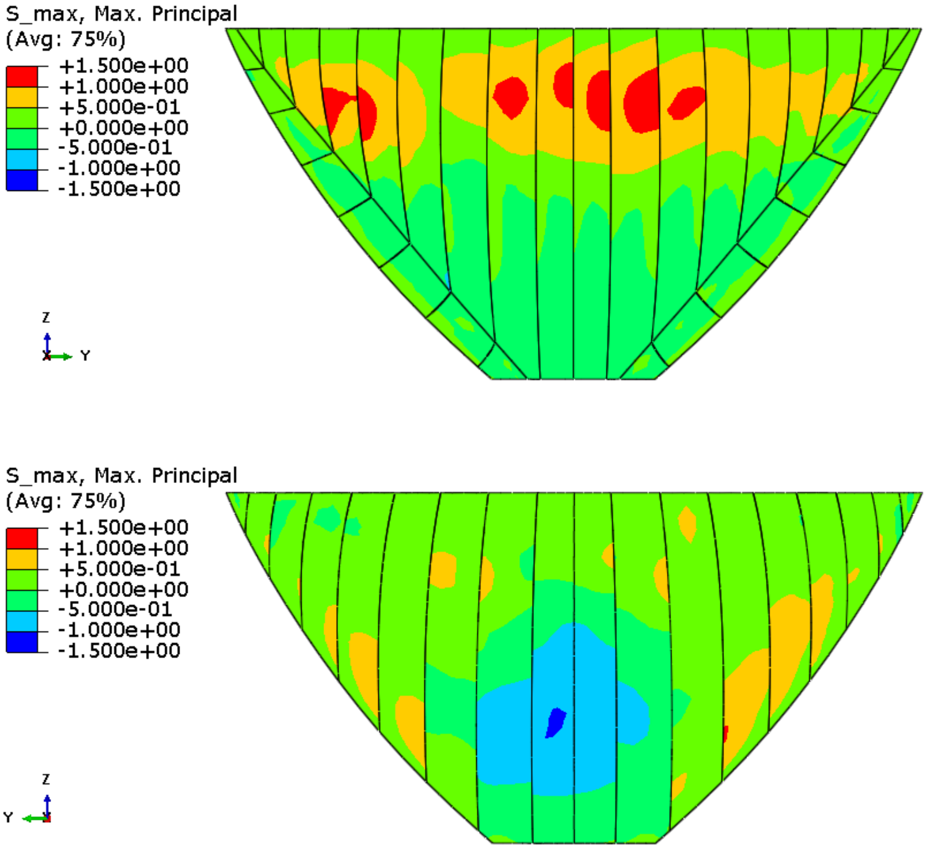

Figure 6-44: Maximum principal stresses [MPa] over all frames for a maximum acceleration of 1.0 m/s² on the downstream and upstream surface

6.9.4.1 Crack Propagation for a Maximum Acceleration of 2.0 m/s²

The effects of the two times scaled acceleration-time history on the structure are depicted in Figure 6-45. An increased acceleration of $a_{max} = 2.0\ m/s^2 (\approx 0.2g)$ already let to 1 small crack after 5 seconds in one block near the mid. Much more cracks appear between 5 and 10 seconds, where the STATUSXFEM variable of less than 1.0 indicates that these elements are just partially cracked. After 15 seconds some elements fully cracked, whereby no further crack propagation is observed in the structure until the end of the simulation at 20 seconds. It can be pointed out that cracks started to appear downstream mostly at a height between 170 and 190 meters. All of them are occurring almost only on the surface and are not propagating much deeper into the structure (Figure 6-46). It is also worth mentioning that the cracks are dependent on the mesh density, because even though elements are allowed to crack the directions cannot change in one element.

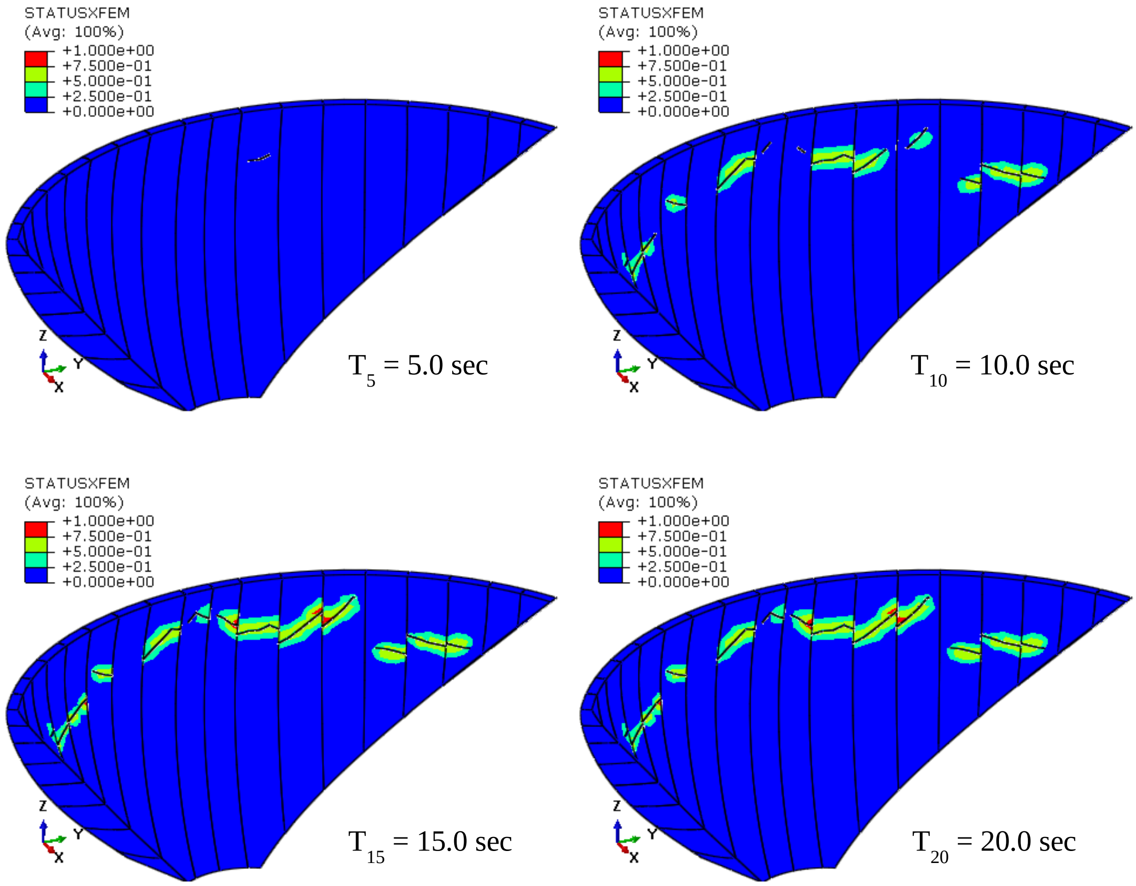

Figure 6-45: Status of XFEM cracks at specific time instants for a maximum acceleration of 2.0 m/s²

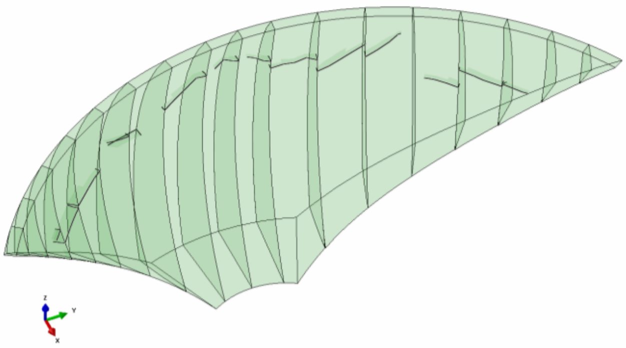

Figure 6-46: Translucent arch dam with XFEM cracks after the earthquake (T=20 seconds) for a maximum acceleration of 2.0 m/s²

Due to the fact that the program algorithm is restricted to only one crack per region more cracks must have occurred on the downstream and also on the upstream surface in each block, because the maximum tensile stress of 2.2 MPa is exceeded in some locations.

6.9.4.2 Crack Propagation in only One Block for Higher Accelerations

Figure 6-46 shows that even acceleration with a maximum 2.0 m/s² leads to cracks in the dam. Nevertheless, they are rather small and only occurring on the surface and are not propagating far into the structure. Additional simulations with higher accelerations are performed for only one block in the middle of the dam to be allowed to develop cracks, because otherwise achieving convergence is unlikely. Figure 6-47 depicts the block of the dam (indicated in black) which is allowed to crack in the simulation with the increased accelerations of 3.0 m/s², 4.0 m/s² and 5.0 m/s². The rest of the model with all contact discretisation's from previous simulations in this section are kept the same.

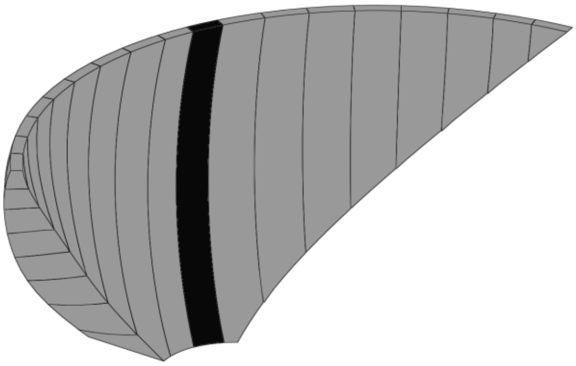

Figure 6-47: Arch dam block (black) which is allowed to crack during simulations with increased accelerations

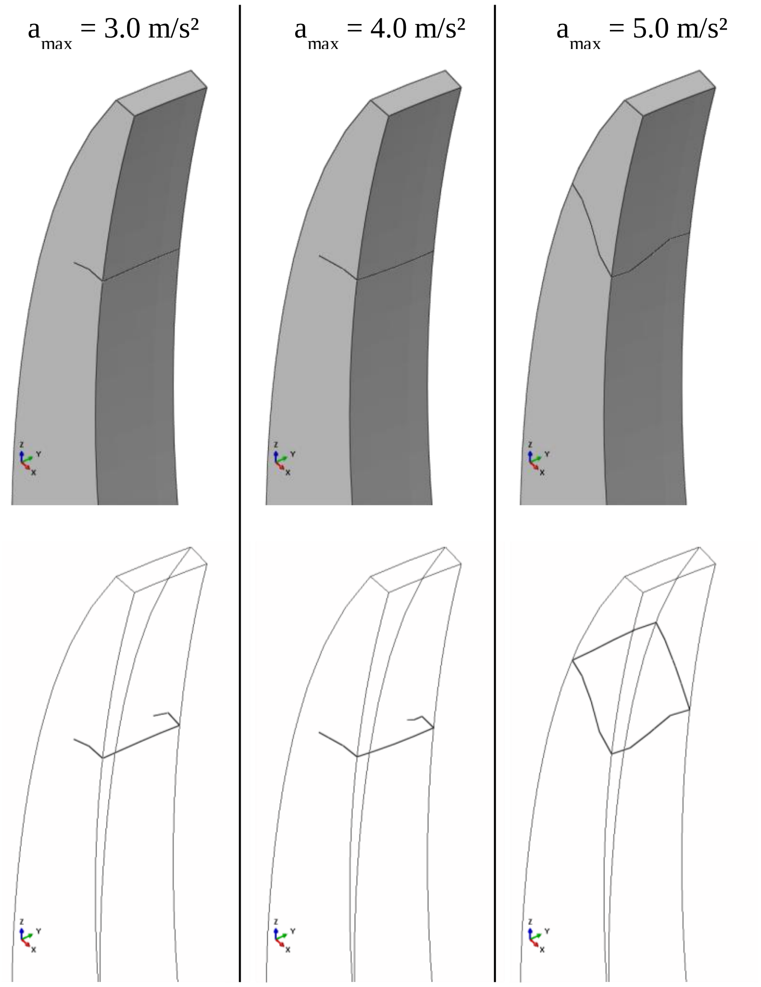

a_{max} = 3.0 m/s² a_{max} = 4.0 m/s² a_{max} = 5.0 m/s²

a) b) c)

Figure 6-48: Crack propagation in the observed block for maximum accelerations of a) 3.0 m/s², b) 4.0 m/s² and c) 5.0 m/s²

Not much difference in the crack propagation in one block and accelerations of 3.0 m/s² and 4.0 m/s² is observed in Figure 6-48. Only a slightly deeper crack is visible after the simulation at 20 seconds. However, the block doesn't fully crack due to this magnitude. On the other hand, an acceleration of 5.0 m/s² let to a crack initiation on the upstream surface, which propagated through the whole block to downstream side already after 9.0 seconds of the seismic excitation. Out of the crack direction from Figure 6-48c it's clear that the block should fall to the downstream side of the dam, but this is in general not a possible failure mechanism because the block joints are radially orientate so slipping in stream direction is locked. Therefore, no block fall occurred during simulation (water pressure in the crack isn't accounted for). It should be pointed out that for such a high acceleration major nonlinearities regarding cracks in other regions would appear which are not accounted for in this model. Nevertheless, detailed simulations of one block allow for predictions regarding the crack initialization and possible directions of the cracked surface.

6.10 Conclusion of the Nonlinear Seismic Simulations

Comparisons between the linear and nonlinear simulations show slightly increased displacements because of the contact formulation at the base, discrete block modelling and shear forces which are mobilized due to the frictional behaviour. The compressive hoop stress evaluation in the main section revealed that on the upstream surface they are slightly reduced and on the downstream surface increased by the nonlinear effects. The tensile stresses on the downstream surface near the base changed to compressive stresses due to the possibility of contact opening between the blocks. A similar behaviour of the system is observed for the vertical stresses, where tensile stresses near the base are almost zero because of the base joint opening.

Evaluations of different reservoir filling levels show that a half full or empty reservoir is influencing the global behaviour of the dam significantly. The hoop and vertical stress distribution changes completely in the main section due to lowering of the reservoir level. The hoop stresses obtained from a half or less-filled reservoir are not sufficient to mobilize the arching effect for heights above 100 meters and 150 meters on the up- and downstream surface, respectively. On the other hand the vertical stresses, especially at the base, are increased due to the dominating dead weight compared to the reduced water pressure.

The maximum opening at the base occurs in the main section. For full reservoir conditions the base opens only on the upstream heel and is increased by seismic effects approx. two times compared to the static results. A half-full reservoir leads to zero opening along the whole contact path, whereas an empty reservoir leads instead to openings on the downstream surface.

The nonlinear material simulations with the XFEM only allow for a qualitative evaluation of the results because of the limitation of one crack per region in the algorithm. For the studied arch dam, the cracks start to initiate downstream for a maximum acceleration of 2.0 m/s² in 2/3 of the total height of the structure for full reservoir conditions. More cracks (crack patterns) must have been occurred due to the exceedance of the tensile strength on the up-and downstream surface. Nevertheless, the knowledge of the location of crack initialization may serve as indicator for possible safety measures, like using high performance concrete in these areas or changing the shape of the structure if it's still in the design phase. Simulations of the crack propagation in one block and higher accelerations of 3.0 m/s², 4.0 m/s² and 5.0 m/s² show that such detailed investigations need simplifications because otherwise reaching convergence is unlikely. On the other hand they allow for predictions regarding the crack initialization and possible directions of the cracked surface.

It is also worth mentioning that during the modelling and simulation with XFEM convergence problems occurred. It turned out that they arose from the mesh density. A refinement along the width of the crest solved this problem. Therefore, it can be stated that the crack propagation (one crack direction per element) and convergence is affected by the mesh topology/density.

As in Chapter 4 here also the negligence of the cohesion in the simulations leads to conservative results regarding openings (zero tensile strength) and relative displacements in the base and between the blocks.

7 CONCLUSION

The focus of this thesis is to show the applicability and limits of nonlinear modelling and simulations of concrete dams at seismic loading. A profound numerical and theoretical knowledge is not sufficient to model such problems. Structural engineers have also to know how concrete dam structures are built, maintained and where problems might occur. Due to the fact that dams are mostly situated in mountainous regions to serve for energy production they are vulnerable to earthquakes. In this case seismic simulations are performed to evaluate and ensure the structural integrity. They are mostly done for linear behaviour of the structure. Nonlinear simulations and models have the disadvantage that for dynamic simulations direct time integration methods have to be used, which have an increased computation time because of the time histories with generally small time steps. Additionally, the computational effort is raised by the nonlinearities, like contacts or material, applied to the model itself.

Apart from the nonlinearities of the model in dynamic simulations the interaction of the dam with the reservoir is an important part. In general, two different possibilities are available, first, the use of an added mass approach and second, direct modelling of the volume with balance equations of the fluid. In this work two of the mostly used possibilities to calculate the interacting water as an added mass are discussed, which are the one by Westergaard (1933) and Zangar et al. (1952). Both made specific simplifications to derive the mass distribution in the depth of the reservoir. Zangar's approach is also applicable to inclined surfaces, but with the drawback that the maximum mass is always at the bottom. His physical model tests and numerical investigations in this study have shown that the maximum pressure moves upwards as the inclination changes. Based on this fact and the use of numerical simulations a new empirical added mass distribution is developed, which accounts for this problem up to a dip of the interacting surface of 30 degrees. The same equation is also applied to seismic simulations of an arch dam and proves the applicability as it shows almost the same results as Zangar's approach. In contrast to added mass approaches a more sophisticated way to simulate the dynamic interaction is to directly model the reservoir based on the acoustic fluid equation. This allows for taking into account compressibility effects, as well as reflections on the reservoir borders, which might have a big influence on the response of the dam. Despite of the convenient implementation, faster computation time and mostly conservative results with added mass approaches, an acoustic fluid volume describes the behaviour of the excited water always more accurately as long as the right boundary conditions are used.

Among the effects of interaction modelling on the seismic displacement of a concrete gravity dam, different levels of detail, friction coefficients and loading conditions are also evaluated. Furthermore, the results are compared with a limit equilibrium method with the assumption of a rigid block by Chopra and Hall (1982) based on Newmark (1965). This method is also referred to as Newmark's Sliding Block Analysis. The comparison shows that the finite element analysis and the simplified method lead to similar results regarding the cumulative displacement of the dam after the earthquake, whereby specific adjustments of parameters for the contact formulation where not necessary. The impact of different modelling techniques of the reservoir (added mass, acoustic fluid) on the displacement is negligible, whereby the simplified formula of the Westergaard added mass leads to overestimated masses at the bottom and hence can influence the contact behaviour badly. Furthermore, the evaluation of a pre- and post-seismic case (grout curtain intact and ruptured) and therefore different pore pressure distributions reveal a major influence and proves that the functionality of a grout curtain is a prerequisite.

The seismic simulations of a 220 meters high arch dam model as part of the "12th international Benchmark Workshop on Numerical Analyses of Dams" by overall 9 participants have been figured out only for linear structural conditions with the focus on different reservoir models. Although each participant had the same structural model and boundary conditions the differences of the structure's response were quiet big. The full illustration with the papers of the workshop and comparison of the results can be found in Zenz and Goldgruber (2014). Investigations of the same structure with differing critical damping factors are performed and show that the common assumption of 5% damping is legit, because slight changes of ±2% don't affect the stresses/displacements significantly.

The model of the benchmark workshop is also investigated by means of nonlinearities in this thesis. Apart from the nonlinear seismic simulations of this structure also the impact of different models for the dead weight case are studied. The consideration of the building stages with separated blocks on the contrary to a fully isotropic and continuous body shows quite big differences. The vertical stresses in the structure are underestimated in the isotropic model, because shear stresses between the blocks are present and a "hanging" effect onto each other is triggered. Therefore, an isotropic unit body approach should be avoided for simulating such structures properly. Another problem in nonlinear static dead weight simulations comes into place with the displacements calculated out of the gravity. In case of structures, which are built according to their design drawings, these displacements are compensated during construction, but stresses remain. If only the structure's response of the dead weight is of interest the impact of these displacements on the stresses is negligible, but surely affects subsequent steps in nonlinear analyses. For the simulations of the hydrostatic load the effects of retained and zero displacements from the gravity load are compared. The results reveal that the impact of pre-displacements in nonlinear simulations of a structure of this size is not negligible. The evaluated hoop stress distribution on the up- and downstream surface changed as well as the radial displacements and the contact opening. Therefore, it can be concluded that, dependent on the static procedure for the dead weight analysis, the overall response of the structure might be changed. Nevertheless, it has been found out, that the slip tolerance parameter used in correspondence with the penalty method of contact simulations, can also influence the global behaviour of such a structure significantly. A wrong, too high, value in the base or block contact, introduces artificial tangential stiffness which is in general not present in reality. Low values correspond to more realistic interactions with the drawback of a higher numerical effort. The slip tolerance should be determined under consideration of the mesh size in the contact plane. In the case of coarse meshes a sensitivity analyses is recommended. However, applying a completely tied contact at the base yields almost identical results compared to the discrete contact regarding stresses and displacements in the structure. Hence, modelling contact at the dam-foundation interface can be neglected if the evaluation of openings isn't the major interest. Furthermore, investigations of the block contact for static loading cases with a full reservoir revealed that even for a low friction coefficient of 0.5 neither openings nor relative displacement occurred. Therefore, for such a loading case (dead weight, full reservoir) this effect is negligible.

Seismic simulations of the nonlinear arch dam are compared with the results of the linear model from the benchmark workshop. Thereby the compressive hoop stresses on the upstream surface in the main section have been reduced, because of the introduced flexibility in the contacts. On the other hand on the downstream surface they are increased by these effects. Tensile stresses between the blocks and the base disappeared, because of the conservative approach of zero tensile strength and no cohesion between them. Furthermore, the impact on the structure of different reservoir water levels is also investigated. The comparison of three different levels (full, half-full, empty) depicts that the arching effect of the dam is almost not mobilized by a half- or less-filled reservoir, but the vertical stresses on the upstream heel are increased due to the dominating dead weight compared to the hydrostatic load. The contact opening along the path where the maximum occurs is approx. two times higher for the seismic full reservoir case. A half-full reservoir leads to zero opening, whereas an empty reservoir leads to openings on the downstream surface, because of the missing hydrostatic water pressure. Investigations of the block contact for the applied seismic acceleration with a maximum of 1.0 m/s^2 and a full reservoir showed that, as for the static loading, even for a low friction coefficient of 0.5 neither openings nor relative displacement occurred. This behaviour doesn’t apply to the empty and half-full reservoir case. Additional simulations with higher accelerations of 3.0 m/s^2 and a larger friction coefficient of 2.0 led to openings and relative displacements for a full reservoir too. Although, the differences compared to a coefficient of only 0.5 for this high acceleration were not as high as one would expect.

The nonlinear material behaviour of the arch dam model with discrete blocks is simulated with XFEM. Because of the limitation of the program, that only one crack per region is allowed, only a qualitative evaluation of the results is possible. Nevertheless, the simulations reveal that cracks start to initiate downstream in heights above 2/3 of the total height of the structure for full reservoir conditions. The knowledge of the location of crack initialization may therefore serve as indicator for possible safety measures. Detailed simulations of only one block region, which is allowed to crack, for significantly higher acceleration up to 5.0 m/s^2 can be used to predict crack initializations and crack surface direction to allow for further investigations of failure mechanisms. It also turned out that convergence issues with XFEM may arise from the mesh topology. A refinement therefore helped in the case of the arch dam model. Nevertheless, it is generally valid that a finer mesh leads normally to more exact solutions, but with a high computational effort. The XFEM still primarily used in research, but shows a high potential for nonlinear material simulations regarding cracks. Its convenient way of implementation and usage is a big advantage in contrast to, e.g. constitutive models with softening. Seismic excitations of arch dams, in coherence with crack propagation, give a fairly good example for its applicability, but needs further research. Also the treatment and application of contact properties in the crack needs further investigations.

Finally, it can be concluded that nonlinear simulations of concrete dam structures regarding contacts and material need skilled and experienced users, not only on a numerical, but also on practical aspects. Commercial numerical programs allow for solving complex problems nowadays in an easy way, with the drawback that unexperienced users might get satisfactory results in the first place. Solving nonlinear problems is always an iterative procedure, where more than one specific solution is possible, dependent on the complexity and grade of nonlinearity. In this case the results one gets from the numerical solver should be treated with caution, because the first result is rarely the right, hence comprehensive evaluations are necessary and comparisons with similar problems recommended.

7.1 Further Research

The investigated concrete dam examples in this thesis should represent typical dimensions of gravity or arch dams, but on the other hand, even if the overall size is similar, each structure is an elaborate prototype and must be treated as such, because of geological conditions and other properties and details. Therefore the presented work gives a general overview and outlook of the possibilities of nonlinear simulations of concrete dams. However, additional research and evaluation of the impact of other loadings and effects remain. Apart from the gravity and hydrostatic water loading on these structures another important non-negligible influence comes from temperature. Dams are generally built in mountainous regions where temperatures on the downstream surface of the concrete surface can vary between -20°C up to +40°C. Further research on the influence of temperature fluctuations in coherence with nonlinear effects, like block opening, should be done.

The continuous reservoir level changes between maximum and minimum operating level during the energy production process is also an important factor in coherence with block openings and should be examined further, especially in combination with the temperature expansion and shrinkage.

Nonlinear material behaviour, by means of crack propagation, the XFEM simulations turned out to be a good choice for such problems. Nevertheless, a lot of further possibilities for the application of this method exist. One might be the crack simulation in the base or between blocks instead of using a contact formulation. Another important factor in case of cracking on the upstream surface of dams is also the water penetration (seepage, uplift), consequently the water pressures in these openings, especially at the base where the highest pressures occur. Further research and development on this topic with XFEM is therefore recommended.

Furthermore, the investigation of completely cracked dam blocks for stability reasons after an earthquake also needs further research. Figure 7-1 constitutes such a failure mechanism.

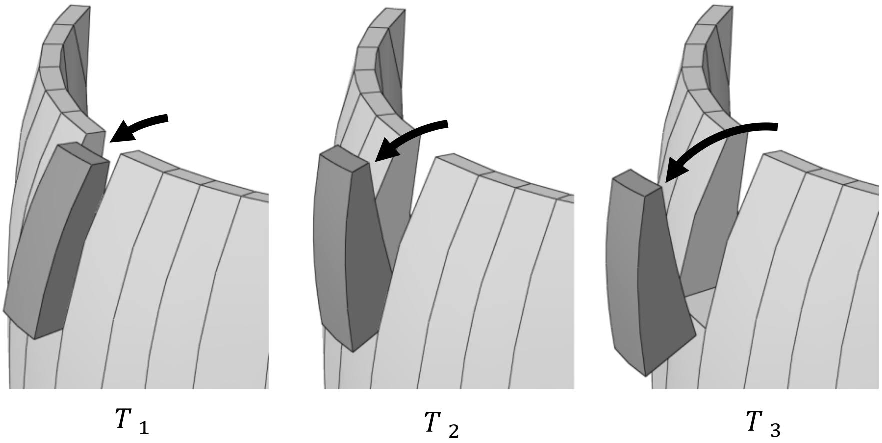

Figure 7-1: Failure mechanism; Falling block of an arch dam

BIBLIOGRAPHY

Adhikari, S., & Srikantha Phani, A. (2007). Rayleigh's Dlassical Damping Revisited. *International Conference on Civil Engineering in the New Millennium: Opportunities and Challenges.* Howrah, India.

Altenbach, H. (2012). *Kontinuumsmechanik.* Berlin Heidelberg: Springer-Verlag.

Ambraseys, N. N., & Menu, J. M. (1988). Earthquake Induced Ground Displacements. *Earthquake Engineering and Structural Dynamics Vol. 16*, 985-1006.

Arabshahi, H., & Lotfi, V. (2009). Nonlinear Dynamic Analysis of Arch Dams with Joint Sliding Mechanism. *Engineering Computations*, 464-482.

Arias, A. (1970). A Measure of Earthquake Intensity. *Seismic Design for Nuclear Power Plants*, 438-483.

ATCOLD. (1991). *Dams in Austria.* Vienna: ATCOLD.

Attarnejad, R., & Lohrasbi, A. R. (2008). Reservoir Length Effect in Calculation Accurate of Dam-Reservoir Interation. *The 14th World Conference on Earthquake Engineering.* Beijing.

Bangash, M. (2001). *Manuals of Numerical Methods in Concrete - Modelling and Applications Validated by Experimental and Site-Monitoring Data.* Reston: Thomas Telford, ASCE Press, 1801 Alexander Bell Drive.

Batchelor, G. K. (2000). *An introduction to Fluid Dynamics.* Cambridge: Cambridge University Press.

Bathe, K. J. (2007). *Finite Elemente Methoden.* Berlin Heidelberg: Springer.

Baumber, T. A. (1992). *Reservoir Length Effect on the Seismic Response of Concrete Gravity Dams.* Hamilton: McMaster University.

Belytschko, T., & Black, T. (1999). Elastic Growth in Finite Elements with Minimal Remeshing. *Interantional Journal for Numerical Methods in Engineering*, 601-620.

Belytschko, T., Liu, W. K., Moran, B., & Elkhodary, K. I. (2014). *Nonlinear Finite Elements for Continua and Structures, Second Edition.* John Wiley & Sons.

Bollrich, G. (2007). *Technische Hydromechanik 1: Grundlagen.* Berlin: HUSS-MEDIEN GmbH.

Bonet, J., & Wood, R. D. (1997). *Nonlinear Continuum Mechanics for Finite Element Analysis.* Cambridge: Cambridge Univeristy Press.

Brusin, M., Brommundt, J., & Stahl, H. (2014). Fluid-Structure Interaction, Arch Dam-Reservoir at Seismic Loading: A solution using FEnas. *12th International Benchmark Workshop on Numerical Analysis of Dams* (pp. 149-164). Graz: ATCOLD.

Caughey, T. K., & O'Kelly, M. E. (1965). Classical Normal Modes in Damped Linear Dynamic Systems. *Journal of Applied Mechanics 32*, 583-588.

Chambart, M., Menouillard, T., Richart, N., Molinari, J. F., & Gunn, R. M. (2014). Dynamic Analysis of an Arch Dam with Fluid-Structure Interaction. *12th International Benchmark Workshop on Numerical Analysis of Dams* (pp. 111-122). Graz: ATCOLD.

Chatterjee, P. (2013, June). Frequency Response Analysis of a Generic Dam-Fluid-Foundation Model. (p. 5). TNO DIANA.

Chen, S.-h., Xu, M.-y., Shahrour, I., & Egger, P. (2003). Analysis of Arch Dams Using Coupled Trial Load and Block Element Methods. *Journal of Geotechnical and Geoenvironmental Engineering 129*, 977-986.

Chopra, A. K. (1968). Earthquake Behavior of Reservoir-Dam Systems. *Journal of Engineering Mechanics ASCE 96 (EM4)*, 1475-1500.

Chopra, A. K. (2008). Earthquake Analysis of Arch Dams: Factors to be Considered. *The 14th World Conference on Earthquake Engineering.* Beijing.

Chopra, A. K. (2011). *Dynamics of Structures.* New Jersey: Prentice Hall.

Chopra, A. K., & Gupta, S. (1982). Hydrodynamic and Foundation Interaction Effects in Frequency Response Functions for Concrete Gravity Dams. *Earthquake Engineering & Structural Dynamics*, 89-106.

Chopra, A. K., & Hall, J. F. (1982). Hydrodynamic Effects in the Dynamic Response of Concrete Gravity Dams. *Earthquake Engineering and Structural Dynamics*, 333-395.

Chopra, A. K., & Hall, J. F. (1991). Earthquake-Induced Base sliding of Concrete Gravity Dams. *Journal of Structural Engineering 117*, 3698-3719.

Clough, R. W., & Penzien, J. (1975). *Dynamics of Structures.* McGraw-Hill Companies.

Dassault Systemes. (2013). *Abaqus 6.13-EF Documentation.* Dassault Systemes.

Davidsson, P. (2004). *Structure-Acoustic Analysis; Finite Element Modelling and Reduction Methods.* Lund: Division of Structural Mechanics, LTH, Lund University.

de Borst, R., Remmers, J. J., Needleman, A., & Abellan, M.-A. (2004). Discrete vs smeared crack models for concrete fracture: bridging the gap. *International Journal for Numerical and Analytical Methods in Geomechanics 28*, 583-607.

Diallo, A., & Robbe, E. (2014). Fluid Structure Interaction, Arch Dam-Reservoir at Seismic Loading. *12th International Benchmark Workshop on Numerical Analysis of Dams* (pp. 177-186). Graz: ATCOLD.

EN 1992-1-1:2004. (2004). *Eurocode 2: Design of Concrete Structures, Part 1-1: General rules and rules for buildings.*

Faggiani, G., & Masarati, P. (2014). Finite Element Modelling of Seismic Fluid-Structure Interaction for a Large Arch Dam. *12th International Benchmark Workshop on Numerical Analysis of Dams* (pp. 87-98). Graz: ATCOLD.

Feldbacher, R., & Zenz, G. (2009). *Naturmessungen an Talsperren im Zusammenspiel mit numerischen Berechnungen.* Graz: Institut für Wasserbau und Wasserwirtschaft, TU Graz.

Fenves, G., & Chopra, A. K. (1984). Earthquake Analysis of Concrete Gravity Dams including Dam-Water-Foundation Rock Interaction and Reservoir Bottom Absorption. *Earthquake Engineering and Structural Dynamics 12*, 663-680.

Fenves, G., & Chopra, A. K. (1985). Simplified Earthquake Analysis of Concrete Gravity Dams: Separate Hydrodynamic and Foundation Interaction Effects. *Journal of Engineering Mechanics 111*, 715-735.

Flesch, R. (1993). *Baudynamik, praxisgerecht, Band 1: Berechnungsgrundlagen.* Berlin: Bauverlag GmbH.

Flesch, R. (1997). *Baudynamik, praxisgerecht, Band 2:Anwendungen und Beispiele.* Berlin: Bauverlag GmbH.

Fok, K.-l., & Chopra, A. K. (1987). Water Compressibility in Earthquake Response of Arch Dams. *Journal of Structural Engineering 113*, 958-975.

Fries, T. P., & Belytschko, T. (2010). The Extended/Generalized Finite Element Method: An Overview of the Method and its Applications. *International Journal for Numerical Methods in Engineering*, 253–304.

Frigerio, A., & Mazzá, G. (2014). The Seismic Behaviour of an Arch Dam-Reservoir Foundation System. *12th International Benchmark Workshop on Numerical Analysis of Dams* (pp. 167-176). Graz: ATCOLD.

Gell, K., & Wittke, W. (1986). A New Design Concept for Arch Dams taking into Account Seepage Forces. *Rock Mechanics and Rock Engineering*, 187-204.

Ghanaat, Y., & Redpath, B. B. (1995). *Measurements of Reservoir-Bottom Reflection Coefficient at Seven Concrete Dam Sites, QUEST Report No. QS95-01.* US Army Corps of Engineers, Waterways Experiment Station and US Bureau of Reclamation.

Giesecke, J., & Mosonyi, E. (2009). *Wasserkraftanlagen, Planung, Bau und Betrieb.* Berlin Heidelberg: Springer.

Goldgruber, M. (2011). *Diskretisierung und numerische Stabilitätsprüfung eines Felskeils im Widerlager am Beispiel der Luzzone Staumauer.* Graz: TU Graz Institut für Wasserbau und Wasserwirtschaft.

Goldgruber, M., & Feldbacher, R. (2013). Empirischer Ansatz zur Ermittlung der mitschwingenden Wassermasse bei dynamischer Wasser-Bauwerks-Interkation. *15. JUWI-Treffen* (pp. 1-6). Graz: Graz University of Technology.

Goldgruber, M., Feldbacher, R., & Zenz, G. (2012). Seismic Stability of a Rock wedge in the Abutment of an Arch Dam. *Geomechanics and Tunneling 5, No. 2*, 186-194.

Goldgruber, M., Shahriari, S., & Zenz, G. (2013). Influence of Damping and Different Interaction Modelling on a High Arch Dam. *Vienna Congress on Recent Advances in Earthquake Engineering and Structural Dynamics*. Vienna.

Goldgruber, M., Shahriari, S., & Zenz, G. (2015). Dynamic Sliding Analysis of a Gravity Dam with Fluid-Structure-Foundation Interaction using Finite Elements and Newmark's Sliding Block Analysis. *Rock Mechanics and Rock Engineering*, in Press.

Gunn, R. M. (2009). *Computational Aspects of Analysis and Design of Dams: Tenth Benchmark Workshop on Numerical Analysis of Dams.*

Hall, J. F. (2006). Problems encountered from the use (or misuse) of Rayleigh Damping. *Earthquake Engineering and Structural Dynamics 35*, 525-545.

Hall, J. F., & Chopra, A. K. (1980). *Dynamic Response of Embankment Concrete-Gravity and Arch Dams Including Hydrodynamic Interaction, Report No. UCB/EERC-80/39.* Berkeley, CA: University of California, Earthquake Engineering Research Center.

Hall, R. L., de Bejar, L., Sjostrom, K. j., & Matheu, E. E. (1998). Effect of Reservoir-Subbottom Energy Absorption on Hydrodynamic Forces on Dams. *Proccedings of the 30th Joint Meeting of The U.S.-Japan Cooperative Program in Natural Resources Panel on Wind and Seismic Effects* (pp. 116-129). Galthersburg: U.S. Department of Commerce.

Hellgren, R. (2014). *Influence of Fluid Structure Interaction on a Concrete Dam during Seismic Excitation.* Stockholm: KTH Royal Institute of Technology.

Hilber, H. M., Hughes, T. J., & Taylor, R. L. (1977). Improved Numerical Dissipation for Time Integration Algorithms in Structural Dynamics. *Earthquake Engineering and Structural Dynamics 5*, 583-292.

Höllinger, F. (1982). *Bebenerregte Schwingungen elastischer Sperrenkonstruktionen - Dissertation.* TU Wien.

Höllinger, F. (1983). Time-Harmonic and Nonstationary Stochastic Vibrations of Arch Dam-Reservoir-Systems. *Acta Mechanica 49*, 153-167.

Holzapfel, G. A. (2000). *Nonlinear Solid Mechanics: A Continuum Approach for Engineering.* Chichester: Wiley.

Holzner, A. (2011). *Integrales Talsperrenmodell zur Gesamtbewertung von Gewölbemauergeometrien - Dissertation.* München: Universität der Bundeswehr München.

Housner, G. W. (1954). Earthquake Pressures on Fluid Containers. *Report EERL-1954-3, Earthquake Engineering Laboratory*.

ICOLD. (2010). *Selecting Seismic Parameters for Large Dams Guidelines, Bulletin 72, Revision 5.3.1.*

ICOLD. (2013). *Guidelines for Use of Numerical Models in Dam Engineering.* Paris: Commission Internationale des Grands Barrages.

Jibson, R. W. (1993). Predicting Earthquake-Induced Landslide Displacements using Newmark's Sliding Block Analysis. *Transportation Research Record 1411*, 9-17.

Jibson, R. W., Harp, E. L., & Michael, J. M. (1998). A Method for producing Digital Probabilistic Seismic Landslide Hazard Maps: An Example from the Los Angeles, California area. *US Geological Survey Open-File Report*, 98-113.

Kampmann, R. (2012). *The Influence of the Compression Interface on the Failure Behavior and Size Effect of Concrete - Disseration.* Florida State University.

Kikstra, W., Sirumbal, F., & Schreppers, G. (2014). HFTD Analysis of an Arched Dam at Seismic Loading. *12th International Benchmark Workshop on Numerical Analysis of Dams* (pp. 77-86). Graz: ATCOLD.

Kolymbas, D. (2007). *Geotechnik Bodenmechanik, Grundbau und Tunnelbau.* Berlin Heidelberg: Springer.

Kuo, J. S. (1982). Fluid-Structure Interactions: Added mass Computation for Incompressible Fluid. *UCB/EERC-82/09 Report, University of California, Berkely*.

Lin, G., Hu, Z. Q., Du, J. G., Wang, Y., & Liu, J. Y. (2008). Effects of Reservoir Boundary Absorption on the Earthquake Response of Arch Dams. *The 14th World Conference on Earthquake Engineering.* Beijing.

Lotfi, V., & Espandar, R. (2002). An Investigation of Joints Behavior in Seismic Response of Arch Dams. *Electronic Journal of Structural Engineering 1*.

Lysmer, J., & Kuhlemeyer, R. L. (1969). Finite Dynamic Model for Infinite Media. *Journal of the Engineering Mechnanics Division 95*, 859-876.

Malla, S. (2014). Earthquake Safety Assessment of Arch Dams based on Nonlinear Dynamic Analysis. *12th International Benchmark Workshop on Numerical Analysis of Dams* (pp. 395-404). Graz: ATCOLD.

Malm, R. (2006). *Shear Cracks in Concrete Structures subjected to In-Plane Stresses; Licentiate Thesis.* Stockholm: Royal Institute of Technology, Department of Civil and Architectural Engineering.

Malm, R. (2009). *Predicting Shear Type Crack Initiation and Growth in Concrete with Non-linear Finite Element Method; Doctoral Thesis.* Stockholm: Royal Institute of Technology, Department of Civil and Architectural Engineering.

Malm, R., Pi Rito, C., Hassanzadeh, M., Rydell, C., & Gasch, T. (2014). Concrete Arch Dam at Seismic Loading with Fluid Structure Interaction. *12th International Benchmark Workshop on Numerical Analysis of Dams* (pp. 139-148). Graz: ATCOLD.

Maltidis, G., & Stempniewski, L. (2014). Fluid Structure Interaction - Arch Dam - Reservoir at Seismic Loading. *12th International Benchmark Workshop on Numerical Analysis of Dams* (pp. 67-76). Graz: ATCOLD.

McGuire, R. K. (1974). Seismic Structural Response Risk Analysis, Incorporating Peak Response Regressions on Earthquake Magnitude and Distance. *Massachusetts Institute of Technology, Dept. of Civil Eng., Research Report 74-51*.

Muto, M., von Gersdorf, N., Duron, Z., & Knarr, M. (2012). Effective Modelling of Dam-Reservoir Interaction Effects using Acoustic Finite Elements. *32nd Annual USSD Conference, Innovative Dam and Levee Design and Construction for Sustainable Water Management* (pp. 1161-1167). New Orleans: U.S. Society on Dams.

Newmark, N. (1959). A Method of Computation for Structural Dynamics. *Journal of Engineering Mechanics, ASCE, 85 (EM3)*, 67-94.

Newmark, N. (1965). Effects of Earthquakes on Dams and Embankments. *Geotechnique 15*, 139-160.

Österreichische Staubeckenkomission im Bundesministerium für Land- und Forstwirtschaft. (2001). *Erdbebenberechnung von Talsperren Band 1.*

Pagitsch, M. (2012). *Arch dam Design and Optimization - Master Thesis.* Graz: Institute for Hydraulic Engineering and Water Resources Management.

Popovici, A., Ilinca, C., & Varvorea, R. (2014). Study on Arch Dam– Reservoir Seismic Interaction. *12th International Benchmark Workshop on Numerical Analysis of Dams* (pp. 123-137). Graz: ATCOLD.

Promper, R. (1992). *Design of Double Curved Arch Dams with the FEM-Program CODCOD - Dissertation.* Vienna: Vienna University of Technology.

Rayleigh, L. (1877). *Theory of Sound (two volumes).* New York: Dover Publications.

Reynolds, D. (1981). *Engineering Principles in Acoustics.* Boston: Allyn and Bacon Inc.

Sarkar, R., Paul, D. K., & Stempniewski, L. (2007). Influence of Reservoir and Foundation on the Nonlinear Dynamic Response of Concrete Gravity Dams. *ISET Journal of Earthquake Technology*, 377-389.

Scheulen, F. (2010). *Numerical Model Validation for Large Concrete Gravity Dams.* United States Society on Dams Conference.

Shahriari, S. (2014). Fluid Structure Interaction, Arch Dam-Reservoir at Seismic Loading. *12th International Benchmark Workshop on Numerical Analysis of Dams* (pp. 165-166). Graz: ATCOLD.

Sohrabi Gilani, M., Feldbacher, R., & Zenz, G. (2009). *Stability of Dam Abutment Including Seismic Loading.* Graz: TU Graz Institut für Wasserbau und Wasserwirtschaft.

Spears, R. E., & Jensen, S. R. (2012). Approach for selection of Rayleigh damping parameters used for time history analysis. *Journal of Pressure Vessel Technology 134*.

Strobl, T., & Zunic, F. (2006). *Wasserbau - Aktuelle Grundlagen, Neue Entwicklungen.* Berlin Heidelberg: Springer.

Tassios, T., & Vintzēleou, E. (1987). Concrete-to-concrete friction. *Journal of Structural Engineering 114*, 832–849.

Technology, M. I. (1976). *SIMQKE - A Program for Artificial Motion Generation.* Massachusetts: Massachusetts Institute of Technology.

Tiliouine, B., & Seghir, A. (1998). Fluid-Structure Models for Dynamic Studies of Dam-Water Systems. *Eleventh European Conference on Earthquake Engineering*, (pp. 6-11). Paris.

Tzenkov, A., Abati, A., & Gatto, G. (2014). Fluid-Structure Interaction Arch Dam - Reservoir at Seismic Loading. *12th International Benchmark Workshop on Numerical Analysis of Dams* (pp. 99-109). Graz: ATCOLD.

U.S. Army Corps of Engineers. (1995). *Engineering and Design, Gravity Dam Design, Engineer Manual 1110-2-2200.* Washington D.C.

U.S. Army Corps of Engineers, Engineer Research and Development Center. (2000). *Evaluation and Comparison of Stability Analysis and Uplift Criteria for Concrete.* ERDC/ITL TR-00-1.

Weber, B. (1994). *Rational Transmitting Boundaries for Time-Domain Analysis of Dam-Reservoir Interaction.* Zürich: Institut für Baustatik und Konstruktion ETH Zürich.

Westergaard, H. M. (1933). Water Pressure on Dams during Earthquakes. *Transactions, ASCE, Vol. 98*, 418-472.

Widmann, R. (2005). *Arch Dams; Experiences - Problems - Developements.* Graz: ATCOLD.

Wieland, M. (2012). Seismic Design and Performance Criteria for Large Storage Dams. *15th World Conference on Earthquake Engineering.* Lisboa.

Wieland, M., & Ahlehagh, S. (2013). Dynamic Stability Analysis of a Gravity Dam Subject to the Safety Evaluation Earthquake. *Proc. 9th Symposium of ICOLD European Club IECS2013, Venice.* Venice.

Wittke, W. (1984). *Felsmechanik. Grundlagen für wirtschaftliches Bauen im Fels.* Berlin Heidelberg: Springer.

Zangar, C. N., & Haefeli, R. J. (1952). Electric Analog indicates Effect of Horizontal Earthquake Shocks on Dams. *Journal of the engineering mechanics division, Vol. 22, No. 4.*

Zenz, G., & Aigner, E. (1997). *Earthquake Induced Joint Opening in Arch Dams.* Proceedings of Numog VI; p. 575-581.

Zenz, G., & Goldgruber, M. (2014). Proceedings of the 12th international benchmark workshop on numerical analysis of dams. *ICOLD - 12th International benchmark workshop on numerical analysis of dams.* Graz: ATCOLD - Austrian National Committee on Large Dams.

Zenz, G., Feldbacher, R., & Goldgruber, M. (2012). *Hydraulic Structures - Research Report.* Graz: Institute for Hydraulic Engineering and Water Resources Management.

Zhang, C., Jin, F., Wang, J., & Xu, Y. (2013). *Seismic Safety Evaluation of Concrete Dams: A Nonlinear Behavioral Approach.* Butterworth Heinemann.

Zienkiewicz, O. C., Taylor, R. L., & Zhu, J. Z. (2013). *The Finite Element Method: Its Basis and Fundamentals.* Butterworth Heinemann.

APPENDIX

A BASICS OF CONTINUUM MECHANICS

An ongoing increase of computer power allows for more and more complex simulations nowadays. Multiphysical problems can be seen as such. So called multiphysics are coupled simulations of physical processes, e.g. an interaction between a structure and a surrounding fluid, sound pressures on structures, electromagnetic waves, among others. Different numerical discretization methods, like finite elements or finite volumes, are used to solve the defining partial differential equations. To model, simulate, interpret and understand such problems properly it is mandatory for an engineer to have a basic knowledge about continuum mechanics. Especially in the case of fluid-structure interaction problems it is important to understand the principles of the two kinematic descriptions of a continuum, the “Lagrangian” and the “Eulerian” description. Besides the kinematic description, this section also gives an introduction to the kinetics of continua, “Conservation of Momentum” principles, “Conservation of Mass” and the “Principle of Virtual Work”. Further discussions of other balance laws and energy principles are found in relevant literature as well as continuum material formulations and thermodynamics.

This section’s notation is based on the book *“Nonlinear Continuum Mechanics for Finite Element Analysis”* by Bonet and Wood (1997). Nevertheless, some parts are also based on the book *“Nonlinear Solid Mechanics – A Continuum Approach for Engineers”* by Holzapfel (2000) and the one commonly taught in German-speaking countries *“Kontinuumsmechanik – Einführung in die materialunabhängigen und materialabhängigen Gleichungen”* by Altenbach (2012).

A.1 Kinematics of the Continuum

Kinematics describes the finite motion and deformation of a body in general. Particular importance is given to the word “finite”. This means that everything is derived on a general basis, without material dependency. Contrary to common engineering problems where an infinitesimal deformation is taken for granted and nonlinear effects of the geometry are neglected. Furthermore, the finite approach makes it possible to describe not only deformable bodies but also fluids. This means the deformation can exceed the initial dimensions (flow of a fluid). A continuum body can be described as a set of material points or particles filling out space at any time. To define the finite motion of such a body it is convenient to focus on one particle. Figure A-1 shows the motion of a deformable body and the particle P between the reference configuration at time t_0 and the current configuration at time t. The assumption has been made that the coordinate systems for both configurations are having the same origin O. In a mathematical way of view the motion of a particle from the reference to the current configuration is described by the following mapping function

$$\boldsymbol{x} = \phi(\boldsymbol{X}, t) \qquad \text{(A-1)}$$

This means that the current position of a particle is a function of its initial position $\boldsymbol{X}$ at time t_0 and time t. Under the premise that the “Jacobi-Determinant” of such a function is not zero,

$$J = det\left(\frac{\partial\phi_i}{\partial \boldsymbol{X_j}}\right) = det\left(\frac{\partial x_i}{\partial \boldsymbol{X_j}}\right) \neq 0 \tag{A-2}$$

there must be an uniquely invertible relation between $\boldsymbol{x}$ and $\boldsymbol{X}$, leading to

$$\boldsymbol{X} = \phi^{-1}(\boldsymbol{x}, t) \tag{A-3}$$

This leads to two different descriptions of a continuum body, the Lagrangian description where quantities are described with respect to the reference configuration/coordinates and the Eulerian description, where quantities are described with respect to the current configuration/coordinates.

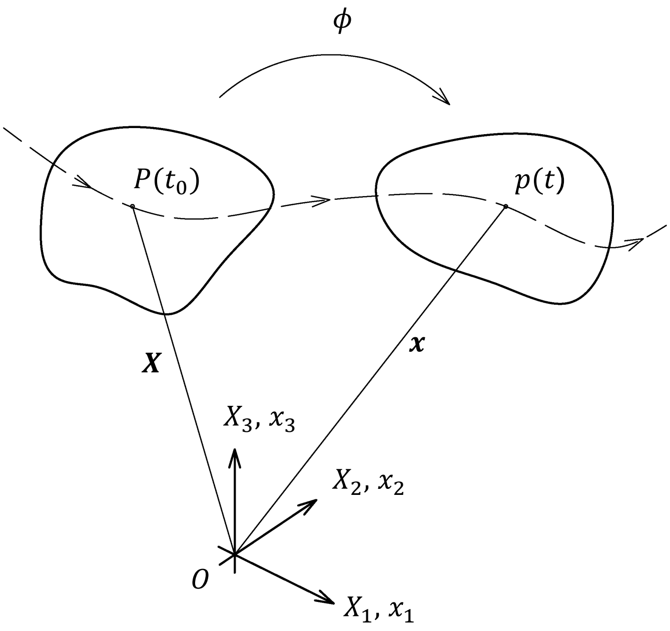

Figure A-1: General motion of a continuum body and a particle P from the reference configuration to the current configuration

A.1.1 The Lagrangian and Eulerian Description

The Lagrangian description, also called “Material Description”, observes a particle with respect to its initial or reference coordinates $\boldsymbol{X}$ at time t. In other words, the observer moves with the particle and measures the quantities with respect to the reference coordinates $\boldsymbol{X}$ as time progresses. This description is mainly used in solid mechanics, where the constitutive behaviour of the body is from interest. The change in density, for instance, while moving through space is then described as

$$\rho_0 = \rho_0(\boldsymbol{X}, t) \tag{A-4}$$

This means that as time progresses, the same particle with its initial coordinate $\boldsymbol{X}$ changes its density.

Contrary, the Eulerian description, also called “Spatial Description”, observes the quantity of a passing material particle at a spatial position in space at time t. The coordinates $\boldsymbol{x}$ sometimes are also denoted as “Laboratory Coordinates”, because of the analogy to fixed in place measuring points in hydraulic model tests, for instance, where a quantity like velocity and its direction is observed.

The density, for example, is now described by its spatial coordinates $\boldsymbol{x}$ and time t

$$\rho = \rho(\boldsymbol{x}, t) \tag{A-5}$$

Note that the density at a spatial point in space changes now as time progresses and particles are passing. In fluid mechanics the quantity of most interest is the velocity and the associated pressure distribution, but not the motion and deformation of a specific particle. So the Eulerian description is the one almost solely used for investigations of fluid mechanical problems.

A.1.2 Material Time Derivatives

The material or total time derivative is essential to describe the motion of particles in space and time. It is defined as the rate of change of physical quantities. For an arbitrary function f (scalar, vector or tensor) the material or total time derivative can be written as

$$\frac{Df}{Dt} \tag{A-6}$$

Here again one has to differ between the Lagrangian and Eulerian description. In the Lagrangian description every quantity is referred to the initial coordinate $\boldsymbol{X}$. In this case the rate of change of a quantity of a particle described by material coordinates simply is

$$\dot{\varphi} = \frac{D\varphi(\boldsymbol{X}, t)}{Dt} = \frac{\partial\varphi(\boldsymbol{X}, t)}{\partial t}\bigg|_{\boldsymbol{X}\,fixed} \tag{A-7}$$

The Eulerian description is a so called field description, which means that every quantity is also dependent on its position in space $\varphi(\boldsymbol{x}, t) = \varphi(\boldsymbol{x}(\boldsymbol{X}, t), t)$. So, the total derivative in Eulerian description is more complex to achieve and with the chain rule one gets

$$\dot{\varphi} = \frac{D\varphi(\boldsymbol{x}, t)}{Dt} = \frac{\partial\varphi(\boldsymbol{x}, t)}{\partial t}\bigg|_{\boldsymbol{x}\,fixed} + \frac{d\boldsymbol{x}}{dt}\frac{\partial\varphi(\boldsymbol{x}, t)}{\partial\boldsymbol{x}}\bigg|_{\boldsymbol{X}\,fixed} \tag{A-8}$$

In a simpler and more common form and applying the del-operator ∇ the material derivative in Eulerian description can be written as

$$\dot{\varphi} = \frac{D\varphi(\boldsymbol{x}, t)}{Dt} = \frac{\partial\varphi}{\partial t} + \boldsymbol{v}\cdot\nabla_x\varphi \tag{A-9}$$

With $\frac{\partial\varphi}{\partial t}$ and $\boldsymbol{v}\cdot\nabla\varphi$ as the local and the convective derivative or rate of change of a quantity at a spatial position, respectively.

A.1.3 Deformation Gradient

To describe geometry changes due to deformation of a continuum body, in particular strains, the deformation gradient tensor $\boldsymbol{F}$ is introduced.

The deformation of a simple line element from the reference configuration to the current configuration is defined by

$$\boldsymbol{F} = \frac{d\boldsymbol{x}}{d\boldsymbol{X}} = \nabla_{\boldsymbol{X}}\boldsymbol{x}(\boldsymbol{X}, t) \tag{A-10}$$

In other words, it's a transformation of a material line element $d\boldsymbol{X}$ from the reference configuration to a material line element $d\boldsymbol{x}$ in the current configuration (Figure A-2). In literature also referred to as "push forward".

$$d\boldsymbol{x} = \boldsymbol{F}d\boldsymbol{X} \tag{A-11}$$

The reverse operation of this transformation between the two configurations can easily be achieved by using the inverse of the transformation gradient tensor $\boldsymbol{F}^{-1}$, which leads to

$$\boldsymbol{F}^{-1} = \frac{d\boldsymbol{X}}{d\boldsymbol{x}} = \nabla_{\boldsymbol{x}}\boldsymbol{X}(\boldsymbol{x}, t) \tag{A-12}$$

or

$$d\boldsymbol{X} = \boldsymbol{F}^{-1}d\boldsymbol{x} \tag{A-13}$$

and is also referred to in literature as "pull back".

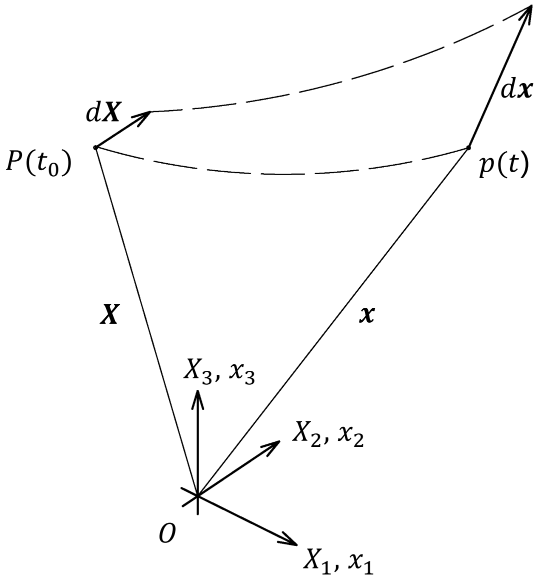

Figure A-2: Transformation of a material line element from the reference to the current configuration

A.1.4 Nonlinear Strain Tensors

As already mentioned before, continuum mechanics in general are addressing finite motions and deformations. Therefore, nonlinear strain measures have to be defined. In the section before the deformation gradient tensor $\boldsymbol{F}$ has been introduced. Not only from a mathematical view, but also relevant in mechanics, it is from interest to split this tensor into two tensors, one describing just the rotation of the element and one the stretch. So $\boldsymbol{F}$ can be written as

$$\boldsymbol{F} = \boldsymbol{R}\boldsymbol{U} = \boldsymbol{V}\boldsymbol{R} \tag{A-14}$$

which is called polar decomposition. Figure A-3 illustrates the two possibilities of the transformation after the decomposition.

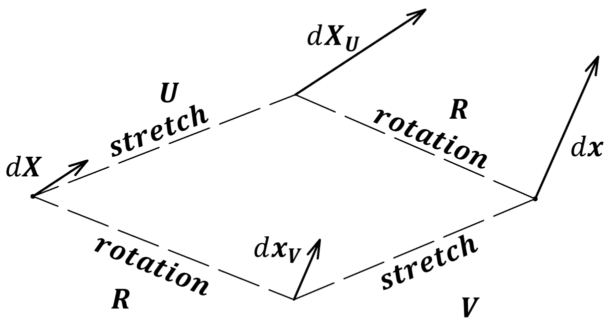

Figure A-3: Depiction of the polar decomposition of the deformation gradient tensor (based on Altenbach (2012))

It can be mathematically proved that $\boldsymbol{U}$ and $\boldsymbol{V}$ are symmetrical and $\boldsymbol{R}$ is orthogonal. So, $\boldsymbol{U}$ and $\boldsymbol{V}$ can be expressed as

$$\boldsymbol{U} = (\boldsymbol{F}^T\boldsymbol{F})^{1/2} \tag{A-15}$$

and

$$\boldsymbol{V} = (\boldsymbol{F}\boldsymbol{F}^T)^{1/2} \tag{A-16}$$

They are called, “Material and Spatial Stretch Tensor”, respectively. From a mathematical point of view these expressions are inconvenient to handle. Hence the two tensors called “Right-Cauchy-Green-Tensor” $\boldsymbol{C}$ and “Left-Cauchy-Green-Tensor” or “Finger-tensor” $\boldsymbol{b}$ are introduced.

$$\boldsymbol{C} = \boldsymbol{U}^2 = \boldsymbol{F}^T\boldsymbol{F} \tag{A-17}$$

$$\boldsymbol{b} = \boldsymbol{V}^2 = \boldsymbol{F}\boldsymbol{F}^T \tag{A-18}$$

The relationship between the strain in the reference configuration and the current configuration can now be written as

$$d\boldsymbol{x} \cdot d\boldsymbol{x} = \boldsymbol{F}d\boldsymbol{X} \cdot \boldsymbol{F}d\boldsymbol{X} = d\boldsymbol{X} \cdot \boldsymbol{F}^T\boldsymbol{F}d\boldsymbol{X} = d\boldsymbol{X} \cdot \boldsymbol{C}d\boldsymbol{X} \tag{A-19}$$

and vice versa from the current configuration to the reference configuration as

$$d\boldsymbol{X} \cdot d\boldsymbol{X} = \boldsymbol{F}^{-1}d\boldsymbol{x} \cdot \boldsymbol{F}^{-1}d\boldsymbol{x} = d\boldsymbol{x} \cdot \boldsymbol{F}^{-T}\boldsymbol{F}^{-1}d\boldsymbol{x} = d\boldsymbol{x} \cdot \boldsymbol{b}^{-1}d\boldsymbol{x} \tag{A-20}$$

For measuring finite deformation in the “Lagrangian Description” a strain tensor operating on the reference configuration has to be defined. Therefore, the so called “Green-Lagrange Strain Tensor” $\boldsymbol{E}$ is well established. The coherence between this tensor and the scalar quantity before and after the deformation can be expressed as

$$\frac{1}{2}(d\boldsymbol{x} \cdot d\boldsymbol{x} - d\boldsymbol{X} \cdot d\boldsymbol{X}) = d\boldsymbol{X} \cdot \boldsymbol{E} d\boldsymbol{X} \tag{A-21}$$

with the “Green-Lagrange Strain Tensor”

$$\boldsymbol{E} = \frac{1}{2}(\boldsymbol{C} - \boldsymbol{I}) = \frac{1}{2}(\boldsymbol{F}^T \boldsymbol{F} - \boldsymbol{I}) = \frac{1}{2}(\boldsymbol{U}^2 - \boldsymbol{I}) \tag{A-22}$$

The same quantity in “Eulerian Description” can be written as

$$\frac{1}{2}(d\boldsymbol{x} \cdot d\boldsymbol{x} - d\boldsymbol{X} \cdot d\boldsymbol{X}) = d\boldsymbol{x} \cdot \boldsymbol{e} d\boldsymbol{x} \tag{A-23}$$

with the “Almansi-Euler Strain Tensor”

$$\boldsymbol{e} = \frac{1}{2}(\boldsymbol{I} - \boldsymbol{b}^{-1}) = \frac{1}{2}(\boldsymbol{I} - (\boldsymbol{F}\boldsymbol{F}^T)^{-1}) = \frac{1}{2}(\boldsymbol{I} - \boldsymbol{V}^{-2}) \tag{A-24}$$

The use of these strain tensors has two major advantages, which are that they are symmetric and in case of rigid body motions the strains are zero.

In terms of “Local Strain” the difference in length before and after deformation based on the initial length is defined as

$$\varepsilon = \frac{|d\boldsymbol{x}| - |d\boldsymbol{X}|}{|d\boldsymbol{X}|} = \frac{|d\boldsymbol{x}|}{|d\boldsymbol{X}|} - 1 = \kappa - 1 \tag{A-25}$$

with κ called the “Local Stretch” or relative change in length. The “Local Strain” gives information of the quantity of the deformation and can be expressed under consideration of the “Green-Lagrange Strain Tensor” and the deformation direction $\boldsymbol{N}$ as

$$\boldsymbol{N} \cdot \boldsymbol{E}\boldsymbol{N} = \frac{1}{2}(\varepsilon^2 + 2\varepsilon) \tag{A-26}$$

For infinitesimal strains, $\varepsilon \ll 1$, ε^2 can be neglected. This assumption yields

$$\varepsilon_{eng} = \boldsymbol{N} \cdot \boldsymbol{E}\boldsymbol{N} \tag{A-27}$$

which is also known as “Engineering Strain”.

Considering two consecutive strains, the sum of them is not the same as of a continuous strain

$$\varepsilon_1 + \varepsilon_2 \neq \varepsilon_{1+2} \tag{A-28}$$

For this case a logarithmic strain measure called “Hencky Strain” is introduced

$$\varepsilon_h = ln(\kappa) \tag{A-29}$$

where $\varepsilon_1 + \varepsilon_2 = \varepsilon_{1+2}$. This strain measure is mostly used for plastic, viscous materials and highly compressible bodies, with the drawback of the calculation of the logarithmic of a matrix.

Overall, following important strain measures can be derived among others (Remark: assuming strain/deformation just in one direction, scalar notation)

Green-Lagrange Strain $$\varepsilon_E = \frac{1}{2}(\kappa^2 - 1) \tag{A-30}$$

Almansi-Euler Strain $$\varepsilon_e = \frac{1}{2}(1 - \kappa^{-2}) \tag{A-31}$$

Engineering Strain $$\varepsilon_{eng} = \kappa - 1 \tag{A-32}$$

Hencky Strain $$\varepsilon_h = ln(\kappa) \tag{A-33}$$

A.2 Kinetics of the Continuum

On the contrary to kinematics where just the motion is investigated, kinetics deals with the motion and its cause. These causes are referred to as forces, which can be separated into body and surface forces in mechanical systems, leading to the concept of stress. Stress is defined as force per unit area in an arbitrary cutting plane in the body. The concept of the Lagrangian and Eulerian description is also present in the concept of stress, so it makes a difference if the stresses are observed in the reference or current configuration. This leads to three different stress representations, called “Cauchy Stress Tensor”, “First Piola-Kirchhoff Tensor” and “Second Piola-Kirchhoff Tensor”.

A.2.1 The Cauchy Stress Tensor

The Cauchy stress tensor is related to the current configuration. Such stresses are called “true stresses”, contrary to those defined in the reference configuration called “nominal stresses”. Figure A-4 shows an arbitrary cut through a continuum body and the force $d\boldsymbol{p}$ related to an area da and its normal vector $\boldsymbol{n}$. Thus, the traction vector $\boldsymbol{t}(\boldsymbol{n})$ is defined as

$$\boldsymbol{t}(\boldsymbol{n}) = \frac{d\boldsymbol{p}}{da} \tag{A-34}$$

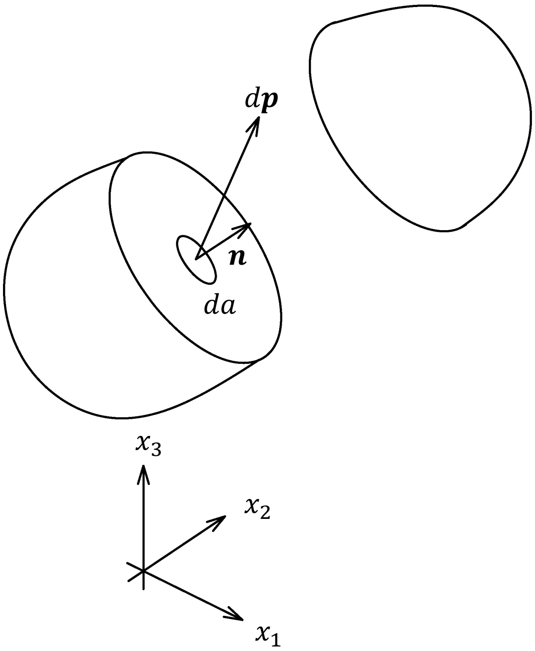

Figure A-4: Arbitrary cut through a continuum body with force, normal vector and area definition

Generally, Cauchy’s stress theorem states that if one knows the traction vectors on three perpendicular planes in the cartesian coordinate system at one specific point, any other stress vector is known by coordinate transformation. Furthermore, there exists a stress tensor $\boldsymbol{\sigma}(x,t)$ which is independent of the normal direction $\boldsymbol{n}$ and the traction vector can then be expressed as

$$\boldsymbol{t}(n,x,t) = \boldsymbol{\sigma}^T(x,t)\boldsymbol{n} \tag{A-35}$$

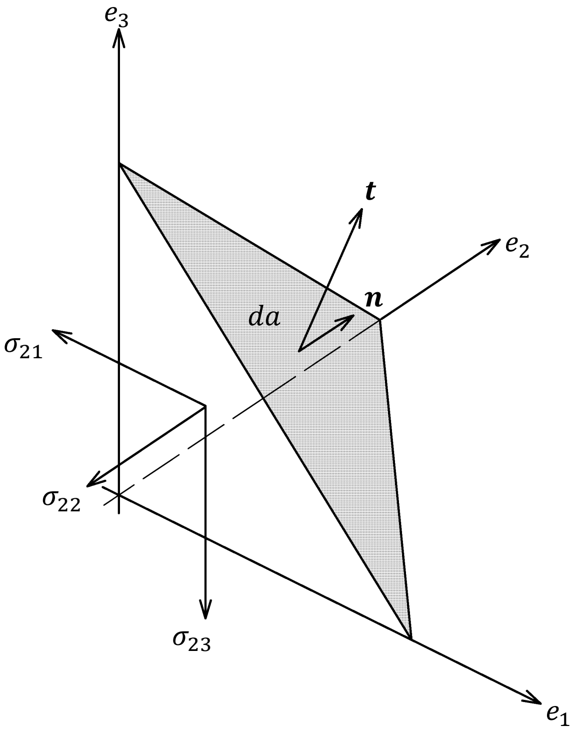

Figure A-5: Stress tensor and traction vector on a tetrahedron element on plane two

According to Figure A-5 the force equilibrium in each direction is

$$t_1 da = \sigma_{11} n_1 da + \sigma_{21} n_2 da + \sigma_{31} n_3 da \tag{A-36}$$

$$t_2 da = \sigma_{12} n_1 da + \sigma_{22} n_2 da + \sigma_{32} n_3 da \tag{A-37}$$

$$t_3 da = \sigma_{13} n_1 da + \sigma_{23} n_2 da + \sigma_{33} n_3 da \tag{A-38}$$

Hence the *“Cauchy Stress Tensor”* is

$$\boldsymbol{\sigma} = \begin{bmatrix} \sigma_{11} & \sigma_{12} & \sigma_{13} \\ \sigma_{21} & \sigma_{22} & \sigma_{23} \\ \sigma_{31} & \sigma_{32} & \sigma_{33} \end{bmatrix} \tag{A-39}$$

The tensor components $i = j$ and $i \neq j$ are called normal stress and shear stress, respectively.

A.2.2 Cauchy’s Laws of Motion

In kinetics of mechanical systems three kinds of forces are acting on a continuum body in general:

- Surface forces
- Volume forces
- Inertia forces

These forces have to satisfy the translational and rotational equilibrium.

The global (integral over the volume of the body) translational equilibrium equation in the current configuration is

$$\underbrace{\int \boldsymbol{\sigma n}\, da}_{surface\ force} + \underbrace{\int \boldsymbol{f}\, dv}_{volume\ force} - \underbrace{\int \rho \dot{\boldsymbol{v}}\, dv}_{inertia\ force} = 0 \tag{A-40}$$

By applying the divergence theorem to the surface force term the surface integral can be converted to a volume integral by

$$\int \boldsymbol{\sigma n}\, da = \int \boldsymbol{div\sigma}\, dv = \int \nabla_{\boldsymbol{x}} \cdot \boldsymbol{\sigma}\, dv \tag{A-41}$$

giving the global translational equilibrium as

$$\int (\nabla_{\boldsymbol{x}} \cdot \boldsymbol{\sigma} + \boldsymbol{f} - \rho \dot{\boldsymbol{v}})\, dv = 0 \tag{A-42}$$

or in local (particle) formulation

$$\nabla_{\boldsymbol{x}} \cdot \boldsymbol{\sigma} + \boldsymbol{f} - \rho \dot{\boldsymbol{v}} = 0 \tag{A-43}$$

This equation, whether in global or local formulation, is called “Cauchy’s First Law of Motion”[3].

A different formulation of this equation yields one of the fundamental equations of physics, the “Conservation of Translational Momentum”

$$\frac{D}{Dt}\int \rho \boldsymbol{v}\ dv = \int \nabla_{\boldsymbol{x}} \cdot \boldsymbol{\sigma}\ dv + \int \boldsymbol{f}\, dv = 0 \tag{A-44}$$

Similar to the translational equilibrium the rotational equilibrium about an arbitrary point x, e.g. the origin, can be written as

$$\underbrace{\int \boldsymbol{x} \times (\boldsymbol{\sigma n})\, da}_{surface\ moment} + \underbrace{\int \boldsymbol{x} \times \boldsymbol{f}\, dv}_{volume\ moment} - \underbrace{\int \boldsymbol{x} \times \rho \dot{\boldsymbol{v}}\, dv}_{inertia\ moment} = 0 \tag{A-45}$$

The application of the divergence theorem on the surface moment term with $\boldsymbol{\epsilon}$ (Levi-Civita symbol) as the third order permutation tensor gives now

$$\int \boldsymbol{x} \times (\boldsymbol{\sigma n})\, da = \int (\boldsymbol{x} \times \nabla_{\boldsymbol{x}} \cdot \boldsymbol{\sigma} + \boldsymbol{\epsilon} : \boldsymbol{\sigma}^T)\, dv \tag{A-46}$$

---

[3] Also referred to as “Newton’s Second Law”

Exchanging this term in the rotational equilibrium gives

$$\int \boldsymbol{x} \times (\underbrace{\nabla_{\boldsymbol{x}} \cdot \boldsymbol{\sigma} + \boldsymbol{f} - \rho\dot{\boldsymbol{v}}}_{\substack{translational\\equilibrium\\=0}})\, dv = \int \boldsymbol{\epsilon}\colon \boldsymbol{\sigma}^T\, dv = 0 \tag{A-47}$$

Hence, the right term of this equation proves that the “Cauchy Stress Tensor” is symmetric.

$$\boldsymbol{\sigma} = \boldsymbol{\sigma}^T \tag{A-48}$$

This proof is called “Cauchy’s Second Law of Motion”.

As for the translational equilibrium, a different formulation yields another fundamental equation in physics called “Conservation of Rotational Momentum”

$$\frac{D}{Dt}\int \boldsymbol{x} \times \rho\boldsymbol{v}\, dv = \int \boldsymbol{x} \times \nabla_{\boldsymbol{x}} \cdot \boldsymbol{\sigma}\, dv + \int \boldsymbol{x} \times \boldsymbol{f}\, \boldsymbol{dv} = 0 \tag{A-49}$$

Note that these “Conservation of Momentum” equations and the “Cauchy Stress Tensor” are defined in the current configuration. These equations can also be derived in the reference configuration. This requires additional stress tensor representation. Stress tensors fulfilling these requirements are the “First Piola-Kirchhoff Stress Tensor” and the “Second Piola-Kirchhoff Stress Tensor”, for instance.

A.2.3 Piola-Kirchhoff Stress Tensors

Stress tensors can also be defined in the reference configuration. For many problems in structural mechanics it’s sufficient to stay in the Lagrangian description. An Eulerian description is not necessary, especially for infinitesimal deformation and small strains. Therefore, additionally to the Cauchy stress tensor another two stress tensors called “First Piola-Kirchhoff Stress Tensor” and the “Second Piola-Kirchhoff Stress Tensor” are introduced.

Relating the actual force in the current configuration to the area in the reference configuration, gives the traction vector to

$$\boldsymbol{t}^P = \frac{d\boldsymbol{p}}{dA} \tag{A-50}$$

Similar to the Cauchy stress tensor the “First Piola-Kirchhoff Stress Tensor” is defined as

$$\boldsymbol{t}^P = \boldsymbol{PN} \tag{A-51}$$

and its relationship to the Cauchy stress tensor can be expressed as

$$\boldsymbol{P} = (det\boldsymbol{F})\boldsymbol{F}^{-1}\boldsymbol{\sigma} \tag{A-52}$$

Due to the fact that the deformation gradient $\boldsymbol{F}$ is not symmetric, the “*First Piola-Kirchhoff Stress Tensor”* isn’t either. An asymmetric tensor can cause problems in combination with constitutive models and numerical algorithms in general. To get a symmetric stress tensor in

Lagrangian description the “pull back” of the force vector in the current configuration is introduced, which gives the force vector in reference configuration to

$$d\boldsymbol{\mathcal{P}} = \boldsymbol{F}^{-1} d\boldsymbol{p} \tag{A-53}$$

Analog to the “First Piola-Kirchhoff Stress Tensor” the stress vector in so called “Total Lagrangian Description“ is

$$\boldsymbol{t}^{S} = \frac{d\boldsymbol{\mathcal{P}}}{dA} = \boldsymbol{SN} \tag{A-54}$$

with $\boldsymbol{S}$ as the “Second Piola-Kirchhoff Stress Tensor”.

Substitution of these terms gives the relationship to the Cauchy stress tensor as

$$\boldsymbol{S} = (det\boldsymbol{F})\boldsymbol{F}^{-1}\boldsymbol{\sigma}\boldsymbol{F}^{-T} \tag{A-55}$$

The “Second Piola-Kirchhoff Stress Tensor” is a symmetric stress tensor.

The “Conservation of Momentum” equations in Lagrangian description are not explicitly mentioned here, but can be found in relevant literature by Bonet and Wood (1997), Holzapfel (2000) or Altenbach (2012).

A.3 Conservation of Mass

The principle of “Conservation of Mass” states that the mass of a body remains constant as long as there is neither loss nor growth over the surface or the inside. In other words the mass of a body or point before and after deformation is the same and therefore constant over the whole time.

$$m = \int \rho(\boldsymbol{x}, t)dv = \int \rho_0(\boldsymbol{X}, t)dV \tag{A-56}$$

Even though the mass remains constant over time, the density and the volume may change. The relationship between the density in reference and current configuration of a particle is

$$\rho_0(\boldsymbol{X}, t) = \rho(\boldsymbol{x}, t)det\boldsymbol{F}(\boldsymbol{X}, t) \tag{A-57}$$

For fluid mechanical problems the rate of change in time of mass moving through the domain is from main interest. Therefore, the total or material time derivative in the current configuration must be calculated, under consideration of the volume v to be also time dependent. The easier way to achieve the material time derivative is to transform the rate of change in density over time into the “Lagrangian Description” first.

Since the density in the reference configuration ρ_0 is constant, the time derivative yields

$$\frac{D}{Dt}\rho_0(\boldsymbol{X}, t) = \frac{D}{Dt}\rho(\boldsymbol{x}, t)det\boldsymbol{F}(\boldsymbol{X}, t) = 0 \tag{A-58}$$

By applying the product rule to the second term of this equation one can write

$$\frac{D}{Dt}\rho(\boldsymbol{x},t)det\boldsymbol{F}(\boldsymbol{X},t) = \frac{D\rho(\boldsymbol{x},t)}{Dt}det\boldsymbol{F}(\boldsymbol{X},t) + \rho(\boldsymbol{x},t)\frac{D}{Dt}det\boldsymbol{F}(\boldsymbol{X},t) = 0 \tag{A-59}$$

The time derivative of $det\boldsymbol{F}$ can be mathematically derived and proved to be

$$\frac{\partial}{\partial t}det\boldsymbol{F}(\boldsymbol{X},t) = det\boldsymbol{F}(\boldsymbol{X},t)\nabla_{\boldsymbol{x}} \cdot \boldsymbol{v} \tag{A-60}$$

Substituting this term and dividing by $det\boldsymbol{F}(\boldsymbol{X},t)$ finally yields

$$\frac{Dm}{Dt} = \dot{m}(t) = \frac{D}{Dt}\int \rho(\boldsymbol{x},t)dv = \int \left[\frac{D\rho(\boldsymbol{x},t)}{Dt} + \rho(\boldsymbol{x},t)\nabla_{\boldsymbol{x}} \cdot \boldsymbol{v}\right] dv = 0 \tag{A-61}$$

Or in local formulation in simplified notation

$$\frac{D\rho}{Dt} + \rho\nabla_{\boldsymbol{x}} \cdot \boldsymbol{v} = 0 \tag{A-62}$$

This equation is known as the “Continuity Equation” or “Conservation of Mass”. It can also be expressed in terms of the spatial rate of the density as

$$\frac{\partial\rho}{\partial t} + \nabla_{\boldsymbol{x}} \cdot \rho\boldsymbol{v} = 0 \tag{A-63}$$

The “Conservation of Momentum” equation from Section A.2.2 and the “Continuity Equation” are the fundamental equations in fluid dynamics.

A.4 Principle of Virtual Work

In terms of finite element analyses in structural mechanics the “Principle of Virtual Work” is the obligatory basis. The idea is to apply a virtual displacement (or in general, a test function) on the body’s current position. The virtual work done by a body or particle is than defined as force times the virtual displacement. The application of this principle to “Cauchy’s First Law of Motion” from Section A.2.2 therefore gives

$$\delta W = \int (\nabla_{\boldsymbol{x}} \cdot \boldsymbol{\sigma} + \boldsymbol{f} - \rho\dot{\boldsymbol{v}}) \cdot \delta\boldsymbol{u}\, dv = 0 \tag{A-64}$$

Subsequently, applying the product rule to $\nabla_{\boldsymbol{x}} \cdot \boldsymbol{\sigma}$ and the divergence theorem yields the “Principle of Virtual Work” equation as

$$\int \boldsymbol{\sigma}: \delta\boldsymbol{e}\, dv - \int (\boldsymbol{f} - \rho\dot{\boldsymbol{v}}) \cdot \delta\boldsymbol{u}\, dv - \int \boldsymbol{t} \cdot \delta\boldsymbol{u}\, da = 0 \tag{A-65}$$

with $\delta\boldsymbol{e}$ as the variation of the “Almansi-Euler Strain Tensor” and $\boldsymbol{t}$ as the traction vector from Section A.2.1.

The procedure of using a test function or in this case the virtual displacement with respect to finite elements is commonly known as the “Weak Form” of a boundary value problem and is based on “Variational Principles”.

A.5 Application of Strain and Stress Tensors

The introduced strain and stress tensors in Section A.1.4, A.2.1 and A.2.3 are defined in different configuration and therefore, they are used for different problems. Nonlinear problems can be classified in general into two types, geometric nonlinearity and material nonlinearity. Furthermore, in geometric nonlinear problems one has to distinguish between large strains and large displacements/rotations. If one wants to model large displacements/rotations with small strains the use of a nonlinear strain measure is mandatory, because infinitesimal strain measures cannot account for rigid body rotations. Thus, one can distinguish[4], according to the expected behaviour of the system, between

- Infinitesimal strains and displacements/rotations
  The engineering strain in combination with “Cauchy’s Stress Tensor” is sufficient. Regardless of the linear geometry, nonlinear material behaviour can also be modelled with this approach.

- Infinitesimal strains – Large displacements/rotations
  In this case, to account for large displacements/rotations, the nonlinear strain according to “Green-Lagrange” is used in coherence with the “Second Piola-Kirchhoff Stress Tensor”. Due to fact that both, the strain and stress measure, are defined in “Lagrangian Description” it’s called “Total Lagrangian Description”.
  Additionally, in structural mechanics, there is another description called “Updated Lagrangian Description”. Contrary to the “Total Lagrangian Description” the reference configuration is now the current configuration. That implies that the strain and stress tensor in Eulerian coordinates have to be used, which are the “Almansi-Euler Strain Tensor” and the “Cauchy Stress Tensor”.
  These two descriptions are applicable to linear and nonlinear material descriptions and will yield the same result, considering the right constitutive tensors, respectively.

- Large strains and displacements/rotations
  The same stress and strain tensors for the “Total Lagrangian Description” are applicable as for system with large displacements/rotations and infinitesimal strains.
  In the “Updated Lagrangian Description” the strain has to be changed to the logarithmic strain measure called natural strain or “Hencky Strain”.
  In this case again, both descriptions are applicable to linear and nonlinear material descriptions, but accompanied by major complexities in the constitutive equations, due to large strains.

---

[4] This allocation of infinitesimal or large strains and displacements/rotations is based mainly on Bathe (2007)

B INTRODUCTION TO THE EXTENDED FINITE ELEMENT METHOD FOR STRONG DISCONTINUITIES (XFEM)

Generally, discontinuities can be categorized in strong (e.g. cracks, dislocations, etc.) and weak ones (e.g. material interaction, pores etc.). This section is only dealing with strong discontinuities by means of cracks and gives a brief introduction to the theory behind the Extended Finite Element Method (XFEM). The following overview of the method is primary based on Belytschko et al. (2014) a more comprehensive description of the overall theory and weak discontinuities can be found in Fries and Belytschko (2010).

B.1 Modelling Discrete Continuities

For modelling discrete discontinuities, such as propagating cracks, the finite element method has some drawbacks, because of its mesh dependency. In case of fracture of a material two common possibilities with the finite element method are:

- The remeshing procedure
  In this method cracks are only allowed to develop along element edges and therefore remeshing is necessary for a proper consideration of the corresponding effects and crack propagation.
  Belytschko et al. (2014) stated the following 4 typical disadvantages:
  1. Feature-conforming mesh generation is more demanding on the mesh generator.
  2. Considerable computational resources are spent on remeshing
  3. Projection schemes can introduce errors into solution
  4. The ever-changing mesh poses difficulties for post-processing and solution interpretation
- Element deletion
  Elements are deleted and their contribution to the global stiffness matrix is omitted. Needless to say that this method is heavily mesh-dependent.

Such procedures are called conforming mesh methods. In contrast to these methods, XFEM allows for cracks which are propagating through the elements and hence isn’t dependent on the mesh topology (non-conforming mesh method). This fact gives some major advantages regarding discretization. The differences in the mesh topology are depicted in Figure B-1 from Belytschko et al. (2014).

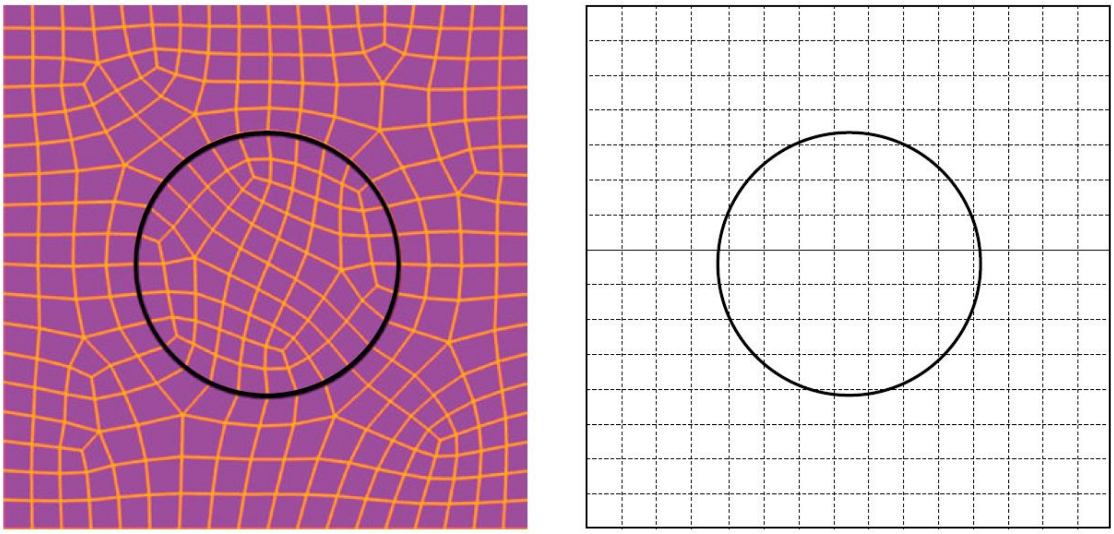

Figure B-1: Conforming mesh required by classical FEM (left) and non-conforming mesh permissible by XFEM (right) by Belytschko et al. (2014)

XFEM originated in 1999 by Belytschko and Black (1999) where they added enrichment functions to the finite element approximation to account for the presence of a crack which can propagate arbitrary through elements. The method is based on so called enriched methods, which are in this case the partition of unity method (PUM) and the generalized finite element method (GFEM).

B.2 Partition of Unity Concept and Enrichment

The concept of partition of unity states that the sum of all values of a function at a specific location $\boldsymbol{X}$ is 1. Expressed mathematically, this fact gives

$$\sum \varphi(\boldsymbol{X}) = 1 \tag{B-1}$$

This also holds for finite element shape functions in the Lagrangian description. Furthermore, any of such functions can be reproduced by the product of functions that satisfy this concept. Under this circumstances the finite element approximation in terms of displacement $\boldsymbol{u}$ can be written as

$$\boldsymbol{u}^h(\boldsymbol{X}) = \sum \boldsymbol{N}_I(\boldsymbol{X}) \Psi(\boldsymbol{X})\, \boldsymbol{u}_I \tag{B-2}$$

with $\Psi(\boldsymbol{X})$ as an arbitrary function fulfilling the concept of unity and $\boldsymbol{N}_I(\boldsymbol{X})$ as the shape functions in Lagrangian coordinates. In standard finite elements $\Psi(\boldsymbol{X})$ is 1. This possibility of introducing a function $\Psi(\boldsymbol{X})$ to the approximations leads to the idea and therefore a major concept of XFEM, to use other function than $\Psi(\boldsymbol{X}) = 1$, like a Heaviside function, which is

$$H(\alpha) = \begin{cases} 1, & \alpha > 0 \\ 0, & \alpha \leq 0 \end{cases} \tag{B-3}$$

This function is eminently suitable for strong discontinuities, where in the pre-crack state the value $H(\alpha)$ would be 0 and after cracking the value is 1. (Figure B-2)

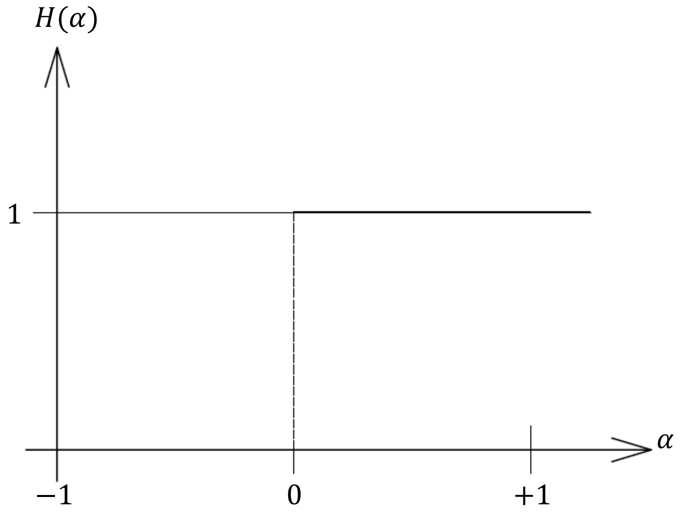

Figure B-2: Illustration of the Heaviside function

The finite element approximation of displacement with the global enriched term (indices I for both terms) describing the crack of an element can now be written as

$$\boldsymbol{u}^h(\boldsymbol{X}) = \underbrace{\sum \boldsymbol{N}_I(\boldsymbol{X})\boldsymbol{u}_I}_{\substack{finite\ element\\ approximation}} + \underbrace{\sum \boldsymbol{N}_I(\boldsymbol{X})H(\alpha)\,\boldsymbol{q}_I}_{Enrichment} \tag{B-4}$$

with the nodal values $\bar{\boldsymbol{q}}$ which are unknown parameters describing the enrichment and approximate the solution. Note that in equation (B-4) the same shape functions $\boldsymbol{N}_I(\boldsymbol{X})$ are used for the finite element displacement and the enrichment for all nodes of the domain (global enrichment)

Important to mention is that the enrichment is only necessary in regions where the crack occurs, which is a key advantage to the PUM and GFEM, where global enrichment functions are used, leading to non-sparse matrices and hence increased computational effort. Belytschko et al. (2014) additionally stated that the combination of the traditional degrees of freedom $\boldsymbol{u}$ and the additional degrees of freedom $\boldsymbol{q}$, consequently lose their kinematic meanings on their own and only their combination give the full description of the solution.

B.3 Level Set Functions and Shifting of the Enrichment

For describing cracks along a surface signed distance functions $\phi(\boldsymbol{X})$, also called level set functions, are mainly used. Such functions in a closed interface of two domains yield positive values in one and negative values in the other domain. In case one-dimensional truss the crack interface is represented by a point. For a two-dimensional problem the crack is simply a line and therefore needs distance functions for the crack in normal and shear direction. Therefore, these functions represent the interface between two domains and are always one dimension higher than the dimension of the interface. Further description of these functions can be found in Belytschko et al. (2014), Fries and Belytschko (2010) and relevant literature and are not further discussed in this section.

The advantage of signed distance functions is the combination with the Heaviside function from equation (B-3).

$$H(\phi(\boldsymbol{X})) = \begin{cases} 1, & \phi(\boldsymbol{X}) > 0 \\ 0, & \phi(\boldsymbol{X}) \leq 0 \end{cases} \tag{B-5}$$

So, the choice of the enrichment function is triggered by the sign of the level set function. The enriched finite element approximation now is

$$\boldsymbol{u}^h(\boldsymbol{X}) = \sum \boldsymbol{N_I}(\boldsymbol{X})\boldsymbol{u_I} + \sum \boldsymbol{N_J}(\boldsymbol{X})H(\phi(\boldsymbol{X}))\,\boldsymbol{q_J} \tag{B-6}$$

Note that the indices $\boldsymbol{J}$ in the enriched term now refer to the set of nodes of elements which are intersected. Whether an element is affected by an intersection or not can easily be determined with the help of the level set function. If the following condition is met the element is intersected.

$$min(\phi(\boldsymbol{X})) \cdot \max(\phi(\boldsymbol{X})) < 0 \tag{B-7}$$

This condition is only fulfilled if the min or max terms have different signs, which is only the case if at least one node of an element is on a different side of the intersection than the others (different signs in the level set function).

In a discrete system the problem occurs that if some elements already have cracks and neighbouring elements don't (unenriched) an incompatibility in the displacement field is incorporated. Therefore a shift in the approximation is introduced as

$$\boldsymbol{u}^h(\boldsymbol{X}) = \sum \boldsymbol{N_I}(\boldsymbol{X})\boldsymbol{u_I} + \sum \boldsymbol{N_J}(\boldsymbol{X})\left[H(\phi(\boldsymbol{X}) - H(\phi(\boldsymbol{X_J}))\right]\boldsymbol{q_J} \tag{B-8}$$

This shifted enrichment recovers the Kronecker-δ property (diagonal matrix) from the finite element approximation from equation (B-2) and the effect on the nodes by $\boldsymbol{q_J}$ vanishes.

Apart from the incompatibility in the displacement field an additional problem occurs in the subset of elements and nodes which are enriched. In the transition zone of the intersection between fully enriched and non-enriched nodes the enrichment function cannot be reproduced exactly and the partition of unity condition is not reached. Figure B-3 by Fries and Belytschko (2010) illustrates this problem.

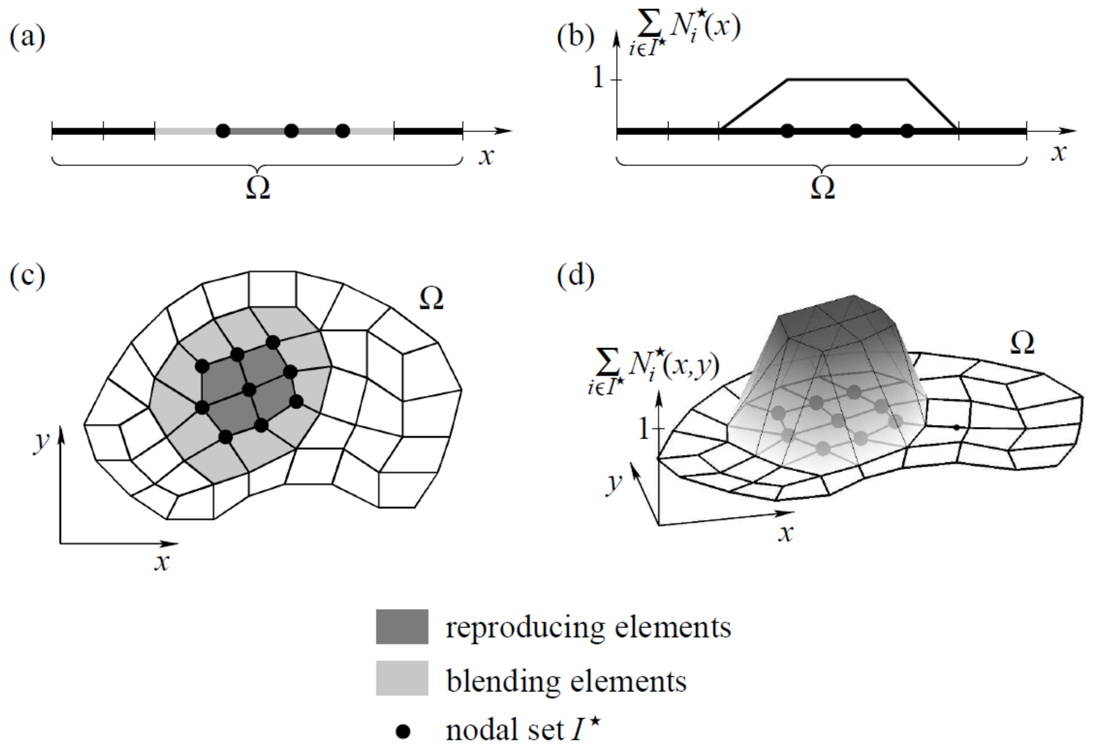

Figure B-3: Example of a discretized domain with a subset of enriched nodes by Fries and Belytschko (2010)

Hence, the elements can be categorized into standard finite elements (no enrichment), reproducing elements (all nodes are enriched) and blending elements (only a couple of nodes are enriched). Figure B-3 indicates that in case of blending elements the partition of unity concept is not fulfilled ($\sum \boldsymbol{N_I}(\boldsymbol{X}) \neq 1$). This fact leads to additional terms in the approximations and therefore may trigger convergence problems. However, different solutions for the problem are discussed in Fries and Belytschko (2010).

B.4 Crack Tip Enrichment

Additionally to the enrichment function describing the interface by a level set function $\phi(\boldsymbol{X})$ it is necessary to define an enrichment function for the crack tip $\psi(\boldsymbol{X})$ in case of strong discontinuities with open interfaces. Among others (see Fries and Belytschko (2010)), in this section only enrichments for brittle cracks in linear elastic fracture mechanics are mentioned, because it delivers a quite good description of the tensile failure of unreinforced concrete. Following enrichment functions describe the near tip behaviour for these assumptions in local coordinates r and θ

$$\psi(\boldsymbol{X}) = \sqrt{r}\left\{\sin\left(\frac{\theta}{2}\right), \sin\left(\frac{\theta}{2}\right)\sin(\theta), \cos\left(\frac{\theta}{2}\right), \cos\left(\frac{\theta}{2}\right)\sin(\theta)\right\} \qquad \text{(B-9)}$$

with r as the enrichment radius and θ as the angle to the tangent at the crack front. Figure B-4 by Fries and Belytschko (2010) illustrates the definition of the crack tip in the local coordinate system.

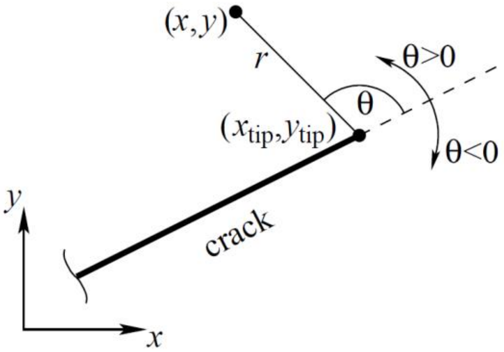

Figure B-4: Crack tip illustration and local coordinate system by Fries and Belytschko (2010)

The enriched finite element approximation from equation (B-8) for strong discontinuities with open interfaces in case of a brittle crack is now

$$\boldsymbol{u}^h(\boldsymbol{X}) = \sum \boldsymbol{N}_I(\boldsymbol{X})\boldsymbol{u}_I + \sum \boldsymbol{N}_J(\boldsymbol{X})\big[H(\phi(\boldsymbol{X}) - H(\phi\big(\boldsymbol{X}_J\big))\big]\,\boldsymbol{q}_J \\ + \sum_{n=1}^{4} \sum \boldsymbol{N}_K(\boldsymbol{X})[\psi^n(\boldsymbol{X}) - \psi^n(\boldsymbol{X}_K))]\,\boldsymbol{q}_K^n \tag{B-10}$$

where index K indicates the node set which is in the near field (determined by the radius r) of the crack tip.

The second term with the Heaviside and level set function is also referred to as step enrichment and the last term as crack tip enrichment. In standard XFEM codes Equation (B-8) with the step enrichment is used along the crack and the combined enrichment from Equation (B-10) is only used in the area of the crack tip.

C LIST OF ICOLD PUBLICATIONS REGARDING NUMERICAL ANALYSIS OF DAMS

C.1 Themes of Benchmark Workshops on Numerical Analysis of Dams from 1991 to 2015

1991 Bergamo (ENEL-ISMES)

- 1A The linear-elastic computation of a double-curvature concrete arch dam with its foundation under self-weight, hydrostatic load, thermal load
- 1B The seismic response of an embankment dam under conditions of both low and medium levels of seismic loadings.

1992 Bergamo (ENEL-ISMES)

- 2A Seismic analysis of the Talvacchia Dam
- 2B Static analysis and dynamic response of El Infiernillo embankment dam

1994 Paris (CFGB and Coyne et Bellier)

- 3A1 Nonlinear analysis of joint behaviour under thermal and hydrostatic loads for an arch dam
- 3A2 Evaluation of critical uniform temperature decrease for a cracked buttress dam
- 3B1 Evaluation of pore pressure and settlements of an embankment dam under static loadings
- 3B2 Dynamic analysis of an embankment dam under a strong earthquake

1996 Madrid (SPANCOLD)

- 4A1 Earthquake response of an arch dam including the nonlinear effects of contraction joint opening
- 4A2 Evaluation of Stress Intensity Factor KI along the tip of a crack in a buttress dam under thermal gradient effects (3D analysis)
- 4B1 Steady state and transient 2D unconfined seepage analysis for different typologies of earthfill dams
- 4B2 Effect of large foundation settlement on an embankment dam

1999 Denver (USCOLD)

- 5A1 Uplift pressure and stress analysis of an arch dam and foundation
- 5A2 Imminent failure flood level evaluation for a gravity dam with interface crack (rock/concrete) and varying uplift pressures
- 5B1 Evaluation of the global factor of safety against failure of an embankment dam
- 5B2 First fill of a rockfill dam - A case study

2001 Salzburg (ATCOLD and VERBUND)

- 6A Evaluation of AAR (Alkali - Aggregate Reaction) effects on the structural behaviour of an arch dam: interpretation of the measured behaviour and forecasting of the future trend
- 6B Prediction of the upstream face deflection of a CFRD during its first impounding
- 6C Interpretation of measurement results

2003 Bucharest (ROCOLD)

- 7A Evaluation of ultimate strength of gravity dams with curved shape against sliding
- 7B Thermal analysis of RCC gravity dam
- 7C Seepage through an earthfill dam - foundation system and piezometric level variation

2005 Wuhan (Wuhan University)

- 8A Evaluation of alkali-aggregate reaction effects on the behaviour of an Italian hollow gravity dam
- 8B Temperature field simulation and crack analysis of a RCC arch dam
- 8C Evaluation of the behavior and safety (static and dynamic) of a rockfill

2007 St Petersburg (VNIIG)

- 9A Analysis of the elastic behaviour of an arch-gravity dam
- 9B Stress-strain state of high rock-fill dam with a central earth core at large amplitude of operation water level changes in the upstream
- 9C Advanced numerical modelling for dams.

2009 Paris (Coyne et Bellier)

- 10A Initial strain and stress development in a thin arch dam considering realistic construction sequence
- 10B Analysis of a concrete faced rockfill dam including concrete face loading and deformation
- 10C Stability of a dam abutment including seismic loading

2011 Valencia (SPANCOLD)

- 11A Effect of concrete swelling on the equilibrium and displacements of an arch dam
- 11B Simulation of the behaviour of prototypes of rockfill dams during overtopping scenarios, seepage analysis and beginning of failure
- 11C Estimation of the probability of failure of a gravity dam for the sliding failure mode
- 11D Seismic behaviour of concrete face rockfill dams

2013 Graz (TU Graz and ATCOLD)

- 12A Fluid Structure Interaction Arch Dam - Reservoir at seismic loading
- 12B Long term behaviour of rockfill dams
- 12C Computational challenges in consequence estimation for risk assessment

2015 Lausanne (Laboratory of Hydraulic Constructions - École Polytechnique Fédérale of Lausanne)

- 13A Seismic safety evaluation of a concrete dam based on guidelines
- 13B Probability of failure of an embankment dam due to slope instability and overtopping
- 13C Safety evaluation of dams

C.2 ICOLD Bulletins regarding Dam Analysis and Seismic Modelling

No. 30	**Finite elements methods in analysis and design of dams**
No. 46	**Seismicity and dam design**
No. 52	**Earthquake analysis for dams**
No. 59	**Dam safety - Guidelines**
No. 61	**Dam design criteria - Philosophy of choice**
No. 62	**Inspection of dams after earthquakes -Guidelines**
No. 62A	**Inspection of dams following earthquake - Guidelines**
No. 72	**Selecting seismic parameters for large dams - Guidelines**
No. 94	**Computer software for dams - Validation**
No. 120	**Design features of dams to resist seismic ground motion**
No. 122	**Computational procedures for dam engineering - Reliability and applicability**
No. 123	**Seismic design and evaluation of structures appurtenant to dams**
No. 137	**Reservoirs and seismicity**
No. 148	**Selecting seismic parameters for large dams - Guidelines**
No. 155	**Guidelines for use of numerical models in dam engineering**